U.PORTO

FEUP FACULDADE DE ENGENHARIA
UNIVERSIDADE DO PORTO

Master's Dissertation in Mechanical Engineering on:

Numerical Micromechanical Analysis on the Influence of Monocrystalline Parameters on the Elastic and Yielding Response of Polycrystalline Aggregates

Author:
Rafael Rui Tenreiro Vieira

Supervisor:
Francisco Andrade Pires, Assistant Professor

Second Supervisors:
Daniel de Bortoli, Ph.D.
Miguel Vieira de Carvalho, M.Eng.

Submitted in fulfilment of the requirements
for the degree of Master in Mechanical Engineering by
Faculty of Engineering of the University of Porto

Porto, October 10, 2018

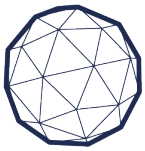

CM2S | Computational Multi-Scale Modeling of Solids and Structures

To my parents
and to Rita.

This page was intentionally left with this sentence.

"Quem quer passar além do Bojador
Tem que passar além da dor."

("Who wants to go beyond the Bojador
Must go beyond pain.")

Fernando Pessoa, *A Mensagem*

This page was intentionally left with this sentence.

Acknowledgements

First of all, I would like to thank my supervisor, Professor Francisco Pires, for all the support and advice given during these last months. His professional, patient and positive attitude, along with his vast experience and knowledge inspired and motivated me (even more) to excel.

Furthermore, I am deeply grateful to Dr. Daniel de Bortoli and Eng. Miguel Carvalho, the second supervisors of this dissertation. I owe a very important debt to them, because of their unlimited patience, profound knowledge and genuine sympathy. In short, their support and suggestions were invaluable. Similarly, a kind word must be given to all the members of CM2S research group for their sympathy and availability.

I would also like to express my acknowledgments to NORTE-01-0145-FEDER-000022 – SciTech – Science and Technology for Competitive and Sustainable Industries, I&D project co-funded by Programa Operacional Regional do Norte ("NORTE2020"), through the Fundo Europeu de Desenvolvimento Regional (FEDER).

Next, I would like to express my gratitude to all the friends I have made in the last five years. It is clear to me that the best part of my adventure at FEUP was all about the moments I shared with them.

Moreover, my deepest gratitude goes to my girlfriend, Rita, with whom I had the pleasure of enjoying the journey of life. Her kindness, friendship and love have been and surely will continue to be priceless.

In addition, I would like to express my sincere appreciation to my family, especially to my grandparents, Luís, Luísa, Altina and Augusto, and to my godmother, Maria da Graça, whose blind confidence in my capabilities have helped me to overcome all the obstacles I have faced until now.

Lastly, my strongest and heartfelt appreciation goes to my parents, Celina and Rui without which nothing of this would have been possible. They provided me all I needed and, above all, they raised me as a critical and free thinker.

My sincere gratitude to all,
Rafael Rui Tenreiro Vieira

This page was intentionally left with this sentence.

Abstract

Numerical Micromechanical Analysis on the Influence of Monocrystalline Parameters on the Elastic and Yielding Response of Polycrystalline Aggregates

In the last decades, multi-scale procedures based on computational homogenisation have established themselves as powerful tools to characterise the constitutive response of heterogeneous materials. In this work, with the intention of gaining a broader understanding of the use of these kind of techniques, they are applied to study the elastic and yielding response of single-phase textureless polycrystalline materials comprising cubic crystals. A finite element code was used to perform the numerical simulations from which the homogenised elastic properties and the global yield stress states, required to calibrate elastic and yielding constitutive laws, were obtained. The analyses were restricted to structured polycrystalline meshes and, in order to identify and study the influence of the critical microscopic features, hundreds of polycrystalline meshes (comprising different morphologies, number of grains and materials) have been studied. The elastic anisotropy of the single-crystals emerged as one of the most relevant microscopic properties for the description of the elastic and yielding response of polycrystals, as it strongly influences the distribution of stresses and strains within the polycrystals in the elastic domain. In particular, it was ascertained that the number of grains required to obtain isotropic elastic responses is directly proportional to the log-Euclidean anisotropy index (Kube, 2016) of the single-crystal and that the stress level required to initiate plastic slip on face-centered cubic aggregates decreases exponentially with the highlighted quantity. Furthermore, it was noticed that, once the global plastic deformation reaches a certain value (below 0.2%), the elastic parameters of face-centered cubic crystals have a reduced impact on the constitutive response of the underlying polycrystals (regardless of whether they are elastically isotropic or anisotropic). These conclusions were supported by testing several yield criteria that attempt to capture the onset of crystallographic slip and the end of the linear elastic stress-strain relation. On the whole, results were consistent with existing analytical and numerical models and, since the procedure followed can be easily adapted to analyse other polycrystalline aggregates, the framework used

has the potential to be employed for more complex materials.

Keywords: Polycrystals; Cubic crystal symmetry; Universal log-Euclidean anisotropy index; Computational homogenisation; Finite element method; Constitutive behaviour.

Resumo

Estudo Numérico Baseado na Análise de Agregados Policristalinos acerca da Influência dos Parâmetros Monocristalinos no Comportamento Constitutivo destes Materiais no Domínio Elástico e no Início da Cedência

Nas últimas décadas, a aplicação de técnicas multi-escala baseadas em homogeneização computacional para a caraterização da resposta constitutiva de materiais heterógeneos tornou-se numa ferramenta poderosa. Neste trabalho, com o intuito de adquirir um maior entendimento acerca deste tipo de procedimentos, o foco é direcionado para a sua utilização no contexto do estudo da resposta constitutiva de materiais policrista-linos no domínio elástico e início da cedência – em particular, estudaram-se agregados policristalinos monofásicos, sem textura e cujos cristais apresentam simetria cúbica. Com vista a obter as propriedades elásticas e as tensões de cedência requeridas para a calibração de leis constitutivas que governam o comportamento dos materiais policristalinos no domínio elástico e início da cedência, foi usado um código de elementos finitos. Todas as simulações numéricas foram realizadas em malhas policristalinas estruturadas e, de modo a tornar possível a identificação e análise do impacto dos parâmetros microscópicos críticos, centenas de policristais foram estudados (entre análises, variou-se a morfologia, o número de grãos do agregado e as propriedades dos materiais, entre outros aspetos). Neste contexto, a anisotropia elástica dos cristais emergiu como uma das variáveis micromecânicas que mais condiciona a resposta macroscópica, tanto no domínio elástico, como no início da cedência, visto que, para baixos níveis (ou ausência) de deformação plástica, ela afeta significativamente a distribuição de tensões e deformações no interior dos policristais. Em específico, verificou-se que o número de grãos necessário para se obter um comportamento elástico isotrópico aumenta proporcionalmente com o índice logarítmico de anisotropia universal (Kube, 2016); simultaneamente, constatou-se que a tensão macroscópica necessária para provocar o início de deslizamento cristalográfico em agregados de cristais cúbicos de faces centradas decresce exponencialmente com o referido índice. Além disto, concluiu-se que, uma vez atingido um certo nível de deformação plástica global (que é sempre inferior a 0.2%), os parâmetros elásticos dos cristais praticamente não afetam a resposta constitutiva de agregados policristalinos

(independentemente de os agregados possuírem um comportamento isotrópico ou anisotrópico no domínio elástico). Estas conclusões foram suportadas através do estudo de diferentes condições de cedência usadas para captar o início do deslizamento cristalográfico e o fim da região onde é válida a relação linear elástica entre tensões e deformações. Em suma, os resultados encontrados são consistentes com modelos analíticos e numéricos já existentes e, dado que o procedimento utilizado pode ser facilmente expandido para analisar outros tipos de policristais, todo o conteúdo usado ao longo deste trabalho tem o potencial necessário para ser empregue na caraterização da resposta constitutiva de materiais policristalinos mais complexos.

Palavras-chave: Policristais; Cristais com simetria cúbica; Índice logarítmico de anisotropia universal; Homogeneização computacional; Método dos elementos finitos; Comportamento constitutivo.

Contents

This page was intentionally left with this sentence.

List of Figures

Chapter 2
Continuum Mechanics, Thermodynamics and Finite Element Method

Chapter 3
Multi-Scale Models based on Computational Homogenisation

Chapter 4
On the Determination of the Elastic Response of Polycrystalline Aggregates

Chapter 5
Influence of the Monocrystalline Parameters on the Elastic Response of Polycrystalline Aggregates

List of Tables

Notation

General Scheme

a	Scalar
$\boldsymbol{a}$	Vector
$\boldsymbol{A}$	Second-order tensor
a, A	Fourth-order tensor
$\mathbf{a}$, $\mathbf{A}$	Finite elements array (vector, tensor)
$\mathscr{A}$	Space, set or body
$\mathfrak{A}$	Constitutive functional

Acronyms and Abbreviations

2D	Two-dimensional
3D	Three-dimensional
bcc	body-centered cubic
CM2S	Computational Multi-Scale Modeling of Solids and Structures
CMSA	Coupled Multi-Scale Analysis
CMT	Continuum Mechanics and Thermodynamics
dev.	deviation
fcc	face-centered cubic
FE	Finite Element
FEM	Finite Element Method
`Links`	Large Srain Implicit Non-Linear Finite Element Analysis of Solid Linking Scales
MEMS	Micro Electro-mechanical Systems
MSM	Multi-Scale Models
MSM-H	Multi-Scale Models based on Computational Homogenisation
NIEC	Number of Independent Elastic Components
NPES	Number of Planes of Elastic Symmetry

RVE	Representative Volume Element
TSV	Thermodynamics with State Variables

Indices

$(\cdot)_d$	Deviatoric component of $(\cdot)$
$(\cdot)_{dim}$	Dimensionless counterpart of $(\cdot)$
$(\cdot)^{\mathrm{DP}}$	Darrieulat and Piot yield function related quantity
$(\cdot)^e$	Elastic part of $(\cdot)$
$(\cdot)^{(e)}$	Element entity (within the Finite Element Method framework)
$(\cdot)^g$	Global entity (within the Finite Element Method framework); $(\cdot)$ expressed in relation to the global coordinate system
$(\cdot)^{\mathrm{H}}$	Hill model related quantity
$(\cdot)^{\mathrm{Hut}}$	Hutchinson approach related quantity
$(\cdot)^{\mathrm{HS}^+}$	Hashin-Shtrikman model related quantity (upper bound)
$(\cdot)^{\mathrm{HS}^-}$	Hashin-Shtrikman model related quantity (lower bound)
${}^h(\cdot)$	Finite element interpolation of $(\cdot)$
$(\cdot)_{\mathrm{iso}}$	Isochoric component of $(\cdot)$
$(\cdot)^l$	$(\cdot)$ expressed in relation to the local coordinate system
${}^{\mathrm{Lin}}(\cdot)$	Linear boundary model related entity
$(\cdot)_n$	$(\cdot)$ at time t_n (beginning of the standard subinterval $[t_n, t_{n+1}]$)
$(\cdot)_{n+1}$	$(\cdot)$ at time t_{n+1} (end of the standard subinterval $[t_n, t_{n+1}]$)
$(\cdot)^p$	Plastic part of $(\cdot)$
${}^{\mathrm{Per}}(\cdot)$	Periodic boundary model related entity
$(\cdot)^{\mathrm{R}}$	Reuss model related quantity
$(\cdot)^s$	Solid part of $(\cdot)$
$(\cdot)^{\mathrm{SC}}$	Self-consistent model related quantity
$(\cdot)^t$	History of $(\cdot)$ up to time t
$(\cdot)_t$	Traction related entity
${}^{\mathrm{Tay}}(\cdot)$	Taylor model related entity
$(\cdot)^{\mathrm{Tr}}$	Tresca yield function related quantity
$(\cdot)_u$	Displacement related entity
${}^{\mathrm{Uni}}(\cdot)$	Uniform boundary traction model related entity
$(\cdot)^v$	Void part of $(\cdot)$
$(\cdot)_{\mathrm{vol}}$	Volumetric component of $(\cdot)$
$(\cdot)^{\mathrm{V}}$	Voigt model related quantity
$(\cdot)^{\mathrm{VM}}$	Von Mises yield function related quantity
$(\cdot)^\alpha$	$(\cdot)$ of slip system α

$(\cdot)_\mu$	Microscopic $(\cdot)$
$\hat{(\cdot)}$	Incremental constitutive function for $(\cdot)$
$(\cdot)^-$	Lower bound of $(\cdot)$
$(\cdot)^+$	Upper bound of $(\cdot)$
$(\cdot)_0$	Associated with the initial configuration

Operators

$\det(\cdot)$	Determinant of $(\cdot)$
$\mathrm{div}_{\boldsymbol{p}}(\cdot)$	Material divergence of $(\cdot)$
$\mathrm{div}_{\boldsymbol{x}}(\cdot)$	Spatial divergence of $(\cdot)$
$\ln(\cdot)$	Natural logarithm (including tensor logarithm) of $(\cdot)$
$\max(\cdot)$	Maximum of $(\cdot)$
$\min(\cdot)$	Minimum of $(\cdot)$
$\mathrm{skew}(\cdot)$	Skew-symmetric part of $(\cdot)$
$\mathrm{sym}(\cdot)$	Symmetric part of $(\cdot)$
$\mathrm{tr}(\cdot)$	Trace of $(\cdot)$
$\delta(\cdot)$	Iterative increment of $(\cdot)$
$\Delta(\cdot)$	Increment of $(\cdot)$
$\nabla_{\boldsymbol{p}}(\cdot)$	Material gradient of $(\cdot)$
$\nabla_{\boldsymbol{x}}(\cdot)$	Spatial gradient of $(\cdot)$
$\nabla^s_{\boldsymbol{p}}(\cdot)$	Symmetric material gradient of $(\cdot)$
$\nabla^s_{\boldsymbol{x}}(\cdot)$	Symmetric spatial gradient of $(\cdot)$
$\partial(\cdot)$	Boundary of the domain $(\cdot)$
$\frac{\partial(\cdot)}{\partial a}$	Derivative of $(\cdot)$ with respect to a
$\dot{(\cdot)}$	Material first order time derivative of $(\cdot)$
$\ddot{(\cdot)}$	Material second order time derivative of $(\cdot)$
$(\cdot)^T$	Transpose of $(\cdot)$
$\boldsymbol{a} \cdot \boldsymbol{b}$	Single contraction of two generic vectors $\boldsymbol{a}$ and $\boldsymbol{b}$
$\boldsymbol{A} \cdot \boldsymbol{b}$	Single contraction of generic tensor $\boldsymbol{A}$ and generic vector $\boldsymbol{b}$ (normally $\cdot$ is omitted and we simply write $\boldsymbol{Ab}$)
$\boldsymbol{A} \cdot \boldsymbol{B}$	Single contraction of generic tensors $\boldsymbol{A}$ and $\boldsymbol{B}$ (normally $\cdot$ is omitted and we simply write $\boldsymbol{AB}$)
$\boldsymbol{a} \times \boldsymbol{b}$	Cross product of generic vector $\boldsymbol{a}$ by vector $\boldsymbol{b}$
$\boldsymbol{a} \otimes \boldsymbol{b}$	Tensor product of generic vectors $\boldsymbol{a}$ and $\boldsymbol{b}$
$\boldsymbol{A} : \boldsymbol{B}$	Double contraction of two generic tensors $\boldsymbol{A}$ and $\boldsymbol{B}$
$a * b$	Appropriate product between two generic entities a and b
$\|\boldsymbol{a}\|$	Euclidean norm of generic vector $\boldsymbol{a}$
$\|\boldsymbol{A}\|$	Euclidean norm of generic tensor $\boldsymbol{A}$

Variables

A^{CB}	Chung-Buessem anisotropy index
A^{L}	Universal log-Euclidean anisotropy index
A^{LM}	Ledbetter-Migliori anisotropy index
A^{U}	Universal anisotropy index
A^{Z}	Zener anisotropy index
A_k	Generic conjugate thermodynamical force
$\mathrm{AVG}(\mathsf{C}^{ij}_{\mathrm{NG}})$	Average of the C^{ij}-type elastic constants of NR realizations of a polycrystal comprising NG grains
$\mathrm{AVG}(\mathsf{C}^{ij}_{\mathrm{NG}})_{dim}$	Dimensionless average of the C^{ij}-type elastic constants of NR realizations of a polycrystal comprising NG grains
$\mathrm{AVG}(E_{\mathrm{NG}})$	Average of the Young's modulus of a polycrystal comprising NG grains
$\mathrm{AVG}(E_{\mathrm{NG}})_{dim}$	Dimensionless average of the Young's modulus of NR realizations of a polycrystal comprising NG grains
$\mathrm{AVG}(E_{\mathrm{NG}})_{\mathrm{NR}}$	Average of the Young's modulus of NR realizations of a polycrystal comprising NG grains
$\mathrm{AVG}(\sigma_y^{\mathrm{T}})$	Average Tresca yield stress
$\mathrm{AVG}(\sigma_y^{\mathrm{VM}})$	Average Von Mises yield stress
$\boldsymbol{a}$, $\boldsymbol{b}$, $\boldsymbol{c}$	Lattice parameters
$A^{\alpha\beta}$	Coplanarity matrix
$\boldsymbol{A}$	Generic set of conjugate thermodynamical forces
a	Consistent spatial tangent modulus
A	Consistent material tangent modulus
$\mathscr{A}$	Set comprising the slip systems
$\boldsymbol{b}$	Body forces vector per unit deformed volume
$\boldsymbol{b}_0$	Body forces vector per unit reference volume
$\boldsymbol{B}$	Left Cauchy-Green strain tensor
$\mathbf{B}$	Discrete symmetric gradient operator
$\mathscr{B}$	Generic continuum body
c	Parametric mapping function
$\boldsymbol{C}$	Right Cauchy-Green strain tensor
C	Elasticity/Stiffness tensor
C^{11}	C^{11}-type elastic constants (set composed of C_{11}, C_{22} and C_{33})
C^{12}	C^{12}-type elastic constants (set composed of C_{12}, C_{13} and C_{23})
C^{44}	C^{44}-type elastic constants (set composed of C_{44}, C_{55} and C_{66})
C^{14}	C^{11}-type elastic constants (set composed of C_{14}, C_{15}, C_{16}, C_{24}, C_{25}, C_{26}, C_{34}, C_{35}, C_{36}, C_{45}, C_{46} and C_{56})
da	Local infinitesimal area in the deformed configuration

da_0	Local infinitesimal area in the reference configuration
$d\boldsymbol{p}$	Local infinitesimal length in the reference configuration
dv	Local infinitesimal volume in the deformed configuration
dv_0	Local infinitesimal volume in the reference configuration
$d\boldsymbol{x}$	Local infinitesimal length in the deformed configuration
$\boldsymbol{d}$	Generic direction in the three-dimensional space
$\boldsymbol{D}$	Stretching tensor
e	Specific energy
e_{adj}	Error of fit to numerical data
E	Young's modulus
E_{NG}, $(E_{\mathrm{NG}})_1$	Young's modulus in a random direction (of a polycrystal comprising NG grains)
E_{tol}	Maximum admissible value for the standard deviation of the Young's modulus in order to obtain an isotropic response
$\boldsymbol{e}_i$	Generic base vector; unit eigenvector of the left stretch tensor associated with the i^{th} eigenvalue
$\boldsymbol{E}^e$	Green-Lagrange elastic strain tensor
$\boldsymbol{E}^{(m)}$	Lagrangian strain tensor of order m
$\boldsymbol{E}^{(2)}$	Green-Lagrange strain tensor
$\mathscr{E}$	Three-dimensional Euclidean space; Elastic domain
$\bar{\mathscr{E}}$	Set of plastically admissible stresses
$\boldsymbol{g}$	Spatial divergence of temperature field
$\boldsymbol{F}$	Deformation gradient
$\mathbf{f}_{int}$	Internal nodal force vector (within the finite element framework)
$\mathbf{f}_{ext}$	External nodal force vector (within the finite element framework)
$\mathfrak{F}$	Constitutive functional for the Cauchy stress tensor
G	Shear modulus
G_1	Resistance to a shearing stress applied across the (110) plane in the $[1\bar{1}0]$ direction (applicable to cubic crystals)
G_2	Resistance to a shearing stress applied across the (100) plane in the [010] direction (applicable to cubic crystals)
$\mathbf{G}$	Discrete spatial gradient operator
$\mathfrak{G}$	Constitutive functional for the specific free energy
$h^{\alpha\beta}$	Hardening coefficients matrix
$\mathfrak{H}$	Constitutive functional for the specific entropy
$\boldsymbol{I}$	Second-order identity tensor
$\mathbf{I}_d$	Deviatoric projection tensor
$\mathbf{I}_S$	Fourth-order symmetric identity tensor
$\mathscr{I}$	Symmetry group of a solid material
$\mathfrak{I}$	Constitutive functional for the heat flux
J	Determinant of the deformation gradient

J_2	Second invariant of the stress deviator $\boldsymbol{s}$
$\boldsymbol{l}_i$	Unit eigenvector of the right stretch tensor associated with the i^{th} eigenvalue
$\boldsymbol{L}$	Spatial velocity gradient
$\boldsymbol{L}_{macro}$	Length of the macroscopic body
$\boldsymbol{L}_{micro}$	Typical dimension of the micro-elements
$\boldsymbol{L}_{\mu}$	Size of the RVE
$\mathscr{L}$	Generic surface of a continuum
K	Bulk modulus; hardening parameter
$\mathbf{K}_T$	Global tangent stiffness matrix
m	Hardening exponent; exponent (parameter) of Darrieulat and Piot yield function
$\mathscr{K}$	Set of kinematically admissible displacements
$\mathscr{K}^*$	Set of minimally constrained kinematically admissible displacements
$\tilde{\mathscr{K}}$	Set of displacement fluctuations
$\tilde{\mathscr{K}}^*$	Set of minimally constrained displacement fluctuations
$\text{MAX}(E_{\text{NG}})$	Maximum value of the Young's modulus of a polycrystal comprising NG grains
$\text{MIN}(E_{\text{NG}})$	Minimum value of the Young's modulus of a polycrystal comprising NG grains
$\boldsymbol{m}$	Slip plane unit normal vector
$\boldsymbol{M}$	Schmid tensor
n	Exponent (parameter) of Darrieulat and Piot yield function
n_{dof}	Number of spatial dimensions
n_{elem}	Number of elements within a generic finite element mesh
n_{gaussp}	Number of considered Gauss points
n_{nodes}	Number of nodes of a generic finite element
n_{poin}	Number of points within a generic finite element mesh
n_{slip}	Number of slip systems
N_i	Shape function associated with node i
NG	Number of grains
NLD	Number of spatial directions
NR	Number of realizations
$\boldsymbol{n}$	Generic unit normal vector to a surface in the deformed configuration
$\boldsymbol{n}_0$	Generic unit normal vector to a surface in the reference configuration
$\mathbf{N}$	Interpolation matrix
$\mathscr{N}$	Set comprising all the grains of the polycrystal
$\boldsymbol{o}$	Origin of a generic lattice
$\mathscr{O}$	The orthogonal group
$\mathscr{O}^+$	The rotation (proper orthogonal) group

p	Cauchy hydrostatic pressure; parameter related to Brenner approach to formulate micro-yielding condition
p_i	Parameter
$\boldsymbol{p}$	Position of a generic particle in the reference configuration
$\boldsymbol{P}$	First Piola-Kirchhoff stress tensor
$\mathfrak{P}$	Constitutive functional for the Piola-Kirchhoff stress tensor
q	Latent hardening ratio
$\boldsymbol{q}$	Position of the center of rotation in a rigid rotation; heat flux
r	Density of heat production
$\boldsymbol{r}$	Position of a generic lattice point
$\boldsymbol{R}$	Generic rotation tensor; rotation tensor obtained from the polar decomposition of $\boldsymbol{F}$
$\mathbf{r}$	Global finite element residual force vector
s	Specific entropy
$\mathrm{STD}(\mathsf{C}^{ij}_{\mathrm{NG}})$	Standard deviation of the C^{ij}-type elastic constants of NR realizations of a polycrystal comprising NG grains
$\mathrm{STD}(\mathsf{C}^{ij}_{\mathrm{NG}})_{dim}$	Dimensionless standard deviation of the C^{ij}-type elastic constants of NR realizations of a polycrystal comprising NG grains
$\mathrm{STD}(E_{\mathrm{NG}})$	Standard deviation of the Young's modulus of a polycrystal comprising NG grains
$\mathrm{STD}(E_{\mathrm{NG}})_{dim}$	Dimensionless standard deviation of the Young's modulus of NR realizations of a polycrystal comprising NG grains
$\mathrm{STD}(E_{\mathrm{NG}})_{\mathrm{NR}}$	Standard deviation of the Young's modulus of NR realizations of a polycrystal comprising NG grains
$\mathrm{STD}(\sigma_y^{\mathrm{T}})$	Standard deviation of Tresca yield stresses
$\mathrm{STD}(\sigma_y^{\mathrm{VM}})$	Standard deviation of Von Mises yield stresses
$\boldsymbol{s}$	Cauchy deviatoric stress tensor; unit vector in the slip direction
$\boldsymbol{S}$	Second Piola-Kirchhoff stress tensor
S	Compliance tensor
t	time
$\boldsymbol{t}$	Cauchy stress vector; surface traction
$\boldsymbol{t}_0^*$	True Reference surface traction
$\boldsymbol{t}_0$	Reference surface traction
U	Strain energy function
$\boldsymbol{u}$	Displacement vector field
$\bar{\boldsymbol{u}}$	Prescribed boundary displacement field
$\tilde{\boldsymbol{u}}$	Displacement fluctuation field
$\boldsymbol{U}$	Right stretch tensor
$\mathbf{u}$	Global finite element vector of nodal displacements
v	volume in the deformed configuration
v_0	volume in the reference configuration

$\boldsymbol{v}$	Velocity vector field
$\boldsymbol{V}$	Left stretch tensor
$\mathscr{V}$	Space of admissible virtual displacements
$\mathscr{V}^*$	Space of minimally constrained admissible virtual displacements
w_i	Weight associated with Gauss point i
$\boldsymbol{W}$	Spin tensor
$\boldsymbol{x}$	Position of a generic particle in the deformed configuration
$\mathscr{Y}$	Yield surface
$\mathcal{Z}$	Set of integers
α	Contraction/dilation ratio; Generic slip system
α, β, γ	Angles between the lattice parameters
α_k	Generic internal variable (can be a scalar, vectorial or tensorial quantity)
$\boldsymbol{\alpha}$	Generic set of internal variables
γ	Glide strain
Γ	Standard integration domain
δ_{ij}	Kronecker delta
ϵ	Rate-sensitivity parameter
$\boldsymbol{\epsilon}^{(m)}$	Eulerian strain tensor of order m
ϵ_{tol}	Tolerance
ε	Equivalent total strain
ε_{dim}	Ratio of equivalent total strain
$\varepsilon_r(E)$	Relative error of the isotropic Young's modulus due to the mesh size
ε_{rr}	Maximum admissible value for the dimensionless standard deviation of the Young's modulus to obtain isotropic responses
$\boldsymbol{\varepsilon}$	Infinitesimal strain tensor
$\boldsymbol{\eta}$	Virtual displacement vector field
$\boldsymbol{\eta}$	Global finite element vector of virtual nodal displacements
θ	Temperature; polar angle
λ_i	Principal stretches
μ	Viscosity
ν	Poisson's ratio
$\boldsymbol{\xi}_i$	Natural coordinate vector; natural coordinates of Gauss point i
ρ	Mass per unit volume
ρ_0	Reference mass per unit volume
σ^{Tr}	Equivalent Tresca stress
σ_y^{uni}	Yield stress under uniaxial stress conditions
σ^{VM}	Effective Cauchy stress (or equivalent von Mises stress)
$\sigma_{dim}^{\mathrm{VM}}$	Ratio of effective Cauchy stress (or ratio of equivalent von Mises stress)
σ_i	Principal Cauchy stress
$\sigma_{i,dim}$	Dimensionless principal Cauchy stress

σ_{max}	Maximum Cauchy principal stress
σ_{min}	Minimum Cauchy principal stress
σ_y	Yield stress
$\sigma_{0.2}$	Conventional macro-yield stress
$\langle\sigma\rangle^r$	Average stress tensor of crystallite r
$\boldsymbol{\sigma}$	Cauchy stress tensor
$\boldsymbol{\sigma}^*$	Prescribed stress state
τ	Schmid resolved shear stress
τ_i	Principal Kirchhoff stress
τ_y	Critical resolved resolved shear stress
$(\hat{\tau}^\alpha)^r$	Reference resolved shear stress
$\langle\tau^\alpha\rangle^r$	Average resolved shear stress on slip system α of grain r
$(\tilde{\tau}^\alpha)^r$	Standard deviation of the resolved shear stress on slip system α of grain r
$\boldsymbol{\tau}$	Kirchhoff stress tensor
ϕ	Polar angle
Φ	Yield function
φ	Deformation mapping function; motion
φ^{iso}	Generic isotropic yield function
φ_1, φ_2, ϕ	Euler angles
ψ	Specific free energy
Ψ	Matrix whose columns include the eigenvectors of the Green-Lagrange strain tensor
Ω	Domain of a generic continuum body in the reference configuration

This page was intentionally left with this sentence.

Chapter 1

Introduction

In this work, we focus on performing numerical simulations with representative volume elements of polycrystals, such that analytical closed-form relations may be proposed to estimate their overall elastic and yielding responses. It is important to keep in mind that the study was restricted to single-phase textureless polycrystalline aggregates composed of cubic crystals and that grain boundaries were the unique type of heterogeneity considered. Another key point to mention is that this work expounds on the description of the elastic and the yielding response of anisotropic polycrystals (a topic which has not been addressed frequently in the past). Furthermore, even for isotropic polycrystals – for which several analytical and numerical models have already been developed – we attempted to provide answers to issues which are still under discussion (for example, the minimum size of representative volume elements for isotropic elastic polycrystals). All in all, not only have we found results consistent with the literature, but we have also helped shedding light into questions of practical relevance which are still open scientific discussions.

Our motivations are addressed in Section 1.1, while the main goal is summarised in Section 1.2. In this Chapter, we also present a literature review in Section 1.3 and discuss the structure of the document in Section 1.4. Finally, we must refer that a compilation of the notation introduced throughout this dissertation is located before the beginning of this Chapter, starting on page xxvii.

1.1 Motivation

The development of new heterogeneous materials has received widespread attention by both scientific and industrial communities over the last decades. The concept behind the development of these new materials is often associated with the introduction of one or more phases into the microstructure of another material with the objective of improving its properties, so that a new material, able to excel in particular contexts, arises (a classical example is the use of composite materials in the aerospace industry

due to their high specific strength when compared to most metallic alloys). One of the difficulties found in the process of developing these new materials is the characterisation of their mechanical behaviour: generally speaking, experimental procedures can be very expensive and time-consuming and analytical methods often incorporate assumptions that lead to coarse results. In this context, it is important to note that most conventional constitutive models assume the materials as homogeneous entities, that is, they assume uniform strain and stress field distributions within the infinitesimal neighbourhood of any macroscopic point. Models relying on the assumption of homogeneity are known as continuous models. Continuous models may be based on phenomenological or micromechanical considerations, but they do not consider all the phenomena taking place at the micro-scale. This is a significant downside of these models, as it is well-established that the macroscopic response is highly dependent on the phenomena taking place at the micro-scale, so that for materials (e.g., composites) with complex microstructures (containing voids, inclusions, etc), it is increasingly difficult to develop continuous models that can accurately describe their macroscopic behaviour. This explains why alternative approaches have been developed in order to predict, in a consistent fashion, the mechanical behaviour of materials with complex microstructures. Amongst them, we must highlight the ones involving *numerical homogenisation*. Within the framework of numerical homogenisation schemes, the stress-strain relation at each macroscopic integration point results from a homogenisation procedure, which follows the solution of a microscopic equilibrium problem over a *Representative Volume Element* (which may be seen as the smallest volume of the material that still contains all important microscopic features).

Within the scope of numerical homogenisation techniques, *Coupled Multi-Scale Analyses* (CMSA) actually associate a Representative Volume Element (RVE) with all integration points at the macro-scale, so that the macroscopic response is obtained without necessarily defining the constitutive equation in an explicit fashion. One of the biggest advantages of the coupled micro-macro scheme stems from the fact that the macroscopic behaviour emerges from the considered microstructure (independently of its complexity). Taking this into consideration and since both the macroscopic and microscopic equilibrium problems are commonly solved with the *Finite Element Method* (FEM), this two-scale scheme demands that, in practice, both problems be solved simultaneously. Despite the conceptual advantages of considering CMSA, the computational costs associated with these schemes are generally prohibitive. Hence, in order to obtain solutions to practical problems, the decoupling of the micro- and macro-scale equilibrium problems is often required.

The decoupled multi-scale approach mostly consists of an attempt to solve both problems separately. In fact, by solving the microscopic equilibrium problem and applying homogenisation procedures we can derive a macroscopic constitutive function that describes the macroscopic response of the material; once the macroscopic

constitutive behaviour is known, the conventional macroscopic equilibrium problem can then be solved independently. This means that we can derive constitutive laws considering exclusively the micro-scale. In general, the objective consists of making several numerical simulations at the micro-scale (involving the necessary loading conditions) so that an analytical relation can be defined to predict the overall behaviour of the material at the macro-scale (within the range of interest). We must be aware of the importance of modelling the microstructure correctly, since the results depend exclusively on the microscopic features embodied in the Representative Volume Elements being analysed. By the same token, despite the efforts directed towards the development of analytical solutions, finding close expressions to predict the macroscopic behaviour of heterogeneous materials (from micro-scale studies) remains an open field in many applications, especially whenever the plastic domain is reached. One of the possible explanations for this fact might result from the evolution of the microscopic morphology as the macroscopic continuum deforms, making it difficult to deduce analytical expressions that typically consider only the initial microstructural state of the material. Despite these downsides, micro-scale analyses based on computational homogenisation seem a very promising approach to study the overall behaviour of materials and may be used to characterize, in a consistent fashion, the constitutive response of new complex, multi-phase materials, provided that their microstructure can be conveniently modelled.

1.2 Main Goal

The main purpose of this work is to estimate the macroscopic elastic and yielding response of polycrystalline aggregates using closed-form analytical expressions deduced from numerical micromechanical analyses. In order to establish these expressions which link the macro- and the micro-scale, the critical microscopic parameters must be pinpointed and several numerical tests have to be performed on distinct representative volume elements, so that we may understand the real influence of key microscopic features.

It is important to remark that we mostly intend to get an in-depth view into the calibration of macroscopic constitutive laws from numerical microscopic analyses. In particular, the focus is placed on the analysis of the elastic response of single-phase textureless aggregates composed of cubic crystals (note that several metals belong to this group of materials). A meaningful point to make, however, is that our intention in this dissertation goes well beyond the characterisation of the elastic response of polycrystalline aggregates, since we were also keen on determining the range of applicability of the elastic constitutive laws (by studying their yielding response). On the whole, we expect that this work might spur further micromechanical studies which may involve more complex polycrystalline aggregates and, ideally, the aforementioned new materials.

1.3 Brief Literature Review

In this Section, we highlight some references that not only describe the state-of-art within the framework of the main topics discussed in this dissertation, but also may be interesting for a more comprehensive overview on particular issues.

1.3.1 Multi-Scale Models

A key point embedded in all theory of micro-macro approaches involves the concept of Representative Volume Elements. The main idea behind the modelling of RVEs is known as the *scale separation principle* and was outlined by Hashin (1983). In a simplistic manner, the scale separation principle imposes that the RVE's size might be small when compared to the macro-continuum domain, but must be significantly larger than its microscopic heterogeneities. This principle makes the continuum mechanics theory also applicable at the micro-scale and is respected by the definitions of RVE's reviewed in Gitman et al. (2007). Amongst those definitions, the one presented by Evesque (2005) is particularly interesting for this dissertation, as it is directed to isotropic granular materials: it states that the RVE may be regarded as the minimum volume from which the macroscopic properties can be extracted, so that it must be large enough when compared to the individual grains.

The variational foundations of *Multi-Scale Models* (MSM) are presented by de Souza Neto and Feijóo (2006) for both small and large strain frameworks. This contribution, along with the ones presented by Reis (2014) and Lopes (2016), might be sufficient for the understanding of the fundamentals required to the numerical implementation of *Multi-Scale Models based on Computational Homogenisation* (MSM-H).

The comparison between coupled and decoupled micro-macro schemes is approached by Watanabe and Terada (2010). Their work reveals the necessity of using decoupled schemes to solve many practical problems of interest, as a consequence of the high computational cost associated with CMSA, so that the main steps involved in a complete micro-macro decoupled procedure are enumerated (we highlight the necessity of deriving a macroscopic constitutive law from the microscopic analyses before the macroscopic equilibrium problem can be solved).

1.3.2 Modelling and Studying Polycrystalline Aggregates

Polycrystalline materials are assemblies of individual crystals (or grains). Their mechanical behaviour mostly is a result of the single crystal behaviour, the distribution of grains orientations and the aggregates morphology, as stated by Quey et al. (2011). The characterisation of the single crystal behaviour and, particularly the material symmetry associated with the single crystals, is discussed, for instance, in Engler and Randle (2009) and Dieter (1988). The concept of texture (which Kocks et al. (2000)

defined as the totality of crystalline orientations) is crucial in order to understand the scope of the polycrystalline aggregates studied in this dissertation (textureless polycrystals) and for a more comprehensive account on this issue, we recommend Suwas and Ray (2014) for an introductory read or Kocks et al. (2000) for a more detailed approach. Finally, the techniques involved in the generation and mesh of polycrystals are addressed by Quey et al. (2011) and Jöchen (2013).

Before going further, it is worth referring to the concept of oligocrystals which basically defines polycrystalline aggregates with a small number of grains. Although materials of interest are generally polycrystals containing a large number of randomly oriented grains (thus isotropic), several micro-components (such as MEMS[1]) are oligocrystals (and thus anisotropic). Prime Faraday (2002) makes an exhaustive review of MEMS, while Ko (2007) shortly addresses the future trends of these microcomponents. The characterisation of the mechanical behaviour of MEMS using experimental procedures is attempted, for instance, by Cho and Chasiotis (2007) and Stanimirović (2009).

1.3.3 Prediction of the Overall Elastic Response of Polycrystals

The onset of the development of analytical models aiming to predict the overall elastic properties of isotropic textureless polycrystalline aggregates is generally associated with Voigt (1910) who developed a model based on the assumption of a constant strain field over the polycrystal's domain (meaning the compatibility of the stress field was not fulfilled). Similarly, Reuss (1929) considered that all grains were subjected to the same stress and presented a analytical model which did not ensure kinematic compatibility. Later, Hill (1952) proved that the uniform strain and stress assumptions of Voigt and Reuss (respectively) were extreme mechanical states; consequently he showed that Voigt and Reuss predictions actually define bounds (known as the first-order bounds) on the mechanical properties of isotropic aggregates; furthermore, Hill suggested that an arithmetic or geometric average of the aforementioned bounds would lead to a more accurate estimate (which became known as Hill estimate). Based on variational principles, Hashin and Shtrikman (1962) proposed tighter bounds (the so called second-order bounds) to the elastic properties and their work was continued by Zeller and Dederichs (1973) who derived expressions for all odd-order bounds; later, Kröner (1977) determined formulas for all even-order bounds. The Self-Consistent estimate (described in Friák et al. (2012)), which ensures kinematic and static compatibility, is always contained between the bounds defined by Zeller and Dederichs (1973) and Kröner (1977). It is well-establish that the proximity of the bounds (for instance, of the Voigt and Reuss estimates) depends on the degree of anisotropy of the constituent crystal. For instance, Kube (2016) showed that, for crystalline aggregates composed of crystals with low anisotropy factors, Hill's

[1]MEMS is the acronym of Micro Electro-mechanical Systems.

estimate is closer to the self-consistent result. Nonetheless, when the constituent crystal has high elastic anisotropy and exhibits non-cubic material symmetry, Hill's model provides, by far, the simplest and most used estimate, despite the fact that it might be far from the self-consistent estimate (Berryman (2005) deduced the self-consistent estimate models for polycrystals containing hexagonal, trigonal and tetragonal symmetries; they cannot be computed in a straightforward fashion and, in general, require the numerical solution of a non-linear system of equations. In fact, analytical estimates just apply in the isotropic limit and are generally difficult to use in case crystallites with non-cubic symmetry are being studied.

Numerically-derived expressions for the elastic properties of single-phase cubic polycrystals have been developed in the last two decades. Böhlke et al. (2010) studied the Young modulus and related its average and standard deviation with the number of grains and the elastic constants of the cubic constituent crystals. Fritzen et al. (2009) also studied the Young's modulus, but focused mostly on the isotropic limit and used unstructured meshes. The Young's modulus of textured polycrystals was addressed by Kamaya (2009) who proposed a model involving the Reuss and Voigt bounds. Finally, Ranganathan and Ostoja-Starzewski (2008a) established bounds for the shear modulus of cubic crystalline aggregates and specified the elastic anisotropy of the constituent crystal and the number of grains as the two factors which affected that bounds (however, they used the Zener anisotropy index, so that the procedure could not be expanded in a straightforward fashion to analyse other types of aggregates).

Similarly, it must not be overlooked that several contributions have been given to the prediction of the minimum size of the RVE of elastic isotropic polycrystals. Among them, we highlight the works of El Houdaigui et al. (2007); Ranganathan and Ostoja-Starzewski (2008b) and Nygårds (2003).

1.3.4 Prediction of the Overall Yielding Response of Polycrystals

In order to predict the overall yielding response of polycrystalline aggregates, it is important to clearly distinguish the concepts of micro- and macro-yield. Briefly, the former is associated with the beginning of crystallographic slip, whilst the later refers to the lowest stress states that lead to a non-linear stress-strain relation. While it is commonly assumed that the macro-yield stresses occur for a level of global plastic strain of 0.2% (Brenner et al., 2009), the micro-yield condition can be defined in several ways. In this context, we highlight the micro-yield conditions suggested by Hutchinson (1970) and subsequently by Brenner et al. (2009) (who fundamentally modified Hutchinson's criterion to take into consideration information about the stress fluctuations within the grains). A compilation of anisotropic models that can be employed to describe the yielding response of polycrystals can be found on Habraken (2004).

In order to capture the overall micro- or macro-yielding response of polycrystalline aggregates, the classic isotropic phenomenological models of Tresca (1864) and of von Mises (1928) can be used. However, when anisotropic polycrystalline aggregates are studied, anisotropic yield functions are more adequate. In particular, Hill (1948) and Barlat and Lian (1989) proposed two of the most widespread anisotropic phenomenological yield functions which are even included in some commercial codes. Nevertheless, it is pertinent to note that both yield functions are restricted to the analysis of materials exhibiting orthotropic symmetry. In contrast, oligocrystals do not exhibit (in principle) any kind of elastic symmetry, so other yield functions that are not founded on this assumption, like the one developed by Karafillis and Boyce (1993), might be more appropriate. Alternatively, micromechanical anisotropic yield functions can be used. An example consists of the one proposed by Darrieulat and Piot (1996) which requires knowing the volume fractions and crystallographic orientations of all grains.

It is common ground that the macroscopic elastic properties, especially the Young's modulus, are intrinsically connected to the levels of elastic deformation when the macro-yield stresses of metallic materials are reached. On the other hand, the micro-yield stresses are mostly dependent on the critical resolved shear stress and on the monocrystalline parameters (namely the elastic anisotropy). In fact, Clausen (1997) and Brenner et al. (2009) have stated that the more anisotropic the single-crystals are, the earlier the onset of micro-plasticity. In addition, Brenner et al. (2009) have shown, using a self-consistent scheme, that the initial micro-yield surfaces of isotropic face-centered cubic (fcc) polycrystals can be reasonably described by the Tresca yield function. Moreover, Scheunemann (2017) performed several microscopic studies on polycrystalline structures and observed that when the levels of macroscopic plastic deformation increase (that is, when we get closer to the macro-yielding stress condition), the shape of the yield surface resembles a von Mises-type yield surface.

1.4 Outline

In this Section, the contents of the remaining Chapters of this document are summarised.

Chapter 2

The fundamentals of continuum mechanics are reviewed here, along with the main features of the application of the finite element method within the context of large-strain continuum mechanics problems.

Chapter 3

The concept of Representative Volume Element is discussed, a variational formulation of large strain multi-scale solid constitutive models is presented and the computational

program (`Links`) used to solve the micro-scale equilibrium problem is introduced.

Chapter 4

Basic concepts concerning polycrystalline aggregates are outlined, before purely analytical methods that intend to predict the overall elastic properties are reviewed. Measures that define the elastic anisotropy of crystals are thoroughly analysed, since the elastic anisotropy seems to be one of the factors that explains the elastic macroscopic response of textureless crystalline materials. The numerical multi-scale framework used to determine the overall elastic response of cubic textureless single-phase polycrystals is detailed.

Chapter 5

Here, the strategy developed to characterize the elastic response of isotropic polycrystals is described. Additionally, several studies which aim to examine the influence of the microscopic parameters on the elastic macroscopic response are reported, so that we are able to characterize the response of isotropic polycrystals (including the determination of the minimum size of the underlying RVE). Finally, the procedure expanded, so that analytical bounds were established for the 21 elastic constants of generic anisotropic polycrystals.

Chapter 6

A single crystal constitutive model formulated under the assumption of large strains is presented. Then, the concepts of micro- and macro-yield are distinguished and several criteria developed to compute the micro-yield stresses are discussed. In order to describe the yielding responses of both isotropic and anisotropic polycrystals, isotropic and anisotropic yield functions are also examined. Lastly, the numerical multi-scale framework used to characterize both micro- and macro-yield behaviours of fcc polycrystals is reported.

Chapter 7

The yielding response of isotropic and anisotropic polycrystals is studied with special attention being devoted to the influence of the elastic properties on the yield surface evolution. The yielding functions of von Mises and Tresca are employed to describe both micro- and the macro-yielding stress states and analytical expressions relating the parameters of the considered functions and the monocrystalline properties are deduced.

Chapter 8

The main conclusions extracted from the work made are summarised. Additionally, suggestions for future research are made.

This page was intentionally left with this sentence.

Chapter 2

Continuum Mechanics, Thermodynamics and Finite Element Method

Materials have complex microstructures made of atoms and subatomic particles whose behaviour might be studied by means of molecular and atomistic theories. These theories rely on a discrete particle approach: the atoms (as well as the subatomic particles) occupy certain positions on space, being separated by gaps. In general, it must be emphasised that quantum physics does not provide an adequate approach for common engineering applications (Holzapfel, 2000). As a matter of fact, these atomistic theories require keeping track of all atoms in a material to describe its behaviour, which is over too complicated for ordinary engineering purposes. Lying at the opposite extreme to quantum physics is *Continuum Mechanics and Thermodynamics* (CMT) (Tadmor et al., 2012). CMT deals with continua which might be defined as bodies that can be repeatedly subdivided into infinitesimal elements without losing the properties of the bulk material. In other words, this approach treats objects as continuous (or piecewise continuous) distributions of matter, completely ignoring that they have, in fact, a discrete (atomic) structure. Unlike quantum physics, CMT actually establishes a theory that (in practice) is useful for describing and predicting the mechanical behaviour of solids for engineering problems of contemporary interest. In fact, whenever the length of the body is much bigger than its atomic structure, CMT is valid. In this Chapter, the fundamentals of CMT will be presented.

In general, CMT is formulated to cope with strains of arbitrary magnitude (usually called *finite strains*, in contrast with *infinitesimal strains*). Appropriate strain measures as well as elementary concepts related with *the kinematics of deformation* are introduced in Section 2.1. The study of kinematics disregard the forces required to impact the motions; the analysis of the forces acting on bodies (which are relevant for the equilibrium problem), along with *stress measures*, are addressed in Section 2.2.

Section 2.3 compiles the *fundamental laws of thermodynamics*, while in Section 2.4 we briefly refer to the *constitutive theory* (which relates the materials' response to the applied loads). By ignoring thermal effects and considering boundary conditions, the *quasi-static initial boundary value problem* is formulated in Section 2.6. Because the constitutive relations are typically non-linear, most solid mechanics problems (which consist of a system of coupled, non-linear partial differential equations) have no analytical solution. Hence, the *Finite Element Method* (FEM), associated with the iterative *Newton-Rapshon method*, is considered, so that a spatial discretisation is performed and the system of non-linear equations might be solved in a implicit fashion. The use of FEM is discussed in Section 2.7 – the deduction of the weak form of equilibrium (made in Section 2.5) plays an important role in this context.

The aim of this Chapter is to present the fundamental topics of CMT. The textbook of de Souza Neto et al. (2008) was the main guide to the construction of this Chapter, although Bonet et al. (2016) and Tadmor et al. (2012) were also relevant and should be consulted if the reader is interested on a more detailed approach. The *Finite Element Method* review is brief and for a more profound read see, for instance, Zienkiewicz et al. (2014) and Zienkiewicz et al. (2013).

2.1 Deformation Kinematics

The kinematics of deformation provides the tools for describing the possible deformations a body can experience without reference to their cause (the relation between deformation and the applied loads is the main focus of Section 2.4). The time derivatives of certain kinematic quantities are introduced, since they are required for the formulation of the virtual work expression of equilibrium (presented in Section 2.5). Nevertheless, it is important to remark that inertial effects will not be taken into account in this work. The concepts and notation introduced in this Section will be repeatedly employed throughout this dissertation.

2.1.1 The Deformation Mapping Function

Provided that a continuum body can assume an infinite number of configurations, it is convenient to identify one of them as the *reference configuration* and compare all the others to this one in order to gauge deformations. The reference configuration should be as convenient as possible to the analysis and it often corresponds to an undeformed one (prior to loading). In this case, let $\mathscr{B}$ be a general continuum body occupying an open region Ω of the three-dimensional (3D) Euclidean space $\mathscr{E}$ with a regular boundary $\partial\Omega$ in its reference configuration. Furthermore, let $\boldsymbol{p}$ denote the position (in the reference configuration) of an arbitrary particle of the body (by particle, we mean an infinitesimal volume of the body). Having in mind that particles cannot be neither created nor destroyed, each particle might be identified by its position at the reference configuration $\boldsymbol{p}$. The deformation of $\mathscr{B}$ is expressed using

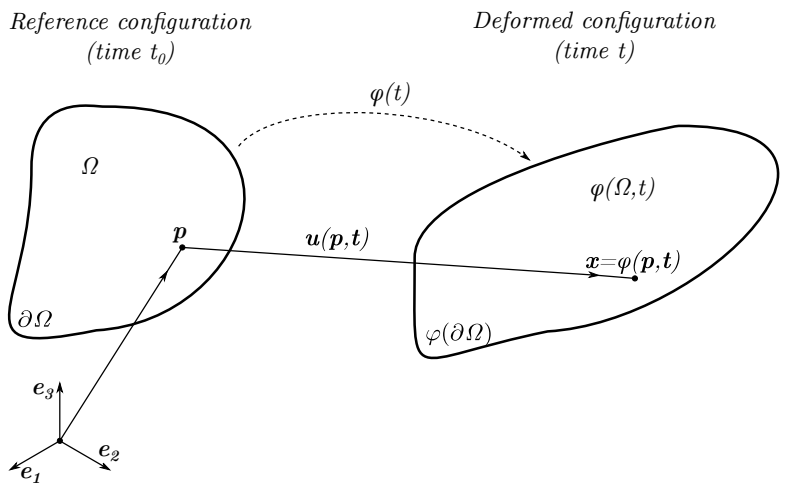

Figure 2.1: Deformation of a generic continuum $\mathscr{B}$.

a smooth one-to-one *deformation mapping function*, φ, which maps the position of every particle in the reference configuration to its new position in the *deformed configuration* (see Figure 2.1). In this case, in the deformed configuration, the body occupies the domain given by $\varphi(\Omega)$ and if $\boldsymbol{x}$ denotes the position of $\boldsymbol{p}$ after the deformation, we may write that

$$\boldsymbol{x} = \varphi(\boldsymbol{p}). \tag{2.1}$$

Generally, the deformation of a continuum varies through time, so that the deformation mapping function is time-dependent and describes the *motion* of $\mathscr{B}$:

$$\boldsymbol{x} = \varphi(\boldsymbol{p}, t), \tag{2.2}$$

with $\boldsymbol{x}$ the position of particle $\boldsymbol{p}$[1] at time t. The displacement vector field $\boldsymbol{u}(\boldsymbol{p}, t)$ of a particle initially positioned at $\boldsymbol{p}$ is defined by:

$$\boldsymbol{u}(\boldsymbol{p}, t) = \varphi(\boldsymbol{p}, t) - \boldsymbol{p}. \tag{2.3}$$

Taking into account equations (2.2) and (2.3), the position of $\boldsymbol{p}$ at the deformed configuration can be written as:

$$\boldsymbol{x} = \boldsymbol{p} + \boldsymbol{u}(\boldsymbol{p}, t). \tag{2.4}$$

It should be reinforced that no restrictions are placed in the magnitude of the displacement. For this reason, the displacements may well be of the order (or even exceed) the continuum body dimensions. Thus, the infinitesimal displacement situation must be seen as a specific case of the general CMT formulation presented.

Deformation requires a change in shape from the initial to the final (deformed) configuration. However, we must keep in mind that motion does not necessarily

[1]Note that the position in the undeformed configuration is used to label the particles.

imply deformation and may be associated with a rigid-body displacement. In case of rigid-body displacements the distance between the material particles is preserved. Rigid-body displacements (Figure 2.2) are discussed below:

1. *Rigid translation.* The displacement vector is constant in space, i.e., independent of $\boldsymbol{p}$, in such a manner that:

$$\boldsymbol{x}(\boldsymbol{p}, t) = \boldsymbol{p} + \boldsymbol{u}(t). \tag{2.5}$$

2. *Rigid rotation.* The displacement vector varies linearly with the distance to a point, $\boldsymbol{q}$, about which the continuum is rotated:

$$\boldsymbol{x}(\boldsymbol{p}, t) = \boldsymbol{q} + \boldsymbol{R}(t)\,(\boldsymbol{p} - \boldsymbol{q}), \tag{2.6}$$

   with $\boldsymbol{R}$ a second-order rotational tensor. Note that $\boldsymbol{q}$ is the center of rotation (remaining in the same position during the whole time).

3. *Combination of a rigid translation and rotation.* Any rigid-body displacement may be interpreted as a rigid translation superimposed on a rigid rotation $\boldsymbol{R}$ about $\boldsymbol{q}$:

$$\boldsymbol{x}(\boldsymbol{p}, t) = \varphi(\boldsymbol{q}, t) + \boldsymbol{R}(t)\,(\boldsymbol{p} - \boldsymbol{q}). \tag{2.7}$$

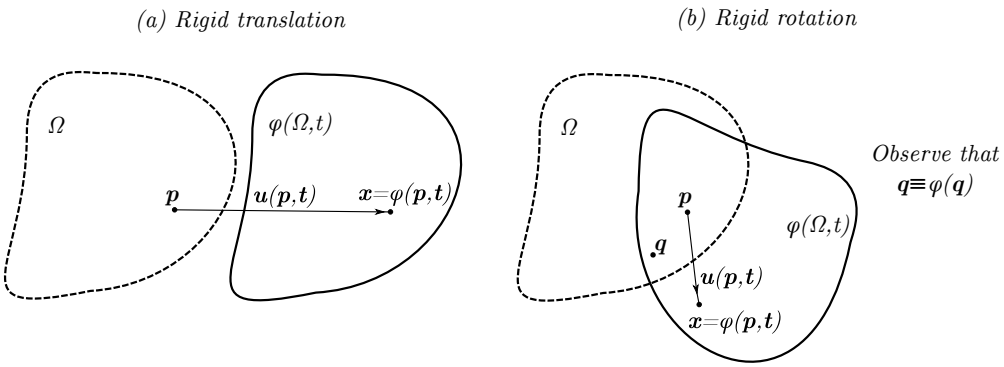

Figure 2.2: Rigid translation (a) and Rigid rotation (b) of a continuum.

A motion might be thereupon a time-dependent deformation of the continuum: this implies that the deformed configuration at a particular time t_1 can be different from the deformed configuration at t_2, as Figure 2.3 reveals. As the deformed configuration varies through time, it may also be referred to as the *current configuration.* Additionally, Figure 2.3 provides a representation of the parametric function $c(t)$, which maps, for a specific particle $\boldsymbol{p}$, the deformation path (in other words, the trajectory of $\boldsymbol{p}$ during the motion of the body).

The velocity of the particle $\boldsymbol{p}$ at time t is given by:

$$\dot{\boldsymbol{x}}(\boldsymbol{p}, t) = \frac{\partial \boldsymbol{x}(\boldsymbol{p}, t)}{\partial t} = \frac{\partial \varphi(\boldsymbol{p}, t)}{\partial t}. \tag{2.8}$$

Since a one-to-one deformation mapping function is used, a particle $\boldsymbol{p}$ cannot be mapped into two different positions. Thus, φ is invertible, allowing an arbitrary particle to be identified by its position at generic time:

$$\boldsymbol{p} = \varphi^{-1}(\boldsymbol{x}, t) = \boldsymbol{x} - \boldsymbol{u}(\varphi^{-1}(\boldsymbol{x}, t), t), \tag{2.9}$$

where φ^{-1} is called reference map.

With the reference map function, we might define a spatial velocity field, which gives the velocity of $\boldsymbol{x}$ at any time:

$$\boldsymbol{v}(\boldsymbol{x}, t) = \dot{\boldsymbol{x}}(\varphi^{-1}(\boldsymbol{x}, t), t). \tag{2.10}$$

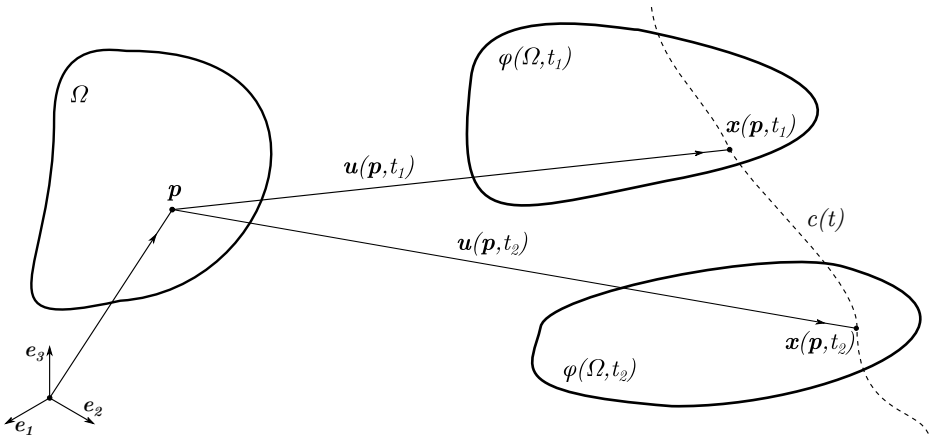

Figure 2.3: The concept of motion. Deformed configurations of $\mathscr{B}$ at times t_1 and t_2, respectively, denoted $\varphi(\mathscr{B}, t_1)$ and $\varphi(\mathscr{B}, t_2)$.

2.1.2 Material and Spatial Descriptions

Since no assumptions were made about the magnitude of the displacements, we must understand that the deformed configuration of $\mathscr{B}$ (represented by $\varphi(\mathscr{B})$) might be significantly different from the initial configuration. Consequently, we can define relevant quantities in terms of either configuration. If the reference configuration is considered, a *material* (or *Lagrangian*) description is adopted, whereas if the current configuration is taken, a *spatial* (or *Eulerian*) description is assumed:

1. *Material description.* This kind of description refers to the behaviour of a material particle in the undeformed configuration $\boldsymbol{p}$. The velocity $\dot{\boldsymbol{x}}$ is an example of a material quantity, since it represents a vectorial field whose argument (besides time t) is $\boldsymbol{p}$. General time-dependent material fields (scalar, vectorial or tensorial) are defined over the domain occupied by the continuum in its reference configuration, Ω.

2. *Spatial description.* This type of description alludes to the behaviour at a spatial position, represented by $\boldsymbol{x}$. Spatial descriptions involve fields defined over $\varphi(\Omega)$ and dependant on both spatial postion, $\boldsymbol{x}$, and time, t. Under these circumstances, it is easy to state that $\boldsymbol{v}$ defines a spatial quantity.

Any field related to the motion of $\mathscr{B}$ can be written in terms of spatial positions or material particles (and time). Throughout this thesis we have worked with both material and spatial entities, so that coherently material and spatial formulations have been presented (e.g. of the weak equilibrium equations).

2.1.3 Deformation Gradient

An essential quantity in finite deformation analyses is the *deformation gradient*, hereafter identified as $\boldsymbol{F}$. This quantity maps vectors from the reference to the spatial configuration and is usually called a "two-point tensor". In short, it provides information on the particles shape change. With the objective of capturing the changes of shape of particles, it is compulsory to consider two neighbouring material particles, $\boldsymbol{p}$ and $\boldsymbol{p} + d\boldsymbol{p}$, of a generic continuum body separated by an infinitesimal distance given by $d\boldsymbol{p}$. As shown in Figure 2.4, after the motion, the particles are, respectively, located at $\boldsymbol{x}$ and $\boldsymbol{x} + d\boldsymbol{x}$.

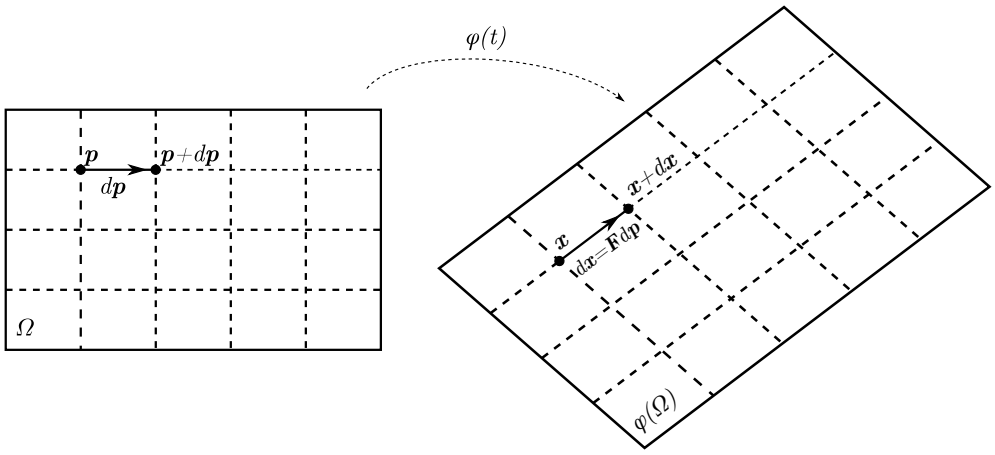

Figure 2.4: The deformation gradient: relation between the relative position of two neighbouring particles before and after the deformation.

The deformation gradient enables the distance between the particles after the motion to be expressed in terms of their relative position in the reference configuration as:

$$d\boldsymbol{x} = \boldsymbol{F} d\boldsymbol{p}. \tag{2.11}$$

Given that the deformation gradient transforms vectors defined in the initial configuration into vectors in the deformed configuration, it must be regarded as a

second-order tensor. Its Cartesian components are explicitly computed from:

$$F_{ij} = \frac{\partial x_i}{\partial p_j}. \tag{2.12}$$

Generally speaking, $\boldsymbol{F}$ is not a symmetric tensor. Besides this, it may be convenient to introduce the concepts of *push forward* and *pull back*, which are commonly employed when we intend to establish the bridge between the material and spatial configurations. Within this framework, the spatial vector $d\boldsymbol{x}$ might be regarded as the push forward equivalent of the material vector $d\boldsymbol{p}$ – the push forward concept is aligned with equation (2.11), since the spatial entity is expressed as a function of the material one. On the other hand, the material vector $d\boldsymbol{p}$ is the pull back equivalent of its spatial counterpart, which may be expressed as follows:

$$d\boldsymbol{p} = \boldsymbol{F}^{-1} d\boldsymbol{x}. \tag{2.13}$$

Defining the material gradient operator of a generic first-order tensorial[2] field $\boldsymbol{a}$ as its derivative with respect to $\boldsymbol{p}$ for a fixed time, it is possible to write

$$\nabla_{\boldsymbol{p}}(\boldsymbol{a}) = \frac{\partial \boldsymbol{a}(\boldsymbol{p}, t)}{\partial \boldsymbol{p}} \tag{2.14}$$

and using the concept of deformation mapping function, equation (2.11) might be rewritten as:

$$\boldsymbol{F}(\boldsymbol{p}, t) = \nabla_{\boldsymbol{p}}[\varphi(\boldsymbol{p}, t)]. \tag{2.15}$$

Making use of equation (2.4), the previous equation reduces to:

$$\boldsymbol{F}(\boldsymbol{p}, t) = \boldsymbol{I} + \nabla_{\boldsymbol{p}}[\boldsymbol{u}(\boldsymbol{p}, t)], \tag{2.16}$$

where $\boldsymbol{I}$ denotes the second-order identity tensor.

Alternatively, $\boldsymbol{F}$ might be defined in terms of the reference map (a spatial description is therefore adopted):

$$\boldsymbol{F}(\boldsymbol{x}, t) = \{\nabla_{\boldsymbol{x}}[\varphi^{-1}(\boldsymbol{x}, t)]\}^{-1}, \tag{2.17}$$

where $\nabla_{\boldsymbol{x}}(\cdot)$ is the spatial gradient operator (applied to $(\cdot)$, defined analogously to its material version (see equation (2.14)).

A case of particular interest occurs when $\boldsymbol{F}$ is uniform (independent of $\boldsymbol{p}$), so that the deformation is called *homogeneous*. When this happens, the deformation mapping function is given by:

$$\varphi(\boldsymbol{p}, t) = \varphi(\boldsymbol{q}, t) + \boldsymbol{F}(\boldsymbol{p} - \boldsymbol{q}) \tag{2.18}$$

for all points $\boldsymbol{p}, \boldsymbol{q} \in \mathscr{B}$. The similarities between equations (2.7) and (2.18) are obvious and, in summary, rigid-body motions constitute homogeneous deformations.

[2]Equation (2.14) remains valid for scalar and generic tensorial fields, replacing $\boldsymbol{a}$ by a or $\boldsymbol{A}$, respectively.

2.1.4 Isochoric/Volumetric Split of the Deformation Gradient

For the purpose of studying the *isochoric* and *volumetric* components of the deformation gradient, it is essential to consider its determinant (denoted $J = \det(\boldsymbol{F})$). In fact, J represents the volume change of a particle:

$$J = \frac{dv}{dv_0}, \tag{2.19}$$

where dv and dv_0 are, respectively, the local current and initial volumes. If the volume is preserved after the deformation, $J = 1$ is satisfied for all material particles. It is important to realize that some restrictions are placed on admissible values of J:

1. *J cannot be null.* This would imply that, at some point, the infinitesimal volume collapses, which is a physically impossible situation (particles cannot be destroyed);
2. *J cannot be negative.* In the undeformed configuration, $J = 1$ and, consequently, a configuration with $J < 0$ cannot be reached without having, at some time, $J = 0$.

All things considered, J must be a positive scalar, i.e. $J > 0$ should be verified in any deformed configuration. With this in mind, two types of deformation can be defined:

1. *Isochoric deformation.* It is a volume-preserving deformation, so particles only change shape. In this case $J = 1$. The deformation gradient associated with an isochoric deformation will be labelled as $\boldsymbol{F}_{\text{iso}}$.
2. *Volumetric deformation.* Consists of an uniform contraction/dilation in all directions. Let l denote the final distance (in a particular direction) between two neighbouring particles and L its corresponding reference quantity; if α represents the contraction/dilation ratio (defined as $\alpha = l/L$), we may write that $dv = \alpha^3 dv_0$. Thus, $J = \alpha^3$. This leads to the volumetric deformation gradient:

$$\boldsymbol{F}_{\text{vol}} = \alpha \boldsymbol{I}, \tag{2.20}$$

   in such a way the volumetric deformation gradient ($\boldsymbol{F}_{\text{vol}}$) is a spherical tensor.

Any deformation can be locally split into a purely volumetric deformation followed by a volume-preserving (isochoric) deformation by means of a *multiplicative decomposition* of the generic deformation gradient:

$$\boldsymbol{F} = \boldsymbol{F}_{\text{iso}} \boldsymbol{F}_{\text{vol}}. \tag{2.21}$$

Alternatively, the multiplicative split may consist of an isochoric deformation followed by a pure volumetric deformation:

$$\boldsymbol{F} = \boldsymbol{F}_{\text{vol}} \boldsymbol{F}_{\text{iso}}. \tag{2.22}$$

Since the volume-preserving component of the deformation gradient must be

associated with a unitary determinant, we write:

$$\boldsymbol{F}_{\text{iso}} = (J)^{-1/3}\boldsymbol{F} \tag{2.23}$$

and, in order to satisfy equations (2.20) to (2.22), we use $(J)^{1/3}$ as the contraction/dilation ratio, so that:

$$\boldsymbol{F}_{\text{vol}} = (J)^{1/3}\boldsymbol{I}. \tag{2.24}$$

2.1.5 Polar Decomposition of the Deformation Gradient

The deformation gradient tensor includes not only a shape-change component[3], but also a rotation component. Therefore, since rotation does not play any role in the deformation process, it is useful to separate the rotation and the shape-change components of $\boldsymbol{F}$. In this context, the *polar decomposition theorem* might be useful. According to the aforementioned theorem (valid for tensors with positive determinant), the deformation gradient tensor can be uniquely split as follows:

$$\boldsymbol{F} = \boldsymbol{R}\boldsymbol{U} = \boldsymbol{V}\boldsymbol{R}, \tag{2.25}$$

where $\boldsymbol{R}$ is the local rotation tensor and $\boldsymbol{U}$ and $\boldsymbol{V}$ are symmetric positive definite tensors called, respectively, right and left stretch tensors. The stretch tensors, used in the left and right polar decomposition, are related by the rotation tensor:

$$\boldsymbol{V} = \boldsymbol{R}\,\boldsymbol{U}\boldsymbol{R}^T. \tag{2.26}$$

Owing to their symmetry, the stretch tensors $\boldsymbol{U}$ and $\boldsymbol{V}$ admit the spectral decomposition:

$$\boldsymbol{U} = \sum_{i=1}^{3} \lambda_i\, \boldsymbol{l}_i \otimes \boldsymbol{l}_i, \tag{2.27}$$

$$\boldsymbol{V} = \sum_{i=1}^{3} \lambda_i\, \boldsymbol{e}_i \otimes \boldsymbol{e}_i, \tag{2.28}$$

in which $\{\lambda_1, \lambda_2, \lambda_3\}$ denote the eigenvalues of both $\boldsymbol{U}$ and $\boldsymbol{V}$, i.e. the *principal stretches*, while $\boldsymbol{l}_i$ and $\boldsymbol{e}_i$ are unit eigenvectors of the right and left stretch tensors. The triads $\{\boldsymbol{l}_1, \boldsymbol{l}_2, \boldsymbol{l}_3\}$ and $\{\boldsymbol{e}_1, \boldsymbol{e}_2, \boldsymbol{e}_3\}$ are called Lagrangian and Eulerian triads and define the Lagrangian and Eulerian *principal directions*. The Lagrangian and Eulerian principal directions are related through:

$$\boldsymbol{l}_i = \boldsymbol{R}\boldsymbol{e}_i. \tag{2.29}$$

To clarify the meaning of the polar decomposition of $\boldsymbol{F}$, see Figure 2.5. As can be seen, if the left polar decomposition is considered, the neighbourhood of $\boldsymbol{p}$ is firstly rotated and then subjected to a shape change, so that $\boldsymbol{F}d\boldsymbol{p} = \boldsymbol{R}(\boldsymbol{U}d\boldsymbol{p})$. Similarly, for

[3]Changes in the shape of the neighbourhood comprise *stretching* (length changes) and *shearing* (changes in angles).

the right decomposition, the material neighbourhood first changes its shape and then is rotated into the deformed (final) configuration (in this case, $\boldsymbol{F}d\boldsymbol{p} = \boldsymbol{V}(\boldsymbol{R}d\boldsymbol{p})$). In summary, a two-stage sequence is performed on both decompositions. Nonetheless, it is important to understand that the right stretch tensor is a material quantity whereas the left stretch tensor is a spatial entity.

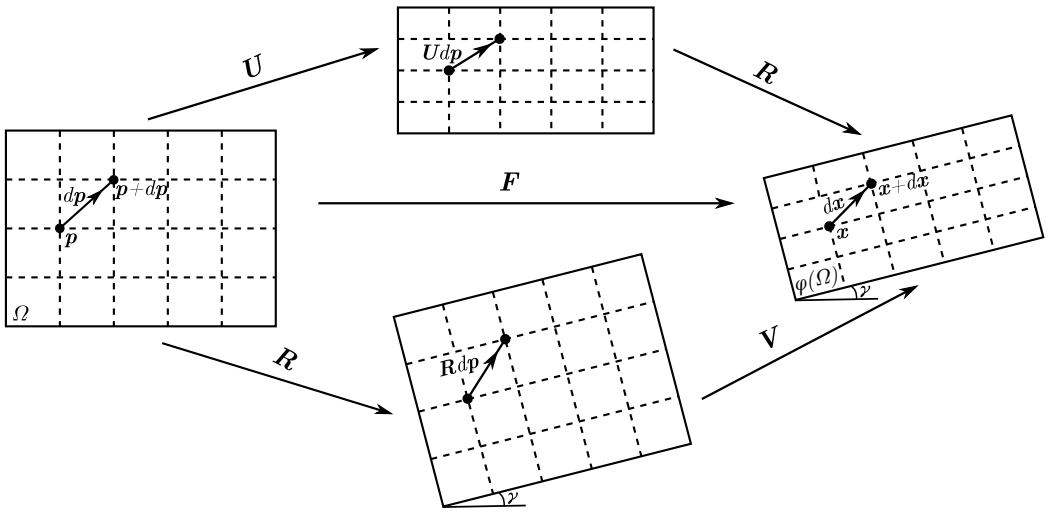

Figure 2.5: Polar decompositions of $\boldsymbol{F}$ as two-stage sequences involving a homogeneous stretching in both axes with a superimposed rigid rotation of angle γ.

Let $\boldsymbol{C}$ and $\boldsymbol{B}$ denote, respectively, the right and left *Cauchy-Green* strain tensors. These tensors are functions of the deformation gradient:

$$\boldsymbol{C} = \boldsymbol{F}^T\boldsymbol{F}, \tag{2.30}$$

$$\boldsymbol{B} = \boldsymbol{F}\boldsymbol{F}^T. \tag{2.31}$$

Considering the definition (2.16) of the deformation gradient, we might rewrite the former expressions in terms of the displacement gradient:

$$\boldsymbol{C} = \boldsymbol{I} + \nabla_{\boldsymbol{p}}(\boldsymbol{u}) + [\nabla_{\boldsymbol{p}}(\boldsymbol{u})]^T + [\nabla_{\boldsymbol{p}}(\boldsymbol{u})]^T \cdot \nabla_{\boldsymbol{p}}(\boldsymbol{u}), \tag{2.32}$$

$$\boldsymbol{B} = \boldsymbol{I} + \nabla_{\boldsymbol{p}}(\boldsymbol{u}) + [\nabla_{\boldsymbol{p}}(\boldsymbol{u})]^T + \nabla_{\boldsymbol{p}}(\boldsymbol{u}) \cdot [\nabla_{\boldsymbol{p}}(\boldsymbol{u})]^T. \tag{2.33}$$

Finally, we can also relate the right and left stretch tensors to the above as follows:

$$\boldsymbol{U} = \sqrt{\boldsymbol{C}} = \sqrt{\boldsymbol{F}^T\boldsymbol{F}}, \tag{2.34}$$

$$\boldsymbol{V} = \sqrt{\boldsymbol{B}} = \sqrt{\boldsymbol{F}\boldsymbol{F}^T}. \tag{2.35}$$

2.1.6 Strain Measures

As explained in the previous Section, in a local sense, pure rotations can be separated from pure stretches by means of the polar decomposition of the deformation gradient.

When the neighbourhood of the generic particle $\boldsymbol{p}$ experiences a pure rotation, the distances between particles within the referred neighbourhood do not change and it is possible to state that the vicinity of $\boldsymbol{p}$ remains *unstrained*. In the absence of straining, the stretch tensors ($\boldsymbol{U}$ and $\boldsymbol{V}$) correspond to the identity tensor $\boldsymbol{I}$. On the contrary, the domain surrounding $\boldsymbol{p}$ is *strained* if the relative positions of neighbouring particles of $\boldsymbol{p}$ change after the deformation: this happens when the stretch tensors depart from $\boldsymbol{I}$. Having said this, it is obvious that both stretch tensors characterize the change of shape of a particle neighbourhood. However, these tensors are irrational functions of the deformation gradient and, as a consequence, they might be difficult to obtain. Indeed, the left and right Cauchy-Green tensors are much more attractive options to use to define strain measures. According to Tadmor et al. (2012), the most convenient variable for solids is $\boldsymbol{C}$. We might observe the usefulness of the right Cauchy-Green tensor by reconsidering Figure 2.5; in addition to this, if we recall the relation established by equation (2.11), the following deduction can be made:

$$\begin{aligned} \|d\boldsymbol{x}\|^2 &= d\boldsymbol{x} \cdot d\boldsymbol{x} \\ &= \boldsymbol{F}d\boldsymbol{p} \cdot \boldsymbol{F}d\boldsymbol{p} \\ &= \boldsymbol{C}d\boldsymbol{p} \cdot d\boldsymbol{p} \\ &= (\boldsymbol{I} + 2\boldsymbol{E}^{(2)})d\boldsymbol{p} \cdot d\boldsymbol{p}, \end{aligned} \tag{2.36}$$

where $\boldsymbol{E}^{(2)}$ is the *Green-Lagrange* strain tensor. This strain measure can be explicitly expressed as a function of the right Cauchy-Green tensor:

$$\boldsymbol{E}^{(2)} = \tfrac{1}{2}(\boldsymbol{C} - \boldsymbol{I}). \tag{2.37}$$

A point often overlooked is that the Green-Lagrange strain tensor is one of a large number of strain measures. The adoption of a particular strain measure is typically dictated by a balance between the phenomenon in question and mathematical convenience. The strain tensor of (2.37) is part of a well-known family of strain tensors called *Lagrangian strain tensors*. The name derives from the fact that all Lagrangian strain measures (generally represented by $\boldsymbol{E}^{(m)}$) are based on the Lagrangian triad introduced in Section 2.1.5. Hence, these tensors are functions of the right stretch tensor:

$$\boldsymbol{E}^{(m)} = \begin{cases} \frac{1}{m}(\boldsymbol{U}^m - \boldsymbol{I}) & , \ m \neq 0 \\ \ln(\boldsymbol{U}) & , \ m = 0 \end{cases} \tag{2.38}$$

where m is a real number and $\ln(\cdot)$ designates the tensor logarithm of $(\cdot)$. The Green-Lagrange strain tensor is obtained when $m = 2$. Alternatively, we might prefer working with strain tensors defined in terms of left stretch tensor:

$$\boldsymbol{\varepsilon}^{(m)} = \begin{cases} \frac{1}{m}(\boldsymbol{V}^m - \boldsymbol{I}) & , \ m \neq 0 \\ \ln(\boldsymbol{V}) & , \ m = 0 \end{cases} \tag{2.39}$$

where $\boldsymbol{\varepsilon}^{(m)}$ identifies the *Eulerian strain tensors*. This group of strain tensors is based on the Eulerian triad. Both families of strain measures are associated with rigid deformations if the stretch tensors are given by $\boldsymbol{I}$. The Lagrangian and Eulerian strain tensors are related by:

$$\boldsymbol{\varepsilon}^{(m)} = \boldsymbol{R}\,\boldsymbol{E}^{(m)}\,\boldsymbol{R}^T. \tag{2.40}$$

Before going further, it is important to establish the bridge between the CMT theory reviewed here (which concerns strain measures) and one of the most used deformation measures in elementary engineering courses, namely the *infinitesimal strain tensor* $\boldsymbol{\varepsilon}$. This strain measure provides significant simplifications when we deal with small displacements gradients, as the reference and the current configurations are supposed coincident. Since the displacement gradient is small, the second-order terms in $\nabla_{\boldsymbol{p}}(\boldsymbol{u})$ can be ignored and, consequently (see equations (2.32) and (2.33)), we have:

$$\boldsymbol{C} \approx \boldsymbol{B} \approx \boldsymbol{I} + \nabla_{\boldsymbol{p}}(\boldsymbol{u}) + [\nabla_{\boldsymbol{p}}(\boldsymbol{u})]^T. \tag{2.41}$$

Combining relation (2.41) with the definition of the Lagrangian and Eulerian strain tensors, respectively, equations (2.38) and (2.40), it is verified, that for any m (under small strains)[4]:

$$\boldsymbol{\varepsilon} \approx \boldsymbol{E}^{(m)} \approx \boldsymbol{\varepsilon}^{(m)}, \tag{2.42}$$

where the infinitesimal strain tensor ε is a linear functional of $\boldsymbol{u}$

$$\boldsymbol{\varepsilon} = \nabla^s_{\boldsymbol{p}}(\boldsymbol{u}), \tag{2.43}$$

being $\nabla^s(\cdot)$ the symmetric gradient of $(\cdot)$:

$$\nabla^s(\cdot) = \tfrac{1}{2}\left[\nabla(\cdot) + \nabla(\cdot)^T\right]. \tag{2.44}$$

2.1.7 Spatial Velocity Gradient

The spatial velocity $\boldsymbol{v}$ was defined in equation (2.10) where its dependence on the current position $\boldsymbol{x}$ is noticeable. The *spatial velocity gradient* results from deriving $\boldsymbol{v}$ with respect to the spatial position $\boldsymbol{x}$, which produces:

$$\boldsymbol{L} = \nabla_{\boldsymbol{x}}(\boldsymbol{v}). \tag{2.45}$$

Using the chain rule, it may be deduced that

$$\boldsymbol{L} = \frac{\partial}{\partial t}\left(\frac{\partial \varphi}{\partial \boldsymbol{p}}\right)\frac{\partial \boldsymbol{p}}{\partial \boldsymbol{x}} = \dot{\boldsymbol{F}}\boldsymbol{F}^{-1}. \tag{2.46}$$

The velocity gradient is normally separated into its symmetric and skew components. The symmetric part will be labelled as $\boldsymbol{D}$ and is often called *stretching* or *rate of deformation tensor*; on the other hand, the skew tensor (hereafter represented

[4]It must be remarked that an error of second order in $\nabla_{\boldsymbol{p}}(\boldsymbol{u})$ is made (which is a small error, since small displacement gradients are assumed).

by $\boldsymbol{W}$) is referred to as the *spin tensor*. Generally speaking, if $\boldsymbol{A}$ is a generic second-order tensor, its symmetric and skew components are defined as:

$$\text{sym}(\boldsymbol{A}) = \tfrac{1}{2}(\boldsymbol{A} + \boldsymbol{A}^T), \tag{2.47}$$

$$\text{skew}(\boldsymbol{A}) = \tfrac{1}{2}(\boldsymbol{A} - \boldsymbol{A}^T), \tag{2.48}$$

we can define the symmetric and skew components of $\boldsymbol{L}$ as:

$$\boldsymbol{D} = \text{sym}(\boldsymbol{L}), \tag{2.49}$$

$$\boldsymbol{W} = \text{skew}(\boldsymbol{L}). \tag{2.50}$$

2.2 Forces and Stresses

The previous Section was dedicated to study the tools available for describing the possible deformations a body can undergo. However, before we can focus on physical and constitutive laws it is necessary to define ways of measuring stresses. To be precise, the stress measures discussed throughout this Section can describe *surface stresses*, which are, roughly speaking, surface forces per unit area. Surface forces can be distinguished from another group of forces known as body forces:

1. *Body Forces.* These consist of forces exerted on the interior of the body (such as magnetic and gravitational forces). Commonly, they are expressed per unit of volume (or mass).

2. *Surface Forces.* Include the boundary forces (forces applied to the boundary of the body which result from interactions with its neighbourhood) and forces transmitted across the interior of the body (forces that arise from internal interactions between its adjacent parts). The dimension of these interactions is force per unit area.

In short, this Section deals with ways of quantifying surface stresses. Similar to strain measures, it should be emphasised that stress measures can be defined in the current or in the initial body configuration. An example of a spatial stress measure is the *Cauchy* stress tensor, whereas the *Second Piola-Kirchhoff* tensor consists of a material stress quantity.

2.2.1 Cauchy Stress Vector

A key element for the description of surface forces is the *Cauchy stress vector*. In order to clarify the physical meaning of this vectorial quantity, we should see Figure 2.6. In that Figure, it is possibly to identify a body $\mathscr{B}$ whose current configuration is given by $\varphi(\mathscr{B})$, a particle located at $\boldsymbol{x}$ and two oriented surfaces of the body ($\mathscr{L}$ and $\mathscr{T}$) with unit normal vector $\boldsymbol{n}$ at the highlighted point. Note that $\boldsymbol{x}$ does not necessarily belong to the boundary of the body. According to Cauchy's axiom, "At $\boldsymbol{x}$, the force per unit infinitesimal area (surrounding the particle) transmitted across

the surface $\mathscr{L}$ (by the material on the side of $\mathscr{L}$ into which $\boldsymbol{n}$ is pointing) upon the material on the other side of $\mathscr{L}$ depends on $\mathscr{L}$ only through its normal $\boldsymbol{n}$". Hence, the force exerted across surfaces $\mathscr{L}$ and $\mathscr{T}$, that share the same normal vector, are the same at the particle located at $\boldsymbol{x}$ (this remains valid for all the surfaces with normal $\boldsymbol{n}$ at $\boldsymbol{x}$, provided that the continuum is in equilibrium). The referred force is the Cauchy stress vector will be denoted $\boldsymbol{t}(\boldsymbol{n}, \boldsymbol{x}, t)$.

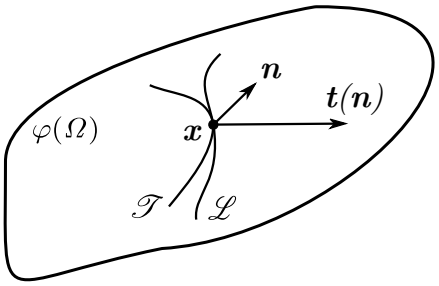

Figure 2.6: The Cauchy Stress Vector at time t, showing its dependence on the normal vector at a point $\boldsymbol{x}$ belonging to the surfaces $\mathscr{L}$ and $\mathscr{T}$.

2.2.2 Cauchy Stress Tensor

Cauchy's Theorem establishes that the dependence of the Cauchy stress vector upon the normal vector $\boldsymbol{n}$ is linear in such a manner that:

$$\boldsymbol{t}(\boldsymbol{n}, \boldsymbol{x}, t) = \boldsymbol{\sigma}(\boldsymbol{x}, t) \cdot \boldsymbol{n}, \tag{2.51}$$

where $\boldsymbol{\sigma}(\boldsymbol{x}, t)$ is the Cauchy stress tensor. This second-order spatial tensor is sometimes referred to as *true stress tensor* and, as it is demonstrated in Section 2.3.2, it consists of a symmetric tensor. Using an orthonormal basis $\{\boldsymbol{e}_1, \boldsymbol{e}_2, \boldsymbol{e}_3\}$, the components of the Cauchy stress tensor (denoted $\boldsymbol{\sigma}_{ij}$) are given by:

$$\boldsymbol{\sigma}_{ij} = (\boldsymbol{\sigma}\, \boldsymbol{e}_i) \cdot \boldsymbol{e}_j. \tag{2.52}$$

The term in parenthesis in equation (2.52) is the force (per unit of area) exerted across a surface with normal vector $\boldsymbol{e}_i$ at the arbitrary point $\boldsymbol{x}$, so that $\boldsymbol{\sigma}_{ij}$ is the magnitude of the projection of that force in the direction of $\boldsymbol{e}_j$. The Cauchy stress tensor components are represented in Figure 2.7: some act perpendicularly to the cube faces (*normal tractions*), while the rest act in a direction parallel to the faces (*shear tractions*). For every point, we should keep in mind that there is always an orthonormal basis $\{\boldsymbol{e}_1^*, \boldsymbol{e}_2^*, \boldsymbol{e}_3^*\}$ (which specifies the *Cauchy principal directions*) that defines a Cauchy stress tensor whose shear components are null. In that case, the normal components are the *Cauchy principal stresses* and correspond to the eigenvalues of $\boldsymbol{\sigma}$. These stress components (generally denoted σ_i) can be also identified in Figure 2.7.

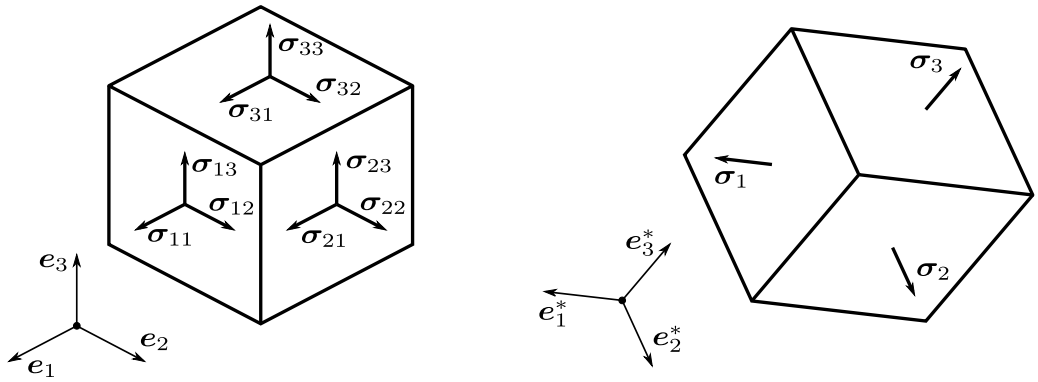

Figure 2.7: Cauchy stress tensor components and principal Cauchy stresses.

Similarly to the isochoric/volumetric decompostion of the deformation gradient, we can separate the Cauchy stress tensor into a volume-preserving and a purely volumetric contribution. Indeed, this split is useful in many practical applications, including metal plasticity (see Section 6.3.1). This split is *additive*:

$$\boldsymbol{\sigma} = \boldsymbol{s} + p\boldsymbol{I}, \tag{2.53}$$

where $\boldsymbol{s}$ is the *deviatoric stress* (volume-preserving component) and $p\boldsymbol{I}$ is the *volumetric stress*. Here, p is the *hydrostatic pressure* (or hydrostatic stress) defined by:

$$p = \frac{1}{3}\mathrm{tr}(\boldsymbol{\sigma}), \tag{2.54}$$

resulting that $\boldsymbol{s}$ is a traceless tensor. It should be remarked that $\mathrm{tr}(\boldsymbol{\sigma})$ (and therefore p) consists of an invariant (meaning that these quantities are independent of the coordinate system used to represent $\boldsymbol{\sigma}$).

2.2.3 First Piola-Kirchhoff Stress Tensor

The Cauchy stress vector $\boldsymbol{t}$ consists, after all, of a force exerted across a surface $\varphi(\mathscr{L})$ (Figure 2.8) per unit of infinitesimal deformed area surrounding the particle located at the point of interest (given by $\boldsymbol{x}$). We might define a vector $\boldsymbol{t}_0$ which defines the force exerted across $\mathscr{L}$ per unit reference area containing the infinitesimal neighbourhood of $\boldsymbol{p}$ (position of the particle in the reference configuration). The normal vector at $\boldsymbol{p}$ might be different from $\boldsymbol{n}$ and will be designated as $\boldsymbol{n}_0$. Additionally, let da_0 denote the infinitesimal area normal to $\boldsymbol{n}_0$ that surrounds $\boldsymbol{p}$ and da its spatial counterpart. The relation between these areas provides a way of obtaining $\boldsymbol{t}_0$, admitting that the Cauchy stress vector is known:

$$\boldsymbol{t}_0 = \frac{da}{da_0}\,\boldsymbol{t}. \tag{2.55}$$

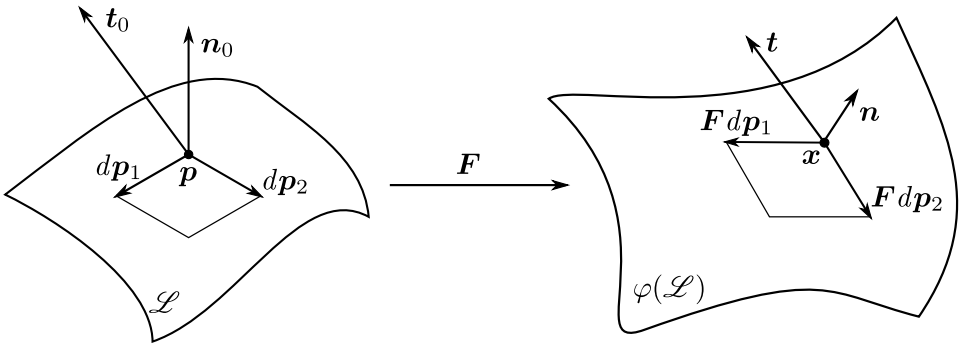

Figure 2.8: Infinitesimal areas surrounding $\boldsymbol{p}$ (da_0) and $\boldsymbol{x}$ (da) in the reference and deformed configuration, respectively. Stress vectors $\boldsymbol{t}_0$ and $\boldsymbol{t}$ (that have the same direction) and the unit outward normal vectors to surfaces $\mathscr{L}$ ($\boldsymbol{n}_0$) and $\varphi(\mathscr{L})$ ($\boldsymbol{n}$) are also represented.

Using equation (2.51), we may rewrite the preceding equation in terms of the Cauchy stress tensor and the unit normal outward vector:

$$\boldsymbol{t}_0 = \frac{da}{da_0}\,\boldsymbol{\sigma}\,\boldsymbol{n}. \tag{2.56}$$

Figure 2.8 also provides a graphical representation of two tangent vectors to $\mathscr{L}$ at $\boldsymbol{p}$ ($d\boldsymbol{p}_1$ and $d\boldsymbol{p}_2$). These infinitesimal vectors must be linearly independent in such a way that their cross product generates a collinear vector to $\boldsymbol{n}_0$ with magnitude da_0:

$$\boldsymbol{n}_0\,da_0 = d\boldsymbol{p}_1 \times d\boldsymbol{p}_2. \tag{2.57}$$

Vectors $d\boldsymbol{p}_1$ and $d\boldsymbol{p}_2$ are mapped into $\boldsymbol{F}d\boldsymbol{p}_1$ and $\boldsymbol{F}d\boldsymbol{p}_2$ and, as a consequence:

$$\boldsymbol{n}\,da = \boldsymbol{F}d\boldsymbol{p}_1 \times \boldsymbol{F}d\boldsymbol{p}_2. \tag{2.58}$$

After some algebraic manipulation of equations (2.57) and (2.58), we get:

$$\frac{da}{da_0}\,\boldsymbol{n} = J\boldsymbol{F}^{-T}\boldsymbol{n}_0. \tag{2.59}$$

Pre-multiplication of both sides of equation (2.59) by $\boldsymbol{\sigma}$ together with the use of equation (2.56) leads to:

$$\boldsymbol{t}_0 = J\,\boldsymbol{\sigma}\,\boldsymbol{F}^{-T}\boldsymbol{n}_0. \tag{2.60}$$

If we define the *first Piola-Kirchhoff* stress tensor as

$$\boldsymbol{P} = J\,\boldsymbol{\sigma}\,\boldsymbol{F}^{-T}, \tag{2.61}$$

we can write a similar version of equation (2.51):

$$\boldsymbol{t}_0 = \boldsymbol{P}\,\boldsymbol{n}_0. \tag{2.62}$$

A key point to understand is that $\boldsymbol{P}$ is not completely linked to the reference

configuration. In detail, note that this tensor relates the normal vector to the reference area $\boldsymbol{n}_0$ (which is a material entity) and the reference surface traction vector $\boldsymbol{t}_0$ (which is collinear to $\boldsymbol{t}$[5] and, in extension, derived from a spatial approach). Hence, the first Piola-Kirchhoff stress tensor consists of an unsymmetric two-point tensor which embodies the current force per unit of reference area.

2.2.4 Second Piola-Kirchhoff Stress Tensor

In contrast to the first Piola-Kirchhoff stress tensor, the *second Piola-Kirchhoff* stress tensor is a material entity. This tensor (denoted $\boldsymbol{S}$) relates the "true reference surface traction" $\boldsymbol{t}_0^*$ and the normal vector to the reference area $\boldsymbol{n}_0$:

$$\boldsymbol{t}_0^* = \boldsymbol{S}\,\boldsymbol{n}_0. \tag{2.63}$$

The true reference surface traction might be interpreted as the pull back equivalent of $\boldsymbol{t}_0$, so that:

$$\boldsymbol{t}_0^* = \boldsymbol{F}^{-1}\,\boldsymbol{t}_0. \tag{2.64}$$

Taking (2.62) into consideration, we obtain:

$$\boldsymbol{t}_0^* = \boldsymbol{F}^{-1}\boldsymbol{P}\,\boldsymbol{n}_0. \tag{2.65}$$

Combining (2.63) and (2.65) leads to:

$$\boldsymbol{F}^{-1}\boldsymbol{P}\,\boldsymbol{n}_0 = \boldsymbol{S}\,\boldsymbol{n}_0. \tag{2.66}$$

The definition of $\boldsymbol{P}$ (equation (2.61)) together with equation (2.66) gives rise to the following expression for the second Piola-Kirchhoff stress tensor:

$$\boldsymbol{S} = J\,\boldsymbol{F}^{-1}\boldsymbol{\sigma}\,\boldsymbol{F}^{-T}, \tag{2.67}$$

which comprises the mathematical definition of $\boldsymbol{S}$. From (2.67), we have

$$\boldsymbol{S}^T = J\,\boldsymbol{F}^{-1}\,\boldsymbol{\sigma}^T\boldsymbol{F}^{-T}, \tag{2.68}$$

so that, $\boldsymbol{S}$ is a symmetric tensor (i.e., $\boldsymbol{S} = \boldsymbol{S}^T$ since $\boldsymbol{\sigma} = \boldsymbol{\sigma}^T$).

2.2.5 Kirchhoff Stress Tensor

Despite being generally unsymmetric, the first Piola-Kirchhoff tensor might be defined in terms of the *Kirchhoff* stress tensor $\boldsymbol{\tau}$ which happens to be a symmetric tensor (this stems from the fact that $\boldsymbol{\sigma}$ is a symmetric tensor). This stress measure reads:

$$\boldsymbol{P} = \boldsymbol{\tau}\,\boldsymbol{F}^{-T}. \tag{2.69}$$

Equation (2.69) together with expression (2.61) provides

$$\boldsymbol{\tau} = J\,\boldsymbol{\sigma}. \tag{2.70}$$

[5] This is a consequence of its own definition which is mathematically given by equation (2.55).

Kirchhoff's principal stresses (τ_i) are often used to formulate constitutive models, and might be calculated from the principal Cauchy stresses (σ_i):

$$\tau_i = J\,\sigma_i. \tag{2.71}$$

2.3 Fundamental Laws of Thermodynamics

Even when thermal effects are neglected (as is the case of this work) and we restrain the analysis to purely mechanical problems, the *fundamental laws of thermodynamics* play an important role in continuum mechanics. As a matter of fact, the laws presented throughout this Chapter place restrictions on the physical processes undergone by matter, but are general in a way they disregard their specific properties (in other words, these laws are valid for any continuum body). The following laws are initially presented with the thermally-related terms, even though they will be ignored when we formulate the purely mechanical problem in Section 2.4.3.

2.3.1 Conservation of Mass

The principle of conservation of mass requires that

$$\dot{\rho} + \rho\ \mathrm{div}_{\boldsymbol{x}}(\dot{\boldsymbol{u}}) = 0, \tag{2.72}$$

with ρ denoting the mass per unit volume in the deformed configuration of the body (for notational convenience, the dependence upon the spatial position $\boldsymbol{x}$ was omitted). Equation (2.72) introduced $\mathrm{div}_{\boldsymbol{x}}(\cdot)$ which denotes the spatial divergence of $(\cdot)$; additionally, $\dot{\rho}$ is the derivative of ρ with respect to time.

2.3.2 Momentum Equilibrium

Let the deformed configuration of body $\mathscr{B}$ (whose domain is denoted $\varphi(\Omega)$ with boundary $\varphi(\partial\Omega)$) be under the action of surface forces, $\boldsymbol{t}(\boldsymbol{n},\boldsymbol{x})$, and body forces $\boldsymbol{b}(\boldsymbol{x})$ (expressed per unit of mass). The principles of linear and angular momentum balance state, respectively, that (the right hand side of the equations represents the inertial effects):

$$\int_{\varphi(\partial\Omega)} \boldsymbol{t}(\boldsymbol{n},\boldsymbol{x})\ da + \int_{\varphi(\Omega)} \rho(\boldsymbol{x})\,\boldsymbol{b}(\boldsymbol{x})\ dv = \int_{\varphi(\Omega)} \rho(\boldsymbol{x})\,\ddot{\boldsymbol{u}}(\boldsymbol{x})\ dv, \tag{2.73}$$

$$\int_{\varphi(\partial\Omega)} \boldsymbol{x}\times\boldsymbol{t}(\boldsymbol{n},\boldsymbol{x})\ da + \int_{\varphi(\Omega)} \boldsymbol{x}\times\rho(\boldsymbol{x})\,\boldsymbol{b}(\boldsymbol{x})\ dv = \int_{\varphi(\Omega)} \boldsymbol{x}\times\rho(\boldsymbol{x})\,\ddot{\boldsymbol{u}}(\boldsymbol{x})\ dv, \tag{2.74}$$

with $\boldsymbol{n}$ identifying the outward unit vector normal to the deformed boundary $\varphi(\partial\Omega)$ of $\mathscr{B}$. From the balance of angular momentum it can be shown that the Cauchy stress tensor is symmetric, i.e. $\boldsymbol{\sigma} = \boldsymbol{\sigma}^T$. By its turn, the balance of linear momentum for $\mathscr{B}$ yields the following partial differential equation (with boundary conditions

established by Cauchy's theorem):

$$\begin{cases} \mathrm{div}_{\boldsymbol{x}}(\boldsymbol{\sigma}) + \boldsymbol{b} = \rho\, \ddot{\boldsymbol{u}} & \text{in } \varphi(\Omega), \\ \boldsymbol{t} = \boldsymbol{\sigma}\boldsymbol{n} & \text{in } \varphi(\partial\Omega), \end{cases} \tag{2.75}$$

Equations (2.75) define the spatial *strong form of equilibrium* (or, alternatively, the *local* or *point-wise* form of equilibrium). Equivalently, the strong equilibrium expression may be stated using a material configuration:

$$\begin{cases} \mathrm{div}_{\boldsymbol{p}}(\boldsymbol{P}) + \boldsymbol{b}_0 = \rho_0\, \ddot{\boldsymbol{u}} & \text{in } \Omega, \\ \boldsymbol{t}_0 = \boldsymbol{P}\boldsymbol{n}_0 & \text{in } \partial\Omega, \end{cases} \tag{2.76}$$

where $\boldsymbol{b}_0$ is the body force vector per unit (reference) volume

$$\boldsymbol{b}_0 = J\,\boldsymbol{b}, \tag{2.77}$$

and ρ_0 is the mass per unit (reference) volume

$$\rho_0 = J\,\rho, \tag{2.78}$$

2.3.3 First Law of Thermodynamics

The *first law of thermodynamics* is a statement of the conservation of energy. In detail, this law postulates that "the rate of internal energy equals the sum of the stress power and heat production subtracted to the spatial divergence of the heat flux" (all expressed per unit deformed volume). In order to mathematically represent this law, it is convenient to define the following scalar fields over $\mathscr{B}$: θ (temperature), e (specific energy), s (specific entropy) and r (density of heat production). With this in mind, the first law of thermodynamics implies the subsequent identity:

$$\rho\,\dot{e} = \boldsymbol{\sigma} : \boldsymbol{D} + \rho r - \mathrm{div}_{\boldsymbol{x}}(\boldsymbol{q}). \tag{2.79}$$

where $\boldsymbol{q}$ is the heat flux and $\boldsymbol{\sigma} : \boldsymbol{D}$ is the stress power (per unit deformed volume).

2.3.4 Second Law of Thermodynamics

The *second law of thermodynamics* states the directionality of thermodynamic processes (i.e., the irreversibility of entropy production). Mathematically, it is given by the next inequality:

$$\rho\,\dot{s} + \mathrm{div}_{\boldsymbol{x}}\left(\frac{\boldsymbol{q}}{\theta}\right) - \frac{\rho r}{\theta} \geq 0. \tag{2.80}$$

2.3.5 Clausius-Duhem Inequality

The *Clausius-Duhem inequality* results from combining equations (2.79) and (2.80):

$$\boldsymbol{\sigma} : \boldsymbol{D} - \rho(\dot{\psi} + s\,\dot{\theta}) - \frac{1}{\theta}\,\boldsymbol{q} \cdot \boldsymbol{g} \geq 0, \tag{2.81}$$

where $\dot{\psi}$ is the time derivative of the *specific free energy* ψ defined by

$$\psi = e - \theta s, \tag{2.82}$$

and $\boldsymbol{g}$ gives the spatial gradient of the temperature field,

$$\boldsymbol{g} = \nabla_{\boldsymbol{x}}(\theta). \tag{2.83}$$

The left hand side of the inequality represents the *dissipation* per unit of deformed volume. Identically, the material version the Clausius-Duhem inequality reads:

$$\boldsymbol{\tau} : \boldsymbol{D} - \rho_0 (\dot{\psi} + s\dot{\theta}) - \frac{J}{\theta} \boldsymbol{q} \cdot \boldsymbol{g} \geq 0. \tag{2.84}$$

2.4 Constitutive Theory

In the light of previous Sections, continuum systems are governed by five differential equations (specifically, the principle of conservation of mass, the first law of thermodynamics and the three equations that result from the balance of linear momentum) with sixteen unknowns[6]:

$$\begin{gathered} \boldsymbol{\sigma} \text{ (6 unknowns)}, \qquad \boldsymbol{x} \text{ or } \boldsymbol{p} \text{ (3 unknowns)}, \qquad \boldsymbol{q} \text{ (3 unknowns)}, \\ \theta \text{ (1 unknown)}, \qquad e \text{ (1 unknowns)}, \qquad s \text{ (1 unknown)}, \qquad \rho \text{ (1 unknown)}, \end{gathered}$$

where the symmetry of the stress tensor was imposed and we had assumed that the heat source r and the body forces $\boldsymbol{b}$ are known external interactions with the vicinity. Therefore, the problem is not well posed and it is necessary to obtain an additional eleven linearly independent equations. These equations must take into consideration the response of materials to mechanical (and thermal) loadings imposed on them. In fact, the material of which the body is made plays a decisive role in its response (in other words, two bodies subjected to the same set of forces may deform differently if the constituent material is different). Hence, we should define laws that capture the behaviour of materials. These laws are called *constitutive models*, allowing the distinction between different types of materials. In this Section, the principles that form the basis of constitutive theories are briefly reviewed.

2.4.1 Constitutive Axioms

In the present context, we shall start by defining a *thermokinetic* process of $\mathscr{B}$ as a pair of fields:

$$\varphi(\boldsymbol{p}, t) \text{ and } \theta(\boldsymbol{p}, t),$$

and *calorodynamic* process $\mathscr{B}$ as a set of fields

$$\boldsymbol{\sigma}(\boldsymbol{p}, t),\ e(\boldsymbol{p}, t),\ s(\boldsymbol{p}, t),\ r(\boldsymbol{p}, t),\ \boldsymbol{b}(\boldsymbol{p}, t) \text{ and } \boldsymbol{q}(\boldsymbol{p}, t)$$

[6] We are taking advantage of the symmetry of the Cauchy stress tensor – if we consider the first Piola-Kirchhoff stress tensor 3 more unknowns would be added.

satisfying the balance of linear momentum and the first and second laws of thermodynamics (Truesdell, 1969). These processes are intrinsically connected with three fundamental axioms that every constitutive model must satisfy:

1. *Principle of thermodynamically compatible determinism.* It states that "the history of the thermokinetic process to which a neighbourhood of a point $\boldsymbol{p}$ of $\mathscr{B}$ has been subjected determines a calorodynamic process for $\mathscr{B}$ at $\boldsymbol{p}$" (Truesdell, 1969). Of particular interest is the case of *simple materials* for which the local history of $\boldsymbol{F}$, θ and $\boldsymbol{g}$ dictates the history of the thermokinetic process. In that case, the local histories of $\boldsymbol{F}$, θ and $\boldsymbol{g}$ characterize a calorodynamic process for $\mathscr{B}$ at $\boldsymbol{p}$, meaning that this principle predicts the existence of constitutive functionals $\mathfrak{F}$, $\mathfrak{G}$, $\mathfrak{H}$ and $\mathfrak{J}$ dependent on these histories, in such a manner that:

$$\boldsymbol{\sigma}(\boldsymbol{p},t) = \mathfrak{F}(\boldsymbol{F}^t(\boldsymbol{p}),\theta^t(\boldsymbol{p}),\boldsymbol{g}^t(\boldsymbol{p})), \tag{2.85}$$

$$\psi(\boldsymbol{p},t) = \mathfrak{G}(\boldsymbol{F}^t(\boldsymbol{p}),\theta^t(\boldsymbol{p}),\boldsymbol{g}^t(\boldsymbol{p})), \tag{2.86}$$

$$s(\boldsymbol{p},t) = \mathfrak{H}(\boldsymbol{F}^t(\boldsymbol{p}),\theta^t(\boldsymbol{p}),\boldsymbol{g}^t(\boldsymbol{p})), \tag{2.87}$$

$$\boldsymbol{q}(\boldsymbol{p},t) = \mathfrak{J}(\boldsymbol{F}^t(\boldsymbol{p}),\theta^t(\boldsymbol{p}),\boldsymbol{g}^t(\boldsymbol{p})), \tag{2.88}$$

   where the superscript t denotes the history (i.e. $\boldsymbol{F}^t(\boldsymbol{p})$ represents the history of the deformation gradient at $\boldsymbol{p}$ up to time t). We must observe that just four of the six fields which compose a calorodynamic process are specified: again, it is considered that the body forces $\boldsymbol{b}$ and the heat supply r are known external interactions of the body with its neighbourhood. Besides, we have decided to allocate a constitutive functional for the specific free energy ψ instead of the specific energy e. Lastly, this principle also implies that the Clausius-Duhem inequality holds for every thermokinetic process of $\mathscr{B}$.

2. *Principle of material objectivity (or frame invariance).* It postulates that constitutive laws are dissociated from the observer. Two motions, φ^* and φ, are connected by a change in the observer, if the following relation is verified:

$$\varphi^*(\boldsymbol{p},t) = \boldsymbol{y}(t) + \boldsymbol{R}(t)\,(\varphi(\boldsymbol{p},t) - \boldsymbol{x}_0), \tag{2.89}$$

   where $\boldsymbol{y}(t)$ is an arbitrary point in space, $\boldsymbol{R}(t)$ is an orthogonal second order tensor (representing a rotation) and $(\varphi(\boldsymbol{p},t) - \boldsymbol{x}_0)$ is the position vector of $\varphi(\boldsymbol{p},t)$ relative to a generic origin $\boldsymbol{x}_0$. Equation (2.89) implies a rigid relative movement between the observers which (according to this principle) must not influence constitutive laws. Putting it differently, this principle requires the constitutive functionals defined in equations (2.85) to (2.88) to satisfy:

$$\boldsymbol{\sigma}^*(\boldsymbol{p},t) = \mathfrak{F}(\boldsymbol{F}^{t*}(\boldsymbol{p}),\theta^t(\boldsymbol{p}),\boldsymbol{g}^{t*}(\boldsymbol{p})), \tag{2.90}$$

$$\psi(\boldsymbol{p},t) = \mathfrak{G}(\boldsymbol{F}^{t*}(\boldsymbol{p}),\theta^t(\boldsymbol{p}),\boldsymbol{g}^{t*}(\boldsymbol{p})), \tag{2.91}$$

$$s(\boldsymbol{p},t) = \mathfrak{H}(\boldsymbol{F}^{t*}(\boldsymbol{p}),\theta^t(\boldsymbol{p}),\boldsymbol{g}^{t*}(\boldsymbol{p})), \tag{2.92}$$

$$\boldsymbol{q}^*(\boldsymbol{p},t) = \mathfrak{J}(\boldsymbol{F}^{t*}(\boldsymbol{p}),\theta^t(\boldsymbol{p}),\boldsymbol{g}^{t*}(\boldsymbol{p})), \tag{2.93}$$

where the vectorial (generically, $\boldsymbol{a}$) and tensorial ($\boldsymbol{A}$) fields corresponding to the motion φ^* are given, respectively, by $\boldsymbol{a}^* = \boldsymbol{R}\boldsymbol{a}$ and $\boldsymbol{A}^* = \boldsymbol{R}\boldsymbol{A}\boldsymbol{R}^T$. Observe that the scalar fields a are independent of the observer, $a^* = a$.

3. *Principle of material symmetry.* This principle is related to the symmetry group $\mathscr{L}$ of a body $\mathscr{B}$, which may be seen as the set of rotations of the initial configuration that do not affect the constitutive functionals. The symmetry group $\mathscr{L}$ of a material body is a subset of the proper orthogonal group $\mathscr{O}^+$. Naming $\boldsymbol{R} \in \mathscr{I}$ as the generic time-independent rotation tensor of the simmetry group of a solid material, the following relations must be satisfied:

$$\mathfrak{F}(\boldsymbol{F}^t, \theta^t, \boldsymbol{g}^t) = \mathfrak{F}([\boldsymbol{F}\boldsymbol{R}]^t, \theta^t, \boldsymbol{g}^t), \tag{2.94}$$

$$\mathfrak{G}(\boldsymbol{F}^t, \theta^t, \boldsymbol{g}^t) = \mathfrak{G}([\boldsymbol{F}\boldsymbol{R}]^t, \theta^t, \boldsymbol{g}^t), \tag{2.95}$$

$$\mathfrak{H}(\boldsymbol{F}^t, \theta^t, \boldsymbol{g}^t) = \mathfrak{H}([\boldsymbol{F}\boldsymbol{R}]^t, \theta^t, \boldsymbol{g}^t), \tag{2.96}$$

$$\mathfrak{J}(\boldsymbol{F}^t, \theta^t, \boldsymbol{g}^t) = \mathfrak{J}([\boldsymbol{F}\boldsymbol{R}]^t, \theta^t, \boldsymbol{g}^t), \tag{2.97}$$

with dependence on $\boldsymbol{p}$ omitted for notational convenience. Frequently, we cope with *isotropic* constitutive models. In that case, the simmetry group of the solid material under analysis coincides with the proper orthogonal group (i.e. $\mathscr{I} \equiv \mathscr{O}^+$) and, as a result, the response of isotropic materials remains the same for all directions.

2.4.2 Thermodynamics with Internal Variables

Constitutive equations (2.85) to (2.88) embody the general constitutive relations and show the dependence of the constitutive functionals upon the histories of $\boldsymbol{F}$, θ and $\boldsymbol{g}$. Although these equations must be satisfied for any constitutive model, in the general form they are presented here, they bear limited practical utility. A particular instance of the general history functional-based constitutive theory with far more application in engineering problems (and that will be used throughout this work) involves *Thermodynamics with State Variables* (TSV). The most obvious feature of TSV relies on the fact that a thermodynamic state is defined in terms of the instantaneous values of the so-called *state variables* (consequently, past histories do not need to be recorded). With this in mind, we can postulate that as long as *state variables models* are assumed, at any time t of a thermodynamic process, the thermodynamic state (given by $\boldsymbol{\sigma}$, ψ, s and $\boldsymbol{q}$) at a generic point can be determined by knowledge of the following finite number of state variables:

$$\{\boldsymbol{F}, \theta, \boldsymbol{g}, \boldsymbol{\alpha}\}$$

where all the variables are defined at time t and $\boldsymbol{\alpha}$ represents the set of internal variables ($\boldsymbol{\alpha} \equiv \{\alpha_k\}$). Note that the set of internal variables may include scalar, vectorial and tensorial quantities linked with, for instance, dissipative mechanisms.

The specific free energy ψ is independent of $\boldsymbol{g}$ (Coleman and Gurtin, 1969).

This statement together with the adoption of a state variables model leads to $\psi = \psi(\boldsymbol{F}, \theta, \boldsymbol{\alpha})$; accordingly, the derivative of ψ with respect to time is:

$$\dot{\psi} = \frac{\partial \psi}{\partial t} = \frac{\partial \psi}{\partial \boldsymbol{F}} : \dot{\boldsymbol{F}} + \frac{\partial \psi}{\partial \theta}\, \dot{\theta} + \sum_k \frac{\partial \psi}{\partial \alpha_k} * \dot{\alpha_k} \tag{2.98}$$

where $*$ denotes the appropriate product operation between $\partial\psi/\partial\alpha_k$ and $\dot{\alpha_k}$, depending on the nature of α_k (scalar, vectorial or tensorial). By substituting equation (2.98) into the Clausius-Duhem inequality (expression (2.81)):

$$\left(\boldsymbol{\sigma}\boldsymbol{F}^{-T} - \rho \frac{\partial \psi}{\partial \boldsymbol{F}}\right) : \dot{\boldsymbol{F}} - \rho \left(s + \frac{\partial \psi}{\partial \theta}\right) \dot{\theta} - \rho \sum_k \frac{\partial \psi}{\partial \alpha_k} * \dot{\alpha_k} - \frac{1}{\theta}\, \boldsymbol{q} \cdot \boldsymbol{g} \geq 0. \tag{2.99}$$

Equivalently, by using identity (2.78), we obtain the material version of (2.99):

$$\left(\boldsymbol{P} - \rho_0 \frac{\partial \psi}{\partial \boldsymbol{F}}\right) : \dot{\boldsymbol{F}} - \rho_0 \left(s + \frac{\partial \psi}{\partial \theta}\right) \dot{\theta} - \rho_0 \sum_k \frac{\partial \psi}{\partial \alpha_k} * \dot{\alpha_k} - \frac{1}{\theta}\, \boldsymbol{q} \cdot \boldsymbol{g} \geq 0. \tag{2.100}$$

The material (or spatial) version of the Clausius-Duhem inequality must hold for any thermokinetic process. Particularly, if we consider a process where the temperature is uniform across the body ($\boldsymbol{g} = \boldsymbol{0}$), the dissipative mechanisms are not active ($\boldsymbol{\alpha} = \boldsymbol{0}$) and the deformation gradient is constant in time ($\dot{\boldsymbol{F}} = 0$), we obtain:

$$\rho_0 \left(s + \frac{\partial \psi}{\partial \theta}\right) \dot{\theta} \geq 0. \tag{2.101}$$

Given that the sign of $\dot{\theta}$ is arbitrary, the only way of satisfying inequality (2.101) (for any process) is if

$$s = -\frac{\partial \psi}{\partial \theta}. \tag{2.102}$$

Equation (2.102) is known as *entropy constitutive relation*. Similarly, if the thermokinetic process involves an uniform temperature across the body and the dissipation mechanisms are not active, it follows that:

$$\boldsymbol{P} = \rho_0 \frac{\partial \psi}{\partial \boldsymbol{F}}. \tag{2.103}$$

The previous equation is referred to as *stress constitutive equation*. Alternative presentations of the constitutive relations for stresses are written in terms of the Cauchy stress tensor:

$$\boldsymbol{\sigma} = \rho \frac{\partial \psi}{\partial \boldsymbol{F}}\, \boldsymbol{F}^T \tag{2.104}$$

or of the Kirchhoff stress tensor:

$$\boldsymbol{\tau} = \rho_0 \frac{\partial \psi}{\partial \boldsymbol{F}}\, \boldsymbol{F}^T. \tag{2.105}$$

With attention to equations (2.102) and (2.103) and defining for each internal

variable α_k the conjugate thermodynamical force A_k as:

$$A_k \equiv \rho_0 \frac{\partial \psi}{\partial \alpha_k}, \tag{2.106}$$

we can rewrite inequality (2.100) as

$$-\sum_k A_k * \dot{\alpha_k} - \frac{1}{\theta}\, \boldsymbol{q} \cdot \boldsymbol{g} \geq 0. \tag{2.107}$$

Admitting that $\boldsymbol{A}$ is the set of conjugate thermodynamical forces ($\boldsymbol{A} \equiv \{A_k\}$), a more compact form of (2.107) can be reached:

$$-\boldsymbol{A} * \dot{\boldsymbol{\alpha}} - \frac{1}{\theta}\, \boldsymbol{q} \cdot \boldsymbol{g} \geq 0. \tag{2.108}$$

To fully characterize the constitutive model, constitutive equations for the flux variables $\dot{\boldsymbol{\alpha}}$ and $\boldsymbol{q}/\theta$ have to be formulated. Generally speaking, these variables are given functions (respectively, f and h) of the state variables:

$$\dot{\boldsymbol{\alpha}} = f(\boldsymbol{F}, \theta, \boldsymbol{g}, \boldsymbol{\alpha}), \tag{2.109}$$

$$\frac{1}{\theta}\, \boldsymbol{q} = h(\boldsymbol{F}, \theta, \boldsymbol{g}, \boldsymbol{\alpha}). \tag{2.110}$$

Before going further, an important point to be made in the discussion of TSV is that the success of this approach is deeply dependent upon the choice of internal variables. Eventually, the choice of internal variables should be driven by the process the body experiences and the material of which the body is made. However, anticipating dissipation mechanisms is generally very difficult and, consequently, selecting internal variables is, frequently, a subjective task. In short, within TSV, we can follow a *phenomenological* or a *micromechanical* approach. In the first case, we focus on elements of matter large enough to be considered continua; on the contrary, micromechanical approaches demand the determination of mechanisms at the atomic, molecular or crystalline levels (de Souza Neto et al., 2008). Despite the fact that purely phenomenological approaches are suited for many applications in solid mechanics, in some cases the inclusion of microscopic information becomes indispensable (e.g., see the discussion made in Section 6.1).

2.4.3 Mechanical Constitutive Initial Value Problem

Internal variable-based constitutive models were addressed in Section 2.4.2, including the entropy equation (2.102), the stress equation (2.103) and the flux variables equations (2.109) and (2.110). In purely mechanical problems, thermal effects are neglected and all thermally-related therms of the referred equations are removed. As a consequence, *mechanical constitutive equations* become:

$$\psi = \psi(\boldsymbol{F}, \boldsymbol{\alpha}), \tag{2.111}$$

$$\boldsymbol{P} = \rho_0 \frac{\partial \psi}{\partial \boldsymbol{F}}, \tag{2.112}$$

$$\dot{\boldsymbol{\alpha}} = f(\boldsymbol{F}, \boldsymbol{\alpha}). \tag{2.113}$$

When the internal variable approach is adopted and thermally-related terms are ignored, the constitutive problem originates a *mechanical constitutive initial value problem* which may be resumed as follows: "Given the initial values of the internal variables $\boldsymbol{\alpha}(t_0)$ and the history of the deformation gradient

$$\boldsymbol{F}(t), \quad t \in [t_0, T]$$

find the functions $\boldsymbol{P}(t)$ and $\boldsymbol{\alpha}(t)$ for the first Piola-Kirchhoff stress and the set of internal variables, such that the constitutive equations:

$$\boldsymbol{P}(t) = \rho_0 \frac{\partial \psi}{\partial \boldsymbol{F}}, \tag{2.114}$$

$$\dot{\boldsymbol{\alpha}}(t) = f(\boldsymbol{F}(t), \boldsymbol{\alpha}(t)), \tag{2.115}$$

are satisfied for every $t \in [t_0, T]$" (de Souza Neto et al., 2008).

2.5 Weak Equilibrium Equations

The strong form of equilibrium was pointed out in equations (2.75) and (2.76). These equations, unlike theirs weak counterpart, demand strong continuity on the dependent field variables (specifically, the components of the displacement vector $\boldsymbol{u}$). Furthermore, the functions that define the components of $\boldsymbol{u}$ must be differentiable up to the order of the partial differential equations that exist in the strong form aforementioned. Generally speaking, we can say that the exact solution for a strong form of equilibrium is usually quite difficult for practical engineering problems (Quek and Liu, 2003). On the contrary, the *weak form of equilibrium* (also called global form of equilibrium) is an integral form which requires a weaker continuity on the field variables. Given these points, the majority of the numerical methods used in the context of CMT (with the objective of generating approximate solutions) involve a spatial discretisation of the weak form of the equilibrium equations (a well-known example, which will be addressed in Section 2.7, is the FEM). In fact, the weak equilibrium statement is the starting point of the displacement-based finite element procedures for the analysis of solid bodies. This weak formulation derives from the application of a variational principle to the equilibrium equations: in this Section, the *Principle of Virtual Work* is used and three versions are presented (*spatial*, *material* and *quasi-static*).

2.5.1 Spatial Version

The *Eulerian* version of the weak equilibrium statement requires the following equality to be satisfied:

$$\int_{\varphi(\Omega)} \left[\boldsymbol{\sigma} : \nabla_{\boldsymbol{x}}(\boldsymbol{\eta}) - (\boldsymbol{b} - \rho\, \ddot{\boldsymbol{u}}) \cdot \boldsymbol{\eta} \right] dv - \int_{\varphi(\partial\Omega)} \boldsymbol{t} \cdot \boldsymbol{\eta}\; da = 0, \quad \forall \boldsymbol{\eta} \in \mathscr{V}, \tag{2.116}$$

where $\boldsymbol{\eta}$ is the virtual displacement vector that belongs to the space of admissible virtual displacements $\mathscr{V}$ (more about this set can be found in Section 2.6). In case the Cauchy stress tensor $\boldsymbol{\sigma}$ is sufficiently smooth, it is possible to prove that the previous equation is equivalent to the strong equilibrium statement[7] (see, for example, de Souza Neto et al. (2008)).

2.5.2 Material Version

If we make use of equation (2.61) and consider the following identity (that holds for a generic vector field $\boldsymbol{a}$):

$$\nabla_{\boldsymbol{x}}(\boldsymbol{a}) = \nabla_{\boldsymbol{p}}(\boldsymbol{a})\, \boldsymbol{F}^{-1}, \tag{2.117}$$

as well as the standard relation for a generic scalar field a (Gurtin, 1981):

$$\int_{\varphi(\Omega)} a(\boldsymbol{x})\; dv = \int_{\Omega} J(\boldsymbol{p})\, a(\varphi(\boldsymbol{p}))\; dv, \tag{2.118}$$

we are able to establish the *Lagrangian* version of equation (2.116):

$$\int_{\Omega} \Big[\boldsymbol{P} : \nabla_{\boldsymbol{p}}(\boldsymbol{\eta}) - (\boldsymbol{b}_0 - \rho_0\, \ddot{\boldsymbol{u}}) \cdot \boldsymbol{\eta} \Big]\; dv - \int_{\partial\Omega} \boldsymbol{t}_0 \cdot \boldsymbol{\eta}\; da = 0, \quad \forall \boldsymbol{\eta} \in \mathscr{V}. \tag{2.119}$$

2.5.3 Quasi-static Version

As it was said before, inertial effects will not be taken into account. This simplification leads to the so called *quasi-static version* of the weak equilibrium statement which can be deduced from equation (2.116) (assuming that the deformed configuration is analysed):

$$\int_{\varphi(\Omega)} \Big[\boldsymbol{\sigma} : \nabla_{\boldsymbol{x}}(\boldsymbol{\eta}) - \boldsymbol{b} \cdot \boldsymbol{\eta} \Big]\; dv - \int_{\varphi(\partial\Omega)} \boldsymbol{t} \cdot \boldsymbol{\eta}\; da = 0, \quad \forall \boldsymbol{\eta} \in \mathscr{V}. \tag{2.120}$$

Its material counterpart is given by:

$$\int_{\Omega} \Big[\boldsymbol{P} : \nabla_{\boldsymbol{p}}(\boldsymbol{\eta}) - \boldsymbol{b}_0 \cdot \boldsymbol{\eta} \Big]\; dv - \int_{\partial\Omega} \boldsymbol{t}_0 \cdot \boldsymbol{\eta}\; da = 0, \quad \forall \boldsymbol{\eta} \in \mathscr{V}. \tag{2.121}$$

In both cases, we must observe that the terms involving time derivatives (in the general expressions (2.116) and (2.119)) were neglected.

2.6 Quasi-Static Initial Boundary Value Problem

In order to formulate the *quasi-static initial boundary value problem*, it is necessary to recall the internal variable-based constitutive models introduced in Section 2.4. In particular, the mechanical constitutive initial value problem shall be considered and, again, we must admit that the set of internal variables is known at the initial

[7] A similar statement can be made in case a material approach is followed.

time (i.e. $\boldsymbol{\alpha}(\boldsymbol{p}, t_0) = \boldsymbol{\alpha}_0(\boldsymbol{p})$). Additionally, the deformation gradient is prescribed, so the function $\boldsymbol{P}(t)$ for the first Piola-Kirchhoff stress tensor is the solution of the aforementioned mechanical constitutive initial value problem[8]. It is noteworthy to mention that the prescription of the deformation gradient is a consequence of equation (2.16). Indeed, the deformation gradient is a consequence of the displacement vector $\boldsymbol{u}$ which is, all things considered, the primary unknown variable of the problem formulated in this Section. To achieve the set objective, it is important to carefully analyse the generic body $\mathscr{B}$ in Figure 2.9 which is subjected to a prescribed history of body forces given by:

$$\boldsymbol{b}(\boldsymbol{x}, t), \quad t \in [t_0, T], \ \boldsymbol{x} \in \varphi(\mathscr{B}). \tag{2.122}$$

Additionally:

- *Natural boundary conditions* are imposed over the portion of the boundary of the body occupying $\partial\Omega_t$ in the reference configuration (the subscript t refers, in this case, to *traction*). In other words, the surface tractions over $\partial\Omega_t$ are prescribed up to generic time T:

$$\boldsymbol{t}(\boldsymbol{x}, t), \quad t \in [t_0, T], \ \boldsymbol{x} \in \varphi(\partial\Omega_t). \tag{2.123}$$

- *Essential boundary conditions* are imposed over the fraction of the boundary[9] of the body given by $\partial\Omega_u$ at time t_0 (the subscript u refers to *displacement*). Essential boundary conditions imply a prescribed motion over $\partial\Omega_u$:

$$\bar{\varphi}(\boldsymbol{p}, t) = \boldsymbol{p} + \bar{\boldsymbol{u}}(\boldsymbol{p}, t), \quad t \in [t_0, T], \ \boldsymbol{p} \in \partial\Omega_u, \tag{2.124}$$

  where $\bar{\boldsymbol{u}}$ is the prescribed boundary displacement field. Consequently, they restrict the space of *kinematically admissible displacements* of $\mathscr{B}$:

$$\mathscr{K} = \left\{ \boldsymbol{u} \mid \boldsymbol{u}(\boldsymbol{p}, t) = \bar{\boldsymbol{u}}(\boldsymbol{p}, t), \ t \in [t_0, T], \ \boldsymbol{p} \in \partial\Omega_u \right\}. \tag{2.125}$$

The points discussed in this Section along with the quasi-static version of the weak equilibrium equations are the elements required to define the quasi-static initial boundary value problem (this is illustrated in Figure 2.10). Its spatial version is stated by de Souza Neto et al. (2008): "Find a kinematically admissible displacement function, $\boldsymbol{u} \in \mathscr{K}$, such that, for all $t \in [t_0, T]$, the virtual work equation is satisfied:

$$\int_{\varphi(\Omega,t)} \left[\boldsymbol{\sigma}(t) : \nabla_{\boldsymbol{x}}(\boldsymbol{\eta}) - \boldsymbol{b}(t) \cdot \boldsymbol{\eta} \right] dv - \int_{\varphi(\partial\Omega_t,t)} \boldsymbol{t}(t) \cdot \boldsymbol{\eta} \, da = 0, \quad \forall \boldsymbol{\eta} \in \mathscr{V}_t, \tag{2.126}$$

where the space of virtual admissible displacements at time t is given by:

$$\mathscr{V}_t = \left\{ \boldsymbol{\eta} \mid \boldsymbol{\eta} = 0 \text{ on } \varphi(\partial\Omega_u, t) \right\}." \tag{2.127}$$

[8] With both first Piola-Kirchhoff and deformation gradient tensors defined, it is possible to obtain, by means of equation (2.61), the Cauchy stress tensor function $\boldsymbol{\sigma}(t)$.

[9] For simplicity, it was supposed that $\partial\Omega_u \cap \partial\Omega_t = \emptyset$.

The material counterpart of (2.126) is also established by de Souza Neto et al. (2008): "Find a kinematically admissible displacement function $\boldsymbol{u} \in \mathscr{K}$, such that, for all $t \in [t_0, T]$,

$$\int_{\Omega} \left[\boldsymbol{P}(t) : \nabla_{\boldsymbol{p}}(\boldsymbol{\eta}) - \boldsymbol{b}_0(t) \cdot \boldsymbol{\eta} \right] \, dv - \int_{\partial\Omega_t} \boldsymbol{t}_0(t) \cdot \boldsymbol{\eta} \, da = 0, \quad \forall \boldsymbol{\eta} \in \mathscr{V}. \tag{2.128}$$

where the space of virtual admissible displacements is given by:

$$\mathscr{V} = \left\{ \boldsymbol{\eta} \mid \boldsymbol{\eta} = 0 \text{ on } \partial\Omega_u \right\}" \tag{2.129}$$

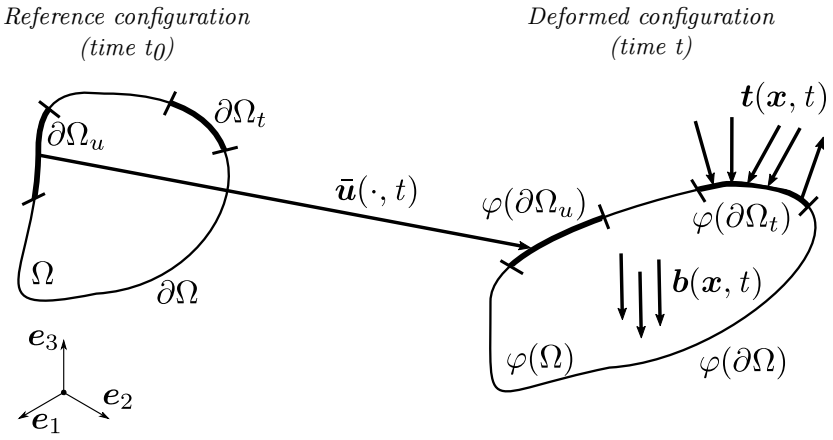

Figure 2.9: Schematic representation of the initial boundary value problem.

2.7 Finite Element Method

The integral (weak) form of the quasi-static initial boundary value problem was the main focus of Section 2.6. We should bear in mind that analytical solutions of equations (2.126) and (2.128) are practically impossible to obtain if solid bodies with complex geometries or made of materials governed by complicated constitutive laws are being analysed. For this reason, numerical methods are often employed, with the FEM being the most widespread within solid mechanics. Since the weak form of the quasi-static initial boundary problem was already established, the content of this Section is reduced to the treatment of the subsequent stages associated with the application of this method to generic solid mechanics problems (formulated under the assumption of large strains). Hence, two major numerical approximations are described (*time* and *spatial discretisation*). Moreover, because the original problem is transformed into a set of *incremental (generally non-linear) algebraic equations*, the *Newton-Rapshon* algorithm is also addressed. A compilation of the main FEM steps is made in Figure 2.10.

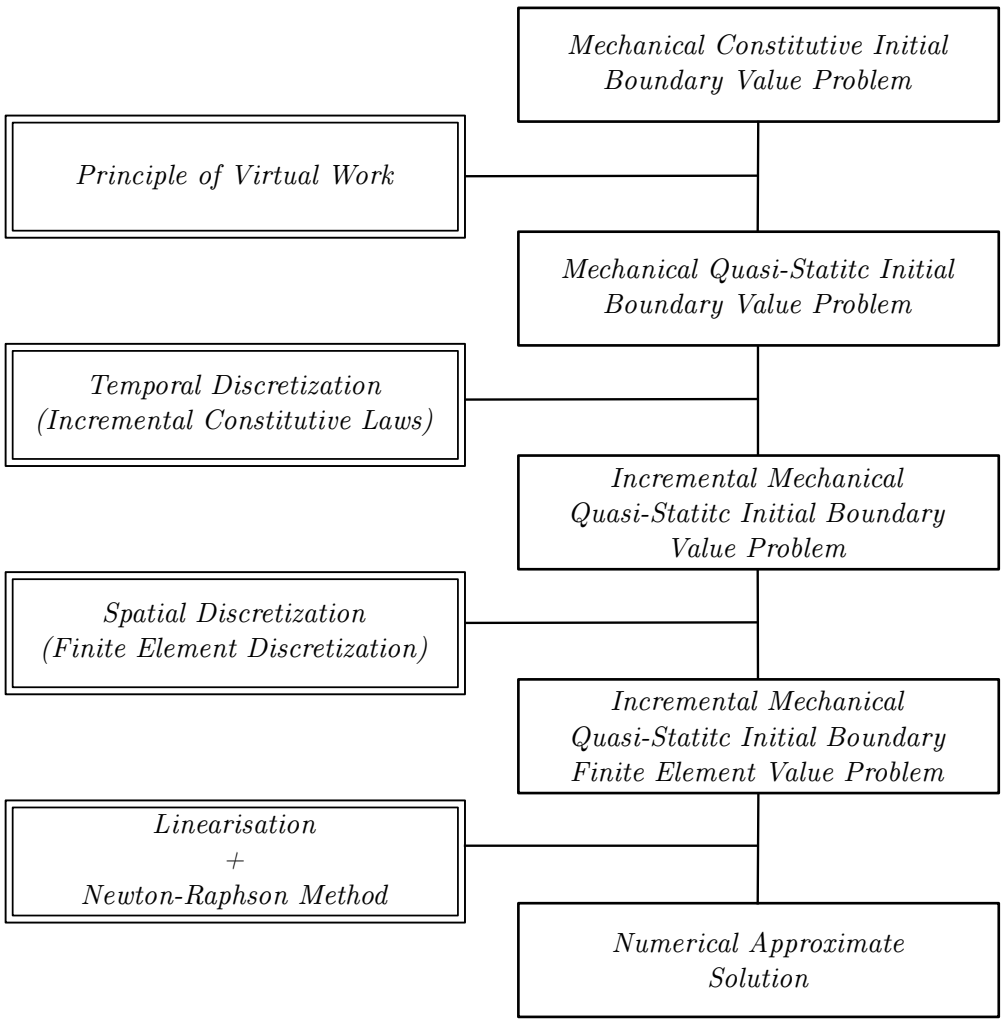

Figure 2.10: Schematic representation of the different tools (left column) and steps (right column) which outcome from FEM approach to a mechanical quasi-static initial boundary value problem.

2.7.1 Temporal Discretisation

In many engineering applications, deformations are considered infinitesimal; at the same time, the focus is often set on *elastic* or *hyperelastic materials* whose behaviour depends solely on the instantaneous value of strains. In some applications, however, these assumptions are not accurate, that is, the response of engineering materials may depend on the deformation history. To put it another way, the constitutive equations of the underlying material model may be *path dependent*, in such a manner that the adoption of an internal variable-based constitutive model is inevitable. It happens that the solution of the mechanical constitutive initial value problem (Section 2.4) is typically not known for complex deformation paths $\boldsymbol{F}(t)$. The FEM provides

approximate solutions for problems comprising path-dependent models: a numerical integration scheme is used for the integration of the constitutive equations. This numerical integration scheme embodies, in summary, an incremental strategy which implies a *time* (or, in quasi-static problems, *pseudo-time*) *discretisation* (the time interval $[t_0, T]$ is decomposed in n subintervals) and admits a specific deformation path along each subinterval (in which the equilibrium equations must be satisfied).

Within the domain of purely mechanical problems and taking into account the generic time increment $[t_n, t_{n+1}]$, it is imposed that the Cauchy stress tensor at the end of the standard subinterval t_{n+1} (denoted $\boldsymbol{\sigma}_{n+1}$) is determined uniquely by a given set of internal variables at time t_n, $\boldsymbol{\alpha}_n$, and the prescribed deformation gradient at time t_{n+1}, $\boldsymbol{F}_{n+1}$, through the integration algorithm. This statement outlines the numerical counterpart of the principle of thermodynamically compatible determinism discussed in Section 2.4.1 and it requires the integration algorithm to define an *incremental constitutive function*, $\hat{\boldsymbol{\sigma}}$, for the stress tensor, such that:

$$\boldsymbol{\sigma}_{n+1} = \hat{\boldsymbol{\sigma}}(\boldsymbol{\alpha}_n, \boldsymbol{F}_{n+1}). \tag{2.130}$$

As the strain increments are decreased, it is expected that the outcome $\boldsymbol{\sigma}_{n+1}$ converges to the exact solution. Furthermore, the numerical constitutive law, which might be non-linear, is *path-independent* within one increment. Putting it differently, within each subinterval, $\boldsymbol{\alpha}_n$ is constant, following that $\boldsymbol{\sigma}_{n+1}$ is a function of $\boldsymbol{F}_{n+1}$ alone. Equivalently, the numerical integration algorithm also determines an incremental constitutive function for the internal variables:

$$\boldsymbol{\alpha}_{n+1} = \hat{\boldsymbol{\alpha}}(\boldsymbol{\alpha}_n, \boldsymbol{F}_{n+1}). \tag{2.131}$$

An interesting point to be made relies on the fact that path-independent constitutive laws (such as finite elasticity laws) can also be expressed by means of incremental constitutive functions, leading to particular cases of the previous general equations (2.130) and (2.131). In short, with the introduction of the numerical integration scheme, the original time-continuum constitutive laws give rise to incremental time-discrete expressions that update the stresses and the internal variables of the model. If we introduce these time-discrete constitutive laws into the weak formulation of the initial boundary value problem formulated in Section 2.6, an *incremental boundary value problem* will be obtained. Its spatial version is stated by de Souza Neto et al. (2008) as follows: "Given the field $\boldsymbol{\alpha}_n$ at time t_n and given the body forces ($\boldsymbol{b}_{n+1}$) and surface traction ($\boldsymbol{t}_{n+1}$) fields at t_{n+1}, find a kinematically admissible configuration $\varphi_{n+1}(\Omega) \in \mathscr{K}_{n+1}$ such that the virtual work equation

$$\int_{\varphi_{n+1}(\Omega)} \left[\hat{\boldsymbol{\sigma}}(\boldsymbol{\alpha}_n, \boldsymbol{F}_{n+1}) : \nabla^s_{\boldsymbol{x}}(\boldsymbol{\eta}) - \boldsymbol{b}_{n+1} \cdot \boldsymbol{\eta} \right] dv - \int_{\varphi_{n+1}(\partial\Omega_t)} \boldsymbol{t}_{n+1} \cdot \boldsymbol{\eta} \; da = 0, \tag{2.132}$$

is satisfied for any $\boldsymbol{\eta} \in \mathscr{V}_{n+1}$, where $\varphi_{n+1}(\Omega)$ is the deformation map at t_{n+1}

$$\boldsymbol{x}_{n+1} = \varphi_{n+1}(\boldsymbol{p}) = \boldsymbol{p} + \boldsymbol{u}_{n+1}(\boldsymbol{p}), \tag{2.133}$$

and

$$\boldsymbol{F}_{n+1} = \nabla_{\boldsymbol{p}}(\varphi_{n+1}) = \boldsymbol{I} + \nabla_{\boldsymbol{p}}(\boldsymbol{u}_{n+1})." \tag{2.134}$$

The space of kinematically admissible displacements at time station t_{n+1} is given by:

$$\mathscr{K}_{n+1} = \left\{ \boldsymbol{u} \mid \boldsymbol{u} = \bar{\boldsymbol{u}}_{n+1} \text{ on } \partial\Omega_u \right\}, \tag{2.135}$$

where $\bar{\boldsymbol{u}}$ is the prescribed boundary displacement at t_{n+1}. Finally, $\mathscr{V}_{n+1}$ introduces the space of kinematically admissible virtual displacements at time t_{n+1} which may be extracted from equation (2.129).

An equivalent incremental constitutive function can be established for the first Piola-Kirchhoff stress tensor:

$$\boldsymbol{P}_{n+1} = \hat{\boldsymbol{P}}(\boldsymbol{\alpha}_n, \boldsymbol{F}_{n+1}). \tag{2.136}$$

With this in mind, we can formulate the material version of the incremental boundary value problem: "Given the field $\boldsymbol{\alpha}_n$ at time t_n and given the body forces ($\boldsymbol{b}_{0,n+1}$) and surface traction ($\boldsymbol{t}_{0,n+1}$) fields at t_{n+1}, find a kinematically admissible configuration $\varphi_{n+1}(\Omega) \in \mathscr{K}_{n+1}$ such that the virtual work equation

$$\int_{\Omega} \left[\hat{\boldsymbol{P}}(\boldsymbol{\alpha}_n, \boldsymbol{F}_{n+1}) : \nabla^s_{\boldsymbol{p}}(\boldsymbol{\eta}) - \boldsymbol{b}_{0,n+1} \cdot \boldsymbol{\eta} \right] dv - \int_{\partial\Omega_t} \boldsymbol{t}_{0,n+1} \cdot \boldsymbol{\eta} \, da = 0, \tag{2.137}$$

is satisfied for any $\boldsymbol{\eta} \in \mathscr{V}_{n+1}$. Observe that $\varphi_{n+1}(\Omega)$ is the deformation map at t_{n+1} given by equation (2.133) and that $\boldsymbol{F}_{n+1}$ is the deformation gradient at the same time (which results from (2.134)). The set $\mathscr{K}_{n+1}$ is given by (2.135)."

2.7.2 Spatial Discretisation

The spatial discretisation, also called *finite element discretisation*, is the main feature of the FEM. A discretisation h of the domain Ω of a generic body $\mathscr{B}$ motivates its division into a finite number of non-overlapping subdomains, each one a *finite element* (FE) occupying a region $\Omega^{(e)}$ (see Figure 2.11). The union (mathematically identified by the conventional union operator symbol $\bigcup$) of all FE domains determines the discretized solid domain:

$${}^h\Omega = \bigcup_{e=1}^{n_{elem}} \Omega^{(e)}, \tag{2.138}$$

where n_{elem} is the number of finite elements within the finite element mesh. The discretized domain approximates the (continuum) domain, that is, ${}^h\Omega \approx \Omega$.

Consider a generic finite element (e) (of an arbitrary finite element mesh) defined by n_{nodes} nodes. Let $N_i^{(e)}(\boldsymbol{x})$ denote the *shape function* associated with node i of the element (e) (whose spatial position is set by $\boldsymbol{x}^i$). Although shape functions within a FE are dictated by the type of element, these functions always satisfy the Kronecker

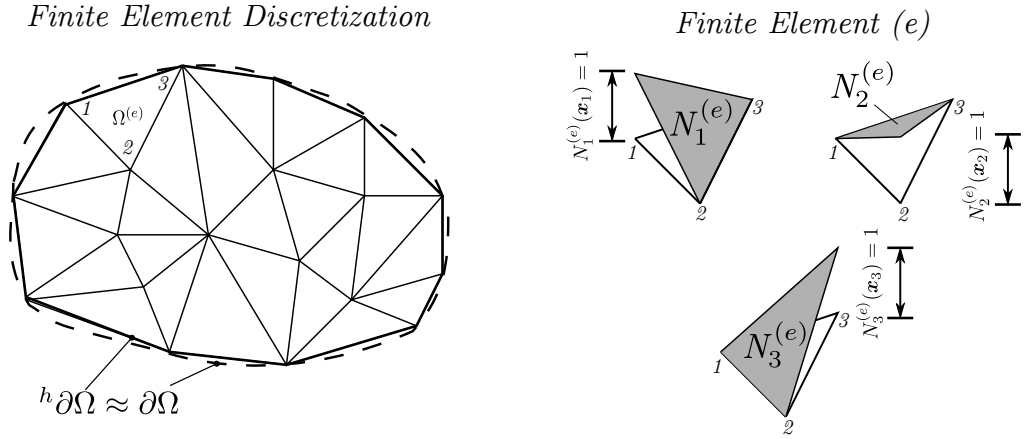

Figure 2.11: Spatial discretisation of a plane domain (mesh of triangular finite elements), including the representation of the shape functions associated with a generic finite element (e) (whose nodes are globally numbered as 1, 2 and 3).

delta property (δ_{ij} denotes the Kronecker delta variable):

$$N_i^{(e)}(\boldsymbol{x}^j) = \delta_{ij} = \begin{cases} 1, & \text{if } j = i \\ 0, & \text{if } j \neq i \end{cases}, \tag{2.139}$$

meaning that the shape function associated with node i has a unit value at i and zero at all other nodes of the element.

For a generic element (e), the *interpolation matrix* $\mathbf{N}^{(e)}$ is given by:

$$\mathbf{N}^{(e)} = \left[\text{diag}\left[N_1^{(e)}(\boldsymbol{x})\right] \ \text{diag}[N_2^{(e)}(\boldsymbol{x})] \ \ldots \ \text{diag}[N_{n_{nodes}}^{(e)}(\boldsymbol{x})] \right], \tag{2.140}$$

where the diagonal matrix associated with node i, $\text{diag}[N_i^{(e)}(\boldsymbol{x})]$, is a square matrix with dimension set by the number of spatial dimensions (n_{dof}):

$$\text{diag}\left[N_i^{(e)}(\boldsymbol{x})\right] = \begin{bmatrix} N_i^{(e)}(\boldsymbol{x}) & 0 & \ldots & 0 \\ 0 & N_i^{(e)}(\boldsymbol{x}) & \ldots & 0 \\ \vdots & \vdots & \ddots & \vdots \\ 0 & 0 & \ldots & N_i^{(e)}(\boldsymbol{x}) \end{bmatrix}_{n_{dof} \times n_{dof}} . \tag{2.141}$$

Another important matrix within this framework is the *global interpolation matrix* $\mathbf{N}^g$. This matrix is defined in an analogous way to $\mathbf{N}^{(e)}$, though considering all n_{poin}[10] nodes within the finite element mesh:

$$\mathbf{N}^g = \left[\text{diag}\left[N_1^g(\boldsymbol{x})\right] \ \text{diag}[N_2^g(\boldsymbol{x})] \ \ldots \ \text{diag}[N_{n_{poin}}^g(\boldsymbol{x})] \right], \tag{2.142}$$

where $\text{diag}[N_i^g(\boldsymbol{x})]$ is the diagonal matrix associated with global node i, which is

[10] Because adjacent elements share nodes, $n_{poin} < n_{elem} \times n_{nodes}$.

given by:

$$\text{diag}\left[N_i^g(\boldsymbol{x})\right] = \begin{bmatrix} N_i^g(\boldsymbol{x}) & 0 & \dots & 0 \\ 0 & N_i^g(\boldsymbol{x}) & \dots & 0 \\ \vdots & \vdots & \ddots & \vdots \\ 0 & 0 & \dots & N_i^g(\boldsymbol{x}) \end{bmatrix}_{n_{dof}\times n_{dof}} . \tag{2.143}$$

It is important to realize that N_i^g is the *global shape function* associated with global node i. Global shape functions also satisfy property (2.139).

The global interpolation matrix plays a crucial role in finite element interpolations. If, as stated before, $\boldsymbol{u}$ defines the displacement vector over the entire domain Ω, the finite element interpolation ${}^h\boldsymbol{u}$ provides an approximation of $\boldsymbol{u}$ over the entire domain. The interpolation function ${}^h\boldsymbol{u}$ depends on the global interpolation matrix, as well as on the *global vector of nodal displacements*:

$$\mathbf{u} = \left\{ u_1^1 \ , \ \dots \ , \ u_{n_{\text{dof}}}^1 \ , \ \dots \ , \ u_i^j \ , \ \dots \ , \ u_1^{n_{poin}} \ , \ \dots \ , \ u_{n_{\text{dof}}}^{n_{poin}} \right\}^T , \tag{2.144}$$

where u_i^j is the i-component at global node j. On the whole, we can state that:

$$\boldsymbol{u}(\boldsymbol{x}) \approx {}^h\boldsymbol{u}(\boldsymbol{x}) = \mathbf{N}^g(\boldsymbol{x})\ \mathbf{u}, \quad \forall {}^h\boldsymbol{u} \in {}^h\mathscr{K} \tag{2.145}$$

where the components of $\mathbf{u}(\boldsymbol{x})$ corresponding to nodal points on $\partial\Omega_u$ satisfy the prescribed kinematic constraints. Moreover, the set ${}^h\mathscr{K}$, generated by the finite element discretisation of the domain Ω, replaces the functional set $\mathscr{K}$ (within the spatial discretisation framework). The finite-dimensional set ${}^h\mathscr{K}$ can be represented as:

$${}^h\mathscr{K} = \left\{ {}^h\boldsymbol{u}(\boldsymbol{x}) = \sum_{j=1}^{n_{poin}} \boldsymbol{u}^j N_j^g(\boldsymbol{x}) \mid \boldsymbol{u}^j = \bar{\boldsymbol{u}}(\boldsymbol{x}^j) \text{ if } \boldsymbol{x}^j \in \partial\Omega_u \right\} \tag{2.146}$$

where $\boldsymbol{u}^j$ is the displacement vector at node j (including all the n_{dof} components of the global vector of nodal displacements $\boldsymbol{u}^g$ associated with node j) and $\bar{\boldsymbol{u}}(\boldsymbol{x}^j)$ is the prescribed displacement at the same node (its spatial position is given by $\boldsymbol{x}^j \in \partial\Omega_u$). Equivalently, if the global vector of virtual nodal displacements has the format:

$$\boldsymbol{\eta} = \left\{ \eta_1^1 \ , \ \dots \ , \ \eta_{n_{\text{dof}}}^1 \ , \ \dots \ , \ \eta_i^j \ , \ \dots \ , \ \eta_1^{n_{poin}} \ , \ \dots \ , \ \eta_{n_{\text{dof}}}^{n_{poin}} \right\}^T , \tag{2.147}$$

the finite element interpolation ${}^h\boldsymbol{\eta}$ of the virtual displacement vector $\boldsymbol{\eta}$ (over the domain Ω) is defined as:

$$\boldsymbol{\eta}(\boldsymbol{x}) \approx {}^h\boldsymbol{\eta}(\boldsymbol{x}) = \mathbf{N}(\boldsymbol{x})\ \boldsymbol{\eta}, \quad \forall {}^h\boldsymbol{\eta} \in {}^h\mathscr{V} \tag{2.148}$$

where ${}^h\mathscr{V}$ is the finite-dimensional subset which reduces $\mathscr{V}$ to:

$${}^h\mathscr{V} = \left\{ {}^h\boldsymbol{\eta}(\boldsymbol{x}) = \sum_{j=1}^{n_{poin}} \boldsymbol{\eta}^j N_j^g(\boldsymbol{x}) \mid \boldsymbol{\eta}^j = 0 \text{ if } \boldsymbol{x}^j \in \partial\Omega_u \right\}. \tag{2.149}$$

Thus, all components of the virtual displacement vector at node j, $\boldsymbol{\eta}^j$, must vanish if j belongs to the boundary $\partial\Omega_u$.

Two other important operators that need to be introduced are the *global discrete symmetric gradient operator* and the *global discrete spatial gradient operator*, respectively denoted $\mathbf{B}^g$ and $\mathbf{G}^g$. These matrices are relevant while discretizing the initial boundary value problem (or, more accurately, its incremental counterpart). The type of problem which is going to be solved affects the format of these matrices. Particularly, for two-dimensional (2D) problems, these matrices are given by:

$$\mathbf{B}^g = \begin{bmatrix} N^g_{1,1} & 0 & N^g_{2,1} & 0 & \dots & N^g_{n_{poin},2} & 0 \\ 0 & N^g_{1,2} & 0 & N^g_{2,2} & \dots & 0 & N^g_{n_{poin},2} \\ N^g_{1,2} & N^g_{1,1} & N^g_{2,2} & N^g_{2,1} & \dots & N^g_{n_{poin},2} & N^g_{n_{poin},1} \end{bmatrix}, \tag{2.150}$$

$$\mathbf{G}^g = \begin{bmatrix} N^g_{1,1} & 0 & N^g_{2,1} & 0 & \dots & N^g_{n_{poin},1} & 0 \\ 0 & N^g_{1,1} & 0 & N^g_{2,1} & \dots & 0 & N^g_{n_{poin},1} \\ N^g_{1,2} & 0 & N^g_{2,2} & 0 & \dots & N^g_{n_{poin},2} & 0 \\ 0 & N^g_{1,2} & 0 & N^g_{2,2} & \dots & 0 & N^g_{n_{poin},2} \end{bmatrix}. \tag{2.151}$$

A generic component of these matrices, $N^g_{i,j}$, is evaluated as:

$$N^g_{i,j} = \frac{\partial N^g_i}{\partial x_j}. \tag{2.152}$$

The element counterpart of these global matrices (also named as *deformation matrices*) come as:

$$\mathbf{B}^{(e)} = \begin{bmatrix} N^{(e)}_{1,1} & 0 & N^{(e)}_{2,1} & 0 & \dots & N^{(e)}_{n_{node},1} & 0 \\ 0 & N^{(e)}_{1,2} & 0 & N^{(e)}_{2,2} & \dots & 0 & N^{(e)}_{n_{node},2} \\ N^{(e)}_{1,2} & N^{(e)}_{1,1} & N^{(e)}_{2,2} & N^{(e)}_{2,1} & \dots & N^{(e)}_{n_{node},2} & N^{(e)}_{n_{node},1} \end{bmatrix}, \tag{2.153}$$

$$\mathbf{G}^{(e)} = \begin{bmatrix} N^{(e)}_{1,1} & 0 & N^{(e)}_{2,1} & 0 & \dots & N^{(e)}_{n_{node},1} & 0 \\ 0 & N^{(e)}_{1,1} & 0 & N^{(e)}_{2,1} & \dots & 0 & N^{(e)}_{n_{node},1} \\ N^{(e)}_{1,2} & 0 & N^{(e)}_{2,2} & 0 & \dots & N^{(e)}_{n_{node},2} & 0 \\ 0 & N^{(e)}_{1,2} & 0 & N^{(e)}_{2,2} & \dots & 0 & N^{(e)}_{n_{node},2} \end{bmatrix}. \tag{2.154}$$

Given all these points, we are now capable of establishing the *finite element equilibrium equation*. Its spatial version results from the substitution of the domain of the body and the associated functional sets for its finite-dimensional counterparts in equation (2.132):

$$\int_{\varphi_{n+1}({}^h\Omega)} \left[\hat{\boldsymbol{\sigma}}^T(\boldsymbol{\alpha}_n, \boldsymbol{F}_{n+1}) \mathbf{B}^g \boldsymbol{\eta} - \boldsymbol{b}_{n+1} \cdot \mathbf{N}^g \boldsymbol{\eta} \right] dv - \int_{\varphi_{n+1}(\partial^h\Omega_t)} \boldsymbol{t}_{n+1} \cdot \mathbf{N}^g \boldsymbol{\eta} \; da = 0, \quad \forall \boldsymbol{\eta} \in {}^h\mathscr{V}, \tag{2.155}$$

which can be rewritten:

$$\left\{ \int_{\varphi_{n+1}({}^h\Omega)} \left[(\mathbf{B}^g)^T \, \hat{\boldsymbol{\sigma}}(\boldsymbol{\alpha}_n, \boldsymbol{F}_{n+1}) - (\mathbf{N}^g)^T \, \boldsymbol{b}_{n+1} \right] dv \right.$$
$$\left. - \int_{\varphi_{n+1}(\partial^h\Omega_t)} (\mathbf{N}^g)^T \, \boldsymbol{t}_{n+1} \, da \right\}^T \cdot \boldsymbol{\eta} = 0, \quad \forall \boldsymbol{\eta} \in {}^h\mathscr{V}. \quad (2.156)$$

The above stated equation must be satisfied for all $\boldsymbol{\eta} \in {}^h\mathscr{V}$, so that the term within the curly braces must vanish. In addition, since the deformation gradient depends on the displacement field, we might sum up the *incremental boundary value finite element problem* as follows: "Find the kinematically admissible global nodal displacement vector $\mathbf{u}_{n+1}$ at time t_{n+1} that satisfies the incremental finite element equilibrium equation:

$$\mathbf{r}(\mathbf{u}_{n+1}) \equiv \mathbf{f}^g_{int}(\mathbf{u}_{n+1}) - \mathbf{f}^g_{ext,n+1} = 0 \quad (2.157)$$

where $\mathbf{f}^g_{int}$ and $\mathbf{f}^g_{ext,n+1}$ are, respectively, the *global vector of nodal internal* and *external forces*:

$$\mathbf{f}^g_{int} = \int_{\varphi_{n+1}({}^h\Omega)} (\mathbf{B}^g)^T \, \hat{\boldsymbol{\sigma}}(\boldsymbol{\alpha}_n, \boldsymbol{F}_{n+1}) \, dv, \quad (2.158)$$

$$\mathbf{f}^g_{ext,n+1} = \int_{\varphi_{n+1}({}^h\Omega)} (\mathbf{N}^g)^T \, \boldsymbol{b}_{n+1} \, dv + \int_{\varphi_{n+1}(\partial^h\Omega_t)} (\mathbf{N}^g)^T \, \boldsymbol{t}_{n+1} \, da." \quad (2.159)$$

Provided that the incremental constitutive functional $\hat{\boldsymbol{\sigma}}(\boldsymbol{\alpha}_n, \boldsymbol{F}_{n+1})$ is generally non-linear (and also as a consequence of geometrical non-linearities), equation (2.157) may be non-linear. This explains the necessity of considering the Newton-Rapshon method (see Section 2.7.3). Another point that must be emphasised is intrinsically connected with the practical procedure to compute the global force vectors of equations (2.158) and (2.159). These vectors are actually obtained as the assemblies:

$$\mathbf{f}^g_{int} = \mathop{\mathsf{A}}_{e=1}^{n_{elem}} \mathbf{f}^{(e)}_{int} \quad (2.160)$$

$$\mathbf{f}^g_{ext} = \mathop{\mathsf{A}}_{e=1}^{n_{elem}} \mathbf{f}^{(e)}_{ext} \quad (2.161)$$

of the *element internal* and *external nodal force vectors*:

$$\mathbf{f}^{(e)}_{int} = \int_{\varphi_{n+1}({}^h\Omega^{(e)})} (\mathbf{B}^{(e)})^T \, \hat{\boldsymbol{\sigma}}(\boldsymbol{\alpha}_n, \boldsymbol{F}_{n+1}) \, dv, \quad (2.162)$$

$$\mathbf{f}^{(e)}_{ext} = \int_{\varphi_{n+1}({}^h\Omega^{(e)})} (\mathbf{N}^{(e)})^T \, \boldsymbol{b}_{n+1} \, dv + \int_{\varphi_{n+1}(\partial^h\Omega^{(e)}_t)} (\mathbf{N}^{(e)})^T \, \boldsymbol{t}_{n+1} \, da. \quad (2.163)$$

A brief note about the *finite element assembly operator* A must be made here: each component of a global force vector is given by the sum of the corresponding components of the element force vector of all elements that share that (global) node.

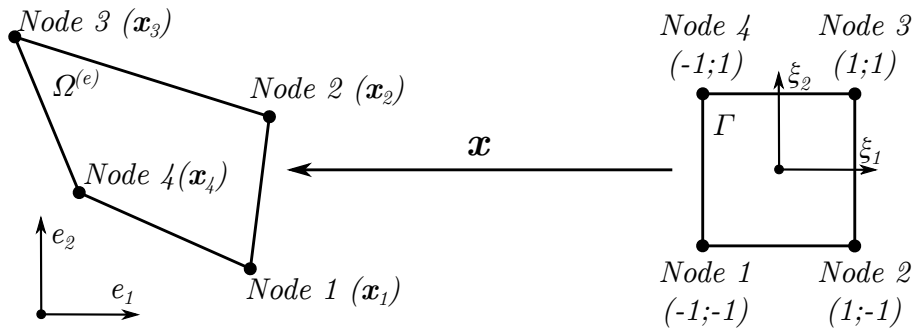

Figure 2.12: The transformation function $\boldsymbol{x}$ which maps the standard domain Γ onto the element domain $\Omega^{(e)}$.

Within the FEM framework, the exact integrals (2.162) and (2.163) are typically evaluated with a *Gaussian quadrature rule*. This numerical method allows integration over the element domain $\Omega^{(e)}$ (or over its boundary $\partial\Omega^{(e)}$) and is usually combined with the use of natural coordinates $\boldsymbol{\xi}$. The use of natural coordinates allows integration over a standard integration domain Γ. Moreover, let $\boldsymbol{x}$ map the standard domain onto the element domain, i.e. $\boldsymbol{x} : \Gamma \rightarrow \Omega^{(e)}$ (check Figure 2.12). Thus, the determinant of the Jacobian of the transformation $\boldsymbol{x}$ is obtained as:

$$j(\boldsymbol{\xi}) = \det\left(\frac{\partial \boldsymbol{x}}{\partial \boldsymbol{\xi}}\right). \tag{2.164}$$

Having said that, the Gaussian quadrature with n_{gaussp} *Gauss points* approximates the integral of a generic function $g(\boldsymbol{x})$ over $\Omega^{(e)}$ as follows:

$$\int_{\Omega^{(e)}} g(\boldsymbol{x})\, d\boldsymbol{x} = \int_{\Gamma} g(\boldsymbol{x}(\boldsymbol{\xi}))\, j(\boldsymbol{\xi})\, d\boldsymbol{\xi} \approx \sum_{i=1}^{n_{gaussp}} w(\boldsymbol{\xi}_i)\, \boldsymbol{g}(\boldsymbol{\xi}_i)\, j(\boldsymbol{\xi}_i) \tag{2.165}$$

where $\boldsymbol{\xi}_i$ identifies the natural coordinates of Gauss point i and $w(\boldsymbol{\xi}_i)$ is the corresponding weight. An alternative notation might be used to indicate that a generic field is being evaluated at $\boldsymbol{\xi}_i$: the subscript i is, in that situation, allocated to the generic field itself (as an illustration, $w(\boldsymbol{\xi}_i) = w_i$).

Equivalently, the integral of a function $g(\boldsymbol{x}^b)$ over a specific part of the element boundary (denoted $\partial\Omega_t^{(e)}$) might also be approximated with the Gaussian quadrature rule. For that purpose, we must take into account that $\boldsymbol{x}^b : \partial\Gamma \rightarrow \partial\Omega_t^{(e)}$ defines the boundary transformation. Thus, the determinant of the Jacobian of this transformation is:

$$j^b(\boldsymbol{\xi}^b) = \det\left(\frac{\partial \boldsymbol{x}^b}{\partial \boldsymbol{\xi}}\right). \tag{2.166}$$

and if, by chance, we consider n_{gaussb} Gauss points, we might write that:

$$\int_{\partial\Omega_t^{(e)}} g(\boldsymbol{x})\, d\boldsymbol{x}^b = \int_{\Gamma} g(\boldsymbol{x}^b(\boldsymbol{\xi}))\, j^b(\boldsymbol{\xi})\, d\boldsymbol{\xi} \approx \sum_{i=1}^{n_{gaussb}} w(\boldsymbol{\xi}_i)\, \boldsymbol{g}(\boldsymbol{\xi}_i)\, j(\boldsymbol{\xi}_i). \tag{2.167}$$

Again, the subscript i is allocated to the fields evaluated at $\boldsymbol{\xi}_i$: e.g. we might write that $w(\boldsymbol{\xi}_i^b) = w_i^b$ (note that, the superscript b was also linked with the field variable).

Altogether, the numerical computation of the element forces come as:

$$\mathbf{f}_{int}^{(e)} \approx \sum_{i=1}^{n_{gaussp}} \mathrm{w}_i \, j_i \, (\mathbf{B}_i^{(e)})^T \, \boldsymbol{\sigma}_{n+1,i} \tag{2.168}$$

$$\mathbf{f}_{ext}^{(e)} \approx \sum_{i=1}^{n_{gaussp}} \mathrm{w}_i \, j_i \, (\mathbf{N}_i^{(e)})^T \, \boldsymbol{b}_{n+1,i} + \sum_{i=1}^{n_{gaussb}} \mathrm{w}_i^b \, j_i^b \, (\mathbf{N}_i^{(e),b})^T \, \boldsymbol{t}_{n+1,i}^b \tag{2.169}$$

Up to this point, we have not made any comments about the way of computing body forces and surfaces tractions at time t_{n+1}. A possible strategy consists of adopting a *proportional loading* procedure in which the highlighted fields at generic time t_{n+1} are proportional to prescribed fields $\tilde{\boldsymbol{b}}$ and $\tilde{\boldsymbol{t}}$. These prescribed fields are constant in time, insomuch that $\boldsymbol{b}_{n+1}$ and $\boldsymbol{t}_{n+1}$ are set by a prescribed load factor, λ_{n+1}, which is fixed for a particular time t_{n+1}, but might vary between time stations. All in all, within the proportional loading technique, the desired body force and surface traction field at time t_{n+1} can be reached by imposing an appropriate load factor at the time of interest. Thus, we have:

$$\boldsymbol{b}_{n+1} = \lambda_{n+1} \, \tilde{\boldsymbol{b}}, \tag{2.170}$$

$$\boldsymbol{t}_{n+1} = \lambda_{n+1} \, \tilde{\boldsymbol{t}}. \tag{2.171}$$

It should be remarked that, since $\tilde{\boldsymbol{b}}$ and $\tilde{\boldsymbol{t}}$ are prescribed fields (constant in time), both body forces and surface tractions fields preserve their direction throughout the deformation process (λ_{n+1} is a scalar).

Before moving on to the Newton-Rapshon method, it should be noticed that a spatial description was used throughout this Section. Alternatively, a material description could have been employed. The material version of the *incremental boundary value finite element problem* (that comprises equations (2.157), (2.173) and (2.174)) is stated as follows: "Find the kinematically admissible global nodal displacement vector $\mathbf{u}_{n+1}$ at time t_{n+1} that satisfies the incremental finite element equilibrium equation:

$$\mathbf{r}(\mathbf{u}_{n+1}) \equiv \mathbf{f}_{int}^{g}(\mathbf{u}_{n+1}) - \mathbf{f}_{ext,n+1}^{g} = 0, \tag{2.172}$$

where $\mathbf{f}_{int}$ and $\mathbf{f}_{ext,n+1}$ are, respectively, the *global vector of nodal internal* and *external forces*:

$$\mathbf{f}_{int}^{g} = \int_{{}^{h}\Omega} (\mathbf{G}^g)^T \hat{\mathbf{P}}(\boldsymbol{\alpha}_n, \boldsymbol{F}_{n+1}) \, dv, \tag{2.173}$$

$$\mathbf{f}_{ext,n+1}^{g} = \int_{{}^{h}\Omega} (\mathbf{N}^g)^T \boldsymbol{b}_{0n+1} \, dv + \int_{\partial {}^{h}\Omega_t} (\mathbf{N}^g)^T \boldsymbol{t}_{0n+1} \, da." \tag{2.174}$$

2.7.3 Newton-Rapshon Method

As suggested before, the discretized version of the incremental boundary value problem (whose spatial and material versions are, respectively, (2.157) and (2.172)) is generally non-linear. Within the FEM framework, non-linear incremental problems are frequently solved with the Newton-Rapshon method. This numerical method provides a computational solution to the aforementioned problem in an efficient and robust way. If correctly implemented, the Newton-Rapshon method might guarantee quadratic rates of asymptotic convergence.

A standard iteration of this numerical method scheme involves the solution of the linearised version of the non-linear incremental finite element equation or, alternatively, of the discrete version of the linearised boundary value problem. If we follow the second alternative, the starting point of the algorithm involves the linearisation of (2.126) (or (2.128)). The linearised virtual work equation in the spatial description is:

$$\int_{\varphi(\Omega)} \mathbf{a} : \nabla_{\boldsymbol{x}}(\delta \boldsymbol{u}) : \nabla_{\boldsymbol{x}}(\boldsymbol{\eta}) \; dv = - \int_{\varphi(\Omega)} \Big[\boldsymbol{\sigma} : \nabla_{\boldsymbol{x}}(\boldsymbol{\eta}) - \boldsymbol{b} \cdot \boldsymbol{\eta} \Big] \; dv + \int_{\varphi(\partial\Omega_t)} \boldsymbol{t} \cdot \boldsymbol{\eta} \; da = 0, \quad \forall \boldsymbol{\eta} \in \mathscr{V}, \quad (2.175)$$

where $\mathbf{a}$ is the tensor generally designated as *consistent spatial tangent modulus* and $\delta \boldsymbol{u}$ is the time and space continuum counterpart of the generic increment of the Newton-Rapshon method $\delta \mathbf{u}$. A time and finite element discretisation of (2.175) leads to:

$$\left\{ \int_{\varphi_{n+1}({}^{h}\Omega)} (\mathbf{G}^g)^T \mathbf{a} \, \mathbf{G}^g \; dv \right\} \delta \mathbf{u} \cdot \boldsymbol{\eta} = - \left\{ \int_{\varphi_{n+1}({}^{h}\Omega)} \Big[(\mathbf{B}^g)^T \hat{\boldsymbol{\sigma}}(\boldsymbol{\alpha}_n, \boldsymbol{F}_{n+1}) - (\mathbf{N}^g)^T \boldsymbol{b}_{n+1} \Big] \; dv - \int_{\varphi_{n+1}(\partial^h\Omega_t)} (\mathbf{N}^g)^T \boldsymbol{t}_{n+1} \; da \right\} \cdot \boldsymbol{\eta}, \quad \forall \boldsymbol{\eta} \in {}^{h}\mathscr{V}. \quad (2.176)$$

The above stated equation must be satisfied for all vectors $\boldsymbol{\eta}$. Thus, the spatial version of the discrete form of the linearised virtual work equation for large strain problems is obtained from (2.176) as:

$$\left\{ \int_{\varphi_{n+1}({}^{h}\Omega)} (\mathbf{G}^g)^T \mathbf{a} \, \mathbf{G}^g \; dv \right\} \delta \mathbf{u} = - \left\{ \int_{\varphi_{n+1}({}^{h}\Omega)} \Big[(\mathbf{B}^g)^T \hat{\boldsymbol{\sigma}}(\boldsymbol{\alpha}_n, \boldsymbol{F}_{n+1}) - (\mathbf{N}^g)^T \boldsymbol{b}_{n+1} \Big] \; dv - \int_{\varphi_{n+1}(\partial^h\Omega_t)} (\mathbf{N}^g)^T \boldsymbol{t}_{n+1} \; da \right\}. \quad (2.177)$$

The generic Netwon-Rapshon iteration (k) relies on solving the linear system of equations for $\delta \mathbf{u}^{(k)}$:

$$\mathbf{K}_T^{(k-1)} \delta \mathbf{u}^{(k)} = -\mathbf{r}^{(k-1)} \quad (2.178)$$

where $\mathbf{r}^{(k-1)}$ is the *residual force*, computed in terms of $\mathbf{u}_{n+1}^{(k-1)}$:

$$\mathbf{r}^{(k-1)} \equiv \mathbf{f}_{int}^{g}(\mathbf{u}_{n+1}^{(k-1)}) - \mathbf{f}_{ext,n+1}^{g}, \tag{2.179}$$

and $\mathbf{K}_T$ identifies the term in curly braces in the left-hand side of (2.177):

$$\mathbf{K}_T^{(k-1)} = \int_{\varphi_{n+1}^{k-1}({}^{h}\Omega)} (\mathbf{G}^g)^T \mathbf{a} \mathbf{G}^g \, dv, \tag{2.180}$$

which is called *global tangent stiffness matrix* and might also be expressed as:

$$\mathbf{K}_T^{(k-1)} = \left. \frac{\partial \mathbf{r}}{\partial \mathbf{u_{n+1}}} \right|_{\mathbf{u}_{n+1}^{(k-1)}}. \tag{2.181}$$

Within the FEM framework, this matrix results from the assemblage of its element counterparts, insomuch that:

$$\mathbf{K}_T = \mathop{\mathsf{A}}_{i=1}^{n_{elem}} \mathbf{K}_T^{(e)}, \tag{2.182}$$

where $\mathbf{K}_T^{(e)}$ is the *element tangent stiffness matrix*:

$$\mathbf{K}_T^{(e)} = \int_{\varphi_{n+1}^{(k-1)}({}^{h}\Omega)} (\mathbf{G}^g)^T \mathbf{a} \mathbf{G}^g \, dv. \tag{2.183}$$

After generating $\delta\mathbf{u}^{(k)}$ (or, in other words, solving the system (2.178)), we may update the global nodal displacement vector:

$$\mathbf{u}_{n+1}^{(k)} = \mathbf{u}_{n+1}^{(k-1)} + \delta\mathbf{u}^{(k)}. \tag{2.184}$$

An alternative procedure (which involves displacement increments) can be used to apply the Newton correction to the global displacement

$$\mathbf{u}_{n+1}^{(k)} = \mathbf{u}_n + \Delta\mathbf{u}^{(k)}, \tag{2.185}$$

being $\Delta\mathbf{u}^{(k)}$ the *incremental displacement vector*:

$$\Delta\mathbf{u}^{(k)} = \Delta\mathbf{u}^{(k-1)} + \delta\mathbf{u}^{(k)}. \tag{2.186}$$

The iterative process occurs until a *convergence criterion*, imposed a priori (by specifying an *equilibrium convergence tolerance* ϵ_{tol}), is satisfied. Let (m) denote the iteration in which the criterion has been achieved. In that case, we may write that:

$$\frac{\left\| \mathbf{r}^{(m)} \right\|}{\left\| \mathbf{f}_{ext,n+1}^{g} \right\|} \leq \epsilon_{tol}. \tag{2.187}$$

The tolerance ϵ_{tol} must be sufficiently small, so that the corresponding displacement vector, $\mathbf{u}_{n+1}^{(m)}$, is accepted as satisfactorily close to the solution of (2.132):

$$\mathbf{u}_{n+1} = \mathbf{u}_{n+1}^{(m)}. \tag{2.188}$$

The Newton-Rapshon iterative process demands an initial guess, $\mathbf{u}_{n+1}^{(0)}$. A

common option involves taking the converged displacement vector at the end of the previous increment as the initial guess:

$$\mathbf{u}_{n+1}^{(0)} = \mathbf{u}_n \tag{2.189}$$

In that case, we have:

$$\Delta\mathbf{u}_{n+1}^{(0)} = 0. \tag{2.190}$$

A review of the Newton-Rapshon method was made here in terms of spatial quantities. Note that a material approach could also have been followed. In that case, the counterpart of equation (2.177) comes as:

$$\left\{ \int_{h\Omega} (\mathbf{G}^g)^T \mathbf{A}\, \mathbf{G}^g \; dv \right\} \delta\mathbf{u} = -\left\{ \int_{h\Omega} \left[(\mathbf{G}^g)^T \hat{\mathbf{P}}(\boldsymbol{\alpha}_n, \boldsymbol{F}_{n+1}) - (\mathbf{N}^g)^T \boldsymbol{b}_{0,n+1} \right] dv - \int_{\partial^h\Omega_t} (\mathbf{N}^g)^T \boldsymbol{t}_{0,n+1} \; da \right\}. \tag{2.191}$$

Equation (2.178) remains valid, but its terms are naturally computed in a different way (respecting equation (2.191)). In particular, it is interesting to analyse the local and global stiffness matrices, since these equations introduce the consistent material tangent modulus, $\mathbf{A}$, which is the material counterpart of $\mathbf{a}$

$$\mathbf{K}_T^{(k-1)} = \int_{h\Omega} (\mathbf{G}^g)^T \mathbf{A}\, \mathbf{G}^g \; dv = \left. \frac{\partial \mathbf{r}}{\partial \mathbf{u_{n+1}}} \right|_{\mathbf{u}_{n+1}^{(k-1)}}, \tag{2.192}$$

$$\mathbf{K}_T^{(e)} = \int_{h\Omega^{(e)}} (\mathbf{G}^g)^T \mathbf{A}\, \mathbf{G}^g \; dv. \tag{2.193}$$

Nonetheless, equation (2.182) remains valid, as well equations equation (2.184) to equation (2.190).

Chapter 3

Multi-Scale Models based on Computational Homogenisation

As seen in Chapter 2, all CMT theory is based on assuming that bodies consist of continuous distributions of matter. Hence, this approach is valid at the micro-scale, provided that its length size is much larger than the underlying atomic structure. In that context, we must bear in mind that microstructures are often composed of different constituents (with distinct properties and shapes) and even cracks and voids. Conventional phenomenological constitutive models might be inadequate if we are dealing with phenomena where complex microscopic mechanisms dictate the macroscopic behaviour (these approaches rapidly lose their predictive capability as the complexity of the strain history increases). Over the last years, the increasing demand for more precise and accurate constitutive models (which comprise the effect of the micro-singularities) along with the development of new research areas (such as biomechanics and multi-physics) has lead to the development of several alternative approaches to the conventional constitutive theories. Perhaps, the simplest option to improve accuracy is to adopt more elaborated phenomenological models, using a large number of internal variables for modelling the relevant microscopic phenomena. A well-kwown downside of this type of models (besides the fact that they require a large number of parameters) lies on the difficulty of formulating evolution laws for all internal variables (de Souza Neto and Feijóo, 2006). Alternatively, the so-called *Multi-Scale Models* (MSM) might be employed. MSM have become the object of intense research within academic circles, since they provide more realistic descriptions of the materials behaviour and overcome the limitations of classical phenomenological constitutive models by comprising an analysis where (at least) two scales are involved: the macro- and the micro-scale. Particularly, *Multi-Scale Models based on Computational Homogenisation* (MSM-H) incorporate microscopic information (such as complex interactions between microstructural constituents which are important to explain the dissipative behaviour of materials) into the constitutive

macroscopic models by means of homogenisation procedures. In this Chapter, MSM-H are addressed. Note that the fundamentals of CMT (discussed in the preceding Chapter) will be used at both scales, since the micro-scale here considered is much larger than the atomic structure of the materials.

In order to establish the bridge between the two aforementioned scales, the concept of *Representative Volume Element* (RVE) assumes extreme relevance. In short, the RVE must contain enough information about the microctructure of the material, so that the effective macroscopic properties can be obtained as the volumetric averages of its microscopic counterparts over the RVE (within the MSM-H framework). Additional comments about RVEs are made in Section 3.1. Once this issue is discussed, we can deal with the kinematic variational formulation of large strain multi-scale solid constitutive models. That is the theme of Section 3.2, in which the foundations of this type of multi-scale models are reviewed. Finally, Section 3.3 presents the computational multi-scale program used to perform the numerical simulations described in subsequent Chapters.

Although the basic points related to MSM-H are addressed here, it is important to note that they are the summary of previous work in this area. Specifically, the work of de Souza Neto and Feijóo (2006) must be consulted for a more comprehensive account on the kinematical variational formulation of small and large strain first-order multi-scale solid constitutive models, whereas Reis (2014) and Lopes (2016) expound on the numerical implementation of MSM-H. Additionally, Watanabe and Terada (2010) separate coupled and decoupled micro-macro schemes and Gitman et al. (2007) compile possible definitions of an RVE.

3.1 Representative Volume Element

Representative Volume Elements are essential to the development of MSM-H, due to the fact that they allow continuum properties, related with the material particle $\boldsymbol{p}$, to be estimated in terms of the microstructure of the particle's neighbourhood. A possible definition for RVE is presented by Nemat-Nasser and Hori (1993): "an RVE for a material point of a continuum mass is a material volume which is statistically representative of the infinitesimal material neighbourhood of that material point." This definition can be perceived quickly from Figure 3.1: if $\boldsymbol{x}$ denotes the spatial position of a material particle at the macro-deformed configuration, the associated RVE must be large enough when compared to the microscopic heterogeneities, but much smaller than the macroscopic continuum (so that it can be statistically representative of the microstructure, but still be considered an infinitesimal neighbourhood of $\boldsymbol{x}$, at the macro-scale). This statement sums up the so-called *scale separation principle* (Hashin, 1983) which has the following mathematical format:

$$L_{micro} \ll L_{\mu} \ll L_{macro} \tag{3.1}$$

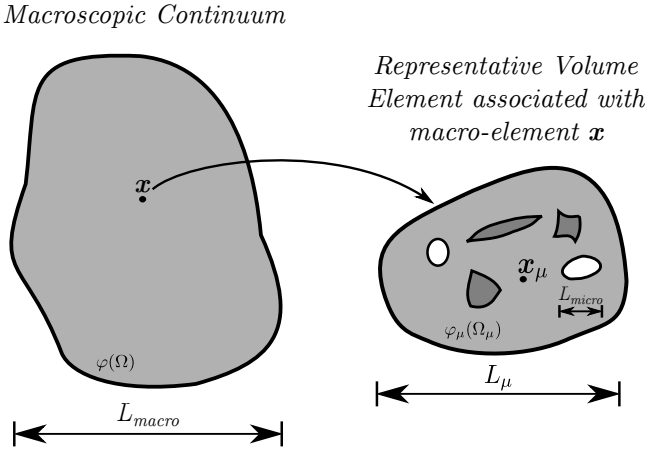

Figure 3.1: Macro-element $\boldsymbol{x}$ of a continuum body (size L_{macro}) with a locally attached microstructure (size of the RVE and size of microstuctural heterogeneities, respectively, given by L_μ and L_{micro}). Voids (white) and inclusions (dark grey) are represented in the RVE.

where L_{micro} is the typical dimension of the *micro-elements* (constituents of the RVE), L_μ the size of the RVE and L_{macro} the length of the (macroscopic) body. The RVE shall reflect a representation of the microstructure of the infinitesimal neighbourhood of $\boldsymbol{x}$ (*macro-element*) and, accordingly, it may include cracks, voids, inclusions, grain boundaries and other defects. It is noteworthy to highlight that this principle just specifies relative dimensions, so that the absolute dimensions of the microconstituents depend on the size of the continuum body and on the objectives of the analysis (and, as a result, they might be very small or very large). The size of an RVE is actually an issue of great concern and several studies have been made over the last years: that is the case of the works of Gitman et al. (2007) and Vieira de Carvalho (2016), just to cite a few examples. The idea that must be kept in mind is that, in order to save CPU time and memory, RVEs should be as small as possible, but still include a very large number of micro-elements. To clarify, we can say that large RVEs demand a lot of computational power to be analysed, especially in case *Coupled Multi-Scale Analysis* (CMSA) are being performed (in CMSA, an RVE is assigned to each integration point of the macroscopic finite element mesh, so that several micro-scale analyses need to be executed[1]). To sum up, although it is true that the RVE should be statistically representative of the local continuum properties, its size should enable an affordable analysis on a computational level[2].

All in all, the micro-heterogeneities and singularities that influence the behaviour

[1]CMSA are briefly addressed in Section 3.2.8. A more comprehensive account, however can be found in Reis (2014) or Watanabe and Terada (2010).

[2]This explains why, in Chapter 5, we have devoted special attention to the determination of the minimum size of the RVE for isotropic elastic polycrystals.

of a material at the macro-scale must be explicitly represented in the RVE. Therefore, the undeformed domain of the RVE, Ω_μ, might be split into a solid region, Ω_μ^s, the and a void part, Ω_μ^v:

$$\Omega_\mu = \Omega_\mu^s \cup \Omega_\mu^v. \tag{3.2}$$

Following the notation from Chapter 2, the boundary of the RVE is $\partial\Omega_\mu$. With the purpose of simplifying the presentation made in Section 3.2, we are going to assume that the void part (which may consist of cracks and pores subjected to self-contact or filled with a pressurized fluid) does not intersect the RVE boundary, that is:

$$\partial\Omega_\mu \cap \bar{\Omega}_\mu^v = \emptyset \tag{3.3}$$

where $\bar{\Omega}_\mu^v$ is the closure set of the void region. Note that in Figure 3.1 the preceding condition is satisfied.

It should be made clear that the definition proposed by Nemat-Nasser and Hori (1993) is not unique. In fact, several authors have come up with different definitions for RVE since Hill (1963) first addressed this issue (Gitman et al. (2007) collects some of the most relevant ones). All definitions require the scale separation principle to be satisfied, so that the homogenisation procedures of the strain and stress fields (detailed in Section 3.2) can be used. The scale separation principle, along with the homogenisation procedures and the Hill-Mandel principle of macro-homogeneity (Hill, 1965; Mandel, 1971) (addressed in ensuing Sections), are the fundamental features of the *scale transition theory* (that form the basis for the development of MSM). In fact, it was assumed that different scales could be identified and distinguished in the solids under analysis. This is not always true (see, for instance, Gitman et al. (2007)), so care must be taken when employing such formulations.

In view of separating CMT concepts related with the macro-scale from its corresponding microscopic quantities, it has been decided to use the $\boldsymbol{x}$ and $\boldsymbol{x}_\mu$ to identify the spatial position of an infinitesimal point in the deformed configuration at the macro-scale and at the micro-scale, respectively. Analogously, $\boldsymbol{p}$ and $\boldsymbol{p}_\mu$ represent their reference configuration counterparts. Indeed, we must remark that microscopic counterparts of entities introduced in Chapter 2 were, in general, labelled with the subscript μ, avoiding the addition of unnecessary variables that would make the text more dense.

3.2 Formulation of Large Strain Multi-Scale Constitutive Models

In this Section, a kinematical variational formulation of large strain first-order multi-scale solid constitutive models based on the volume average of the strain and the stress tensors over the RVE is introduced. At the outset (Section 3.2.1), the homogenisation of the deformation gradient is covered. Then, the additive

split of the microscopic displacement and the admissible microscopic displacement field are shown in Section 3.2.2. The aforementioned topics, along with the RVE equilibrium equations (reviewed in Section 3.2.3) and the Hill-Mandel principle (Section 3.2.4) play an important role defining the microscopic equilibrium problem, which is summarised in Section 3.2.5 (for the establishment of referred problem, it is also necessary to consider the constitutive equation (2.85)). It is essential to realize that the microscopic first Piola-Kirchhoff stress tensor can be obtained after the microscopic equilibrium problem (formulated in terms of referential entities) is solved (and, therefore, by means of the homogenisation, its macroscopic counterpart can be obtained – see Section 3.2.6). It happens that the kinematically admissible displacement fluctuation field over the RVE must be established before the microscopic equilibrium problem is solved: different classes of MSM are described in Section 3.2.7. In Section 3.2.8, coupled and decoupled multi-scale schemes are distinguished.

3.2.1 Homogenised Deformation Gradient

A key point of MSM-H involves adopting homogenisation procedures, so that the transition of scales might be enforced. Putting it differently, macroscopic quantities can be computed as the volume averages of their microscopic counterparts within the MSM-H framework. Accordingly, the *homogenised* or *macroscopic deformation gradient*, $\boldsymbol{F}$, at a point $\boldsymbol{x}$ of the macro-continuum, might be obtained as the *volume average* of its microscopic counterpart, $\boldsymbol{F}_\mu$, over the undeformed configuration of the RVE associated with the point $\boldsymbol{x}$:

$$\boldsymbol{F}(\boldsymbol{x},t) = \frac{1}{v_{0,\mu}} \int_{\Omega_\mu} \boldsymbol{F}_\mu(\boldsymbol{x}_\mu,t)\ dv, \tag{3.4}$$

where Ω_μ identifies the reference configuration of the RVE and $v_{0,\mu}$ defines the microscopic volume associated with that configuration. Recalling that the microscopic deformation gradient is given by equation (2.16), we can rewrite the last expression in terms of the material gradient[3] of the microscopic displacement field $\boldsymbol{u}_\mu$:

$$\boldsymbol{F}(\boldsymbol{x},t) = \boldsymbol{I} + \frac{1}{v_{0,\mu}} \int_{\Omega_\mu} \nabla_{\boldsymbol{p}}[\boldsymbol{u}_\mu(\boldsymbol{x}_\mu,t)]\ dv. \tag{3.5}$$

Invoking Gauss's theorem, we obtain:

$$\boldsymbol{F}(\boldsymbol{x},t) = \boldsymbol{I} + \frac{1}{v_{0,\mu}} \int_{\partial\Omega_\mu} \boldsymbol{u}_\mu(\boldsymbol{x}_\mu,t) \otimes \boldsymbol{n}_{0,\mu}(\boldsymbol{p}_\mu)\ da, \tag{3.6}$$

in such a manner that the macroscopic deformation gradient is calculated as the integral over the boundary $\partial\Omega_\mu$ of the tensorial product between the microscopic displacement field $\boldsymbol{u}_\mu$ and the outward unit normal vector to the above-mentioned boundary $\boldsymbol{n}_{0,\mu}(\boldsymbol{p}_\mu)$.

[3]The material gradient operator is denoted $\nabla_{\boldsymbol{p}}$. Nonetheless, observe that we could also use $\nabla_{\boldsymbol{p}_\mu}$ to identify this tensor.

3.2.2 RVE Kinematics

Within the large strain framework, the macroscopic deformation gradient is generally computed in the macro-element (macroscopic point) associated with the RVE of interest. As a consequence, equations (3.5) and (3.6) place constraints on the possible microscopic displacement fields. In fact, a field $\boldsymbol{u}_\mu$ is *kinematically admissible* in case the following necessary condition is verified:

$$\boldsymbol{u}_\mu \in \mathscr{K}_\mu^*, \tag{3.7}$$

being $\mathscr{K}_\mu^*$ the *minimally constrained set of kinematically admissible microscopic displacements*, which is:

$$\mathscr{K}_\mu^* \equiv \Bigg\{ \boldsymbol{u}_\mu, \text{ sufficiently regular } | \int_{\Omega_\mu} \nabla_{\boldsymbol{p}}[\boldsymbol{u}_\mu(\boldsymbol{x}_\mu, t)]\, dv = v_{0,\mu}\,[\boldsymbol{F}(\boldsymbol{x}, t) - \boldsymbol{I}] \Bigg\}. \tag{3.8}$$

Or, equivalently,

$$\mathscr{K}_\mu^* \equiv \Bigg\{ \boldsymbol{u}_\mu, \text{ sufficiently regular } | \int_{\partial\Omega_\mu} \boldsymbol{u}_\mu(\boldsymbol{x}_\mu, t) \otimes \boldsymbol{n}_{0,\mu}(\boldsymbol{p}_\mu)\, da = v_{0,\mu}\,[\boldsymbol{F}(\boldsymbol{x}, t) - \boldsymbol{I}] \Bigg\}. \tag{3.9}$$

It is important to realize that definition (3.9) for $\mathscr{K}_\mu^*$ incorporates boundary displacements. Besides, by *sufficiently regular*, it is meant that all operations in which the displacement field vector $\boldsymbol{u}_\mu$ is involved make sense (de Souza Neto and Feijóo, 2006).

Without loss of generality, the microscopic kinematically admissible displacement field $\boldsymbol{u}_\mu$ may be decomposed as follows:

$$\boldsymbol{u}_\mu(\boldsymbol{x}_\mu, t) = [\boldsymbol{F}(\boldsymbol{x}, t) - \boldsymbol{I}]\, \boldsymbol{p}_\mu + \tilde{\boldsymbol{u}}_\mu(\boldsymbol{x}_\mu, t), \tag{3.10}$$

where the left and right terms of the right-hand side are, respectively, the *linear displacement*, which varies linearly with $\boldsymbol{p}_\mu$, and the *displacement fluctuation* $\tilde{\boldsymbol{u}}_\mu$. Since the prescribed macroscopic deformation gradient is assumed constant throughout the RVE (first-order MSM are being considered), the linear displacement is known, making $\tilde{\boldsymbol{u}}_\mu$ as the actual unknown variable of the microscopic equilibrium problem.

By substituting (3.10) into the general CMT expression (2.16), we may express the microscopic deformation gradient $\boldsymbol{F}_\mu$ in terms of the displacement fluctuation field $\tilde{\boldsymbol{u}}_\mu$:

$$\boldsymbol{F}_\mu(\boldsymbol{x}_\mu, t) = \boldsymbol{F}(\boldsymbol{x}, t) + \nabla_{\boldsymbol{p}}(\tilde{\boldsymbol{u}}_\mu[\boldsymbol{x}_\mu, t)]. \tag{3.11}$$

In this case, the microscopic deformation gradient $\boldsymbol{F}_\mu(\boldsymbol{x}_\mu, t)$ is obtained as the sum

of the *homogeneous straining component* $\boldsymbol{F}(\boldsymbol{x},t)$ and the *strain fluctuation field* $\nabla_{\boldsymbol{p}}[\tilde{\boldsymbol{u}}_\mu(\boldsymbol{x}_\mu,t)]$ (which normally varies in $\boldsymbol{x}_\mu$). This decomposition, coupled with equation (3.4), leads to:

$$\boldsymbol{F}(\boldsymbol{x},t) = \boldsymbol{F}(\boldsymbol{x},t) + \frac{1}{v_{0,\mu}} \int_{\Omega_\mu} \nabla_{\boldsymbol{p}}[\tilde{\boldsymbol{u}}_\mu(\boldsymbol{x}_\mu,t)]\ dv, \tag{3.12}$$

that is,

$$\int_{\Omega_\mu} \nabla_{\boldsymbol{p}}[\tilde{\boldsymbol{u}}_\mu(\boldsymbol{x}_\mu,t)]\ dv = 0. \tag{3.13}$$

Again, using the Gauss theorem, we obtain:

$$\int_{\partial\Omega_\mu} \tilde{\boldsymbol{u}}_\mu(\boldsymbol{x}_\mu,t) \otimes \boldsymbol{n}_{0,\mu}(\boldsymbol{p}_\mu)\ da = 0. \tag{3.14}$$

The previous condition allows determining the *minimally constrained space of displacement fluctuations*:

$$\tilde{\mathscr{K}}_\mu^* \equiv \left\{ \tilde{\boldsymbol{u}}_\mu,\ \text{sufficiently regular} \mid \int_{\partial\Omega_\mu} \tilde{\boldsymbol{u}}_\mu(\boldsymbol{x}_\mu,t) \otimes \boldsymbol{n}_{0,\mu}(\boldsymbol{p}_\mu)\ da = 0 \right\}. \tag{3.15}$$

Further constraints are generally placed, so that, the *actual kinematically admissible displacement fluctuation field* must satisfy:

$$\tilde{\boldsymbol{u}}_\mu \in \tilde{\mathscr{K}}_\mu \subset \tilde{\mathscr{K}}_\mu^* \tag{3.16}$$

where $\tilde{\mathscr{K}}_\mu$ is the *actual set of kinematically admissible fluctuation fields*. Equivalently, the *actual set of kinematically admissible displacement fields* is $\mathscr{K}_\mu$, which might be regarded as a translation of space $\tilde{\mathscr{K}}_\mu$:

$$\mathscr{K}_\mu = \left\{ \boldsymbol{u}_\mu(\boldsymbol{x}_\mu,t) = [\boldsymbol{F}(\boldsymbol{x},t) - \boldsymbol{I}]\,\boldsymbol{p}_\mu + \tilde{\boldsymbol{u}}_\mu(\boldsymbol{x}_\mu,t) \mid \tilde{\boldsymbol{u}}_\mu(\boldsymbol{x}_\mu,t) \in \tilde{\mathscr{K}}_\mu \right\}. \tag{3.17}$$

For the variational characterisation of the equilibrium of the RVE, both sets $\tilde{\mathscr{K}}_\mu$ and $\mathscr{K}_\mu$ are crucial. Besides them, the *space of virtual kinematically admissible displacements of the RVE* is also necessary. This set reads:

$$\mathscr{V}_\mu \equiv \left\{ \boldsymbol{\eta}_\mu = \boldsymbol{v}_\mu^1 - \boldsymbol{v}_\mu^2 \mid \boldsymbol{v}_\mu^1, \boldsymbol{v}_\mu^2 \in \mathscr{K}_\mu \right\}, \tag{3.18}$$

where, in coherence with the notation introduced, $\boldsymbol{\eta}_\mu$ represents the vector of microscopic virtual kinematically admissible displacements. From definition (3.17) and from the fact that $\tilde{\mathscr{K}}_\mu$ is itself a vector space, we may conclude that:

$$\mathscr{V}_\mu \equiv \tilde{\mathscr{K}}_\mu, \tag{3.19}$$

i.e. the space of virtual displacements coincides with the actual space of kinematically admissible fluctuations.

The derivative with respect to time of (3.10) leads to:

$$\dot{\boldsymbol{u}}_\mu(\boldsymbol{x}_\mu, t) = \dot{\boldsymbol{F}}(\boldsymbol{x}, t)\,\boldsymbol{p}_\mu + \dot{\tilde{\boldsymbol{u}}}_\mu(\boldsymbol{x}_\mu, t). \tag{3.20}$$

Using the same arguments that lead to (3.19), we have:

$$\dot{\tilde{\boldsymbol{u}}}_\mu \in \mathscr{V}_\mu. \tag{3.21}$$

3.2.3 Equilibrium of the RVE

In the present context, we are assuming that the concepts of CMT presented in Chapter 2 are valid at the micro-scale. Therefore, the fundamental laws of thermodynamics are valid, so that the material version of the strong form of equilibrium at the micro-scale derives from (2.76) (inertial effects are neglected):

$$\begin{cases} \mathrm{div}_{\boldsymbol{p}}[\boldsymbol{P}_\mu(\boldsymbol{x}_\mu, t)] + \boldsymbol{b}_{0,\mu}(\boldsymbol{x}_\mu, t) = 0 & ,\ \forall \boldsymbol{x}_\mu \in \Omega^s_\mu, \\ \mathrm{div}_{\boldsymbol{p}}[\boldsymbol{P}_\mu(\boldsymbol{x}_\mu, t)] + \boldsymbol{b}_{0,\mu}(\boldsymbol{x}_\mu, t) = 0 & ,\ \forall \boldsymbol{x}_\mu \in \Omega^v_\mu, \\ \boldsymbol{P}_\mu(\boldsymbol{x}_\mu, t)\,\boldsymbol{n}_{0,\mu}(\boldsymbol{p}_\mu) = \boldsymbol{t}_{0,\mu}(\boldsymbol{x}_\mu, t) & ,\ \forall \boldsymbol{x}_\mu \in \partial\Omega_u, \\ \left\| \boldsymbol{P}_\mu(\boldsymbol{x}_\mu, t)\,\boldsymbol{n}_{0,\mu}(\boldsymbol{p}_\mu) \right\| = 0 & ,\ \forall \boldsymbol{x}_\mu \in \partial\Omega^v_u, \end{cases} \tag{3.22}$$

where $\boldsymbol{P}_\mu$ is the microscopic first Piola-Kirchhoff stress tensor, $\boldsymbol{b}_{0,\mu}$ is the body force per unit microscopic reference volume and $\boldsymbol{t}_{0,\mu}$ is the external surface traction measured per unit microscopic reference boundary area. In addition, the jump $\left\| \boldsymbol{P}_\mu(\boldsymbol{x}_\mu, t)\,\boldsymbol{n}_{0,\mu}(\boldsymbol{p}_\mu) \right\|$ of vector field $\boldsymbol{P}_\mu(\boldsymbol{x}_\mu, t)\,\boldsymbol{n}_{0,\mu}(\boldsymbol{p}_\mu)$ across the solid-void interface $\partial\Omega^v_u$ must be null in order to guarantee the continuity of the aforementioned vector field.

By the same token, the virtual work principle might be used to determine the weak equilibrium equations. Its material version results from (2.119) (again, the inertially-related therms are removed):

$$\int_{\Omega_\mu} \boldsymbol{P}_\mu(\boldsymbol{x}_\mu, t) : \nabla_{\boldsymbol{p}}(\boldsymbol{\eta}_\mu)\; dv - \int_{\Omega_\mu} \boldsymbol{b}_{0,\mu}(\boldsymbol{x}_\mu, t) \cdot \boldsymbol{\eta}_\mu\; dv - \int_{\partial\Omega_\mu} \boldsymbol{t}_{0,\mu} \cdot \boldsymbol{\eta}_\mu\; da = 0, \quad \forall \boldsymbol{\eta}_\mu \in \mathscr{V}_u. \tag{3.23}$$

The voids may influence the mechanical state of the RVE, since that they are not necessarily empty. If we separate the solid and void parts in equation (3.23), we may write that:

$$\begin{aligned} &\int_{\Omega^s_\mu} \boldsymbol{P}_\mu(\boldsymbol{x}_\mu, t) : \nabla_{\boldsymbol{p}}(\boldsymbol{\eta}_\mu)\; dv - \int_{\Omega^s_\mu} \boldsymbol{b}_{0,\mu}(\boldsymbol{x}_\mu, t) \cdot \boldsymbol{\eta}_\mu\; dv - \int_{\partial\Omega_\mu} \boldsymbol{t}_{0,\mu} \cdot \boldsymbol{\eta}_\mu\; da \\ &\quad + \int_{\Omega^v_\mu} \boldsymbol{P}_\mu(\boldsymbol{x}_\mu, t) : \nabla_{\boldsymbol{p}}(\boldsymbol{\eta}_\mu)\; dv - \int_{\Omega^v_\mu} \boldsymbol{b}_{0,\mu}(\boldsymbol{x}_\mu, t) \cdot \boldsymbol{\eta}_\mu\; dv = 0, \quad \forall \boldsymbol{\eta}_\mu \in \mathscr{V}_u. \end{aligned} \tag{3.24}$$

Let $\boldsymbol{t}^v_{0,\mu}$ denote the internal traction exerted upon the solid domain Ω^s_μ across the solid-void interface, $\partial\Omega^v_\mu$. Because the voids are in equilibrium, the following identity

is verified:

$$\int_{\Omega_\mu^v} \boldsymbol{P}_\mu(\boldsymbol{x}_\mu,t):\nabla_{\boldsymbol{p}}(\boldsymbol{\eta}_\mu)\ dv - \int_{\Omega_\mu^v} \boldsymbol{b}_{0,\mu}(\boldsymbol{x}_\mu,t)\cdot\boldsymbol{\eta}_\mu\ dv + \int_{\partial\Omega_\mu^v} \boldsymbol{t}^v_{0,\mu}(\boldsymbol{x}_\mu,t)\cdot\boldsymbol{\eta}_\mu\ da = 0,\quad \forall\boldsymbol{\eta}_\mu\in\mathscr{V}_u. \quad (3.25)$$

Altogether, the weak equilibrium statement (3.23) is equivalent to:

$$\int_{\Omega_\mu^s} \boldsymbol{P}_\mu(\boldsymbol{x}_\mu,t):\nabla_{\boldsymbol{p}}(\boldsymbol{\eta}_\mu)\ dv - \int_{\Omega_\mu^s} \boldsymbol{b}_{0,\mu}(\boldsymbol{x}_\mu,t)\cdot\boldsymbol{\eta}_\mu\ dv - \int_{\partial\Omega_\mu} \boldsymbol{t}_{0,\mu}(\boldsymbol{x}_\mu,t)\cdot\boldsymbol{\eta}_\mu\ da - \int_{\partial\Omega_\mu^v} \boldsymbol{t}^v_{0,\mu}(\boldsymbol{x}_\mu,t)\cdot\boldsymbol{\eta}_\mu\ da = 0,\quad \forall\boldsymbol{\eta}_\mu\in\mathscr{V}_u. \quad (3.26)$$

Note that the internal tractions $\boldsymbol{t}^v_{0,\mu}$ vanish, in case of empty pores. On the contrary, in case the voids are filled with a pressurized fluid, these tractions are not negligible.

3.2.4 Hill-Mandel Principle of Macro-Homogeneity

The Hill-Mandel principle of macro-homogeneity (Hill, 1965; Mandel, 1971) is one of the key points of MSM-H. This principle establishes the link between the macroscopic stress power and its corresponding microscopic quantity (essentially, a bridge between scales is created). In detail, it postulates that the macroscopic stress power is equivalent to the volume average of the microscopic stress power over the RVE:

$$\boldsymbol{P}(\boldsymbol{x},t):\dot{\boldsymbol{F}}(\boldsymbol{x},t) = \frac{1}{v_{0,\mu}}\int_{\Omega_\mu} \boldsymbol{P}_\mu(\boldsymbol{x}_\mu,t):\dot{\boldsymbol{F}}_\mu(\boldsymbol{x}_\mu,t)\ dv, \quad (3.27)$$

where $\dot{\boldsymbol{F}}_\mu$ is the microscopic deformation gradient rate and $\dot{\boldsymbol{F}}$ is its macroscopic counterpart. The derivative of expression (3.11) with respect to time allows the time derivative of the microscopic deformation gradient, $\dot{\boldsymbol{F}}_\mu(\boldsymbol{x}_\mu,t)$ to be determined in terms of its corresponding macroscopic quantity, $\dot{\boldsymbol{F}}(\boldsymbol{x},t)$:

$$\dot{\boldsymbol{F}}_\mu(\boldsymbol{x}_\mu,t) = \dot{\boldsymbol{F}}(\boldsymbol{x},t) + \nabla_{\boldsymbol{p}}[\dot{\tilde{\boldsymbol{u}}}_\mu(\boldsymbol{x}_\mu,t)]. \quad (3.28)$$

The substitution of (3.28) into (3.27) gives:

$$\boldsymbol{P}(\boldsymbol{x},t):\dot{\boldsymbol{F}}(\boldsymbol{x},t) = \boldsymbol{P}(\boldsymbol{x},t):\dot{\boldsymbol{F}}(\boldsymbol{x},t) + \frac{1}{v_{0,\mu}}\int_{\Omega_\mu} \boldsymbol{P}_\mu(\boldsymbol{x}_\mu,t):\nabla_{\boldsymbol{p}}[\dot{\tilde{\boldsymbol{u}}}_\mu(\boldsymbol{x}_\mu,t)]\ dv, \quad (3.29)$$

and, consequently:

$$\int_{\Omega_\mu} \boldsymbol{P}_\mu(\boldsymbol{x}_\mu,t):\nabla_{\boldsymbol{p}}[\dot{\tilde{\boldsymbol{u}}}_\mu(\boldsymbol{x}_\mu,t)]\ dv = 0,\quad \forall\dot{\tilde{\boldsymbol{u}}}_\mu\in\mathscr{V}_\mu. \quad (3.30)$$

Considering:

- An integration by parts of the left-hand side of (3.30);
- The strong form of equilibrium, (3.22); and

- The absence of body forces acting on the void part (a correct assumption if the voids contain a fluid phase):

$$\boldsymbol{b}_{0,\mu}(\boldsymbol{x}_\mu, t) = 0, \quad \forall \boldsymbol{x}_\mu \in \Omega_\mu^v, \tag{3.31}$$

it follows that the Hill-Mandel principle is reduced to:

$$\int_{\Omega_\mu^s} \boldsymbol{b}_{0,\mu}(\boldsymbol{x}_\mu, t) \cdot \dot{\tilde{\boldsymbol{u}}}_\mu \, dv - \int_{\partial\Omega_\mu} \boldsymbol{t}_{0,\mu}(\boldsymbol{x}_\mu, t) \cdot \dot{\tilde{\boldsymbol{u}}}_\mu \, da = 0, \quad \forall \dot{\tilde{\boldsymbol{u}}}_\mu \in \mathscr{V}_u. \tag{3.32}$$

Because $\mathscr{V}_u$ is a vector space, the Hill-Mandel principle holds if and only if each integral in (3.32) vanishes:

$$\int_{\Omega_\mu^s} \boldsymbol{b}_{0,\mu}(\boldsymbol{x}_\mu, t) \cdot \dot{\tilde{\boldsymbol{u}}}_\mu \, dv = 0 \quad \forall \dot{\tilde{\boldsymbol{u}}}_\mu \in \mathscr{V}_u, \tag{3.33}$$

$$\int_{\partial\Omega_\mu} \boldsymbol{t}_{0,\mu}(\boldsymbol{x}_\mu, t) \cdot \dot{\tilde{\boldsymbol{u}}}_\mu \, da = 0 \quad \forall \dot{\tilde{\boldsymbol{u}}}_\mu \in \mathscr{V}_u. \tag{3.34}$$

From (3.21), we can conclude that the afore stated principle demands that the virtual work of the external surface traction and body force field of the RVE vanish:

$$\int_{\Omega_\mu^s} \boldsymbol{b}_{0,\mu}(\boldsymbol{x}_\mu, t) \cdot \boldsymbol{\eta}_\mu \, dv = 0, \quad \forall \boldsymbol{\eta}_\mu \in \mathscr{V}_u, \tag{3.35}$$

$$\int_{\partial\Omega_\mu} \boldsymbol{t}_{0,\mu}(\boldsymbol{x}_\mu, t) \cdot \boldsymbol{\eta}_\mu \, da = 0, \quad \forall \boldsymbol{\eta}_\mu \in \mathscr{V}_u. \tag{3.36}$$

Considering the consequences (3.35) and (3.36) of the Hill-Mandel principle, $\boldsymbol{b}_{0,\mu}$ and $\boldsymbol{t}_{0,\mu}$ might be interpreted as mere reactions to the kinematical constraints imposed upon the RVE. To understand the previous statement, note that both $\boldsymbol{b}_{0,\mu}$ and $\boldsymbol{t}_{0,\mu}$ belong to a functional space orthogonal to $\mathscr{V}_u$; in that case and since $\mathscr{V}_u$ is determined when the kinematic constraints are specified, the referred vectors are said to be *purely reactive* (they cannot be prescribed independently and are defined by the multi-scale model adopted – see Section 3.2.7 for more on this topic).

In view of what was discussed throughout this Section, the material version of the weak equilibrium form (3.26) reads:

$$\int_{\Omega_\mu^s} \boldsymbol{P}_\mu(\boldsymbol{x}_\mu, t) : \nabla_{\boldsymbol{p}}(\boldsymbol{\eta}_\mu) \, dv - \int_{\partial\Omega_\mu^v} \boldsymbol{t}_{0,\mu}^v(\boldsymbol{x}_\mu, t) \cdot \boldsymbol{\eta}_\mu \, da = 0, \quad \forall \boldsymbol{\eta}_\mu \in \mathscr{V}_u. \tag{3.37}$$

3.2.5 Micro-scale Equilibrium Problem

Until this point, the response of the material at the micro-scale was left open. However, since CMT concepts are applicable, the general constitutive theory might be employed to describe the material's behaviour at the micro-scale. If we ignore thermal effects and consider a purely mechanical problem, the microscopic material version of the stress constitutive equation (2.85) can be represented as:

$$\boldsymbol{P}_\mu(\boldsymbol{x}_\mu, t) = \mathfrak{P}_\mu(\boldsymbol{F}_\mu^t(\boldsymbol{x}_\mu)), \quad \forall \boldsymbol{x}_\mu \in \Omega_\mu^s. \tag{3.38}$$

where $\mathfrak{P}_\mu$ is the stress constitutive functional depending upon the local history of the microscopic deformation gradient $\boldsymbol{F}_\mu^t$. Provided that the microscopic deformation gradient might be obtained from (3.11), equation (3.38) may be rewritten as:

$$\boldsymbol{P}_\mu(\boldsymbol{x}_\mu, t) = \mathfrak{P}_\mu\big(\big\{\boldsymbol{F}(\boldsymbol{x}, t) + \nabla_{\boldsymbol{p}}[\tilde{\boldsymbol{u}}_\mu(\boldsymbol{x}_\mu, t)]\big\}^t\big), \quad \forall \boldsymbol{x}_\mu \in \Omega_\mu^s, \tag{3.39}$$

with the superscript t denoting, again, the history. Equation (3.39) explicitly shows the dependence of the stress constitutive function upon the unknown variable of the problem $\tilde{\boldsymbol{u}}_\mu$. This unknown variable is, after all, the solution of the *microscopic equilibrium problem*. The material version of the aforementioned problem can be written as follows: "Given that the history of the macroscopic deformation gradient at the point of interest $\boldsymbol{x}$ of the macro-continuum is known, find the displacement fluctuation field $\tilde{\boldsymbol{u}}_\mu \in \mathscr{V}_\mu \subset \tilde{\mathscr{K}}_\mu^*$ that satisfies the weak equilibrium statement (3.37)."

Neglecting the internal tractions exerted across the solid-void interface and taking (3.39) into account, it is possible to formulate a simplified version of the microscopic equilibrium problem (particularly relevant in the context of this dissertation): "Given that the history of the macroscopic deformation gradient at the point of interest $\boldsymbol{x}$ of the macro-continuum is known, find the displacement fluctuation field $\tilde{\boldsymbol{u}}_\mu \in \mathscr{V}_\mu \subset \tilde{\mathscr{K}}_\mu^*$, such that the following variational identity is verified:

$$\int_{\Omega_\mu^s} \mathfrak{P}_\mu\big(\big\{\boldsymbol{F}(\boldsymbol{x}, t) + \nabla_{\boldsymbol{p}}[\tilde{\boldsymbol{u}}_\mu(\boldsymbol{x}_\mu, t)]\big\}^t\big) : \nabla_{\boldsymbol{p}}(\boldsymbol{\eta}_\mu)\, dv = 0, \quad \forall \boldsymbol{\eta}_\mu \in \mathscr{V}_u." \tag{3.40}$$

It is assumed that the constitutive response of the material (expressed in terms of the stress constitutive functional $\mathfrak{P}_\mu$) is known. However, it is important to remark that the space vector $\mathscr{V}_u$ must be specified in order to make the microscopic equilibrium problem well-posed. In other words, the kinematical constraints prescribed on the RVE must be determined in view of solving the microscopic equilibrium problem. These kinematical constraints define a space $\mathscr{V}_u$, which is, in fact, a subset of the minimally constrained set of kinematically admissible displacement fluctuations $\mathscr{V}_u^*$ that ensures relation (3.4). Different kinematically admissible displacement fluctuation fields are discussed in Section 3.2.7.

3.2.6 Homogenised Stress Tensor

Once the equilibrium problem is solved (and, as a result, $\tilde{\boldsymbol{u}}_\mu$ is known), the microscopic stress tensor may be determined using equation (3.39). As we are following a material approach, the microscopic first Piola-Kirchhoff stress tensor is generated. Following a procedure analogous to the one described in Section 3.2.1, the *homogenised* or *macroscopic first Piola-Kirchhoff stress tensor* consists of the volume average of its microscopic counterpart over the RVE (associated with the point $\boldsymbol{x}$ of the macro-continuum):

$$\boldsymbol{P}(\boldsymbol{x}, t) = \frac{1}{v_{0,\mu}} \int_{\Omega_u} \boldsymbol{P}_\mu(\boldsymbol{x}_\mu, t)\, dv. \tag{3.41}$$

The microscopic stress tensor is obtained from the constitutive stress equation, in such a manner that we may write:

$$\boldsymbol{P}(\boldsymbol{x},t) = \mathfrak{P}_\mu\big(\big\{\boldsymbol{F}(\boldsymbol{x},t) + \nabla_{\boldsymbol{p}}[\tilde{\boldsymbol{u}}_\mu(\boldsymbol{x}_\mu,t)]\big\}^t\big)\ dv. \tag{3.42}$$

Moreover, it can be proven (see, for instance, de Souza Neto and Feijóo (2006)) that the following relation might also be used with the purpose of expressing $\boldsymbol{P}$ in terms of microscopic quantities:

$$\boldsymbol{P}(\boldsymbol{x},t) = \frac{1}{v_{0,\mu}}\left(\int_{\partial\Omega_u} \boldsymbol{t}_{0,\mu}\otimes\boldsymbol{p}_\mu\ da - \int_{\Omega_u}\boldsymbol{b}_{0,\mu}\otimes\boldsymbol{p}_\mu\ dv\right). \tag{3.43}$$

As can be perceived from Figure 3.2, the connection between the micro- and the macro-scale is established by the homogenized first Piola-Kirchhoff stress tensor, calculated from equation (3.41). Once this entity is computed, the consistent material tangent modulus $\mathbf{A}$ can also be computed:

$$\mathbf{A} = \frac{\partial \boldsymbol{P}}{\partial \boldsymbol{F}}. \tag{3.44}$$

The relation between the first Piola-Kirchhoff stress tensor and the Cauchy stress tensor was stated before in equation (2.61). The *material volume average* of the first Piola-Kirchhoff stress tensor (and of the deformation gradient) gives:

$$\boldsymbol{\sigma}(\boldsymbol{x},t) = \frac{1}{J_\mu}\left(\frac{1}{v_{0,\mu}}\int_{\Omega_\mu}\boldsymbol{P}_\mu(\boldsymbol{x}_\mu,t)\ dv\right)\left(\frac{1}{v_{0,\mu}}\int_{\Omega_\mu}\boldsymbol{F}_\mu(\boldsymbol{x}_\mu,t)\ dv\right). \tag{3.45}$$

Alternatively, the macroscopic Cauchy stress tensor might be obtained as the *spatial volume average* of its microscopic counterpart:

$$\boldsymbol{\sigma}(\boldsymbol{x},t) = \frac{1}{v_\mu}\int_{\varphi_\mu(\Omega_\mu)}\boldsymbol{\sigma}_\mu(\boldsymbol{x}_\mu,t)\ dv, \tag{3.46}$$

being $\boldsymbol{\sigma}_\mu$ the microscopic Cauchy stress tensor, v_μ the deformed volume of the RVE and $\varphi_\mu(\Omega_\mu)$ the corresponding (deformed) configuration. It must be remembered that (2.61) is non-linear, so that the macroscopic Cauchy stress tensor computed from (3.45) might not be *mechanically equivalent* to the one resulting from the spatial volume average equation (3.46). To summarize, it is vital to understand that, in general[4] (Nemat-Nasser, 1999):

$$\boldsymbol{\sigma} = \frac{1}{v_\mu}\int_{\varphi_\mu(\Omega_\mu)}\boldsymbol{\sigma}_\mu(\boldsymbol{x}_\mu,t)\ dv \neq \frac{1}{J}\boldsymbol{P}\boldsymbol{F}^T = \frac{1}{J_\mu}\left(\frac{1}{v_{0,\mu}}\int_{\Omega_\mu}\boldsymbol{P}_\mu\ dv\right)\left(\frac{1}{v_{0,\mu}}\int_{\Omega_\mu}\boldsymbol{F}_\mu\ dv\right). \tag{3.47}$$

[4]Nonetheless, there are some situations in which the material and spatial averaging procedures lead to mechanically equivalent stress tensors. The equivalence between spatial and material volume averaging of stress in large strain multi-scale constitutive models is the subject of analysis of de Souza Neto and Feijóo (2008).

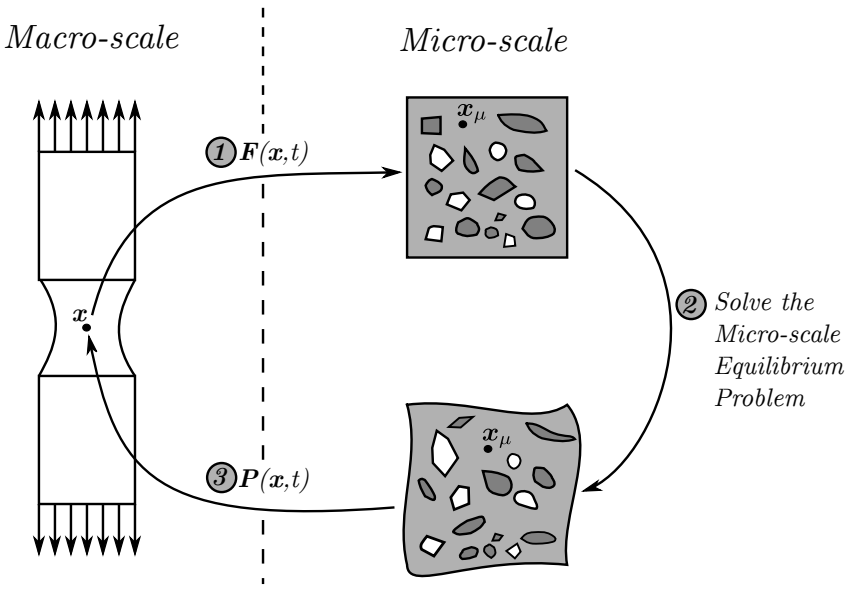

Figure 3.2: Representation of a multi-scale model.

3.2.7 Classes of Multi-Scale Models

For the microscopic equilibrium problem to be well-posed, it is necessary to specify the kinematical constraints imposed on the RVE. This actually relies on choosing an appropriate space $\tilde{\mathscr{K}}_\mu$, which is a subset of the minimally constrained space of displacement fluctuations $\tilde{\mathscr{K}}_\mu^*$. The crucial point to be mentioned here is that the referred set must be aligned with the specific nature of the microstructure that we are going to study. To put it another way, $\tilde{\mathscr{K}}_\mu$ must restrict the solution of the microscopic equilibrium problem in a fashion that the model might reproduce the real behaviour of the solid as faithfully as possible.

In this Section, four different classes of MSM will be addressed. We must remark that these classes differ from one another solely in the space $\tilde{\mathscr{K}}_\mu$. For this reason, the RVE domain or the microscopic constitutive functional are left as arbitrary, since they are not differentiating factors between the models. The models that are going to be covered are presented below (along with the notation used to identify the corresponding space of admissible displacement fluctuations):

1. *Taylor model* or *rule of mixtures*: ${}^{\text{Tay}}\tilde{\mathscr{K}}_\mu$;
2. *Linear boundary model*: ${}^{\text{Lin}}\tilde{\mathscr{K}}_\mu$;
3. *Periodic boundary model*: ${}^{\text{Per}}\tilde{\mathscr{K}}_\mu$;
4. *Uniform boundary traction model*: ${}^{\text{Uni}}\tilde{\mathscr{K}}_\mu$.

The models are enumerated in order of decreasing *stiffness*. The stiffness of a MSM increases as the kinematical constraints imposed on the RVE are more severe. Having

said that, it is possible to state that:

$$^{\text{Tay}}\tilde{\mathscr{K}}_\mu \subset {}^{\text{Lin}}\tilde{\mathscr{K}}_\mu \subset {}^{\text{Per}}\tilde{\mathscr{K}}_\mu \subset {}^{\text{Uni}}\tilde{\mathscr{K}}_\mu, \tag{3.48}$$

that is, the Taylor and the Uniform traction models give, respectively, the most and the least kinematically constrained solutions to the microscopic equilibrium problem. This relation will become clearer at the end of this Section, after all the spaces $\tilde{\mathscr{K}}_\mu$ have been defined in Sections 3.2.7.1 to 3.2.7.4.

3.2.7.1 Taylor Model

The Taylor model is the simplest and most restrictive of the models that will be presented here. Within this model, it is assumed that the fluctuation displacement vanishes over the entire solid domain of the RVE, inasmuch as:

$$\tilde{\boldsymbol{u}}_\mu(\boldsymbol{x}_\mu, t) = \boldsymbol{0}, \quad \forall \boldsymbol{x}_\mu \in \Omega_\mu^s. \tag{3.49}$$

As a consequence the microscopic displacement field $\boldsymbol{u}_\mu$ varies linearly with $\boldsymbol{p}_\mu$ (see Figure 3.3)

$$\boldsymbol{u}_\mu(\boldsymbol{x}_\mu, t) = \left[\boldsymbol{F}(\boldsymbol{x}, t) - \boldsymbol{I}\right] \boldsymbol{p}_\mu, \quad \forall \boldsymbol{x}_\mu \in \Omega_\mu^s \tag{3.50}$$

and the microscopic deformation gradient, $\boldsymbol{F}_\mu(\boldsymbol{x}_\mu, t)$, coincides with its macroscopic counterpart, $\boldsymbol{F}(\boldsymbol{x}, t)$:

$$\boldsymbol{F}_\mu(\boldsymbol{x}_\mu, t) = \boldsymbol{F}(\boldsymbol{x}, t), \quad \forall \boldsymbol{x}_\mu \in \Omega_\mu^s. \tag{3.51}$$

In short, we verify that a homogeneous strain is considered, even though the microstructure might be heterogeneous.

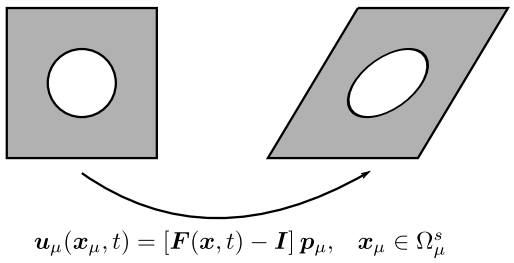

Figure 3.3: Schematic representation of the Taylor model.

All things considered, the set of microscopic kinematically admissible displacement fluctuations is given by:

$$^{\text{Tay}}\tilde{\mathscr{K}}_\mu \equiv \left\{ \tilde{\boldsymbol{u}}_\mu, \text{ sufficiently regular} \mid \tilde{\boldsymbol{u}}_\mu = \boldsymbol{0}, \quad \forall \boldsymbol{x}_\mu \in \Omega_\mu^s \right\}. \tag{3.52}$$

Before going further, some comments about the Taylor model must be made:

- The consequences (3.35) and (3.36) of the Hill-Mandel principle of macro-homogeneity are satisfied (as well as imposition (3.16)), as long as the microscopic reference body force $\boldsymbol{b}_{0,\mu}$ and the external surface traction $\boldsymbol{t}_{0,\mu}$ belong to the space of all sufficiently regular field over the corresponding domain;
- An important downside of the Taylor model relies on the fact that it does not consider the mechanical interactions amongst different heterogeneities of the RVE (for instance, between distinct solid phases and amongst a solid phase and a void). Provided that the strain field near the interface between solid phases can decisively influence the macroscopic behaviour of the material, the Taylor model might be quite limited when dealing with multiphase materials.

3.2.7.2 Linear Boundary Model

This model comprises a null displacement fluctuation over the RVE boundaries:

$$\tilde{\boldsymbol{u}}_\mu(\boldsymbol{x}_\mu, t) = \boldsymbol{0}, \quad \forall \boldsymbol{x}_\mu \in \partial\Omega_\mu. \tag{3.53}$$

This leads to:

$$\boldsymbol{u}_\mu(\boldsymbol{x}_\mu, t) = [\boldsymbol{F}(\boldsymbol{x}, t) - \boldsymbol{I}]\, \boldsymbol{p}_\mu, \quad \forall \boldsymbol{x}_\mu \in \partial\Omega_\mu, \tag{3.54}$$

i.e. the microscopic displacement field $\boldsymbol{u}_\mu$ is a linear function of $\boldsymbol{p}_\mu$ over the RVE boundaries $\partial\Omega_\mu$ (see Figure 3.4).

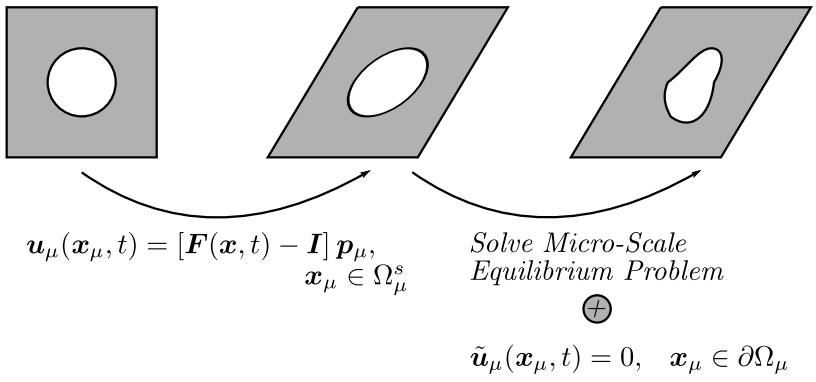

Figure 3.4: Schematic representation of the linear boundary model.

Accordingly, the space of microscopic kinematically admissible displacement fluctuations is reduced to:

$$^{\text{Lin}}\tilde{\mathscr{K}}_\mu \equiv \left\{ \tilde{\boldsymbol{u}}_\mu, \text{ sufficiently regular} \mid \tilde{\boldsymbol{u}}_\mu = \boldsymbol{0}, \quad \forall \boldsymbol{x}_\mu \in \partial\Omega_\mu \right\}. \tag{3.55}$$

Note that:

- The space $^{\text{Lin}}\tilde{\mathscr{K}}_\mu$ is evidently a subset of the minimally constrained set of kinematically admissible displacement fluctuations, so that (3.16) is ensured;

- The external surface traction $\boldsymbol{t}_{0,\mu}$ must belong to the space of all sufficiently regular fields over the RVE boundaries. In that case, $\boldsymbol{t}_{0,\mu}$ is orthogonal to ${}^{\mathrm{Lin}}\tilde{\mathscr{K}}_{\mu}$ and equation (3.36) is verified;
- The body force field $\boldsymbol{b}_{0,\mu}$ has to be orthogonal to ${}^{\mathrm{Lin}}\tilde{\mathscr{K}}_{\mu}$ (because of (3.35)). Henceforth, the body force field must vanish over the RVE domain:

$$\boldsymbol{b}_{0,\mu}(\boldsymbol{x}_{\mu}, t) = \boldsymbol{0}, \quad \forall \boldsymbol{x}_{\mu} \in \Omega_{\mu}. \tag{3.56}$$

3.2.7.3 Periodic Boundary Model

The periodic boundary model gives rise to one of the most widespread formulations within the micromechanics framework. This model is generally used to describe the response of materials with periodic (or almost periodic) microstructures. The periodic microstructure is represented by means of a periodic repetition of the RVE. Consequently, a key point of this model emerges: displacements on opposite boundary sides must be compatible.

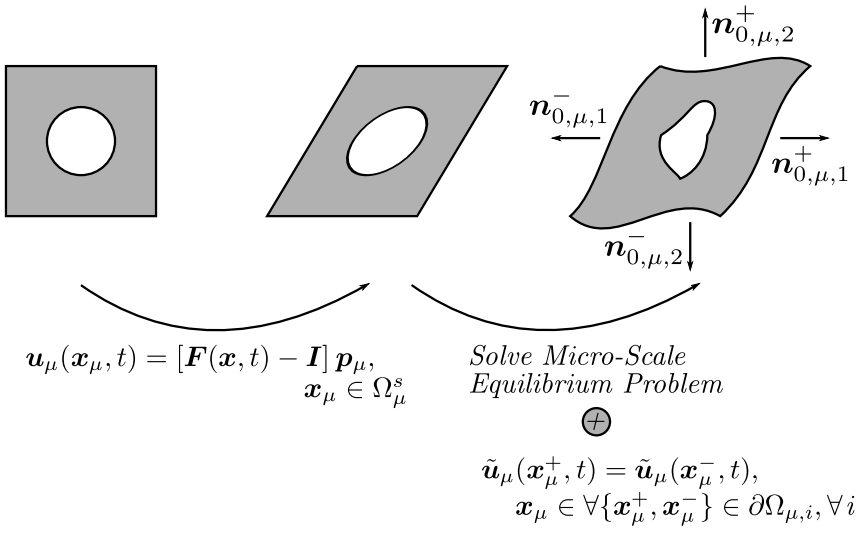

Figure 3.5: Schematic representation of the periodic boundary model.

At the outset, the boundary of the RVE $\partial\Omega_{\mu}$ must be split into n_{boun} pairs of cell sides ($\partial\Omega_{\mu,i}$ denotes pair i). It follows that

$$\partial\Omega_{\mu} = \bigcup_{i=1}^{n_{bound}} \partial\Omega_{\mu,i}. \tag{3.57}$$

Each pair i of cell sides has the following format:

$$\partial\Omega_{\mu,i} = \partial\Omega^{+}_{\mu,i} \cup \partial\Omega^{-}_{\mu,i}, \tag{3.58}$$

so that it comprises two equally sized subsets, $\partial\Omega^{+}_{\mu,i}$ and $\partial\Omega^{-}_{\mu,i}$, whose normal vectors are respectively given by $\boldsymbol{n}^{+}_{0,\mu,i}$ and $\boldsymbol{n}^{-}_{0,\mu,i}$ (Figure 3.5). Note that for each point $\boldsymbol{x}^{+}_{\mu} \in \Omega^{+}_{i}$, there is a corresponding pair $\boldsymbol{x}^{-}_{\mu} \in \Omega^{-}_{i}$. In that case:

$$\boldsymbol{n}^{+}_{0,\mu} = -\,\boldsymbol{n}^{-}_{0,\mu}. \tag{3.59}$$

As stated above, the displacement fluctuations on opposite boundary sides cannot be prescribed independently. In detail, it should be remarked that the periodic microstructure is obtained from the periodic repetition of the RVE. With that in mind, the displacement fluctuation field has to be *periodic* on the boundary of the RVE:

$$\tilde{\boldsymbol{u}}_{\mu}(\boldsymbol{x}^{+}_{\mu}, t) = \tilde{\boldsymbol{u}}_{\mu}(\boldsymbol{x}^{-}_{\mu}, t). \tag{3.60}$$

This assumption allows the definition of the space of kinematically admissible displacement fluctuations:

$$^{\mathrm{Per}}\tilde{\mathscr{K}}_{\mu} \equiv \Big\{ \tilde{\boldsymbol{u}}_{\mu},\ \text{sufficiently regular} \mid \tilde{\boldsymbol{u}}_{\mu}(\boldsymbol{x}^{+}_{\mu}, t) = \tilde{\boldsymbol{u}}_{\mu}(\boldsymbol{x}^{-}_{\mu}, t), \quad \forall \partial\Omega_{\mu,i} \wedge \forall \{\boldsymbol{x}^{+}_{\mu}, \boldsymbol{x}^{-}_{\mu}\} \in \partial\Omega_{\mu,i} \Big\}. \tag{3.61}$$

Some remarks concerning the periodic boundary model:

- The minimally constrained displacement fluctuation set $\tilde{\mathscr{K}}_{\mu}$ contains $^{\mathrm{Per}}\tilde{\mathscr{K}}_{\mu}$ (thus, equation (3.16) is satisfied);
- The *reactive* external surface traction $\boldsymbol{t}_{0,\mu}$ is *anti-periodic* on the boundary of the RVE:

  $$\boldsymbol{t}_{0,\mu}(\boldsymbol{x}^{+}_{\mu}, t) = -\,\boldsymbol{t}_{0,\mu}(\boldsymbol{x}^{-}_{\mu}, t) \tag{3.62}$$

  so its orthogonality to $^{\mathrm{Per}}\tilde{\mathscr{K}}_{\mu}$ is ensured (and so is the Hill-Mandel statement (3.36));
- The absence of body forces is demanded to satisfy (3.35). Under those circumstances, (3.56) is still applicable. As in the linear boundary model, accelerations must also vanish;
- The periodic boundary model intends to represent the response of materials with periodic microstructures. Nevertheless, it should be made clear that this does not imply periodicity neither in the micro-heterogeneities nor in the micro-singularities distribution over the RVE. In addition, the periodic repetition of the RVE is not necessarily global, meaning that the macroscopic body might not consist of the repetition of a single RVE (the periodicity might be local, as suggested by Guedes and Kikuchi (1990));
- When compared to the other models described throughout this Section, the

periodic boundary constraint appears to converge faster to the theoretical solutions, with increasing RVE size (Kanit et al., 2003; Terada et al., 2000). Putting it differently, smaller RVEs (and, thereupon, less computational effort) are required to obtain results of a given quality, compared to the other constraints presented here;

- Periodic boundary models are often associated with conforming finite element meshes over the micro-cells. On the contrary, more sophisticated strategies need to be employed to enforce a periodic displacement fluctuation field on non-conforming finite element meshes. One of these techniques involves the so-called *Mortar periodic boundary models* (for further details on this issue, consult Reis and Andrade Pires (2014)).

3.2.7.4 Uniform Boundary Traction Model

The uniform boundary traction model (Figure 3.6) gives the least constrained solution to the microscopic equilibrium problem (3.40). As a matter of fact, no additional restrictions are placed on the set of minimally constrained fluctuation displacements, so that

$$
\begin{aligned}
{}^{\text{Uni}}\tilde{\mathscr{K}}_{\mu} &\equiv \tilde{\mathscr{K}}_{\mu}^{*} \equiv \\
&\equiv \left\{ \tilde{\boldsymbol{u}}_{\mu},\ \text{sufficiently regular} \mid \int_{\partial\Omega_{\mu}} \tilde{\boldsymbol{u}}_{\mu}(\boldsymbol{x}_{\mu},t) \otimes \boldsymbol{n}_{0,\mu}(\boldsymbol{p}_{\mu})\ da = 0 \right\}. \quad (3.63)
\end{aligned}
$$

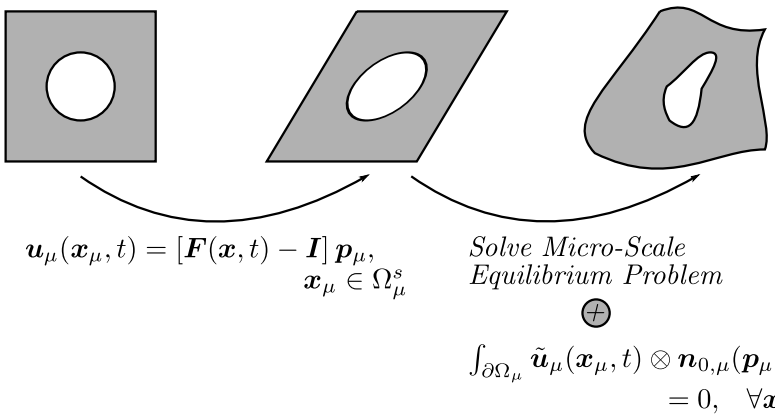

Figure 3.6: Schematic representation of the uniform boundary traction model.

Within the uniform boundary traction model framework is worth highlighting the following points:

- The name of this model results from the fact that an uniform traction over the boundary of the RVE is obtained, as a consequence of the chosen vector space ${}^{\text{Uni}}\tilde{\mathscr{K}}_{\mu}$. In the present context, the external surface traction (which verifies

equation (3.36)) is given by:

$$\boldsymbol{t}_{0,\mu} = \boldsymbol{P}(\boldsymbol{x},t)\,\boldsymbol{n}_{0,\mu}(\boldsymbol{x}_\mu,t) = \boldsymbol{P}_\mu(\boldsymbol{x}_\mu,t)\,\boldsymbol{n}_{0,\mu}(\boldsymbol{x}_\mu,t), \quad \forall \boldsymbol{x}_\mu \in \partial\Omega_\mu; \tag{3.64}$$

- Similarly to the linear and the periodic boundary constraints, this model requires the absence of body forces and accelerations. Thus, assumption (3.56) is valid in view of satisfying (3.35);
- When dealing with large strains, this class of kinematical constraints may lead to unrealistic or meaningless results, since *spurious effects* might appear (Coenen et al., 2012).

3.2.8 Coupled and Decoupled Multi-Scale Analyses

As we previously made clear, continuum mechanics problems (formulated at the macro-scale) can be solved by means of a two-scale technique based on the homogenisation theory, that is, using MSM-H. A key point of these approaches may be outlined as follows: the solution of the micro-scale boundary value problem must be known in order to solve the macroscopic equilibrium problem (observe that this conclusion can be extracted from Figure 3.2). Alternatively, we may say that the macroscopic constitutive response is defined by the solution of the micro-scale equilibrium problem; that is, the relation between the macroscopic deformation gradient and the macroscopic Piola-Kirchhoff stress tensor (see equation (2.114)) is an implicit function of the solution of the micro-scale equilibrium problem.

In coupled multi-scale studies, the macroscopic constitutive behaviour must be known at each one of the integration points of the macroscopic mesh. This means that several micro-scale equilibrium problems (in equal number to the number of integration points at the macro-scale) have to be solved in every iteration (made at a generic time station t) of the macroscopic equilibrium problem. Hence, even though there are many conceptual advantages of using CMSA, for practical issues, the computational power required is generally excessive.

Decoupled micro-macro schemes can be used as an alternative to coupled multi-scale studies. In short, decoupling strategies are an attempt to solve the micro- and the macro-scale equilibrium problems separately. In order to do that, a macroscopic constitutive function is established and several microscopic studies are carried out, so that the parameters which capture the macroscopic constitutive behaviour can be obtained; then, the calibrated macroscopic constitutive function is used to model the macroscopic behaviour of the material being analysed and the macroscopic equilibrium problem is solved. Within the context of decoupled multi-scale schemes, it is worth to mention the work of Watanabe and Terada (2010) where the whole procedure is discussed step by step.

Altogether, it must be remembered that the macroscopic constitutive response can be outlined by means of micro-scale studies in case the homogenisation theory is applied. In fact, the studies further reported in this dissertation are restricted to the micro-scale, as our intention was to derive analytical laws that describe the response of polycrystalline aggregates in the elastic and yielding domain. Therefore, we may conclude that neither "true" coupled nor "true" decoupled multi-scale approaches were followed, as we did not solve macroscopic problems using the constitutive laws derived from the microscopic analyses performed.

3.3 Numerical Approximation

A finite element-based procedure may be employed to obtain numerical solutions to the weak version of the microscopic equilibrium problem (3.40). Since the underlying principles are fairly similar to those scrutinised in Section 2.7, for the sake of brevity and objectivity, we will not expound on this subject (details about the numerical implementation of MSM-H can be found, for instance, on Reis (2014) and Lopes (2016)). As a matter of fact, in what follows, we quickly focus on the computational multi-scale program used to perform the numerical simulations necessary to achieve the main objective of this work (i.e., the calibration of macroscopic constitutive laws from micro-scale studies).

3.3.1 `Links` Program

In this work, a multi-scale program called `Links` (acronym of Large Strain Implicit Non-Linear Finite Element Analysis of Solids Linking Scales) was used to perform the numerical micro-scale simulations required to calibrate constitutive laws. In this context, it must be emphasised that `Links`[5] allows not only micro-, but also macro- and coupled multi-scale finite-element analyses using a wide range of constitutive models under the general assumption of large deformations. Within the context of microscopic analyses using `Links`, the main features (namely inputs and outputs) are represented in Figure 3.7. Observe that further post-processing of the outputs represented was demanded in order to obtain the results shown in next Chapters.

[5] A detailed revision of `Links` – whose source code is written in `Fortran` – is made on Ferreira (2017).

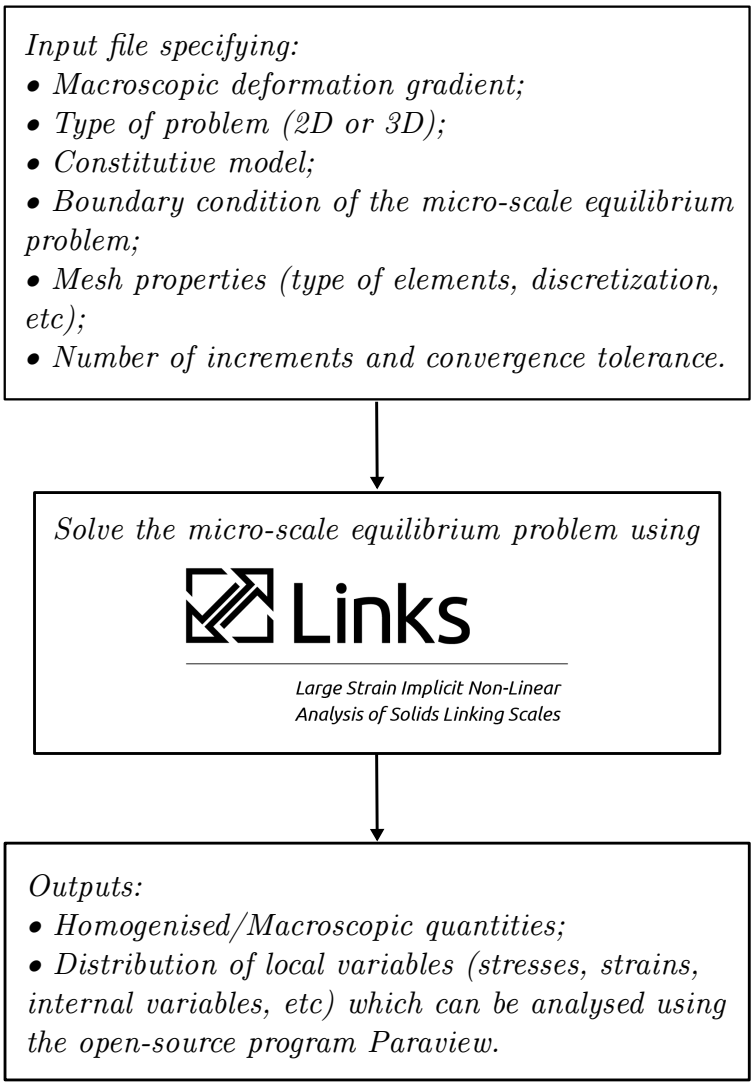

Figure 3.7: Main inputs and outputs of the `Links` program within the context of microscopic analyses.

This page was intentionally left with this sentence.

Chapter 4

On the Determination of the Elastic Response of Polycrystalline Aggregates

As we have seen in Section 3.2.8, the macroscopic constitutive behaviour of a generic material can be determined from micro-scale analyses, provided that the main microstructural features are known and, equally important, can be modelled accurately. Within that framework, the fundamentals of the homogenisation theory reviewed in Chapter 3 are of paramount concern and numerical simulations using the FEM are generally employed. The preceding statement is corroborated in Watanabe and Terada (2010), where the three main steps associated with this numerical micro-scale framework are summarised: at first, a macroscopic constitutive model has to be to ascribed to the material; then, several numerical tests are conducted (possibly on different microscopic specimens) and critical variables are pinpointed, so that, at the final stage, the constitutive law is calibrated based on the numerical data. It is noteworthy that the micro-scale numerical scheme described by Watanabe and Terada (2010) is foremost an attempt to provide constitutive laws that approximate the response of the materials at the macro-scale. By applying these kind of procedures, CMSA (computationally very costly) can be avoided and conventional macroscopic analysis founded on the numerically-derived constitutive models can be performed. Moreover, experimental procedures (expensive and time-consuming) can be minimized and the design of new materials might be optimized. All in all, numerical micro-scale studies directed towards the determination of the macroscopic constitutive behaviours are being widespread amongst industrial and scientific communities and it is expected that they will be increasingly used in the characterisation of new heterogeneous materials, which are generally composed of two or more constituents. Having said that, it is also relevant to understand that, until now, the application of these micro-scale approaches (involving the homogenisation theory) has been mainly constricted to the elastic domain and to single-phase materials. This explains why we

decided to drive our efforts to the prediction of the elastic (and yielding[1]) response of single-phase textureless polycrystalline aggregates, as it was easier to validate the results found using both analytical and numerical methods.

Since we have set our focus on the determination of the elastic macroscopic behaviour of polycrystalline aggregates it is important to review the constitutive laws used to describe the elastic response of these materials at the macro-scale (whose parameters we want to calibrate from the micro-scale studies). With that in mind, Section 4.1 introduces crystalline materials, before a revision of the linear elasticity framework (applicable to polycrystals) is made in Section 4.2 (particular emphasis is placed on the effect of material symmetries). Then, in Section 4.3, we discuss the analytical methods developed to predict the elastic response of polycrystalline aggregates. Within the framework of the analytical methods, the elastic characterisation of the constituent single-crystal is of primary importance and we must highlight the impact of the elastic anisotropy on the overall elastic response of polycrystalline aggregates. For the most part, one of the scalar entities addressed in Section 4.4 is used to quantify the elastic anisotropy of the crystallites within the aggregates – in this work, as a result of the discussion made, the log-Euclidean universal anisotropy index was chosen. Finally, in Section 4.5, the procedure associated with the numerical multi-scale technique that we employed with the objective of describing the elastic response of polycrystals is scrutinised.

The topics brought to light throughout this Chapter compile information from different areas related to mechanical engineering. For more information on the relevant material science, we suggest Dieter (1988); Engler and Randle (2009) and Suwas and Ray (2014); similarly, a more comprehensive account on the linear elasticity framework can be found on Bower (2009) and Ting (1996). The log-Euclidean universal anisotropy index is thoroughly explained in Kube (2016) while Kube and de Jong (2016) give an interesting assortment of the analytical methods used to predict the effective elastic response of polycrystals. Lastly, some aspects of the numerical procedure described in Section 4.5 are expounded on Carvalho (2015); Jöchen (2013); Quey et al. (2011) and Vieira de Carvalho (2016).

4.1 Brief Introduction to Crystalline Materials

Engler and Randle (2009); Kocks et al. (2000) and other authors suggested that a material may be called crystalline in case it exhibits discrete translation symmetry at the atomic level. By the same token, those works postulate that crystalline materials comprise atoms, molecules or ions packed in a *unit cell* whose repetition, in all spatial directions, produces the *crystal lattice*. In light of those definitions, we might conclude that the concept of unit cell is vital within the present framework as it

[1] See Chapters 6 and 7.

comprises the pattern which generates the crystal lattice by translation. In Figure 4.1, a generic unit cell is sketched.

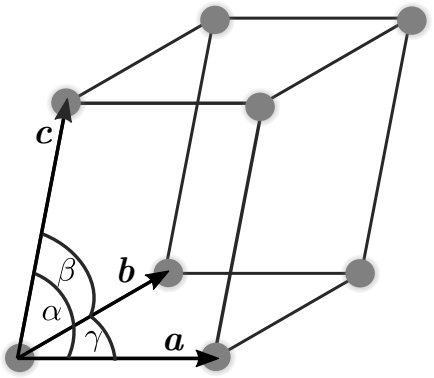

Figure 4.1: Generic triclinic ($\boldsymbol{a} \neq \boldsymbol{b} \neq \boldsymbol{c}$; $\alpha \neq \beta \neq \gamma$) unit cell (atoms are represented by the grey circles).

Usually, unit cells are characterised by three linearly independent unit vectors $\boldsymbol{a}$, $\boldsymbol{b}$ and $\boldsymbol{c}$, as well as the angles α, β and γ between them. From the definition of crystalline materials, the noncoplanar vectors ($\boldsymbol{a}$, $\boldsymbol{b}$ and $\boldsymbol{c}$) are also lattice parameters, as they identify the relative position of each lattice point (identified by vector $\boldsymbol{r}$) from an arbitrary origin (whose spatial position is given by $\boldsymbol{o}$):

$$\boldsymbol{r} = \boldsymbol{o} + k_a \cdot \boldsymbol{a} + k_b \cdot \boldsymbol{b} + k_c \cdot \boldsymbol{c}, \quad k_i \in \mathbb{Z}, \quad i = a, b, c. \tag{4.1}$$

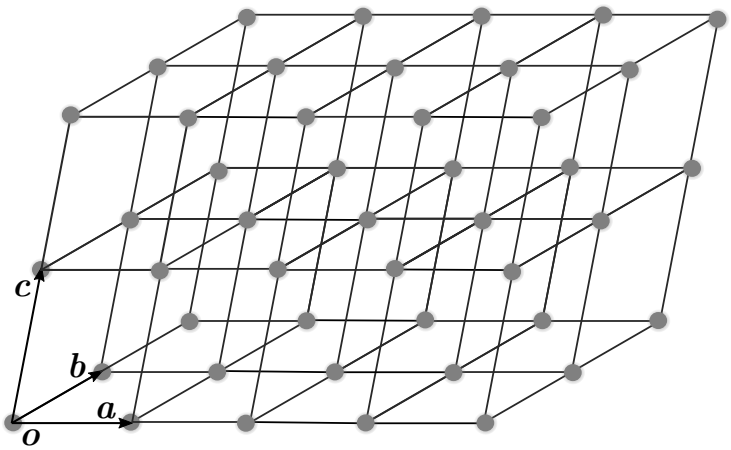

Figure 4.2: Generic 3D lattice: perfect periodicity is assumed and all atoms may be obtained from the origin $\boldsymbol{o}$ and the lattice parameters $\boldsymbol{a}$, $\boldsymbol{b}$ and $\boldsymbol{c}$. In this particular case, the lattice comprises a triclinic crystal system with primitive lattice centering.

A generic lattice is shown in Figure 4.2 where the perfect periodicity depicted

contrasts with the aspect of real crystals, which normally include the so-called lattice defects. The aforementioned Figure also creates room for the discussion of one of the most relevant properties of crystals: their *inherent symmetry*. From its own definition, crystals exhibit translational symmetry, but, in order to completely characterize a certain crystal, all of its inherent symmetries must be outlined (Engler and Randle, 2009). In fact, if we observe Figure 4.2, we might note that rotating the crystal 180 degrees about each one of the axes defined by the lattice vectors, leaves the crystal unchanged; in that case, we say that the crystal exhibits two-fold symmetry around those axes. Similarly, a generic crystal has six-fold, four-fold or three-fold symmetry around a certain axis if it remains unchanged after being rotated, respectively, 60, 90 and 120 degrees about it. All six-, four-, three- and two-fold symmetries are examples of rotational symmetries. Taking this into consideration we might understand that, in the most general case, rotational/mirror and translational symmetries may be combined, so that crystals may exhibit compound symmetries. The inherent symmetries of a lattice define its *crystal system* (or lattice type); all 7 types of crystal systems are characterized in Table 4.1.

Table 4.1: Characterisation of the 7 crystal systems/lattice types.

Crystal system	**Inherent symmetries** (besides translation symmetry)	**Unit cell parameters**
Triclinic	None	$\boldsymbol{a} \neq \boldsymbol{b} \neq \boldsymbol{c}$ $\alpha \neq \beta \neq \gamma$
Monoclinic	One two-fold rotation axis	$\boldsymbol{a} \neq \boldsymbol{b} \neq \boldsymbol{c}$ $\alpha = \beta = 90^\circ \neq \gamma$
Orthorombic	Three two-fold rotation axis	$\boldsymbol{a} \neq \boldsymbol{b} \neq \boldsymbol{c}$ $\alpha = \beta = \gamma = 90^\circ$
Tetragonal	One four-fold rotation axis	$\boldsymbol{a} = \boldsymbol{b} \neq \boldsymbol{c}$ $\alpha = \beta = \gamma = 90^\circ$
Rhombohedral	One three-fold rotation axis	$\boldsymbol{a} = \boldsymbol{b} = \boldsymbol{c}$ $\alpha = \beta = \gamma \neq 90^\circ$
Hexagonal	One six-fold rotation axis	$\boldsymbol{a} = \boldsymbol{b} = \boldsymbol{c}$ $\alpha = \beta = 90^\circ$, $\gamma = 120^\circ$
Cubic	Four three-fold rotation axis	$\boldsymbol{a} = \boldsymbol{b} = \boldsymbol{c}$ $\alpha = \beta = \gamma = 90^\circ$

Adding to the inherent symmetry of crystals, there are various *lattice centerings* which must be considered in order to describe the geometric arrangement of the lattice points (and, consequently, the translational symmetry of the crystal). The lattice centering groups are detailed in Table 4.2.

Table 4.2: Characterisation of the possible lattice centerings.

Lattice centering	**Position of the lattice points**
Primitive	On the unit cell's corners
Body-centered	On the unit cell's corners and at its center
Face-centered	On the unit cell's corners and at the center of their faces
Base-centered	On the unit cell's corners and at the center of the bases of the cell

The well-known *Bravais lattices* arise from the combination of the crystal systems with the lattice centerings. As some of the combinations are equivalent, there are only 14 Bravais lattices (which are characterised in Table 4.3).

Table 4.3: Defining the 14 Bravais lattices.

Crystal system	**Lattice centering**
Triclinic	Primitive
Monoclinic	Primitive Base-centered
Orthorombic	Primitive Body-centered Face-centered Base-centered
Tetragonal	Primitive Body-centered
Rhombohedral	Primitive
Hexagonal	Primitive
Cubic	Primitive Body-centered Face-centered

In this work, we direct our attention towards *face-centered* and *body-centered cubic* Bravais lattices (denoted, respectively, fcc and bcc). One of the reasons for this derives from the fact that most metals of interest in mechanical engineering, at room temperature, are found in one of the highlighted crystalline patterns (examples of metals with fcc crystal structure include silver, aluminium, gold, copper, nickel and lead, whereas alpha iron and tungsten are metals with bcc lattices). The unit cells associated with these two Bravais lattices are represented in Figure 4.3 where three mutually perpendicular axes were placed through one of the corners of the cubic unit cell. All crystallographic planes and directions are normally expressed with respect to those three axes in terms of *Miller indices*. If the position of the origin of the referential is given by $\boldsymbol{o}$, a generic crystallographic direction can be represented as $[uvw]$, where the three Miller indices u, v and w are the integers used in equation (4.1). This definition entails that some crystallographic directions are equivalent, as they can be represented by the same Miller indices, depending upon the specific choice of axes (and, consequently of $\boldsymbol{o}$). A group of equivalent directions is said to be a family of directions and is generically represented as $\langle uvw \rangle$ (where $[uvw]$ is one of the directions belonging to the group). On the other hand, in order to define crystallographic planes, the basis of the reciprocal lattice vectors (denoted $\boldsymbol{a}_r$, $\boldsymbol{b}_r$ and $\boldsymbol{c}_r$) has to be considered. These vectors are related to the original basis according to equation (4.2).

$$\boldsymbol{i} \cdot \boldsymbol{j}_r = \begin{cases} 1, & \text{if } \boldsymbol{j} = \boldsymbol{i} \\ 0, & \text{if } \boldsymbol{j} \neq \boldsymbol{i} \end{cases}, \; \boldsymbol{i}, \boldsymbol{j} = \boldsymbol{a}, \boldsymbol{b}, \boldsymbol{c}. \tag{4.2}$$

In that case, the reciprocal lattice vectors are linearly independent and a vector $\boldsymbol{n}$, normal to a generic crystallographic plane (hkl) can be defined from the reciprocal basis in a such a way the following relation is verified:

$$\boldsymbol{n} = h \cdot \boldsymbol{a}_r + k \cdot \boldsymbol{b}_r + l \cdot \boldsymbol{c}_r, \;\; h, k, l \in \mathcal{Z}. \tag{4.3}$$

We must remark that not only the three Miller indices, h, k and l must be integers, as they also should be written in lowest terms (that is, the greatest common divisor of h, k and l should be one). Because of the referred properties, it can be proven that a crystallographic plane (hkl) intersect the three "original" axes (defined by the lattice parameters) in the points $\boldsymbol{a}/h$, $\boldsymbol{b}/k$ and $\boldsymbol{c}/l$ or some multiple thereof (if one of the Miller indices is zero, the plane contains the corresponding axis and the intersection takes place at infinity). Similarly to crystallographic directions, equivalent crystallographic planes are grouped in families of planes (and, analogously, the family of planes containing (hkl) is given by $\{hkl\}$).

In practice, neither lattices are perfect arrays of atoms nor they have an infinite extension. To put it differently, regular arrays of atoms are repeated over large distances compared to the atomic-scale, but, generally speaking, they do not extend

for the whole length of the material[2]. As a consequence, most metals are called *polycrystals* as they are essentially aggregates of crystals/grains. In these polycrystalline aggregates, each grain consists of a volume in which the arrangement of the atoms is nearly identical. Therefore, adjoining grains, encompassing arrangements of atoms oriented differently, are separated through *grain boundaries* which, in turn, constitute narrow zones where the lattice of two adjoining grains is not alligned.

In Figure 4.4, the morphology of two polycrystals with 10 and 25 grains can be depicted. Observe that each grain is assigned a different color, according to its specified orientation. The set composed of the orientations of all grains is called *texture*. Several authors (e.g., Kocks et al. (2000) and Suwas and Ray (2014)) pay utmost attention to the description of texture, since it strongly affects the constitutive response of materials. In general, polycrystalline materials might consist of textureless or textured aggregates, depending on whether they contain randomly oriented grains or grains aligned with some preferred orientation(s). The orientation of each particular grain is ordinarily described by a set of three angles, known as *Euler angles* – see Appendix A for more on this topic.

In this work, heterogeneities other than grain boundaries (e.g., inclusions or voids) were not considered. Besides this, we directed our attention towards cubic textureless polycrystals, that is, we have dealt with aggregates composed of randomly oriented grains whose lattices exhibit cubic symmetry.

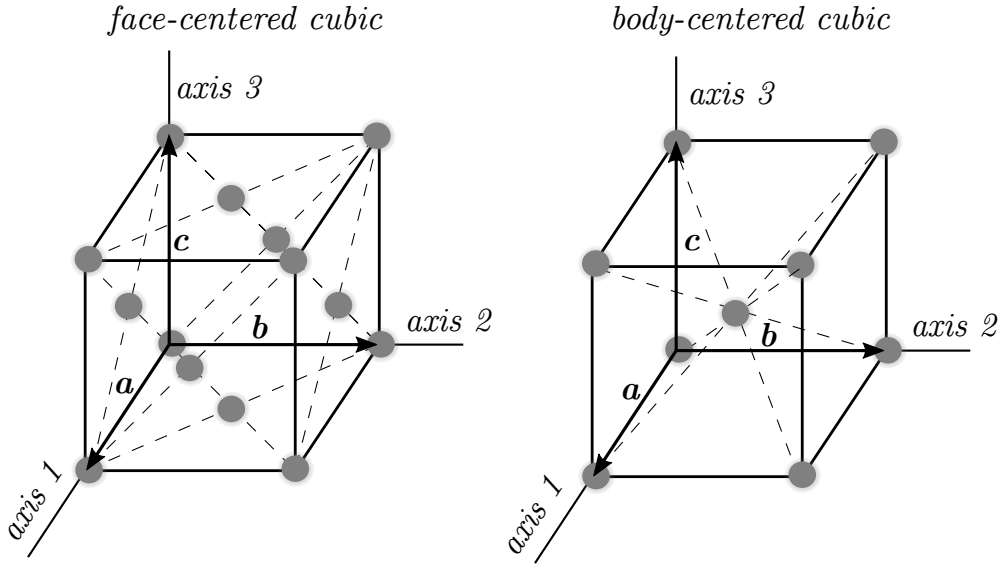

Figure 4.3: Unit cell associated with face-centered and body-centered cubic Bravais lattices.

[2]Jet engine turbine blades constitute examples of monocrystalline materials: the whole manufacturing process linked with these materials, especially the crystallisation stage, is strictly controlled.

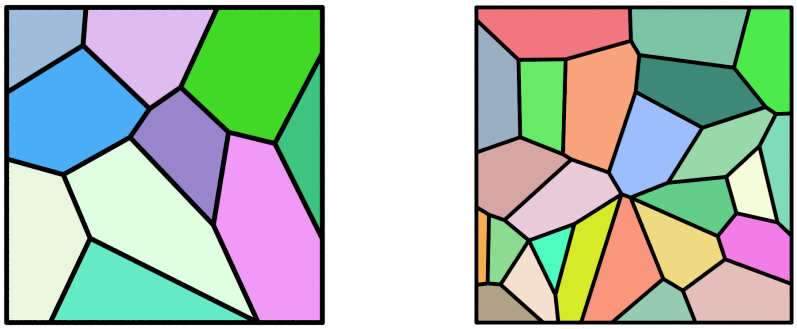

Figure 4.4: Generic polycrystals with 10 (left) and 25 (right) grains (these 2D representations were generated with the open-source software package `Neper` (Quey et al., 2011)).

4.2 Linear Elasticity Framework

Polycrystalline aggregates (and many other materials with practical interest) usually deform in the elastic domain before reaching plasticity. In the elastic domain, the strain levels can often be considered *infinitesimal* and the deformed configuration of the material is basically coincident with its original shape. Furthermore, since the stress and strain levels involved are low, a linear relation between these quantities is generally assumed. With this in mind, the generic constitutive relation (2.103) developed in consistency with the large-strain continuum mechanics formulation is replaced by the *generalized Hooke's law*:

$$\boldsymbol{\sigma} = \mathbf{C} : \boldsymbol{\varepsilon}, \tag{4.4}$$

in which a linear relation between the Cauchy stress tensor $\boldsymbol{\sigma}$ and the infinitesimal srain tensor $\boldsymbol{\varepsilon}$ is established by means of a fourth-rank tensor, known as the *stiffness* or *elasticity* tensor. This linear mapping between the strain and stress tensor is sometimes expressed in the following fashion:

$$\boldsymbol{\varepsilon} = \mathbf{S} : \boldsymbol{\sigma}, \tag{4.5}$$

in which $\mathbf{S}$ defines the *compliance* tensor, defined as the inverse of the elasticity tensor:

$$\mathbf{S} = \mathbf{C}^{-1}. \tag{4.6}$$

The stiffness tensor (or alternatively the compliance tensor) must describe the elastic behaviour of solids. Owing to the fact that $\mathbf{C}$ is a fourth-order tensor, it may seem that 81 different components have to be defined in order to fully characterize the linear elastic behaviour. Fortunately, the maximum number of independent elasticity constants is actually reduced because:

- The Cauchy stress tensor is symmetric ($\boldsymbol{\sigma} = \boldsymbol{\sigma}^T$) and, as a consequence:

$$\mathsf{C}_{ijkl} = \mathsf{C}_{jikl}; \tag{4.7}$$

- The infinitesimal strain tensor is also symmetric ($\boldsymbol{\varepsilon} = \boldsymbol{\varepsilon}^T$), so that:

$$\mathsf{C}_{ijkl} = \mathsf{C}_{ijlk}. \tag{4.8}$$

Combining equations (4.7) and (4.8), we may obtain the condition of *minor symmetry* which reduces the number of independent elastic parameters to 36 (a similar relation is verified for the compliance tensor):

$$\mathsf{C}_{ijkl} = \mathsf{C}_{jikl} = \mathsf{C}_{ijlk}. \tag{4.9}$$

Within this framework, it is imperative to introduce the concept of *strain energy function* (denoted U), which is related to the capacity of materials to store energy in the elastic domain. This strain energy function is defined as:

$$U = \frac{1}{2}\,\mathsf{C}_{ijkl} : \varepsilon_{kl} : \varepsilon_{ij}, \tag{4.10}$$

while its derivative with respect to the infinitesimal strain tensor originates the Cauchy stress tensor

$$\sigma_{ij} = \frac{\partial U}{\partial \varepsilon_{ij}}. \tag{4.11}$$

The preceding equation and the following definition of the stiffness tensor:

$$\mathsf{C}_{ijkl} = \frac{\partial \sigma_{ij}}{\partial \varepsilon_{kl}} \tag{4.12}$$

might be combined, thusly:

$$\mathsf{C}_{ijkl} = \frac{\partial^2 U}{\partial \varepsilon_{kl}\,\partial \varepsilon_{ij}}. \tag{4.13}$$

Since the double differentiations on (4.13) are interchangeable, we may obtain the condition of *major symmetry* of the elasticity tensor:

$$\mathsf{C}_{ijkl} = \mathsf{C}_{klij}. \tag{4.14}$$

From conditions (4.9) and (4.14), we can finally identify all the symmetries of the stiffness tensor:

$$\mathsf{C}_{ijkl} = \mathsf{C}_{jikl} = \mathsf{C}_{ijlk} = \mathsf{C}_{klij}. \tag{4.15}$$

Considering the symmetries of the elasticity tensor (and, evidently, the symmetries of the Cauchy stress tensor and of the infinitesimal strain tensor), it is very common to rewrite the generalized Hooke's law in a matrix notation. This procedure is particularly convenient for finite element schemes, inasmuch as storing the components of fourth-rank tensor in 2D arrays, along with replacing second-order tensors with single-column matrices, generates an increase in efficiency. The most widespread

procedure used to perform these transformations involves Voigt scheme, albeit we should make it clear that there are other alternative techniques. If we adopt Voigt scheme, the generalized Hooke's law in matrix basis reads:

$$\begin{Bmatrix} \sigma_{11} \\ \sigma_{22} \\ \sigma_{33} \\ \sigma_{23} \\ \sigma_{13} \\ \sigma_{12} \end{Bmatrix} = \begin{bmatrix} \mathsf{C}_{1111} & \mathsf{C}_{1122} & \mathsf{C}_{1133} & \mathsf{C}_{1123} & \mathsf{C}_{1113} & \mathsf{C}_{1112} \\ & \mathsf{C}_{2222} & \mathsf{C}_{2233} & \mathsf{C}_{2223} & \mathsf{C}_{2213} & \mathsf{C}_{2212} \\ & & \mathsf{C}_{3333} & \mathsf{C}_{3323} & \mathsf{C}_{3313} & \mathsf{C}_{3312} \\ & & & \mathsf{C}_{2323} & \mathsf{C}_{2313} & \mathsf{C}_{2312} \\ & & & & \mathsf{C}_{1313} & \mathsf{C}_{1312} \\ \text{sym.} & & & & & \mathsf{C}_{1212} \end{bmatrix} \begin{Bmatrix} \varepsilon_{11} \\ \varepsilon_{22} \\ \varepsilon_{33} \\ 2\varepsilon_{23} \\ 2\varepsilon_{13} \\ 2\varepsilon_{12} \end{Bmatrix}, \tag{4.16}$$

where the strain vector is also named as the *engineering strains vector*, since the shear components are multiplied by a factor of 2. Given that the shear stresses are not multiplied by the referred factor, it becomes apparent that Voigt scheme induces a different treatment to stress and strain quantities. It must be remarked, however, that this conclusion is not always apparent, provided that there are many alternative versions of (4.16) in which the indices $ijkl$ (that preserve the tensor character of $\boldsymbol{\sigma}$, $\mathbf{C}$ and $\boldsymbol{\varepsilon}$) are not employed. One of those alternative presentations of the generalized Hooke's law relies on adopting the indices mn, as we show in equation (3.17)[3]:

$$\begin{Bmatrix} \sigma_1 \\ \sigma_2 \\ \sigma_3 \\ \sigma_4 \\ \sigma_5 \\ \sigma_6 \end{Bmatrix} = \begin{bmatrix} \mathsf{C}_{11} & \mathsf{C}_{12} & \mathsf{C}_{13} & \mathsf{C}_{14} & \mathsf{C}_{15} & \mathsf{C}_{16} \\ & \mathsf{C}_{22} & \mathsf{C}_{23} & \mathsf{C}_{24} & \mathsf{C}_{25} & \mathsf{C}_{26} \\ & & \mathsf{C}_{33} & \mathsf{C}_{34} & \mathsf{C}_{35} & \mathsf{C}_{36} \\ & & & \mathsf{C}_{44} & \mathsf{C}_{45} & \mathsf{C}_{46} \\ & & & & \mathsf{C}_{55} & \mathsf{C}_{56} \\ \text{sym.} & & & & & \mathsf{C}_{66} \end{bmatrix} \begin{Bmatrix} \varepsilon_1 \\ \varepsilon_2 \\ \varepsilon_3 \\ \varepsilon_4 \\ \varepsilon_5 \\ \varepsilon_6 \end{Bmatrix}. \tag{4.17}$$

All things considered, the matrix representation (4.17) of the constitutive equation (4.4) is possible due to the symmetries of the stress, strain and stiffness (compliance) tensors. In fact, as we might see from relations (4.16) and (4.17), the elasticity matrix includes just 21 independent elastic constants, owing to the fact that it possesses minor and major symmetries.

The number of independent elastic parameters is actually reduced in many cases, as most materials possess planes of elastic symmetry. In Section 4.2.1, the effect of material symmetries is discussed with particular emphasis being placed on the stress-strain relations of textureless polycrystalline aggregates comprising grains with cubic Bravais lattices. Since the description of the behaviour of linear elastic materials may be based on elastic constants other than the components of the stiffness (compliance) matrix, in Section 4.2.2, we introduce alternative elastic parameters.

[3]The Voigt mapping transformation scheme involved in the transformation $\mathsf{C}_{ijkl} \longrightarrow \mathsf{C}_{mn}$ (which is consistent with the transformations $\boldsymbol{\sigma}_{ij} \longrightarrow \boldsymbol{\sigma}_m$ and $\varepsilon_{kl} \longrightarrow \varepsilon_n$) is detailed in Appendix B.1.

4.2.1 Effect of Material Symmetries

When polycrystalline aggregates encompass a very large number of randomly oriented grains, they may be considered *isotropic* (or *quasi-isotropic*). In that case, the elastic properties of the material remain the same, independently of the loading direction and just 2 of the 21 elastic parameters are independent.

From another point of view, we can say that isotropic materials have an infinite number of symmetry planes, i.e., the number of axes around which the specimen can be turned without changing the elastic response is infinite. The isotropic constitutive relation in matrix notation is presented below:

$$\begin{Bmatrix} \sigma_1 \\ \sigma_2 \\ \sigma_3 \\ \sigma_4 \\ \sigma_5 \\ \sigma_6 \end{Bmatrix} = \begin{bmatrix} \mathsf{C}_{11} & \mathsf{C}_{12} & \mathsf{C}_{12} & 0 & 0 & 0 \\ & \mathsf{C}_{11} & \mathsf{C}_{12} & 0 & 0 & 0 \\ & & \mathsf{C}_{11} & 0 & 0 & 0 \\ & & & \mathsf{C}_{44} & 0 & 0 \\ & & & & \mathsf{C}_{44} & 0 \\ \text{sym.} & & & & & \mathsf{C}_{44} \end{bmatrix} \begin{Bmatrix} \varepsilon_1 \\ \varepsilon_2 \\ \varepsilon_3 \\ \varepsilon_4 \\ \varepsilon_5 \\ \varepsilon_6 \end{Bmatrix}, \tag{4.18}$$

where the following identity is verified:

$$\mathsf{C}_{44} = \frac{\mathsf{C}_{11} - \mathsf{C}_{12}}{2}. \tag{4.19}$$

Despite the fact that many polycrystalline systems of interest can be considered isotropic, a similar assumption cannot be made regarding their constituent single-crystals. For this reason, when we analyse textureless *oligocrystals* (polycrystalline aggregates which enclose a small number of randomly oriented grains), the general constitutive law (4.17) has to be employed. Oligocrystals are examples of anisotropic solids whose elastic behaviour is defined by 21 elastic constants. In contrast with isotropic solids, anisotropic specimens do not possess planes of elastic symmetry and, as a consequence, their elastic response depends on the orientation of the external loadings.

On balance, we must understand that isotropic and anisotropic solids lie at opposite extremes and that the elastic response of a generic specimen may be defined by a certain number of independent constants located between 2 and 21. Generally speaking, ascertaining a specific constitutive law to a material requires the knowledge of the number and the type of planes of elastic symmetry and, as a general rule, we can outline that the increase in the number of symmetry elements is ordinarily associated with a reduction in the number of independent elastic parameters.

In this work, we are principally interested in polycrystals composed of crystals with cubic lattices which, individually, are monocrystalline speciments possessing 9 different planes of elastic symmetry. These cubic monocrystals exhibit cubic symmetry and 3 independent elastic constants are sufficient to describe their elastic behaviour. For this reason, their strain-stress relation is given by (4.18), but, unlike

isotropic specimens, C_{44} cannot be calculated from equation (4.19) (in Section 4.3, this question is treated in greater detail). Table 4.4 compiles the elastic constants of several cubic crystals metals.

In this Section, we have characterized the elastic framework involving oligocrystals, cubic monocrystals and isotropic polycrystalline aggregates (which constitute, respectively, anisotropic, cubic and isotropic solids). Nevertheless, it is important to notice that besides anisotropic, cubic and isotropic materials, other 5 groups of solids emanate based on the number and the type of planes of elastic symmetry. An assortment of all groups of material symmetry is made in Appendix B.2, where the number of planes of elastic symmetry, the number of independent elastic constants and the specific formats of the elasticity matrices are shown for each class.

Table 4.4: Elastic constants for cubic crystals at room temperature[a].

Bravais Lattice	**Material**	C_{11}	C_{12}	C_{44}
Face-centered cubic	Ag	124.0	93.4	46.1
	Al	107.3	60.9	28.3
	Au	192.9	163.8	41.5
	Cu	168.4	121.4	75.4
	Ni	246.5	147.3	124.7
	Pb	49.5	42.3	14.9
Body-centered cubic	Fe	231.4	134.7	116.4
	W	522.4	204.4	160.8

[a]Data from Freund and Suresh (2004) (the axes of reference were taken parallel to the cube axes of the crystals). All elastic constants expressed in $\mathrm{GN/m^2}$.

4.2.2 Elastic Parameters

In the isotropic constitutive law defined by equations (4.18) and (4.19), the two independent elastic parameters used were the stiffnesses C_{11} and C_{12}. Albeit these constants can be used, the isotropic law is frequently expressed in terms of alternative *elastic parameters*, such as the *Young's modulus* (denoted E) and the *Poisson's ratio* (represented as ν). The isotropic elasticity matrix expressed in terms of E and ν is presented below:

$$\mathbf{C} = \frac{E}{(1+\nu)(1-2\nu)} \begin{bmatrix} 1-\nu & \nu & \nu & 0 & 0 & 0 \\ & 1-\nu & \nu & 0 & 0 & 0 \\ & & 1-\nu & 0 & 0 & 0 \\ & & & \frac{1-2\nu}{2} & 0 & 0 \\ & & & & \frac{1-2\nu}{2} & 0 \\ \text{sym.} & & & & & \frac{1-2\nu}{2} \end{bmatrix}. \tag{4.20}$$

Other widely used elastic parameters include the *bulk modulus* K and the *shear modulus* G. More than the mathematical expressions that relate these elastic parameters (which are presented in Appendix B.3 for isotropic solids), we must be aware of their physical meaning. A brief review about the elastic parameters E, ν, G and K is made in what follows:

- *Young's modulus.* Constitutes a measure of the stiffness of the solid (as the Young's modulus increases, the stiffness of the solid also increases). It is particularly interesting in uni-axial tensile tests, as it establishes the bridge between the exerted load per unit area and the infinitesimal longitudinal length change; in particular, the ratio between the normal stress and the longitudinal stretch gives the Young's modulus. As a consequence, the Young's modulus must always be a positive quantity and it possesses the dimensions of stress ($\mathrm{N/m^2}$);
- *Poisson's ratio.* It is a measure of compressibility of the solid (when $\nu = 0,5$, the solid is incompressible). In uni-axial tensile tests, it expresses the ratio between the strain in a direction normal to the load direction (typically referred to as transverse direction) and the deformation in the direction of the load (named axial or longitudinal strain). The Poisson's ratio is a dimensionless quantity and, for stable materials, it varies between -1 and $0,5$ (in many isotropic metals, $\nu = 1/3$, in such a way that $E \approx K$ and $G \approx 3/8\,E$);
- *Shear modulus.* It quantifies the resistance of the solid to isochoric shear deformations. It is very convenient to use the shear modulus when the material is submitted to torsion or pure or simple shear, as it provides ratio between the tangential force per unit area (shear stress) and the angle of shear (shear strain). This elastic parameter must always be a positive entity, albeit being generally smaller than the Young's modulus (it is also expressed in $\mathrm{N/m^2}$);
- *Bulk modulus.* This quantity measures the resistance of the solid to volumetric deformations, as it defines the quotient between the applied pressure and infinitesimal volume contraction. Similar to the shear and the Young's modulus, it has the dimensions of stress and it is positive (typically, it is larger than E).

The aforementioned elastic parameters may be generalised to describe the elastic response of anisotropic solids. If we attend on the definitions of each one of the elastic parameters, we might note that they were introduced with respect to one (in the cases of E and K) or two (G and ν) specific directions; at the same time, no restrictions were placed on the values of the elastic parameters with respect to different directions, so that they might vary according to the loading direction (that is, the elastic parameters do not necessarily have to be isotropic).

In Nordmann et al. (2018), an expression which defines the Young's modulus

with respect to a generic direction $\boldsymbol{d}$ is presented:

$$E(\boldsymbol{d}) = \left[\boldsymbol{d} \otimes \boldsymbol{d} : \mathbf{S} : \boldsymbol{d} \otimes \boldsymbol{d}\right]^{-1}. \tag{4.21}$$

Equivalently, the bulk modulus with respect to direction $\boldsymbol{d}$ reads:

$$K(\boldsymbol{d}) = \frac{1}{3}\left[\boldsymbol{I} : \mathbf{S} : \boldsymbol{d} \otimes \boldsymbol{d}\right]^{-1}. \tag{4.22}$$

Lastly, note that a pair of directions $(\boldsymbol{d}, \boldsymbol{n})$ – where $\boldsymbol{n}$ is a normal vector to $\boldsymbol{d}$ (i.e., it defines the transverse or tangential direction) – is required to define the shear modulus,

$$G(\boldsymbol{d}, \boldsymbol{n}) = \frac{1}{2}\left[\frac{\sqrt{2}}{2}(\boldsymbol{d} \otimes \boldsymbol{n} + \boldsymbol{n} \otimes d) : \mathbf{S} : (\boldsymbol{d} \otimes \boldsymbol{n} + \boldsymbol{n} \otimes \boldsymbol{d})\frac{\sqrt{2}}{2}\right]^{-1}, \tag{4.23}$$

and the Poisson's ratio,

$$\nu(\boldsymbol{d}, \boldsymbol{n}) = E(\boldsymbol{d}) \cdot \boldsymbol{d} \otimes \boldsymbol{d} : \mathbf{S} : \boldsymbol{n} \otimes \boldsymbol{n}. \tag{4.24}$$

The expressions provided by Nordmann et al. (2018) are the basis for the graphical representation of these elastic parameters in all directions of the 3D space. This graphical output is informative for non-isotropic solids (such as oligocrystals) in which the elastic properties vary in every direction; on the contrary, the graphical representation of isotropic elastic properties originates a sphere. To materialise the graphical representation of the elastic properties, Nordmann et al. (2018) adopts a a spherical coordinate system and discusses possible values for the normal vector $\boldsymbol{n}$ (observe that there are infinite directions orthogonal to a generic direction $\boldsymbol{d}$). In the referred work, details about the computational framework associated with the numerical implementation of expressions (4.21) to (4.24) are also given and a `Matlab`® source code is shared. In the context of this dissertation, the above mentioned `Matlab`® script was used to obtain graphical visualizations of the elastic parameters in Chapter 5.

4.3 Analytical Predictions of the Elastic Response of Polycrystals

It is not unusual to use the term polycrystal to designate isotropic textureless aggregates, as a significant fraction of the crystalline systems of interest are assemblies containing a large number of small and randomly oriented grains. Even though the elastic characterisation of non-isotropic crystalline systems has sporadically drawn the attention of specific niches (two examples involve the segments of the market specialised on *Micro-Electromechanical Systems* – MEMS – and on monocrystalline jet engine turbine blades), it is apparent that the determination of the elastic response of isotropic aggregates has much more utility for a wider range of industries. This

certainly helps to explain why several analytical expressions have been formulated with the objective of estimating the elastic response of isotropic polycrystals (in contrast, there are fewer analytical models developed to estimate the elastic constants of other – non-isotropic – crystalline systems).

In this Section, we aim to succinctly cast the most relevant analytical models which were developed to predict the elastic response of isotropic polycrystalline aggregates. All of the formulations reviewed in what follows are sustained on the idea that the overall elastic response of isotropic polycrystals is dependent on the monocrystalline elastic parameters. In fact, all methods addressed establish closed-form expressions, which relate the two elastic parameters of the isotropic aggregates with the elastic constants of the constituent crystals. In light of what we have just stated, it is not surprising to find that the complexity of the analytical expressions escalates as the constituent crystals comprise fewer elements of elastic symmetry (this issue is expounded on Berryman (2005), where analytical expressions for hexagonal, trigonal and tegragonal aggregates are detailed). As a consequence, and due to the spectrum of polycrystals studied in the context of this dissertation, we have opted to reduce the presentation of mathematical expressions to the case of polycrystals whose constituent crystals exhibit cubic symmetry, so that we do not complicate the treatment of this topic more than strictly necessary.

Before we proceed, a key point concerning the prediction of the elastic response of isotropic polycrystals comprising cubic grains has to be outlined, as it further simplifies our subsequent exposition. What happens is that one of the elastic parameters that characterizes the elastic behaviour of these aggregates, namely the bulk modulus, is uniquely determined from the single-crystal elastic parameters C_{11} and C_{12} (Gairola and Kröner, 1981):

$$K = \frac{\mathsf{C}_{11} - 2\mathsf{C}_{12}}{3}. \tag{4.25}$$

To put it another way, the bulk modulus of materials with cubic symmetry is an isotropic property, even though the elastic behaviour of the specimen is not (in other words, cubic crystals have $K(\boldsymbol{d}) = k$, although similar relations do not stand for the other elastic parameters). As a consequence, aggregates of cubic crystals necessarily have bulk modulus identical to the one exhibited by the constituent grains. Alternatively, we may say that for aggregates of cubic crystals, the bulk modulus is a scalar invariant of the elasticity tensor (Ledbetter and Naimon, 1974).

Given these points, for textureless aggregates enclosing cubic crystals, it is sufficient to point out one analytical expression (concerning one elastic parameter other than the bulk modulus) to characterize their elastic response. From Sections 4.3.1 to 4.3.3, we will report several analytical predictions for the shear modulus, since the original presentations of the analytical methods discussed here were based on that parameter. However, note that the predictions of other isotropic elastic constants can be easily obtained (for all methods) using the relations listed in Appendix B.3

– for example, the isotropic Young's modulus can be calculated from the isotropic shear and bulk modulus using the following expression:

$$E = \frac{9KG}{3K + G}. \tag{4.26}$$

4.3.1 Voigt, Reuss and Hill Estimates

Voigt (1910) provided the first compelling contribution to the prediction of the elastic behaviour of isotropic polycrystals by assuming that all grains are subjected to the same state of strain. Hence, the model of *Voigt* suggests that the strain is uniform throughout the aggregate, fulfilling the requirement of kinematic compatibility, but failing to ensure compatibility of the stress field. For isotropic aggregates of cubic crystals, this method leads to the following expression for the shear modulus:

$$G^{\mathrm{V}} = \frac{\mathsf{C}_{11} - \mathsf{C}_{12} + 3\,\mathsf{C}_{44}}{5}, \tag{4.27}$$

where $(\cdot)^{\mathrm{V}}$ is a quantity related with Voigt model.

Some years later, Reuss (1929) proposed an alternative formulation in which a uniform stress field throughout the polycrystal was assumed. Thus, according to the model of *Reuss*, all grains experience identical stresses, so that the compatibility of the stress field was verified (on the contrary, kinematic compatibility was not satisfied). In case the constituent crystal exhibits cubic symmetry, this model (identified by the superscript R) conduces to the following result:

$$G^{\mathrm{R}} = \frac{\mathsf{C}_{11}^2 + \mathsf{C}_{11}\,\mathsf{C}_{12} - 2\,\mathsf{C}_{11}\,\mathsf{C}_{44} - 2\,\mathsf{C}_{12}^2 + 6\,\mathsf{C}_{12}\,\mathsf{C}_{44}}{3\,(\mathsf{C}_{11} - \mathsf{C}_{12}) - 4\,\mathsf{C}_{44}}. \tag{4.28}$$

All in all, Voigt (1910) and Reuss (1929) presented two different approaches embodying two completely opposite hypothesis. It was Hill (1952) who proved that these two models defined two extreme mechanical states and that the elastic response of isotropic polycrystals always lies somewhere in the middle of the predictions of Voigt and Reuss. In other words, Voigt and Reuss estimates actually determine bounds on the elastic properties, the latter being smaller. That being said, Hill (1952) advocated that improved estimates (known as *Hill*, H, or *Voigt-Reuss-Hill* estimates) of the elastic properties could be obtained in case the arithmetic average (a) or the geometric average (g) of the Voigt and Reuss estimates was considered:

$$G^{\text{H-a}} = \frac{G^{\mathrm{V}} + G^{\mathrm{R}}}{2}, \tag{4.29}$$

$$G^{\text{H-g}} = \sqrt{G^{\mathrm{V}}\,G^{\mathrm{R}}}. \tag{4.30}$$

It should be mentioned that Hill estimate is based solely on empirical data, i.e., it has no theoretical foundation. However, due to its simplicity, it is widely used, especially when the constituent crystal does not exhibit cubic symmetry (Berryman, 2005).

4.3.2 Hashin-Shtrikman Bounds

As mentioned earlier, Voigt and Reuss estimates actually define bounds on the isotropic elastic properties, so that they are known as the *first-order bounds*. These estimates sometimes give rise to coarse predictions of the elastic properties, as they can be significantly different from one another. Taking advantage of variational principles (valid regardless of the shape and behaviour of the crystals involved), Hashin and Shtrikman (1962) developed tighter bounds, which are ordinarily designated as *second-order bounds*. In fact, not only did the *Hashin-Shtrikman* model provide better estimates for the elastic properties than the first-order Reuss and Voigt models, as it was also verified that the first-order bounds were the worst possible bounds that could be obtained with their formulation.

Considering cubic crystal aggregates, the lower (HS^-) and upper (HS^+) bounds of Hashin-Shtrikman for the shear modulus can be calculated from:

$$G^{HS^-} = G_1 + 3\left(\frac{5}{G_2 - G_1} - 4\beta^{HS^-}\right)^{-1}, \tag{4.31}$$

$$G^{HS^+} = G_2 + 2\left(\frac{5}{G_1 - G_2} - 6\beta^{HS^+}\right)^{-1}, \tag{4.32}$$

where

$$\beta^{HS^-} = \frac{3(K + 2G_1)}{5G_1(3K + 4G_1)}, \tag{4.33}$$

$$\beta^{HS^+} = \frac{3(K + 2G_2)}{5G_2(3K + 4G_2)}. \tag{4.34}$$

In (4.33) and (4.34), two important quantities related with cubic crystals were invoked, namely, the shear moduli G_1 and G_2. These quantities are related with the resistance of cubic crystals to shearing stresses applied across particular planes in specific directions: G_1 represents the resistance to a shearing stress applied across the (110) plane in the $[1\bar{1}0]$[4] direction, while G_2 establishes the resistance to shear across the (100) plane in the [010] direction. In such case, we have

$$G_1 = \frac{\mathsf{C}_{11} - \mathsf{C}_{12}}{2}, \tag{4.35}$$

$$G_2 = \mathsf{C}_{44}. \tag{4.36}$$

The values of the shear moduli G_1 and G_2 are related with the elastic anisotropy of cubic crystals as we may see in Section 4.4.

4.3.3 High-Order Bounds and Self-Consistent Estimate

The idea of Hashin and Shtrikman (1962) of producing tighter bounds was extended by Zeller and Dederichs (1973) and Kröner (1977) who (respectively) derived expres-

[4]The bar indicates that one of the integers used in the linear combination of the lattice parameters is negative (in this case, and according to (4.1), $u = -1$).

sions for all odd- and even-order bounds. It happens that when the order of the bounds is sufficiently high, they may coincide and a singular estimate – known as the *self-consistent* estimate – can be obtained. This self-consistent estimate embodies, theoretically speaking, the most accurate analytical prediction, as it ensures compatibility of the strain and the stress fields over the whole aggregate. For single-phase polycrystals with cubic crystals, we may write the following third degree polynomial equation whose positive root establishes the self-consistent estimate for the shear modulus (Friák et al., 2012):

$$a_3^{\mathrm{SC}}(G^{\mathrm{SC}})^3 + a_2^{\mathrm{SC}}(G^{\mathrm{SC}})^2 + a_1^{\mathrm{SC}}(G^{\mathrm{SC}}) + a_0^{\mathrm{SC}} = 0, \quad (G^{SC}) > 0, \tag{4.37}$$

where the coefficients of the polynomial expression (4.37) are defined as follows:

$$a_3^{\mathrm{SC}} = 8, \tag{4.38}$$
$$a_2^{\mathrm{SC}} = 9K + 4G_1, \tag{4.39}$$
$$a_1^{\mathrm{SC}} = -3G_2(K + 4G_1), \tag{4.40}$$
$$a_0^{\mathrm{SC}} = -6KG_2G_1. \tag{4.41}$$

Schematically, we can relate the analytical estimates reviewed before as follows[5]:

$$G^{\mathrm{R}} \leqslant G^{\mathrm{HS}^-} \leqslant ... \leqslant G^{\mathrm{SC}} \leqslant ... \leqslant G^{\mathrm{HS}^+} \leqslant G^{\mathrm{V}}. \tag{4.42}$$

We must remark that equation (4.42) would still be valid, even if we were dealing with a different elastic parameter. This is verified in Table 4.5, where analytical estimates of the Young's modulus are presented (the values considered to the elastic constants of the constituent single-crystals are the ones shown in Table 4.4). They provide a comparative analytical ground for the numerical studies reported in Chapter 5.

Table 4.5: Analytical estimates of the Young's Modulus for polycrystalline aggregates encompassing a large number of small and randomly oriented cubic grains (all values expressed in $\mathrm{GN/m^2}$).

	Material	E^{R}	E^{HS^-}	E^{SC}	E^{HS^+}	E^{V}
fcc	Ag	70.9	79.6	82.6	84.3	91.4
	Al	70.1	70.4	70.4	70.4	70.7
	Au	68.4	76.7	79.4	80.9	87.0
	Cu	109.4	124.0	129.4	132.4	144.7
	Ni	203.7	220.3	224.6	227.3	241.7
	Pb	18.9	22.8	24.7	25.8	28.9
bcc	Fe	194.5	208.8	212.4	214.6	227.1
	W	409.8	409.8	409.8	409.8	409.8

[5]Hill estimate was not incorporated as it may be larger or smaller than the self-consistent estimate. Moreover, analytical bounds of a order higher than the second were generically represented by "...".

4.4 Elastic Anisotropy of Single-Crystals

We have already made clear that three independent elastic parameters are required to define the elastic response of cubic crystals. In reality, these three independent elastic constants are related with the three basic, independent modes of elastic deformation which were identified by Cottrell (1964): dilatation by a hydrostatic stress (first mode), shear on a cubic face in the direction of an axis (second mode) and shear across a plane rotated 45 degrees about a crystal axis $\boldsymbol{a}$ in a direction which makes -45 degrees with the crystal axis $\boldsymbol{a}$ (third mode). It is interesting to note that all these deformation modes are associated with a specific elastic parameter, namely, the bulk modulus K (first mode), the shear moduli G_2 (second mode) and the shear moduli G_1 (third mode). As we have discussed in Section 4.3, the bulk modulus is isotropic and the shear moduli G_1 and G_2 differ. Based on these two starting points, Zener and Siegel (1949) proposed an *anisotropy factor* which quantified the ratio between the shear moduli G_2 and G_1. This quantity is known as the *Zener anisotropy index* and it embodies the first measure elaborated to determine the orientation dependence of the elastic moduli. Since then, other (more complex and universal) anisotropy indexes were developed with the objective of quantifying how directionally dependent the elastic properties of a crystal are.

We should be aware that, fundamentally, all crystals are elastically anisotropic (Chung and Buessem, 1967). Moreover, it is important to realize that the anisotropy exhibited by polycrystalline aggregates results from two main sources: the elastic anisotropy of the constituent crystal (crystallographic anisotropy) and the anisotropy which results from the texture of the polycrystal (morphological anisotropy) (Jöchen, 2013; Kocks et al., 2000). Since we are interested in predicting the elastic response of textureless polycrystals, it becomes obvious that their elastic anisotropy outcomes exclusively from the elastic anisotropy of the constituent crystal. To put it differently, if the constituent crystal is elastically isotropic, the response of the aggregate will also be isotropic, regardless of the number of grains. In this dissertation, since we are interested in phenomena (elastic and yielding response of polycrystalline aggregates) massively influenced by the crystalline anisotropy, it is of paramount concern being able to quantify the extent of anisotropy.

This Section covers the most relevant measures of the elastic anisotropy of single-crystals. We must draw attention to the fact that the early proposals of Zener and Siegel (1949) and Chung and Buessem (1967) (respectively, treated in Sections 4.4.1 and 4.4.2) are pertinent only for cubic crystals, whereas the indexes developed by Ledbetter and Migliori (2006), Ranganathan and Ostoja-Starzewski (2008b) and Kube (2016) (Sections 4.4.3 to 4.4.5) are universal, in such a way that they are applicable to all seven crystal symmetries (some authors postulate that the index proposed by Ledbetter and Migliori (2006) cannot be used with non-cubic crystals, although the original article stated otherwise). Moreover, it is important to

mention that the discussion of the elastic anisotropy of crystalline materials had to be preceded by the presentation of the analytical methods made in Section 4.3, as some of those methods (especially Voigt and Reuss models) provide estimates to the elastic properties that are used to quantify the elastic anisotropy. Nonetheless, we must also notice that the elastic anisotropy of the constituent crystals influences the analytical predictions of the polycrystalline elastic properties: for instance, when the crystals within the aggregate are isotropic, the Voigt and Reuss estimates coincide.

4.4.1 Zener Anisotropy Index

As we mentioned before, Zener and Siegel (1949) established that the elastic anisotropy of cubic crystallites could be extracted from the ratio between the shear moduli G_1 and G_2:

$$A^{\mathrm{Z}} = \frac{G_2}{G_1}, \tag{4.43}$$

where A^{Z} is the *Zener anisotropy factor*. Taking into consideration equations (4.19), (4.35) and (4.36), we can, therefore, define an expression for the elastic constant C_{44} of cubic crystals:

$$\mathsf{C}_{44} = \frac{A^{\mathrm{Z}}(\mathsf{C}_{11} - \mathsf{C}_{12})}{2}, \tag{4.44}$$

so that when $A^{\mathrm{Z}} = 1$, we retrieve (4.19). In other words, the Zener anisotropy factor yields unity when the crystal has infinite planes of elastic symmetry and it is greater or smaller than unity when the crystal is anisotropic. Note that bigger deviations from unity (regardless of whether $A^{\mathrm{Z}} > 1$ or $A^{\mathrm{Z}} < 1$) entail an increase in the level of anisotropy.

Despite being widely known and applied in many contexts, this anisotropy measure has some recognised downsides: firstly, it is only applicable to cubic crystals; secondly, it has a non-unique nature, as we could have used $(A^{\mathrm{Z}})^{-1}$ to quantify anisotropy (Ranganathan and Ostoja-Starzewski, 2008b) and, finally, values smaller or greater than $A^{\mathrm{Z}} = 1$ are admissible to quantify anisotropy[6].

4.4.2 Chung-Buessem Anisotropy Index

Chung and Buessem (1967) suggested that the difference between Voigt and Reuss estimates of the elastic properties of polycrystalline aggregates was related to the elastic anisotropy of the constituent crystal. In accordance with that idea, the *anisotropy factor of Chung-Buessem* A^{CB} was proposed:

$$A^{\mathrm{CB}} = \frac{(G^{\mathrm{V}} - G^{\mathrm{R}})}{2G^{\text{H-a}}}. \tag{4.45}$$

[6]This is generally reported as a major disadvantage of the anisotropy measure proposed by Zener, even though it justifies the shape of the graphical representation of $E(\boldsymbol{d})$ of cubic crystallites (see Section 5.1.1.1).

Note that within aggregates comprising isotropic crystals both strain and stress fields are uniform (so that Voigt (1910) and Reuss (1929) assumptions are true); in that situation, both Voigt and Reuss estimates coincide and $A^{\mathrm{CB}} = 0$. Moreover, since $G^{\mathrm{V}} \geqslant G^{\mathrm{R}}$ (Hill model), the Chung-Buessem anisoropy factor is always greater than or equal to zero (regardless of whether $A^{\mathrm{Z}} < 1$ or $A^{\mathrm{Z}} > 1$). These conclusions can also be drawn from the following equation, which presents the relation between A^{Z} and A^{CB}:

$$A^{\mathrm{CB}} = \frac{3\,(A^{\mathrm{Z}} - 1)^2}{3\,(A^{\mathrm{Z}} - 1)^2 + 25\,A^{\mathrm{Z}}}. \tag{4.46}$$

In short, the Chung-Buessem anisotropy factor overcomes one of the shortcomings associated with the Zener anisotropy index, as it is always positive. Nonetheless, it can only be used to quantify the elastic anisotropy of cubic crystals and it is empirically motivated (Ranganathan and Ostoja-Starzewski, 2008b).

4.4.3 Ledbetter-Migliori Anisotropy Index

Ledbetter and Migliori (2006) advocated that the ratio of the maximum and minimum shear sound-wave velocities among all propagation and polarization directions (respectively v_{max} and v_{min}) could be used to quantify the elastic anisotropy of crystallites, so that they defined *Ledbetter-Migliori anisotropy index* as follows:

$$A^{\mathrm{LM}} = \left(\frac{v_{max}}{v_{min}}\right)^2. \tag{4.47}$$

Although Ledbetter and Migliori (2006) claimed that (4.47) could be used with crystals of any lattice type, several authors argue otherwise. Amongst the critics, we highlight Kube (2016), who indicated that the influence of the bulk modulus to the anisotropy (which must be taken into account for non-cubic crystals) was not considered, and Ranganathan and Ostoja-Starzewski (2008b) who questioned the non-unique nature of (4.47) (for instance, they affirmed that Ledbetter and Migliori (2006) could have defined $(A^{\mathrm{LM}})^{-1}$ as the Ledbetter-Migliori anisotropy index instead of (A^{LM})).

4.4.4 Universal Elastic Anisotropy Index

In contrast with all the measures reviewed in previous Sections, Ranganathan and Ostoja-Starzewski (2008b) developed a *universal elastic anisotropy index* (denoted A^{U}) which accounts for the contribution of both the shear and the bulk modulus. Consequently, this universal anisotropy index is arguably applicable to quantify the anisotropy of any type of crystalline system. Besides this, it also overcomes the non-uniqueness dilemma, as it constitutes a scalar parameter based on the double contraction of the elasticity tensor of Voigt (1910) and the compliance tensor of Reuss (1929); in fact, Ranganathan and Ostoja-Starzewski (2008b) verified that this

scalar-parameter yielded a minimum value of 6 when both models are valid (i.e., when the crystallites are isotropic), so that A^{U} was defined in order to make its minimum be null in the case of isotropy:

$$A^{\mathrm{U}} = \mathbf{C}^{\mathrm{V}} : \mathbf{S}^{\mathrm{R}} - 6. \tag{4.48}$$

Both stiffness and compliance tensors of isotropic materials may be expressed in terms of the corresponding isotropic shear and bulk modulus[7]:

$$\mathbf{C} = 2G\,\mathbf{I}_d + K\,\boldsymbol{I}\otimes\boldsymbol{I}, \tag{4.51}$$

$$\mathbf{S} = \frac{1}{2G}\,\mathbf{I}_d + \frac{1}{K}\,\boldsymbol{I}\otimes\boldsymbol{I}. \tag{4.52}$$

In that case, it can be proved (Ranganathan and Ostoja-Starzewski, 2008b) that equation (4.48) may be replaced by the next expression:

$$A^{\mathrm{U}} = 5\,\frac{G^{\mathrm{V}}}{G^{\mathrm{R}}} + \frac{K^{\mathrm{V}}}{K^{\mathrm{R}}} - 6. \tag{4.53}$$

Note that, similarly to the Chung-Buessem anisotropy index, the universal anisotropy index is always positive. Moreover, it is noteworthy to mention that the universal anisotropy index is based on the fractional difference between the first-order bounds on the bulk and the shear modulus, so that larger fractional differences entail stronger degrees of anisotropy. Finally, a parallel can be drawn between this index and the Zener and the Chung-Buessem anisotropy factors (in that case we shall consider that $K^{\mathrm{V}} = K^{\mathrm{R}}$):

$$A^{\mathrm{U}} = \frac{6}{5}\left(\sqrt{A^{\mathrm{Z}}} - \frac{1}{\sqrt{A^{\mathrm{Z}}}}\right)^2, \tag{4.54}$$

$$A^{\mathrm{U}} = 10\left(\frac{A^{\mathrm{CB}}}{1 - A^{\mathrm{CB}}}\right). \tag{4.55}$$

The presented expressions clearly show the non-unique nature of A^{Z} (the same results would be obtained if the referred index was replaced by its inverse) and that the Chung-Buessem anisotropy factor predicts much lower values for the elastic anisotropy than other measures (Ranganathan and Ostoja-Starzewski, 2008b).

[7] $\mathbf{I}_d$ is the deviatoric projection tensor given by:

$$\mathbf{I}_d = \mathbf{I}_S - \frac{1}{3}\boldsymbol{I}\otimes\boldsymbol{I}, \tag{4.49}$$

where $\mathbf{I}_S$ denotes the fourth-order symmetric identity tensor; in index notation, this tensor reads:

$$\mathbf{I}_{ijkl} = \frac{1}{2}(\delta_{ik}\delta_{jl} + \delta_{il}\delta_{jk}). \tag{4.50}$$

4.4.5 Universal Log-Euclidean Anisotropy Index

Ranganathan and Ostoja-Starzewski (2008b) filled an important gap in the literature by elaborating an anisotropy measure which is valid regardless of the symmetry of the crystal. Despite this, their universal index is a relative measure of anisotropy, inasmuch as a crystal having $A^{\mathrm{U}} = 3$ is not necessarily twice as anisotropic as another with $A^{\mathrm{U}} = 1.5$ (Kube, 2016). In order to overcome the highlighted downside, Kube (2016) formulated a *universal log-Euclidean anisotropy index* (denoted A^{L}) which provides an absolute measure of anisotropy valid for all crystalline systems. This log-Euclidean anisotropy index is conceptually similar to the universal anisotropy index, but it is based on a absolute distance in the log-Euclidean space applied to the elasticity tensors of Voigt and Reuss – this distance is defined as:

$$d^L(\mathbf{C}^V, \mathbf{C}^R) = ||\ln(\mathbf{C}^V) - \ln(\mathbf{C}^R)||. \tag{4.56}$$

Considering equation (4.51) and scaling the log-Euclidean distance d^L, so that the universal log-Euclidean anisotropy factor yields zero in the case of isotropic crystals, Kube (2016) reached the following expression for A^{L}:

$$A^{\mathrm{L}} = \sqrt{5\left[\ln\left(\frac{G^{\mathrm{V}}}{G^{\mathrm{R}}}\right)\right]^2 + \left[\ln\left(\frac{K^{\mathrm{V}}}{K^{\mathrm{R}}}\right)\right]^2}. \tag{4.57}$$

We must remark that equation (4.57) is valid for the general case of a triclinic crystalline system, in which 21 elastic constants have to be considered in order to obtain A^{L}. With this in mind, Kube (2016) developed a general `Matlab®` function which returns the universal log-Euclidean anisotropy index from the 21 elastic (perchance independent) parameters of a crystalline material. Moreover, he used the referred function to calculate the anisotropy of 2176 crystal compounds, so that the anisotropies of crystals with different symmetries can be easily compared. In this context, it is interesting to mention the work of Kube and de Jong (2016), who compared the average of the Voigt and Reuss estimates (Hill estimate) with the self-consistent value for the referred 2176 crystalline materials and concluded that they are generally further away when the elastic anisotropy increases (this is substantiated by Table 4.5, taking into consideration the anisotropy factors shown in Table 4.6).

For the particular case of cubic crystals, the universal log-Euclidean anisotropy index can be related to the previously discussed measures of elastic anisotropy using the following expressions:

$$A^{\mathrm{L}} = \sqrt{5}\left[\ln\left(\frac{(2+3\,A^{\mathrm{Z}})(3+2\,A^{\mathrm{Z}})}{25\,A^{\mathrm{Z}}}\right)\right], \tag{4.58}$$

$$A^{\mathrm{L}} = \sqrt{5}\ln\left(\frac{1+A^{\mathrm{CB}}}{1-A^{\mathrm{CB}}}\right), \tag{4.59}$$

$$A^{\mathrm{L}} = \sqrt{5}\ln\left(1 + \frac{A^{\mathrm{U}}}{5}\right). \tag{4.60}$$

In Table 4.6 we present the values of elastic anisotropy of several cubic crystals (the values considered to the elastic constants of the constituent single-crystals are the ones shown in Table 4.4 and due to the fact that the Ledbetter-Migliori anisotropy index is not obtained from these constants, we decided not to incorporate this index).

Given all the points discussed previously, in this work, we decided to quantify the elastic anisotropy of the crystallites by means of the universal log-Euclidean anisotropy index, as it can be used to deal with all crystalline systems and because it provides an absolute measure of anisotropy (so it is straightforward to determine the relations between the anisotropy of two distinct crystalline materials). We must remark, however, that previous studies performed to estimate the elastic and yielding response of polycrystalline aggregates comprising cubic crystals typically used the Zener anisotropy factor (for instance, we may refer the studies of Ranganathan and Ostoja-Starzewski (2008a) and Brenner et al. (2009)).

Table 4.6: Anisotropies of cubic crystals quantified using the Zener, the Chung-Buessem, the universal and the log-Euclidean universal anisotropy indexes.

	Material	A^{Z}	A^{CB}	A^{U}	A^{L}
fcc	Ag	3.013	0.139	1.614	0.626
	Al	1.220	0.005	0.048	0.021
	Au	2.852	0.126	1.443	0.567
	Cu	3.209	0.154	1.824	0.696
	Ni	2.514	0.097	1.094	0.443
	Pb	4.139	0.222	2.857	1.011
bcc	Fe	2.407	0.090	0.987	0.403
	W	1.011	0.000	0.000	0.000

4.5 Numerical Multi-Scale Framework to Characterize the Elastic Response of Polycrystalline Aggregates

As mentioned in Section 3.2.8, the macroscopic constitutive response of a generic material may be derived from micro-scales studies in case the homogenisation theory is applied. Based on this principle, we have directed our attention towards the characterization (through numerical microscopic studies) of the elastic response of polycrystalline aggregates comprising small and randomly oriented cubic crystals. Note that, since we have not made any simplifications regarding the possible elastic symmetries of the aggregates, 21 elastic parameters have to be defined in order to describe their elastic response.

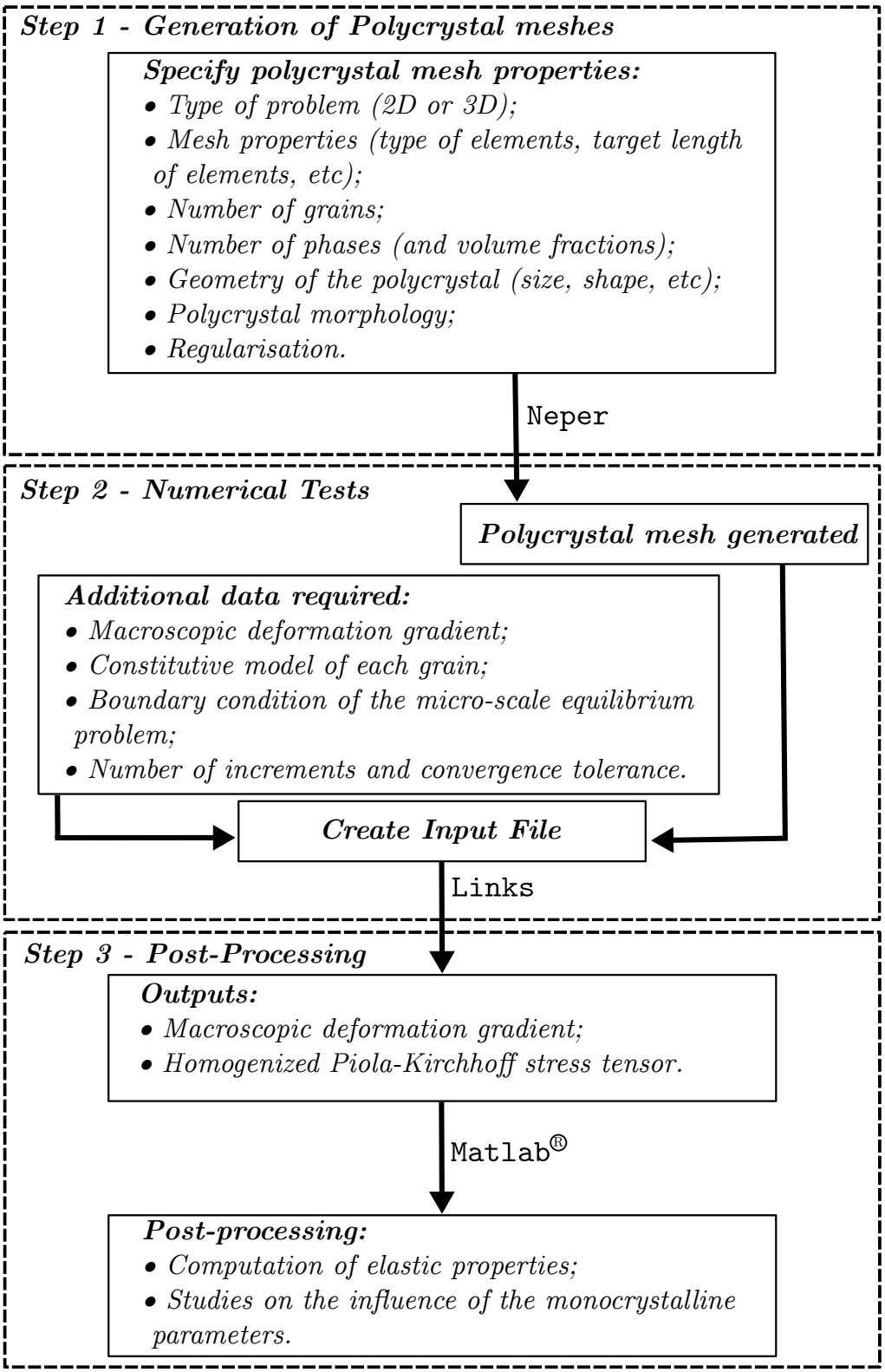

Figure 4.5: Numerical multi-scale scheme associated with the determination of the macroscopic constitutive response of cubic crystal aggregates.

In summary, three main stages may be identified: the generation of the polycrystalline meshes to be analysed (step one); the numerical tests conducted in each of the specimens generated (step two) and the post-processing of the numerical results (step three), which involves not only the computation of the 21 elastic constants associated with a specific polycrystal, but also the identification of the critical microscopic parameters and the inference of relations that influence the macroscopic behaviour. The general diagram related with the mentioned numerical multi-scale framework can be seen in Figure 4.5, while the description of each one of the stages is made in Sections 4.5.1 to 4.5.3.

4.5.1 Polycrystal Generation

In order to generate polycrystal meshes (that can be analysed using the FEM), the free open-source software package `Neper`, developed by Quey et al. (2011), was used. Since `Neper` is highly versatile, in this Section we only focus on the generation and meshing of the single-phase randomly oriented crystal aggregates analysed in subsequent Chapters[8].

The generation of polycrystal meshes includes two main steps, namely, the generation of the polycrystal morphology and its subsequent meshing. Regarding the generation of the morphology, `Neper` may represent the microstructures of single-phase textureless polycrystals as *Poisson-Voronoi mosaics* (also called *Poisson-Voronoi tessellations*). In short, a Poisson-Voronoi tessellation of a polycrystal is mostly a set of grains with polyhedral shape which is obtained from a theoretical recrystallization process in which all the crystals start to grow isotropically from randomly distributed points at the same time (Jöchen, 2013; Quey et al., 2011). This idealisation of crystal growth motivates the development of grain boundaries exactly at the bisector of the distance between two initial crystal nuclei (Jöchen, 2013; Quey et al., 2011). Albeit there are some recognised shortcomings of modelling the polycrystals as Poisson-Voronoi mosaics, these are widely accepted and used. Nonetheless, the meshing of Poisson-Voronoi mosaics provides several challenges, as they may incorporate a large number of small faces and edges at the intersection of the polyhedra – consequently, a high degree of refinement is required to assure convergence (Quey et al., 2011). In order to avoid overly refined meshes, a process of *regularisation* was implemented in `Neper` and, as a result, standard or regularised Poisson-Voronoi tessellations can be produced – the main concept of regularisation is to remove the small length entities (faces and edges), so that the target length of the mesh elements can be increased (Quey et al., 2011). After Poisson-Voronoi tessellations are generated, two main meshing procedures can be applied: *structured* and *unstructured meshing*. In Figure 4.6, structured and unstructured meshes with two different levels of mesh refinement are shown, so the following aspects might be observed:

[8]In this Section, we are not interested in describing the functionalities of `Neper` – to gain insight into its use, we suggest referring to its reference manual (Quey, 2018).

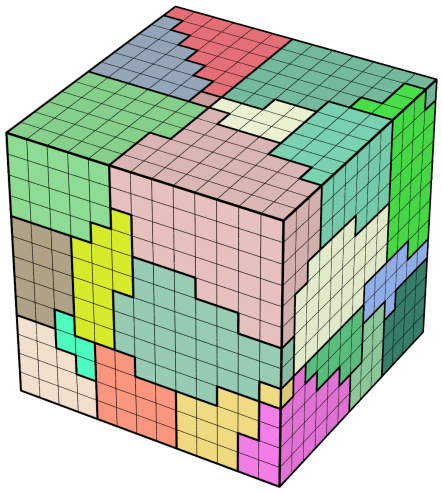

(a) Structured mesh with 2197 elements.

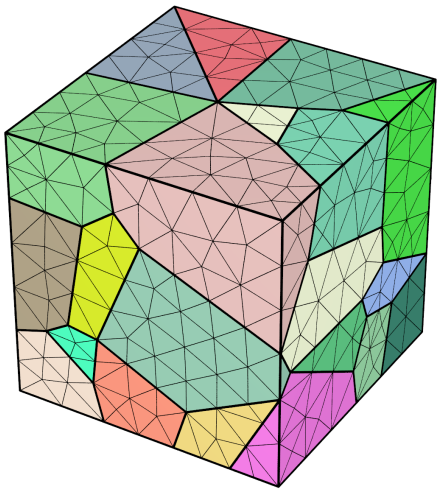

(b) Unstructured mesh with 2997 elements.

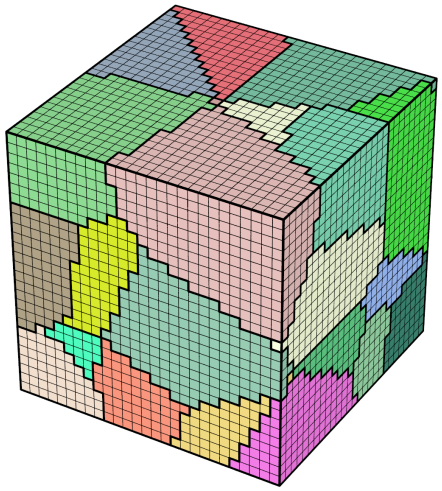

(c) Structured mesh with 19683 elements.

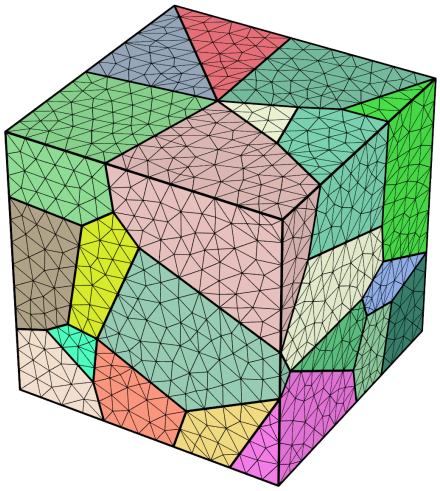

(d) Unstructured mesh with 17618 elements.

Figure 4.6: Polycrystal structured and unstructured meshes of the same polycrystal morphology comprising 25 grains (different levels of mesh refinement are represented). All polycrystal meshes were obtained with `Neper`.

- The main advantage of unstructured meshing relies on the fact that the grain boundaries and the mesh topology coincide (Fritzen et al., 2009; Jöchen, 2013). On the other hand, and recalling the discussion made in Section 3.2.7.3, periodic mesh topologies are difficult to obtain with unstructured meshes, so that alternative boundary models (uniform traction or linear) are generally employed and, as a result, the required RVE size to obtain a solution of a given quality is increased (consequently, more computational effort is required);

- The alternative meshing technique (structured meshing) involves block grid-structures, so that the grain boundaries do not match the element boundaries; hence, it is difficult to obtain accurate representations of the field variables (e.g., stresses and strains) at the grain boundaries and we must note that grid density affects both the accuracy of the method and the resolution of the boundaries (Fritzen et al., 2009; Jöchen, 2013).

In this work, we have used only structured meshes involving *F-bar eight-noded hexahedra* (only 3D analyses were considered). This is because structured meshes with periodic topologies can be easily obtained and, as a result, a meaningful reduction of the computational resources needed can be achieved. However, since the field variables at the grain boundaries are not accurately represented, the impact of adopting this meshing technique has to be considered – this issue is discussed with particular detail in Sections 5.1.3 and 5.2.2.

4.5.2 Numerical Tests to Obtain Homogenised Properties

After generating the polycrystal meshes with `Neper`, numerical tests were performed using `Links`, the in-house program addressed in Section 3.3.1. Given that the main features of `Links` have already been introduced, in this Section we will outline the numerical tests that have to be performed in order to extract the homogenised/macroscopic elastic properties of the polycrystalline aggregates.

A key point to mention involves the constitutive model associated with each grain. In fact, the hyperelastic Saint-Venant Kirchhoff law was used:

$$\boldsymbol{S} = \mathbf{C} : \boldsymbol{E}^{(2)}. \tag{4.61}$$

It must be noted that this law was employed due to the fact that it was part of the constitutive model available in `Links`[9]. Nonetheless, what is important to mention is that the whole framework presented in Section 4.2 is still applicable. In fact, the Saint-Venant Kirchhoff hyperelastic law can be seen as extension of the generalized Hooke's law to cope with large strains, inasmuch as it establishes a linear relation between the second Piola-Kirchhoff stress tensor $\boldsymbol{S}$ and the Green-Lagrange strain tensor $\boldsymbol{E}^{(2)}$. After all, equation (4.61) can be written in a matrix basis – adopting Voigt notation, we get:

$$\begin{Bmatrix} S_1 \\ S_2 \\ S_3 \\ S_4 \\ S_5 \\ S_6 \end{Bmatrix} = \begin{bmatrix} \mathsf{C}_{11} & \mathsf{C}_{12} & \mathsf{C}_{13} & \mathsf{C}_{14} & \mathsf{C}_{15} & \mathsf{C}_{16} \\ & \mathsf{C}_{22} & \mathsf{C}_{23} & \mathsf{C}_{24} & \mathsf{C}_{25} & \mathsf{C}_{26} \\ & & \mathsf{C}_{33} & \mathsf{C}_{34} & \mathsf{C}_{35} & \mathsf{C}_{36} \\ & & & \mathsf{C}_{44} & \mathsf{C}_{45} & \mathsf{C}_{46} \\ & & & & \mathsf{C}_{55} & \mathsf{C}_{56} \\ \text{sym.} & & & & & \mathsf{C}_{66} \end{bmatrix} \begin{Bmatrix} E_1^{(2)} \\ E_2^{(2)} \\ E_3^{(2)} \\ E_4^{(2)} \\ E_5^{(2)} \\ E_6^{(2)} \end{Bmatrix}. \tag{4.62}$$

[9] The full description of model is delayed to Section 6.1.

In light of (4.62), 21 elastic constants have to be defined to characterize the elastic macroscopic response. In order to obtain each of these constants, different deformation gradients must be prescribed, each ensuring that only one component of the Green-Lagrange strain tensor is non-zero. To be more precise, six different microscopic analyses, each associated with a deformation gradient that yields only one non-zero component of the Green-Lagrange strain tensor, have to be made, so that each one of those analyses provides a column of the stiffness matrix. As an example, in case the only non-null component of the strain tensor is $E_1^{(2)}$, we may obtain the elastic components belonging to the first column of the elasticity matrix:

$$\mathsf{C}_{i1} = \frac{S_i}{E_1^{(2)}}, \quad i = 1, 2, 3, 4, 5, 6. \tag{4.63}$$

In order to delineate what specific deformation gradients should be prescribed to the microscopic cells, we must notice that the combination of equations (2.30), (2.37) and (2.42) leads to:

$$\boldsymbol{\varepsilon} \approx \boldsymbol{E}^{(2)} = \frac{1}{2}(\boldsymbol{F}^T\boldsymbol{F} - \boldsymbol{I}). \tag{4.64}$$

Another important point involves the spectral decomposition of $\boldsymbol{E}^{(2)}$:

$$\boldsymbol{E}^{(2)} = \sum_{i=1}^{3} \lambda_i^{\boldsymbol{E}^{(2)}}\, \boldsymbol{l}_i^{\boldsymbol{E}^{(2)}} \otimes \boldsymbol{l}_i^{\boldsymbol{E}^{(2)}}, \tag{4.65}$$

where $\lambda_i^{\boldsymbol{E}^{(2)}}$ and $\boldsymbol{l}_i^{\boldsymbol{E}^{(2)}}$ are, respectively, the eigenvalues and the eigenvectors of $\boldsymbol{E}^{(2)}$. Note that the eigenvalues $\lambda_i^{\boldsymbol{E}^{(2)}}$ are the roots of the following polynomial equation:

$$\det(\boldsymbol{E}^{(2)} - \lambda_i^{\boldsymbol{E}^{(2)}}\boldsymbol{I}) = 0, \tag{4.66}$$

while the eigenvectors result from the resolution of equation (4.67).

$$(\boldsymbol{E}^{(2)} - \lambda_i^{\boldsymbol{E}^{(2)}}\boldsymbol{I})\boldsymbol{l}_i^{\boldsymbol{E}^{(2)}} = 0, \quad i = 1, 2, 3. \tag{4.67}$$

Rearranging (4.64), we have:

$$\boldsymbol{F}^T\boldsymbol{F} = 2\,\boldsymbol{E}^{(2)} + \boldsymbol{I}, \tag{4.68}$$

and taking (4.65) into consideration, we can obtain the eigenvalues of the deformation gradient (denoted $\lambda_i^{\boldsymbol{F}}$)[10]:

$$\lambda_i^{\boldsymbol{F}} = \sqrt{2\,\lambda_i^{\boldsymbol{E}^{(2)}} + 1}, \quad i = 1, 2, 3. \tag{4.69}$$

In such case, we can express the deformation gradient as follows:

$$\boldsymbol{F} = \psi \begin{bmatrix} \lambda_1^{\boldsymbol{F}} & 0 & 0 \\ 0 & \lambda_2^{\boldsymbol{F}} & 0 \\ 0 & 0 & \lambda_3^{\boldsymbol{F}} \end{bmatrix} \psi^T \tag{4.70}$$

[10]Note that this implies that we are dealing with symmetric deformation gradients.

where ψ is the matrix whose columns are the eigenvectors of the Green-Lagrange strain tensor.

All things considered, and admitting that the non-null components of the strain tensor are equal to 10^{-5} (just 1 increment is considered), the 6 deformation gradients that must be prescribed to the polycrystal meshes are listed in Table 4.7 – note that we could have chosen another value for the non-null components of the Green-Lagrange strain tensor, since the only requirement was to ensure a small level of strain.

Table 4.7: Deformation gradients prescribed[a] to the polycrystal meshes, so that their elastic response can be determined.

$\boldsymbol{E}^{(2)}$	$\boldsymbol{F}$
$\begin{bmatrix} 1 & 0 & 0 \\ 0 & 0 & 0 \\ 0 & 0 & 0 \end{bmatrix} \cdot 10^{-5}$	$\begin{bmatrix} 1.000001 & 0 & 0 \\ 0 & 1 & 0 \\ 0 & 0 & 1 \end{bmatrix}$
$\begin{bmatrix} 0 & 0 & 0 \\ 0 & 1 & 0 \\ 0 & 0 & 0 \end{bmatrix} \cdot 10^{-5}$	$\begin{bmatrix} 1 & 0 & 0 \\ 0 & 1.000001 & 0 \\ 0 & 0 & 1 \end{bmatrix}$
$\begin{bmatrix} 0 & 0 & 0 \\ 0 & 0 & 0 \\ 0 & 0 & 1 \end{bmatrix} \cdot 10^{-5}$	$\begin{bmatrix} 1 & 0 & 0 \\ 0 & 1 & 0 \\ 0 & 0 & 1.000001 \end{bmatrix}$
$\begin{bmatrix} 0 & 0 & 0 \\ 0 & 0 & 1 \\ 0 & 1 & 0 \end{bmatrix} \cdot 10^{-5}$	$\begin{bmatrix} 1 & 0 & 0 \\ 0 & 1 & 0.00001 \\ 0 & 0.00001 & 1 \end{bmatrix}$
$\begin{bmatrix} 0 & 0 & 1 \\ 0 & 0 & 0 \\ 1 & 0 & 0 \end{bmatrix} \cdot 10^{-5}$	$\begin{bmatrix} 1 & 0 & 0.00001 \\ 0 & 1 & 0 \\ 0.00001 & 0 & 1 \end{bmatrix}$
$\begin{bmatrix} 0 & 1 & 0 \\ 1 & 0 & 0 \\ 0 & 0 & 0 \end{bmatrix} \cdot 10^{-5}$	$\begin{bmatrix} 1 & 0 & 0 \\ 0 & 1 & 0.00001 \\ 0 & 0.00001 & 1 \end{bmatrix}$

[a] In the numerical simulations, the deformation gradients prescribed to the micro-cells were rounded to 16 decimal places.

4.5.3 Post-Processing

In the previous Section we have presented the deformation gradients that must be prescribed to the polycrystal meshes in order to compute their elastic properties. Nonetheless, these are not calculated directly by `Links`. In reality, `Links` computes the homogenized Piola-Kirchhoff stress tensor, from which, using equations (2.61) and (2.67), we may obtain the homogenized Second Piola-Kirchhoff stress tensor and, consequently, by means of the Saint-Venant Kirchhoff law, extract the elastic properties. The calculation of the elastic properties associated with a specific polycrystal mesh, along with all the manipulation of the numerical results generated with `Links`, was performed using `Matlab`®. As a matter of fact, we must draw attention to the fact that complex post-processing was involved in this work, since we have to developed a significant number of `Matlab`® routines which make it possible to move from the prescribed deformation gradient and the homogenized Piola-Kirchhoff stress tensor (output of `Links`) to the graphical (and non-graphical) results presented in Chapter 5. Almost all of these scripts were designed from scratch, albeit we have also incorporated routines mentioned in Nordmann et al. (2018), Kube (2016) and Vieira de Carvalho (2016).

To sum up, the post-processing step includes two main stages: the determination of the elastic properties of the microscopic cells (which calibrate the constitutive law for the specific cases being analysed) and the inference of critical relations (which might calibrate the constitutive law for cases that have not been analysed). While the first stage is straightforward, the second one is much more complex and requires several numerical tests to be performed, so that general tendencies can be identified and explained based on specific microscopic parameters. In order to infer these critical relations, it is crucial to realize that the global behaviour of polycrystals is mainly controlled by the distribution of grain orientations and by the single-crystal behaviour. Since we are dealing with randomly oriented aggregates, we expect that, when the number of grains is sufficiently large, the elastic parameters of the crystals (or any other quantity that results from their combination, such as the elastic anisotropy) become the most important factors. That being said, in Chapter 5, we fundamentally studied the influence of the monocrystalline parameters on the elastic response of polycrystalline aggregates.

Before going further, it is important to explicitly refer the possible advantages of following these type of numerical multi-scale schemes in relation to the conventional analytical methods. In fact, it may be argued that some analytical methods (like the ones presented in Section 4.3) have already established the connection between the elastic constants of polycrystals and those of their constituent crystals. However, it must not be forgotten that these analytical methods are solely applicable to isotropic aggregates, whilst general numerical procedures (like the one presented here) can be used with both isotropic and anisotropic aggregates. Moreover, we must realize that the most accurate analytical methods (for example, the self-consistent

model) yield complex expressions for the elastic constants of isotropic polycrystals comprising non-cubic crystallites; on the contrary, the expansion of our procedure to analyse other types of polycrystals (for instance, incorporating crystals with base-centered hexagonal Bravais lattices) is straightforward. Equally important, even in the case of cubic-crystal isotropic aggregates, analytical methods provide no answer to relevant issues such as the number of grains that an aggregate must include in order to be isotropic; again, our methodology might clarify this topic. All things considered, microscopic analyses based on computational homogenisation might shed light into open questions concerning the description of the constitutive behaviour of cubic crystal aggregates. In the long run, these schemes might also be employed to characterize novel (more advanced) materials, so that experimental procedures can be reduced and the whole manufacturing process accelerated and optimized.

Chapter 5

Influence of the Monocrystalline Parameters on the Elastic Response of Polycrystalline Aggregates

In Chapter 4, we have described a numerical procedure that can be employed to determine the elastic properties of polycrystalline aggregates. Even though it can be applied to establish the elastic response of any polycrystalline aggregate, it is important to understand that it must be complemented with the recognition of the micro-scale variables that together lead to that behaviour. In other words, it is of paramount concern to understand what microscopic parameters influence the global response of the materials analysed, so that critical relations (linking the two scales) can be inferred. These critical relations may play a decisive role in optimising the design of materials, since they define what microstructural features should be valued in order to improve the macroscopic performance. In this Chapter, as we are focusing on single-phase aggregates encompassing randomly oriented cubic crystals, we expect that their global behaviour may be characterized considering solely the monocrystalline elastic parameters and, for that reason, we have placed our efforts on the development of laws that can quantify the influence of these microscopic parameters on the aggregates macroscopic response. In fact, we have conducted several studies to shed light into the following aspects:

1. The circumstances in which a polycrystal can be considered isotropic (i.e., the specification of the number of grains needed to obtain an isotropic response);
2. The determination of the elastic properties of isotropic polycrystals (that is, the definition of the value of one elastic property other than the bulk modulus);
3. The determination of the elastic properties of anisotropic polycrystals (which involves considering the 21 elastic constants that govern their behaviour).

Because most polycrystalline systems of interest are isotropic, the first two questions

assume pivotal importance and especially the second has received widespread attention in the past (see, for instance, Section 4.3). This justifies why our main focus was to study the minimum number of grains required to obtain isotropic responses. Indeed, not only is this issue far from being resolved, as it is also important for the characterisation of isotropic polycrystals and micro-components such as MEMS. In order to define the minimum size of the RVE for isotropic elastic polycrystals, a strategy which is based on the analysis of statistical measures of the spatial distribution of the Young's modulus has been developed considering several realisations of the same polycrystals. The mentioned strategy, which also allows the computation of the isotropic elastic parameters, is detailed in Section 5.1. In that Section, some preliminary studies, which attempt to quantify the influence of microscopic parameters on the homogenized elastic properties, are also reported, so that in Section 5.2 we are in condition to characterize the elastic response of isotropic polycrystals (responding to the first two topics identified in the list presented earlier). After that, in Section 5.3, the above referred strategy is adapted, making it possible to characterise the elastic response of anisotropic polycrystals – in particular, we derive bounds for the 21 elastic constants which depend only on the number of grains of the aggregates and on the monocrystalline parameters.

The work reported throughout this Chapter was often compared to previous studies. Besides the analytical estimates enumerated in the previous Chapter, we used as a basis of comparison the works of: Böhlke et al. (2010) who studied the spatial distribution of the Young's modulus for cubic crystal aggregates comprising a variable numbers of grains; of Fritzen et al. (2009) who examined the Young's modulus of isotropic periodic unstructured meshes; and finally of El Houdaigui et al. (2007); Ranganathan and Ostoja-Starzewski (2008a) and Nygårds (2003) who focused on the number of grains required to obtain an isotropic elastic behaviour.

5.1 Strategy and Initial Studies on the Characterisation of the Elastic Response of Polycrystals

When we are attempting to determine the elastic response of a textureless polycrystal, two situations may occur:

1. The number of grains is sufficiently large, so that the elastic response of the polycrystal is isotropic; in such cases, 2 elastic properties describe the whole elastic response of the specimen;
2. The number of grains is below the minimum required to obtain isotropic responses and, consequently, the aggregate is elastically anisotropic, i.e., 21 elastic constants are necessary to fully characterize its elastic response.

Provided that the number of grains for which the elastic response of polycrystals

can be considered isotropic is not well-established[1], a procedure which allows the determination of 21 elastic constants has to be employed when we intend to determine the elastic response of a generic polycrystal. The straightforward analysis of the 21 elastic constants calculated is not a practical way of characterising isotropic polycrystals, whose elastic response can be totally described by just 2 parameters. This explains why we have developed a strategy which mostly consists of condensing the information provided by the 21 elastic constants into two scalar parameters that can be used to integrally describe the elastic response of isotropic polycrystals (including the prediction of the number of grains necessary to obtain isotropic responses). The main idea behind this strategy is explained in Section 5.1.1, albeit the full comprehension of the method also requires reading Section 5.1.2. In addition, we must remark that even though the method is originally presented as a procedure that can be used to characterize isotropic polycrystals, in Section 5.3 it has been adapted to describe the elastic behaviour of anisotropic aggregates. All in all, it provides a basis for the analysis of the elastic response of isotropic and anisotropic polycrystalline materials. That being said, we must remark that this Section not only introduces the strategy used to characterize the elastic response of isotropic and anisotropic polycrystals, but it also summarises the initial studies that have been performed in order to understand the influence of the microscopic parameters on the macroscopic response. In particular, in Sections 5.1.3 and 5.1.4 the influence of the mesh and of the number of grains on the macroscopic elastic behaviour is studied with special emphasis being placed on the derivation of relations between the homogenized elastic parameters, the monocrystalline constants and the factors being studied (mesh and number of grains).

Before moving forward, we must realize that the procedure described in Section 5.1.1 involves the computation of the 21 elastic constants associated with a polycrystal mesh. That is accomplished using the numerical procedure described in Section 4.5: in Table 5.1, we listed most of the parameters required to perform the underlying numerical tests, as well as the values that we have ascribed to them. Within this context, a few comments must be made:

- Six analyses must be performed on 3D cubic polycrystal meshes, otherwise it would not be possible to extract the 21 elastic constants;
- Regularized Poisson-Voronoi tessellations of polycrystals were considered instead of the traditional standard Poisson-Voronoi tessellations. As a consequence, we expect that there are less small entities (like edges and faces), so that lower levels of discretisation may be used without negatively impacting on the results (when compared to the conventional case);
- All the analyses were performed on single-phase cubic crystal aggregates with cubic shape. Moreover, we considered only structured meshes comprising

[1]Note that answering this issue is precisely one of the main objectives of this Chapter.

hexahedral elements due to the fact that the computational costs could be significantly reduced in doing so. Adding to this, periodic topologies are obtained, thus, with the use of periodic boundary condition, faster convergence to a reference solution, with increasing RVE sizes (i.e. number of grains), is achieved.

Table 5.1: Parameters specified in the numerical simulations performed (for the determination of the elastic response of polycrystals).

Parameter	**Assigned value(s)**
Definition of the polycrystal mesh	
Type of Problem	3D
Mesh properties	Structured meshes with F-bar eight-noded hexahedra. The level of discretisation varied between analyses
Number of grains	Varied between analyses
Number of phases	1 (single-phase)
Polycrystal geometry	Cubic shape[a], as showed in Figure 4.6
Polycrystal morphology	Regularized Poisson-Voronoi tessellations
Additional data required	
Macroscopic deformation gradient	Six different gradients (defined in Table 4.7) must be prescribed for each polycrystal mesh
Constitutive model of each grain	Saint-Venant Kirchhoff law has been assumed. The monocrystalline elastic constants varied between analyses
Boundary condition	Periodic
Load incrementation	1 increment (unitary load factor)

[a]The length of the side of the cube is not important, since size effects were not considered (due to using a first-order homogenisation scheme).

5.1.1 Strategy Developed to Characterize Isotropic Polycrystals

As we referred in the beginning of this Chapter, first of all, we are concerned about the characterisation of isotropic aggregates. This includes two main points: predicting their elastic response (i.e., their 2 independent elastic constants) and establishing

the domain in which those predictions are valid (by defining the minimum number of grains for which those results prevail). Because we are dealing with cubic crystal

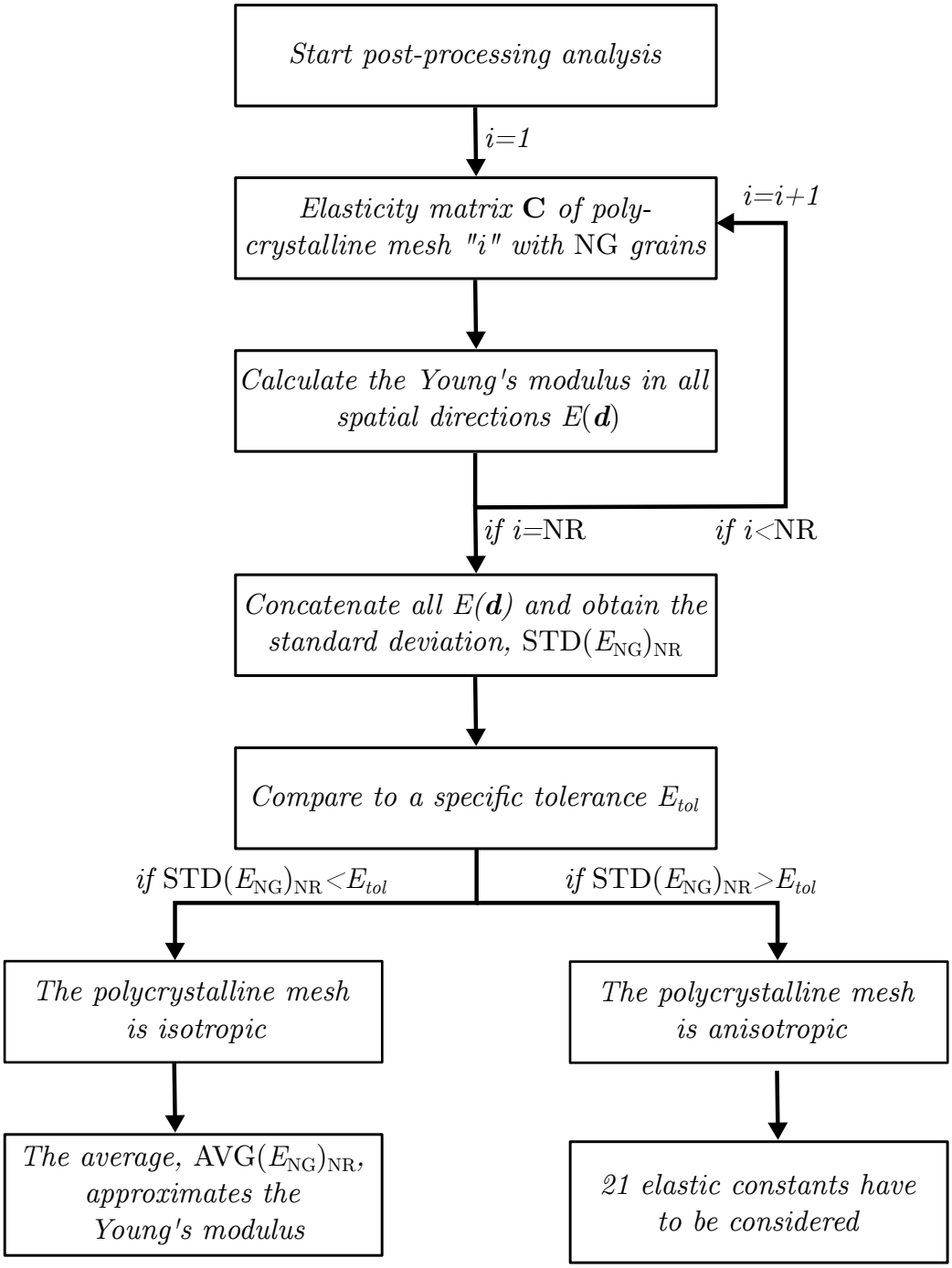

Figure 5.1: Strategy developed to characterize the elastic response of isotropic polycrystalline aggregates.

aggregates, we already know one elastic parameter (bulk modulus), so that only one additional elastic property has to be determined. However, as explained before, 21 elastic constants are computed for each polycrystal mesh, since we do not know beforehand how many elastic parameters are independent. The direct analysis of sets of 21 elastic parameters is undoubtedly an impractical way of extracting the additional independent parameter and, more importantly, of checking whether a polycrystal is isotropic. Moreover, as explained in Section 5.1.2, NR realisations of polycrystals with NG grains have to be considered, so that, in practice $21 \cdot \mathrm{NR}$ elastic constants are calculated. Under these circumstances, we have developed a robust way of satisfying our interests which is based on the analysis of the spatial distribution of the Young's modulus – the strategy is schematically represented in Figure 5.1 and, as it may be seen, a single scalar parameter is considered to verify if polycrystals with NG grains are isotropic. Furthermore, regarding the notation introduced, note that $\mathrm{AVG}(E_{\mathrm{NG}})$ and $\mathrm{STD}(E_{\mathrm{NG}})$ denote, respectively, the average and the standard deviation of the Young modulus of a polycrystal mesh comprising NG grains, while $\mathrm{AVG}(E_{\mathrm{NG}})_{\mathrm{NR}}$ and $\mathrm{STD}(E_{\mathrm{NG}})_{\mathrm{NR}}$ identify the average and the standard deviation when NR realisations of the same polycrystal with NG grains are considered (the meaning of these quantities is made clear in Section 5.1.2). Lastly, we must draw the attention to the flexibility of our procedure, as the tolerance E_{tol} can be defined according to the degree of precision that we want to impose.

It is important to justify why the spatial distribution of the Young's modulus is chosen to evaluate if polycrystalline aggregates are isotropic, as we could have chosen to make similar assumptions from the spatial distribution of the shear modulus or of the Poisson's ratio. In fact, not only is the Young's modulus the most used parameter to characterize the mechanical response of materials, as its spatial distribution can be computed in a more direct way than that of the shear modulus and the Poisson's ratio (in each spatial direction, multiple Poission's ratios and shear moduli can be defined, depending on the normal direction $\boldsymbol{n}$ considered[2]).

5.1.1.1 Young's Modulus of Cubic Crystals

To illustrate the strategy introduced in Section 5.1.1, in this Section, we focus on the graphical representation of the Young's modulus of cubic crystallites (using $\mathrm{NR} = 1$). In order to make this possible, each spatial direction must be defined. Following the approach of Nordmann et al. (2018), we have adopted a spherical coordinate system, so that a generic spatial direction $\boldsymbol{d}$ can be expressed in the following fashion:

$$\boldsymbol{d} = \left\{ \sin(\phi) \cdot \cos(\theta) \;\; , \;\; \sin(\phi) \cdot \sin(\theta) \;\; , \;\; \cos(\phi) \right\}^T \tag{5.1}$$

where $\phi \in [0, \pi]$ is the polar angle and $\theta \in [0, 2\pi]$ is the azimuth angle. Taking expression (5.1) into account and using (4.21), in Figure 5.2, we have represented

[2]Equations (4.23) and (4.24) might be useful to understand the mentioned issue. A more detailed examination of this topic, however, is provided by Nordmann et al. (2018).

the spatial distribution of the Young's modulus of several cubic crystals (the axes of reference were taken parallel to the cube axes of the crystals and 16200 spatial directions, i.e. 180 equally-spaced azimuth angles and 90 equally-spaced polar angles, were considered). Despite the fact that all the specimens exhibit cubic symmetry, we can see that the spatial distribution of the Young's modulus varies severely. In short, two major tendencies can be identified:

- The crystals with Zener anisotropy indexes larger than 1 (Aluminium, Copper, Lead and Tungsten[3]) have the maximum and minimum Young's moduli, respectively, at $\langle 111 \rangle$ and $\langle 100 \rangle$ crystallographic directions, while in the specimens with $A^{\mathrm{Z}} < 1$ what occurs is exactly the opposite (the elastic constants of these crystals are listed in Table 5.2);

Table 5.2: Elastic constants for cubic crystals with $A^{\mathrm{Z}} < 1$ at room temperature[a].

Material	C_{11}	C_{12}	C_{44}	A^{Z}	A^{L}
Cr	339.8	58.6	99.0	0.704	0.066
Nb	240.2	125.6	28.2	0.492	0.265

[a]Data from Freund and Suresh (2004) (the axes of reference were taken parallel to the cube axes of the crystals). All elastic constants expressed in $\mathrm{GN/m^2}$.

- The crystals with larger anisotropies (that is, with larger log-Euclidean anisotropy factors) are associated with larger (relative) variations of the Young's modulus and with surfaces whose deviation from perfect spheres (the isotropic case) is more pronounced. To illustrate this[4], note that Lead has the largest ratio $(\mathrm{MAX}(E_1) - \mathrm{MIN}(E_1))/\mathrm{AVG}(E_1)$, as well as the largest anisotropy. On the contrary, the log-Euclidean anisotropy factor of Tungsten is null, so that the Young's modulus is basically constant in all spatial directions and the shape of the surface is very similar to a perfect sphere.

All in all, this Section allows us to conclude that the standard deviation of the Young's modulus (which is related to the maximum and minimum values of the Young's modulus) is deeply connected with the anisotropy of the crystalline specimens. In fact, the greater the anisotropy of the crystallites, the greater the variation of the Young's modulus. Moreover, note that the standard deviation obtained for the crystallites corresponds to a upper bound for the standard deviation of textureless polycrystalline specimens: the anisotropy of an aggregate of crystals randomly oriented cannot be larger than the anisotropy of the constituent crystals (since there are no other sources

[3]The elastic constants of these single-crystals are given in Table 4.4.

[4]In Figure 5.2, the extreme values in the colorbars are the minimum and maximum values of the Young's modulus (hereafter denoted by $\mathrm{MIN}(E_1)$ and $\mathrm{MAX}(E_1)$).

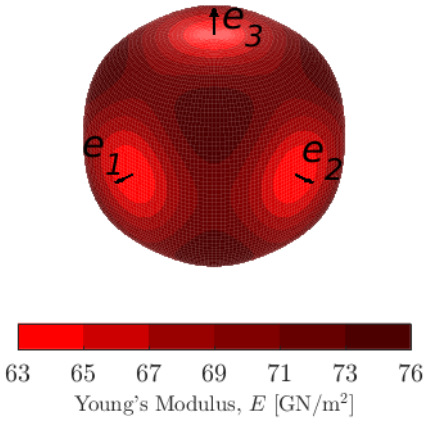

(a) Aluminium (Al).

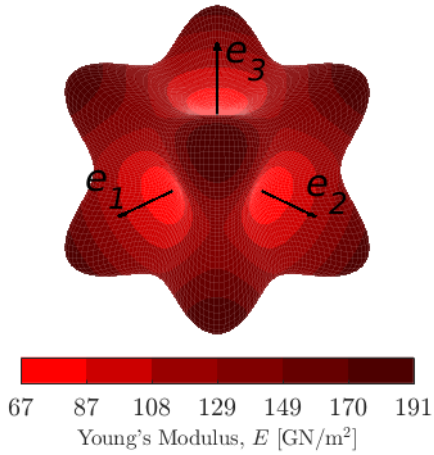

(b) Copper (Cu).

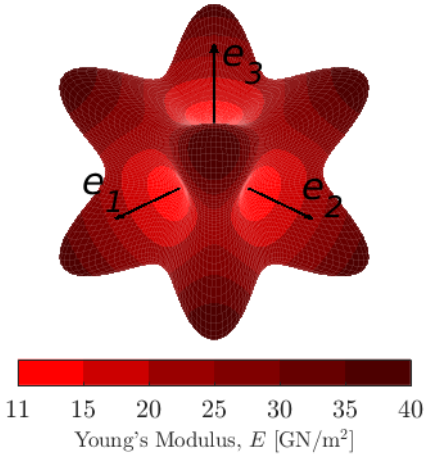

(c) Lead (Pb).

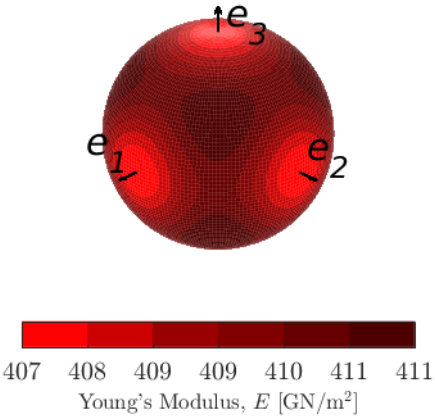

(d) Tungsten (W).

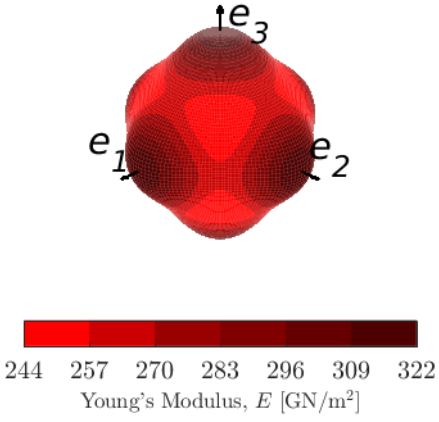

(e) Chromium (Cr).

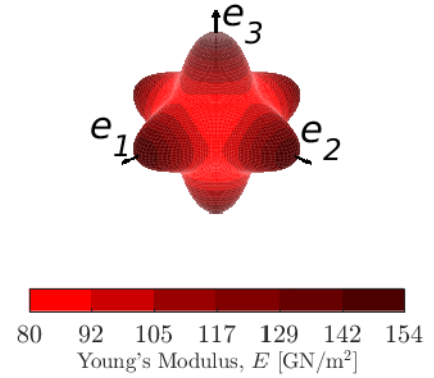

(f) Niobium (Nb).

Figure 5.2: Graphical representation of the Young's modulus of cubic single-crystals.

of anisotropy). This means that when the number of grains increases, the effect of the anisotropy of each individual grain is gradually diluted and, in the limit when the aggregates encompass a very large number of crystals, their elastic behaviour will be the same in all directions. In other words, when the number of grains is sufficiently high, the spatial distribution of the Young's modulus consists of a perfect sphere and the average value coincides with the isotropic Young's modulus.

5.1.2 Study on Influence of the Number of Realisations

When we look at two realisations of polycrystals comprising the same constituent crystal and the same number of grains, we may verify that their elastic response is different. Hence, it is important to note that the set composed of the morphology and of the distribution of grain orientations (a *realisation*) may also influence the elastic behaviour of polycrystalline specimens. Since we are focusing on textureless polycrystals, considering different realisations will not influence the elastic response of polycrystals encompassing isotropic crystals or with a large number of grains (that is, isotropic polycrystals). In contrast, in case we are analysing polycrystalline specimens enclosing a small number of crystals with high elastic anisotropy, different elastic responses will be found for distinct realisations. The preceding statement is corroborated by Figure 5.3, where we can see the spatial distribution of the Young's modulus of two different realisations of polycrystals comprising 10 grains of Copper. As a complement, Table 5.3 contains the statistical description of the spatial distribution of the Young's modulus for both polycrystal meshes.

Table 5.3: Statistical description of the spatial distribution of the Young's modulus of polycrystals of Copper with 10 grains (the values of the Young's modulus are expressed in $\mathrm{GN/m^2}$).

Realisation	AVG(E_{10})	STD(E_{10})	MIN(E_{10})	MAX(E_{10})
1	133.3	10.7	111.4	163.5
2	129.2	12.0	102.5	156.4
Relative difference[a] (%)	3.1	12.1	4.3	8.0

[a]The relative differences were calculated taking the values associated with "Realisation 1" as the reference values.

Both the graphical representation and the statistical description of the spatial distribution of the Young's modulus associated with the considered realisations are noticeably different. Indeed, we may say that the elastic response of aggregates of Copper with 10 grains is dependent on both the monocrystalline elastic constants of Copper and on the morphology and distribution of grain orientations. In particular, it must be noted that the relative difference associated with the standard deviation of

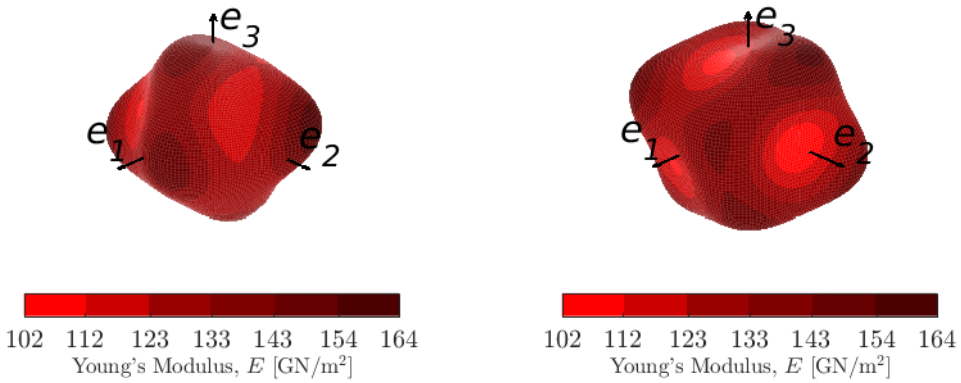

(a) Realisation 1. (b) Realisation 2.

Figure 5.3: Graphical representation of the Young's modulus of polycrystal meshes of Copper with 10 grains and 125 elements.

the Young's modulus is reasonably larger than that of the average. As a consequence, studying a small number of realisations might conduce to misleading conclusions, especially regarding the minimum number of grains necessary to obtain isotropic responses. Thus, it is apparent that, in order to verify if, generally speaking, polycrystals enclosing NG grains of a certain material are isotropic, we must consider various realisations. In this context, provided that several realisations are taken into consideration, two possibilities arise with the objective of characterising polycrystals of the same material with the same number of grains:

1. Calculate, for each one of the realisations, the average and the standard deviation of the Young's modulus and, in the end, calculate the average of the averages and the average of the standard deviations (and assume those values as being representative for the group of polycrystals studied);

2. Consider the spatial distributions of the Young's modulus of all the realisations and calculate the average and the standard deviation of the set comprising the Young's modulus in all spatial directions of all realisations (and assume those values as being representative for the group of polycrystals studied).

The two possibilities mentioned generate different results only for the standard deviation of the Young's modulus. On the one hand, the first method yields a value for the standard deviation which represents the average dispersion of the Young's modulus, but does not give an idea about the range of values assumed by the Young's modulus (considering all realisations). On the other hand, the second approach provides a value for the standard deviation which may be used to estimate the maximum and minimum values registered for the Young's modulus (considering all realisations). This is because the set comprising all Young's modulus follows, when

a large number of realisations is considered, a normal distribution[5] (Böhlke et al., 2010; Fritzen et al., 2009). In such instance, we can affirm, with 99.7% certainty, that the Young's modulus in a random direction of a particular realisation, $(E_{\mathrm{NG}})_1$, is located in the following interval:

$$(E_{\mathrm{NG}})_1 \in \left[\mathrm{AVG}(E_{\mathrm{NG}})_{\mathrm{NR}} - 3 \cdot \mathrm{STD}(E_{\mathrm{NG}})_{\mathrm{NR}}, \mathrm{AVG}(E_{\mathrm{NG}})_{\mathrm{NR}} + 3 \cdot \mathrm{STD}(E_{\mathrm{NG}})_{\mathrm{NR}}\right], \quad (5.2)$$

where $\mathrm{AVG}(E_{\mathrm{NG}})_{\mathrm{NR}}$ and $\mathrm{STD}(E_{\mathrm{NG}})_{\mathrm{NR}}$ denote, respectively, the average and the standard deviation of the Young's modulus of NR realisations of polycrystals with NG grains. In such instance, the minimum and the maximum values registered for the Young's modulus coincide (with 99.7% of certainty) with the bounds of the interval (5.2). It is apparent that being capable of estimating the range of values assumed by the Young's modulus (considering all realisations) gives a better perception of the anisotropy than computing an average value for the standard deviation (which does not give a trustworthy indication of the range of values assumed by Young's modulus). This is the reason why we decided to consider the second approach for the purpose of characterising several realisations of the same polycrystal.

Now that we have defined the method to describe several realisations of a particular polycrystal, we have to decide how many realisations we must take into consideration. It is evident that accounting more realisations entails an increase of the computational resources needed. In order to determine that, we studied a "population" of 500 realisations of polycrystals of Copper with NG = 10 grains (all polycrystal meshes with 125 elements). In detail, we focused on the average and on the standard deviation of groups of NR realisations (with NR $<$ 500) and compared those values with the statistics of the population (by calculating relative errors). Because groups comprising a small number of realisations could generate different results depending on which specific realisations were contained in them, we have considered 20 different groups of NR realisations, so that for each value of NR, we obtained 20 estimates for the average and 20 estimates for the standard deviation. Firstly, we considered the average of the estimates, in such a way that we have calculated the relative errors (for each considered value of NR) using the average of the averages and the average of the standard deviations – the results obtained following this line of thought are shown in Figure 5.4.

[5]Note that just one realisation already involves the calculation of 16200 values for the Young's modulus.

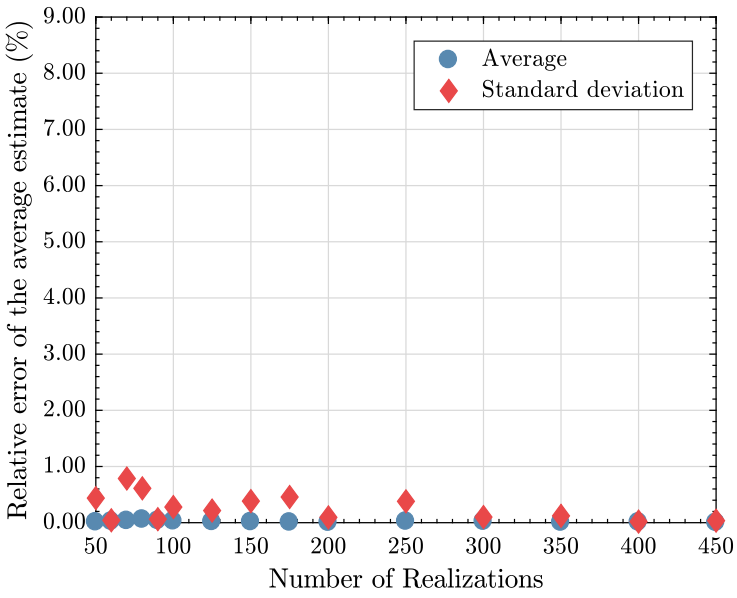

Figure 5.4: Evolution of the average relative errors of the estimates (of the average and of the standard deviation of the Young's modulus) with the number of realisations considered (20 tests were performed on a population comprising 500 realisations of polycrytals of Copper with 10 grains).

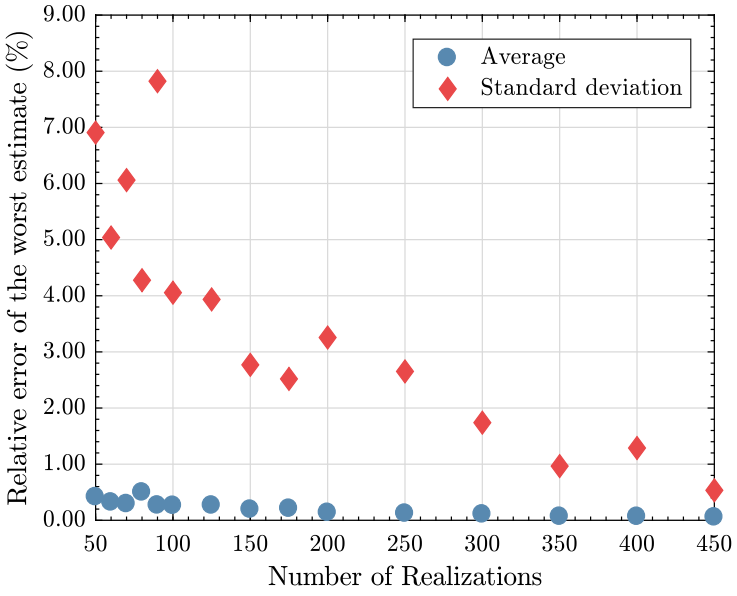

Figure 5.5: Evolution of the maximum relative errors of the estimates (of the average and of the standard deviation of the Young's modulus) with the number of realisations considered (20 tests were performed on a population comprising 500 realisations of polycrytals of Copper with 10 grains).

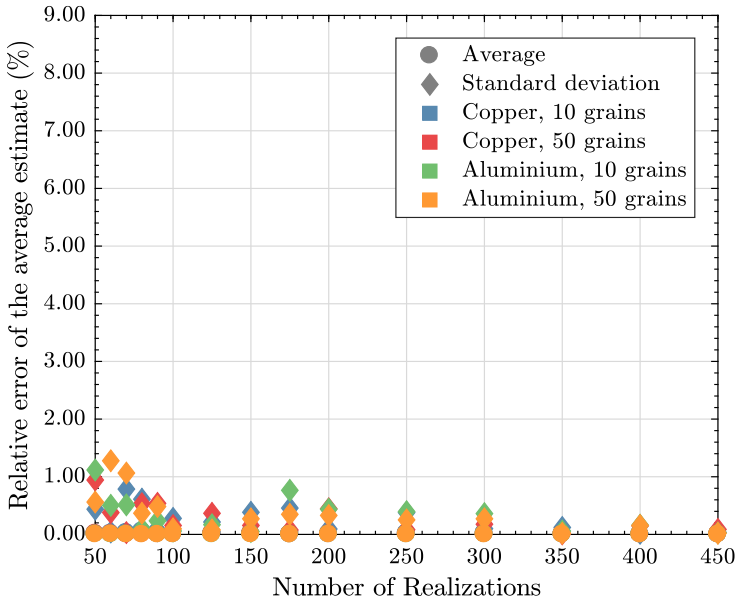

Figure 5.6: Evolution of the average relative errors of the estimates (of the average and of the standard deviation of the Young's modulus) with the number of realisations considered (20 tests were performed on 4 populations, each one comprising respectively 500 realisations of polycrytals of Copper with 10 grains, Copper with 50 grains, Aluminium with 10 grains and Aluminium with 50 grains).

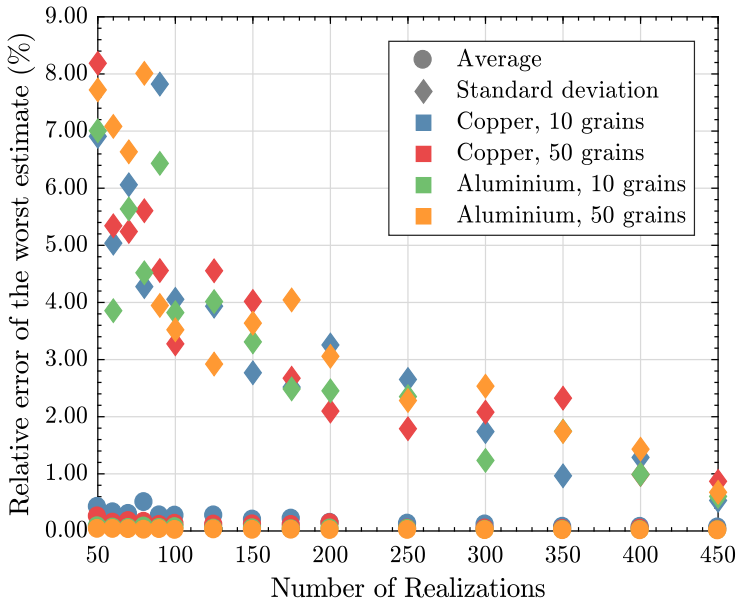

Figure 5.7: Evolution of the maximum relative errors of the estimates (of the average and of the standard deviation of the Young's modulus) with the number of realisations considered (20 tests were performed on 4 populations, each one comprising respectively 500 realisations of polycrytals of Copper with 10 grains, Copper with 50 grains, Aluminium with 10 grains and Aluminium with 50 grains).

As can be seen, the average relative error is below 1% for all values of NR (this conclusion is valid for both statistical parameters, even though the relative errors associated with the standard deviation are larger than the ones associated with the average). In order to complement our analysis, we studied the maximum relative error obtained for each value of NR – see Figure 5.5. This Figure confirms that the relative errors which result from considering 50 or more realisations (of the total 500) are fairly low – in fact, the maximum relative error obtained for the standard deviation is under 5% in case 100 or more realisations are taken into account. These tendencies were verified for other polycrystals, as we may see in Figures 5.6 and 5.7.

From the previously reported results, we decided to consider 100 different realisations of all polycrystals studied in this work. Observe that this number ensures that the average and the standard deviation of the Young's modulus are reasonably close to the values that would be obtained with a larger number of realisations, while reducing the associated computational cost (even with parallel processing considering more than 100 realisations would be impractical, taking into consideration the volume of studies that we were interested in performing). Moreover, considering a random group of 100 realisations provides normal distribution of the Young's modulus (considering all directions and all realisations), as we might see from Figure 5.8 where a sample of 100 realisations of polycrystals of Copper with 10 grains was considered. In that case, the average and the standard deviation of the group of realisations can be used to characterize the range of values assumed by the Young's modulus for all polycrystals of NG grains using expression (5.2). Thus, the low relative differences obtained for the statistical parameters coupled with normal distribution of the Young's modulus lead to the conclusion that 100 different realisations are sufficient to characterize polycrystals with any number of grains with the desired accuracy.

An important point to be made is related to the value of the average of the Young's modulus: indeed, we may notice that this value is extremely close to the self-consistent estimate (which is valid for isotropic polycrystals). As a matter of fact, this is not surprising, since it has been long known that the average of the Young's modulus (and of the other elastic properties) considering a very large number of realisations of polycrystals comprising any number of grains turns out to be isotropic (Kanit et al., 2003). In light of the previous statement, it can be concluded that the response of isotropic aggregates can be computed from numerical tests performed solely on non-isotropic polycrystalline aggregates (the general idea is to perform simulations on NR realisations of polycrystals with NG grains, so that the response of a polycrystal comprising $NR \cdot NG$ grains can be deduced). Some authors (for instance El Houdaigui et al. (2007)) have put this issue in different terms: according to them, the *effective* elastic properties of a (isotropic) polycrystal can be obtained from the ensemble average of their *apparent* elastic properties (obtained using oligocrystals). Even though following this type of approach is attractive (due to the fact that the

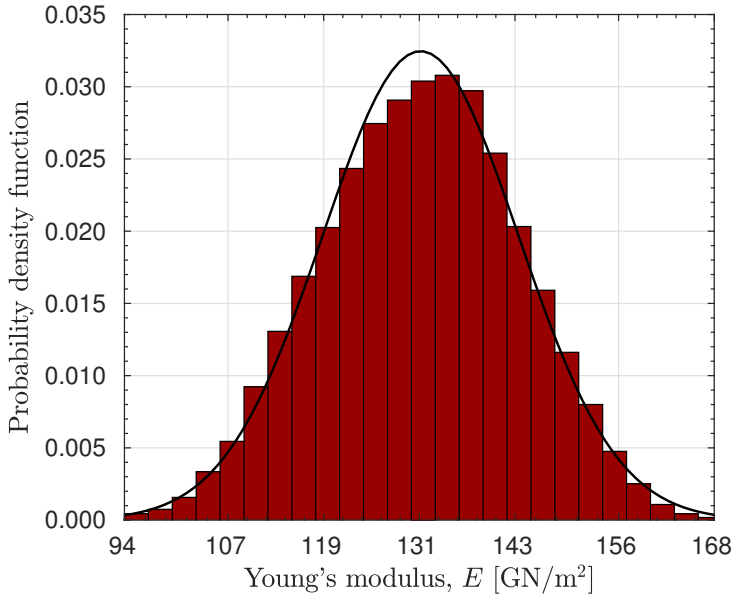

Figure 5.8: Histogram and normal distribution of the Young's modulus, considering 100 realisations of polycrystals of Copper with 10 grains.

computational effort could be drastically reduced), it does not allow the determination of the number of grains necessary to obtain isotropic responses. Since this question is of primary importance within the context of this work, we have to study polycrystals comprising distinct numbers of grains – the evolution of the elastic response with the number of grains is discussed in Section 5.1.4, after the influence of the mesh size is treated in the following Section.

5.1.3 Study on the Influence of the Mesh

It must not be forgotten that numerical procedures are associated with numerical errors. Within the context of polycrystalline aggregates, the numerical error associated with the level of refinement of the polycrystal meshes is particularly important in case structured meshes are used (as we referred in Section 4.5.1). This is because the level of refinement affects not only the resolution of the discretisation error, but also the resolution of the grain boundaries (and, consequently, the representation of the strain and stress fields at these locations). With the objective of getting a broader understanding of the influence of the level of discretisation on the elastic characterisation of block-structured polycrystalline meshes, we have performed several tests which are presented and discussed throughout this Section.

First and foremost, it is important to realize that studies on the influence of the mesh size are computationally costly, insomuch that it is unrealistic to perform this type of studies on polycrystal meshes encompassing a very large number of grains and of elements per grain. Under these circumstances, we have directed our attention

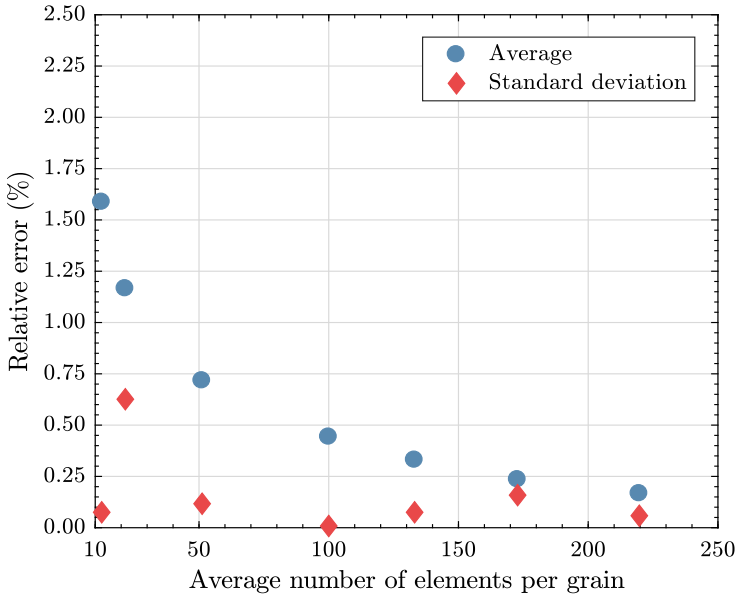

Figure 5.9: Influence of the level of refinement on the estimates of the average and of the standard deviation of the Young's modulus of polycrystal meshes of Copper with 10 grains (100 different realisations were considered).

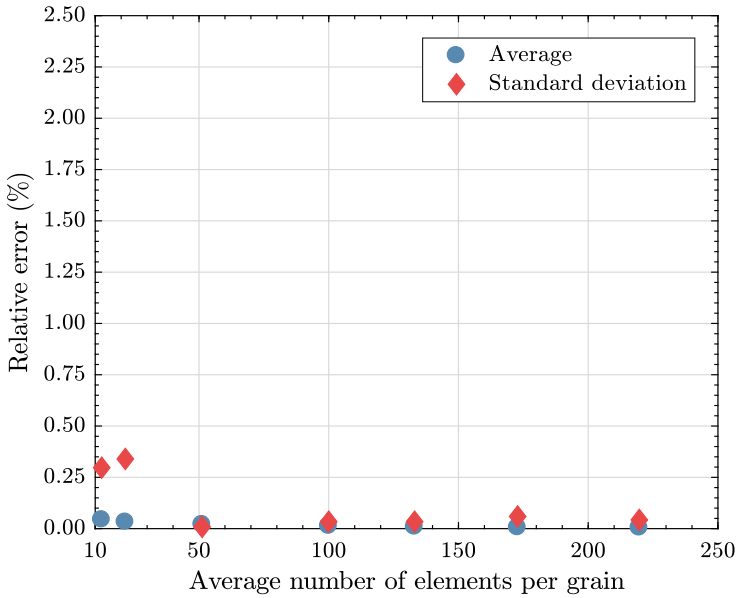

Figure 5.10: Influence of the level of refinement on the estimates of the average and of the standard deviation of the Young's modulus of polycrystal meshes of Aluminium with 10 grains (100 different realisations were considered).

towards groups of NR = 100 realisations of polycrystals of Copper and Aluminium with NG = 10 grains and we have compared the average and the standard deviation obtained with low refinement meshes with their "highly refined" counterparts. Note

that Copper and Aluminium were chosen because they exhibit considerably different degrees of anisotropy (see Table 4.6). The results obtained are shown in Figures 5.9 and 5.10, where we have plotted the relative errors of the average and of the standard deviation in terms of the average number of elements per grain. The reference values (necessary for the calculation of the relative errors) were, respectively, the average and the standard deviation of the group of 100 realisations of polycrystal meshes with the highest level of refinement – which consisted of 4096 elements or, alternatively, 410 elements per grain on average.

From the analysis of Figures 5.9 and 5.10, it can be extracted that the relative error of the standard deviation is always under 1%, even though it does not follow any trend (indeed, more refined meshes do not provide necessarily more accurate results). On the contrary, the relative error associated with the average decreases hyperbolically as the number of elements per grain rises. Observe that this tendency can be easily seen for Copper, albeit it is also true for the polycrystal meshes of Aluminium. Because the same 100 realisations and the same levels of discretisation for the aggregates of Copper and Aluminium are being analysed, this discrepancy in the results is undoubtedly justified by the different elastic behaviours of the constituent crystals. In order to gain an in-depth view into the influence of the elastic behaviour of the single-crystals, we have considered the same 100 realisations comprising 10 grains and studied the evolution of the average and of the standard deviation of the Young's modulus with the mesh size for aggregates comprising other cubic crystals (whose elastic constants are all indicated in Table 4.4).

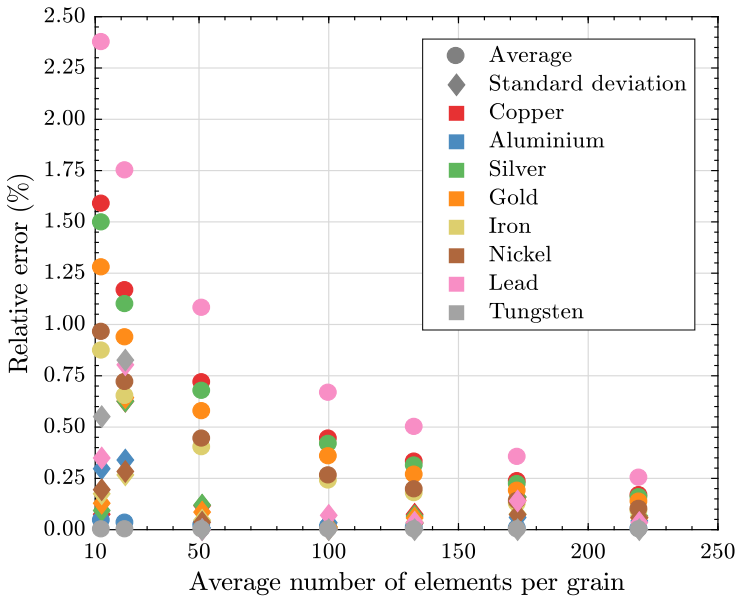

Figure 5.11: Influence of the level of mesh refinement on the estimates of the average and of the standard deviation of the Young's modulus of polycrystal meshes with 10 grains (100 different realisations were considered).

From Figure 5.11, it can be seen that the conclusions drawn with respect to both parameters were confirmed. On the one hand, the relative error associated with the standard deviation is always very low and the impact of the mesh size can be neglected (for example, the standard deviation of the Young's modulus of polycrystal meshes of Copper with 10 grains and 125 elements is near 12 GN/m^2, so that a relative error of 1% entails that the value obtained with highly refined meshes would be located between 11.88 and 12.12 GN/m^2 – this variation is not significant and can be ignored). On the other hand, it becomes clear that the relative error associated with the average of the Young's modulus decreases hyperbolically for all materials comprising anisotropic crystals. Moreover, in contrast to what occurs with the standard deviation, the relative error of the average of the Young's modulus must not be overlooked, since it embodies the relative error of the numerical estimate of the isotropic Young's modulus (it must not be forgotten that, because we are considering several realisations, the average of the Young's modulus provides an estimate for the isotropic Young's modulus, as we have mentioned in Section 5.1.2). Having said that, it is pertinent to study in greater depth the evolution of this error with the mesh size. With that purpose, we must note that Nickel and Iron have very similar anisotropies (but different elastic constants) and that the evolution of the relative error of the average of the Young's modulus of the polycrystal meshes comprising these two crystals is very similar. In short, this occurs because the error obtained for the average of the Young's modulus is dependent on the anisotropy of the constituent crystal: accordingly, the largest error is verified for polycrystals of the most anisotropic crystal considered (Lead) and it diminishes as the anisotropy of the constituent crystal decreases, so that the smallest error is linked to the polycrystals of Tungsten (which consists of a nearly isotropic crystallite). Under these circumstances, it must be remembered that polycrystals comprising isotropic grains are homogeneous, so that the strain and stress fields are uniform over the whole polycrystals (at the micro-scale). In such cases, the level of discretisation of the polycrystal mesh is not important and one element per grain is enough to provide accurate results. By opposition, when the crystals exhibit some degree of anisotropy, the strain and stress fields over the polycrystal meshes are not uniform and it is expected that both the strain and stress vary in the interior of the grains (*intragranular* variations) and between grains (*intergranular* variations). As a consequence, greater variations will occur for aggregates comprising more anisotropic crystals and that more refined meshes will provide different (and more accurate) representations of the strain and stress fields. In Figures 5.12 and 5.13, the strain and stress fields of the same polycrystal morphology of Copper and Aluminium are shown with two different levels of mesh refinement (the microscopic cells were submitted to a macroscopic deformation gradient which yields deformation only in the direction of the axis $\boldsymbol{e}_1$, i.e., the only non-null component of the Green-Lagrange strain tensor is $E_{11}^{(2)}$). These were obtained considering the ratio between the local and global measures

of strain and stress adopted. In this case, the *equivalent strain* ε and the *effective Cauchy stress* σ^{VM} (also known as the *equivalent von Mises stress*) were studied. The macroscopic equivalent strain and the macroscopic effective Cauchy stress are given by:

$$\varepsilon = \sqrt{\frac{2}{3}}||\boldsymbol{E}_d^{(0)}||, \tag{5.3}$$

$$\sigma^{\mathrm{VM}} = \sqrt{3\,J_2}, \tag{5.4}$$

where $\boldsymbol{E}_d^{(0)}$ is obtained from the *Hencky tensor* $\boldsymbol{E}^{(0)}$ (defined in equation (2.38)) as follows:

$$\boldsymbol{E}_d^{(0)} = \boldsymbol{E}^{(0)} - \frac{1}{3}\mathrm{tr}(\boldsymbol{E}^{(0)}), \tag{5.5}$$

and J_2 denotes the invariant of the stress deviator $\boldsymbol{s}$ which reads:

$$J_2 = \frac{1}{2}\,\boldsymbol{s} : \boldsymbol{s}. \tag{5.6}$$

In consistency with the notation scheme introduced in previous Chapters, ε_μ and σ_μ^{VM} define the microscopic/local counterparts of the macroscopic/homogenized equivalent strain ε and effective Cauchy stress σ^{VM} (so that they are obtained using expressions similar to the ones presented above, albeit involving microscopic quantities). In that case, the ratio of equivalent strain $\varepsilon_{\mu,dim}$ and the ratio of equivalent stress $\sigma_{\mu,dim}^{\mathrm{VM}}$ come as:

$$\varepsilon_{\mu,dim}(\boldsymbol{x}_\mu) = \frac{\varepsilon_\mu(\boldsymbol{x}_\mu)}{\varepsilon}, \tag{5.7}$$

$$\sigma_{\mu,dim}^{\mathrm{VM}}(\boldsymbol{x}_\mu) = \frac{\sigma_\mu^{\mathrm{VM}}(\boldsymbol{x}_\mu)}{\sigma^{\mathrm{VM}}}. \tag{5.8}$$

Note that the use of these measures allows the analysis of strain and stress fields without considering the influence of the specific resistance of the microscopic cells to the prescribed deformation gradients. Moreover, it must be highlighted that they also give a more straightforward way of verifying the non-uniformity of the strain and stress fields: the greater the dispersion of the strain and stress ratios from unity, the less uniform is the distribution of strains and stresses (respectively). The non-uniformity of the strain and stress fields is deeply connected to the anisotropy of the constituent crystal (as mentioned above), which can be inferred from Figures 5.12 and 5.13 (the polycrystals of Copper incorporate wider relative variations of strain and stress). Besides this, it must be noted that the variation of strains and stresses is larger between different grains than within the interior of the grains. To put it differently, intergranular variations of the field variables are more relevant than their intragranular variation. For this reason, the correct representation of the grain boundaries is of primary importance, since otherwise unduly high strain and stress gradients will appear at these locations. When considering structured meshes,

the level of discretisation influences the representation of the field variables at the grain boundaries and more refined meshes provide more realistic descriptions of the intergranular variations of the strain and stress. Consequently, the homogenized response is affected by these local phenomena and small variations of the elastic properties are verified, depending on the level of discretisation of the mesh.

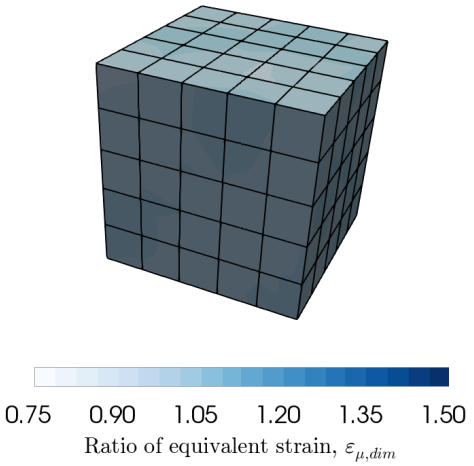

(a) Strain field of a 10-grain polycrystal mesh of Aluminium (125 elements).

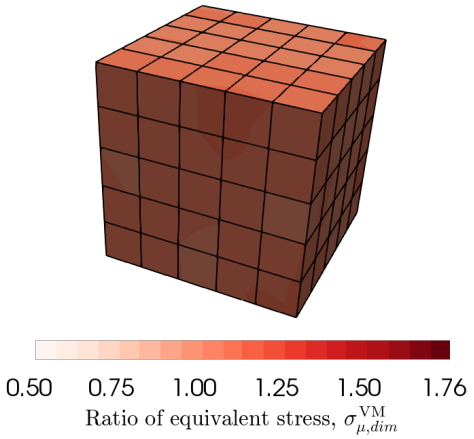

(b) Stress field of a 10-grain polycrystal mesh of Aluminium (125 elements).

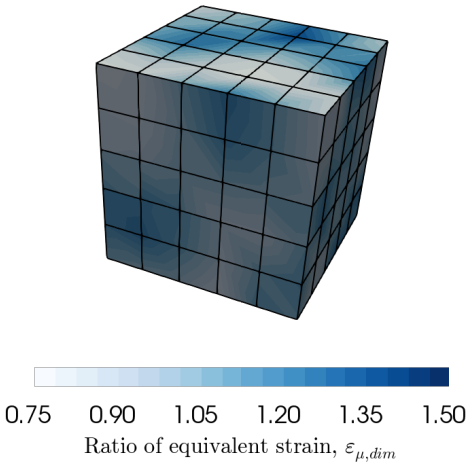

(c) Strain field of a 10-grain polycrystal mesh of Copper (125 elements).

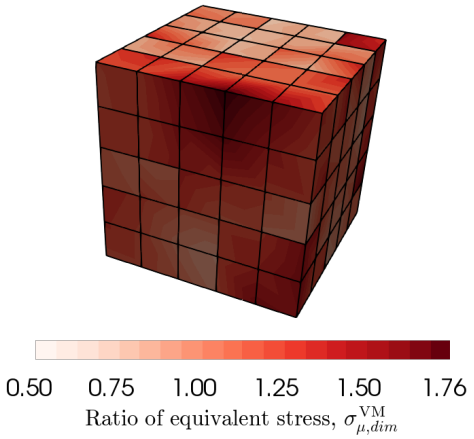

(d) Stress field of a 10-grain polycrystal mesh of Copper (125 elements).

Figure 5.12: Representations of the relative strain and stress fields of the same polycrystal mesh comprising 125 elements and 10 grains of Aluminium and Copper (both polycrystal meshes were submitted to the same solicitation).

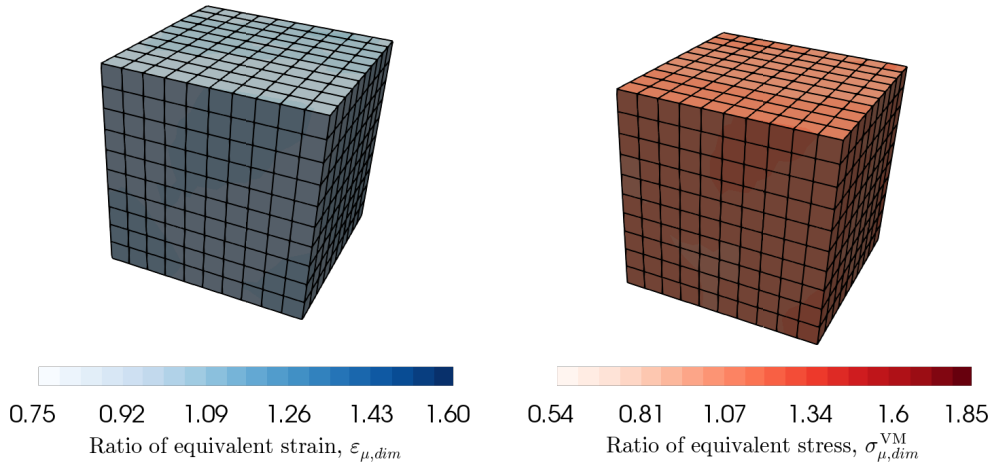

(a) Strain field of a 10-grain polycrystal mesh of Aluminium (1000 elements).

(b) Stress field of a 10-grain polycrystal mesh of Aluminium (1000 elements).

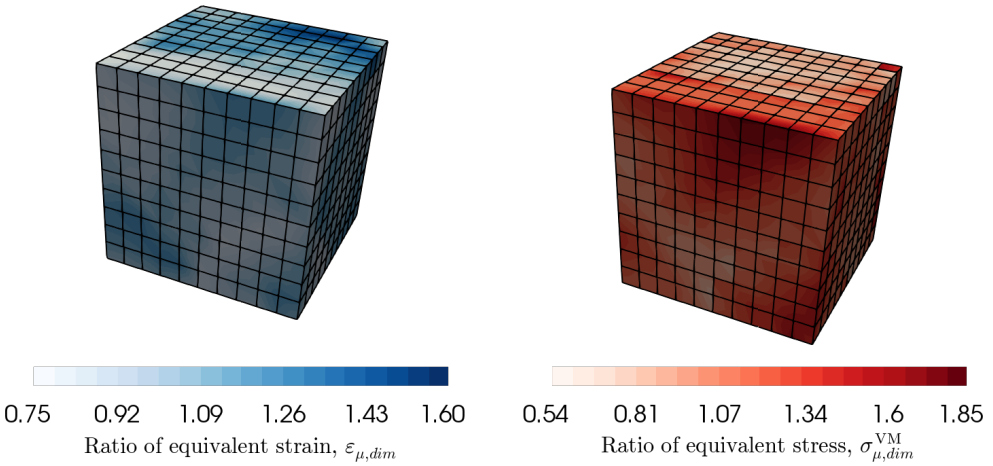

(c) Strain field of a 10-grain polycrystal mesh of Copper (1000 elements).

(d) Stress field of a 10-grain polycrystal mesh of Copper (1000 elements).

Figure 5.13: Representations of the relative strain and stress fields of the same polycrystal mesh comprising 1000 elements and 10 grains of Aluminium and Copper (both polycrystal meshes were submitted to the same solicitation).

All in all, the correct representation of the stress and strain fields (especially at the grain boundaries) is dependent on the level of discretisation. As a consequence, the characterisation of the elastic response of polycrystals through numerical studies is also reliant on the mesh size, even though it must be remarked that, since the elastic constants are computed from homogenized quantities, the errors resulting from the use of low refinement meshes are not high. As a matter of fact, using more refined meshes (and, consequently, reproducing more accurately the local phenomena) achieves greater importance when the anisotropy of the crystals increase, but, even in those cases, it is expected that accurate estimates can be obtained for the elastic

parameters even with low refinement meshes. Nonetheless, it is relevant to relate the error associated with a certain level of mesh refinement with the anisotropy of the cubic crystals. For that purpose, we consider again the representation of the relative error associated with the average of the Young's modulus in terms of the mesh refinement (Figure 5.14). At this point, we have assigned rational functions to the variations of the relative errors associated with each one of the materials:

$$e_r(E) = \frac{p_1}{n_{epg} + p_2}, \tag{5.9}$$

where $e_r(E)$ denotes the relative error associated with the average of the Young's modulus of the 100 realisations (that is, the relative error associated with the numerical estimate of the isotropic Young's modulus), n_{epg} represents the number of elements per grain and p_1 and p_2 are the parameters that we want to relate with the elastic anisotropy of the constituent crystals. In fact, only p_1 depends on the anisotropy of the constituent crystals, as we might see from Figures 5.15 and 5.16. These parameters can be estimated through fitting (5.9) to the results as:

$$p_1 = 0.68 \cdot A^{\mathrm{L}}, \tag{5.10}$$

$$p_2 = 17.36, \tag{5.11}$$

so that a new expression for the relative error can be derived:

$$e_r(E) = \frac{0.68 \cdot A^{\mathrm{L}}}{n_{epg} + 17.36}. \tag{5.12}$$

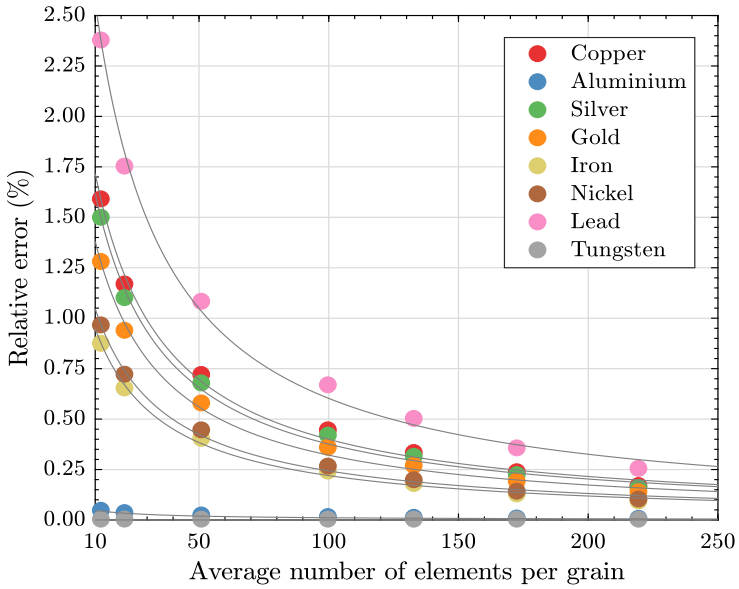

Figure 5.14: Curve fitting for the influence of the level of refinement on the estimates of the average of the Young's modulus of polycrystal meshes with 10 grains (100 different realisations were considered).

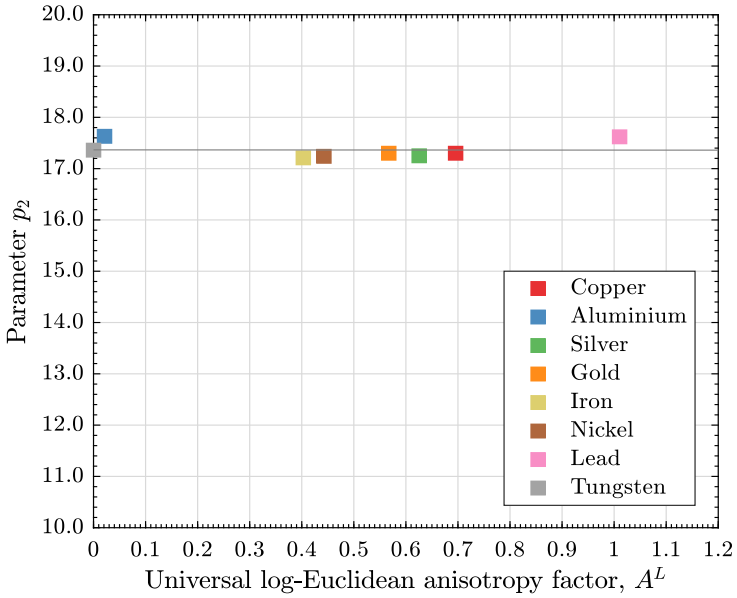

Figure 5.15: Dependency of the parameter p_1 on the elastic anisotropy of the single-crystals.

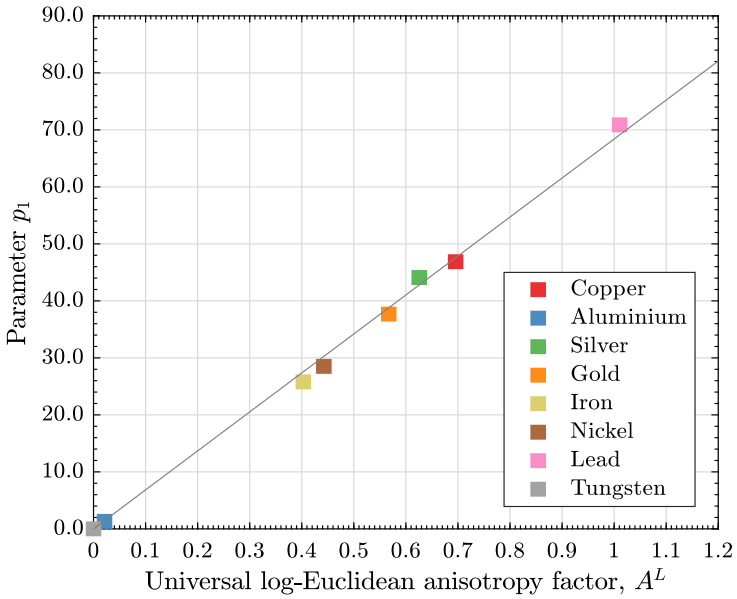

Figure 5.16: Dependency of the parameter p_2 on the elastic anisotropy of the single-crystals.

Note that (5.12) provides an estimate for the relative error of the isotropic Young's modulus. From another standing point, equation (5.12) can be used to predict the relative error associated with the elastic characterisation of isotropic polycrystalline specimens through numerical studies. Alternatively, from the manipulation of the referred equation, we may get the minimum number of elements per grain required

to obtain estimates for the isotropic elastic properties in case a certain relative error is considered satisfactory:

$$n_{epg} = \frac{0.68 \cdot A^{\mathrm{L}}}{e_r(E)} - 17.36. \tag{5.13}$$

5.1.4 Study on the Influence of the Number of Grains

Until this point, we have seen that the range of the Young's modulus of polycrystals enclosing a certain number of grains and particular cubic crystals can be estimated from the consideration of 100 realisations of those polycrystal meshes. Furthermore, we have also remarked that the average of the Young's modulus of 100 realisations provides an estimate for the isotropic Young's modulus. Finally, in the previous Section, we have inferred the influence of the mesh size on the characterization of the Young's modulus range and we have verified that the average Young's modulus is affected by the level of refinement, albeit the relative errors associated with the use of low refinement meshes are generally small (and dependent on the anisotropy of the single-crystal); on the other hand, it must be emphasized that the relative error of the standard deviation of the Young's modulus (associated with the use of low refinement meshes) can be neglected. On balance, the mesh size plays an influential role when we are dealing with the prediction of the elastic properties, but, roughly speaking, it does not affect the evaluation of the anisotropy of the polycrystal. To put it differently, in order to evaluate the impact of the number of grains on the elastic response of the polycrystal meshes, low levels of discretisation can be employed mainly due to two reasons:

1. The fact that we are considering 100 realisations always leads to average Young's modulus which are estimates of the isotropic Young's modulus. In that case, the average Young's modulus will be approximately constant for all different numbers of grains considered. Moreover, using equation (5.12), we can correct the numerical estimates for the isotropic elastic properties (independently of the number of grains of the aggregates and of the discretisation employed);

2. The increase in the number of grains mostly decreases the global anisotropy of the polycrystal meshes. In that instance, the number of grains is basically linked to the value of the standard deviation of the Young's modulus (that is, to the range of the Young's modulus). As we have mentioned, the standard deviation of the Young's modulus remains unchanged for different levels of mesh discretisation, so that, the assessment of the impact of the number of grains on the elastic response of polycrystals can be made with low refinement meshes.

All things considered, in order to analyse the influence of the number of grains of the polycrystalline aggregates on the range of the Young's modulus, we studied

polycrystalline meshes with 10 elements per grain (on average). Because the range of the Young's modulus is deeply connected to the anisotropy of the polycrystal meshes, studying the influence of the number of grains creates room for the determination of the minimum number of grains required to achieve isotropic responses (which is one of the primary objectives of this Chapter). Provided that the anisotropy of the crystallites is the only source of anisotropy of the polycrystalline meshes, we expect that this parameter will play a pivotal role in the evolution of the range of the Young's modulus. With that in mind, in Figures 5.17 and 5.18 we have covered the evolution of the Young's modulus range with the number of grains for polycrystals of Copper and Aluminium, so that the impact of the anisotropy of the single-crystals becomes evident. Indeed, for all numbers of grains considered, the relative range of the Young's modulus[6] is larger for the polycrystals of Copper than for the polycrystals of Aluminium. This can be also perceived from Figures 5.19 and 5.20 where the spatial distribution of the Young's modulus for different numbers of grains is shown: as might be seen, for polycrystals of Aluminium, the shape of the spatial distribution of the Young's modulus is alike a sphere even if few grains are encompassed; on the contrary, for Copper, 500 grains are necessary to obtain a shape similar to a perfect sphere (as a consequence, the number of grains required to reach the isotropic limit is higher for the aggregates of Copper).

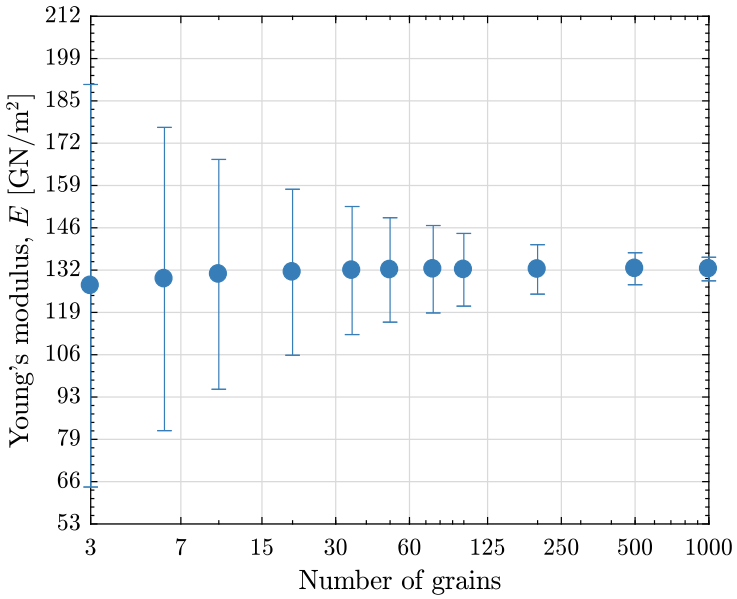

Figure 5.17: Evolution of the Young's modulus range (three standard deviations are considered) with the number of grains for polycrystals of Copper.

[6]The relative range of the Young's modulus can be characterized using the ratio :

$$\frac{\mathrm{STD}(E_{\mathrm{NG}})_{100}}{\mathrm{AVG}(E_{\mathrm{NG}})_{100}}. \tag{5.14}$$

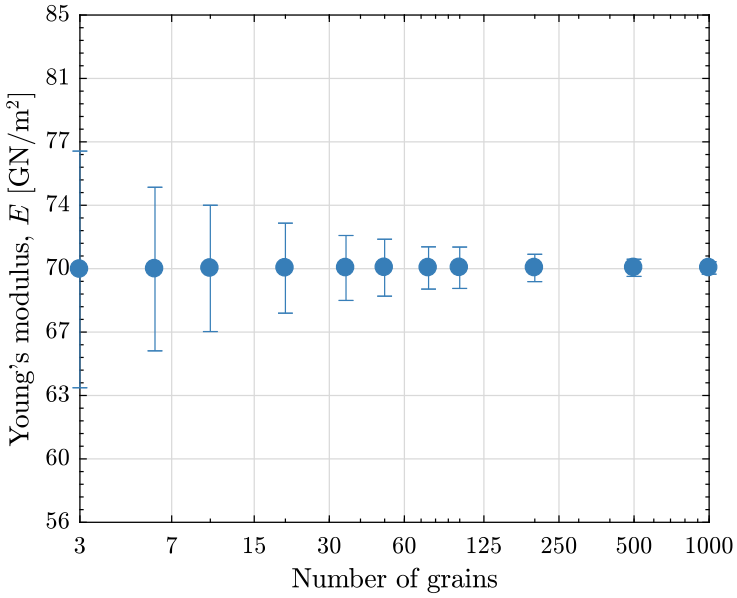

Figure 5.18: Evolution of the Young's modulus range (three standard deviations are considered) with the number of grains for polycrystals of Aluminium.

As expected, the average of the Young's modulus remains nearly the same for all the numbers of grains. In particular, it was ascertained that the average value was always very close to the upper Hashin-Shtrkiman bound (defined in Table 4.5 for both isotropic aggregates of Copper and Aluminium). Taking this into account, and in order to make it easier to compare the evolution of the Young's modulus range for polycrystals comprising different materials, it is convenient to consider dimensionless measures of the average and of the standard deviation of the Young's modulus which are based on the upper Hashin-Shtrikman bound. These dimensionless measures are given by[7]:

$$\mathrm{AVG}(E_{\mathrm{NG}})_{dim} = \frac{\mathrm{AVG}(E_{\mathrm{NG}})}{E^{\mathrm{HS}^+}}, \tag{5.15}$$

$$\mathrm{STD}(E_{\mathrm{NG}})_{dim} = \frac{\mathrm{STD}(E_{\mathrm{NG}})}{E^{\mathrm{HS}^+}}. \tag{5.16}$$

Using these dimensionless quantities, the evolution of the dimensionless Young's modulus range (of the polycrystals of Copper and Aluminium) against the number of grains were plotted in Figure 5.21. This provides an alternative way of drawing the same conclusions that we have already mentioned before (concerning the average and the standard deviation of the Young's modulus). Therefore, since these measures facilitate comparison among different materials, in the rest of this Section, we have worked exclusively with them. This is because our main objective in what follows is

[7] In expressions (5.15) and (5.16), as well as in all equations where the dimensionless average and standard deviation appear, the subscript indicating the number of realisations is omitted for notational convenience.

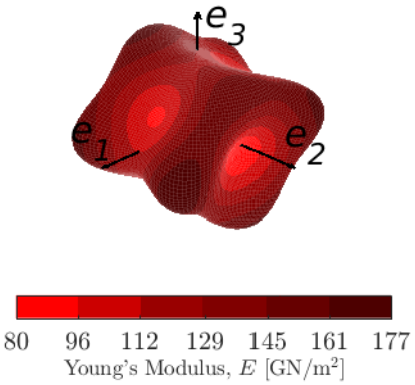

(a) 3-grain polycrystal of Copper.

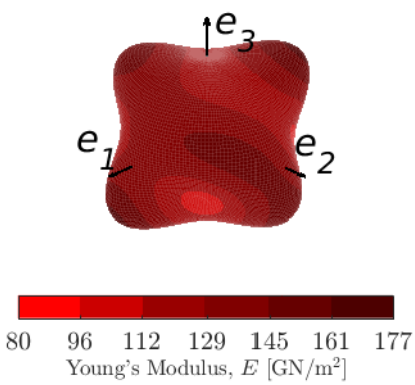

(b) 6-grain polycrystal of Copper.

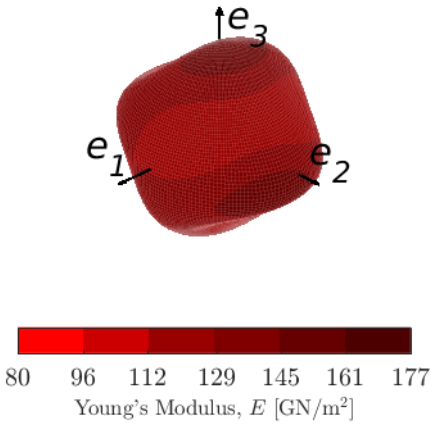

(c) 10-grain polycrystal of Copper.

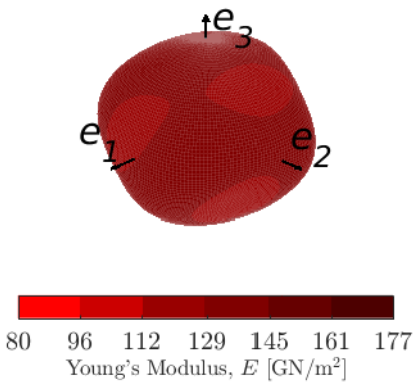

(d) 35-grain polycrystal of Copper.

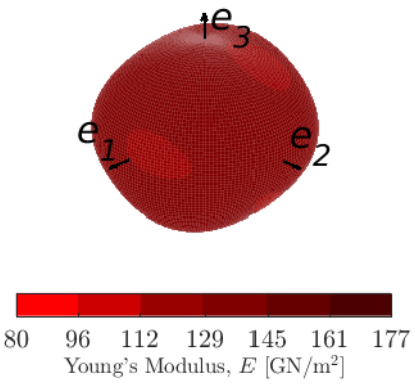

(e) 100-grain polycrystal of Copper.

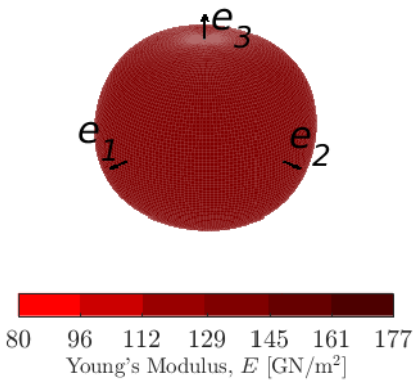

(f) 500-grain polycrystal of Copper.

Figure 5.19: Spatial distribution of the Young's modulus of polycrystals of Copper.

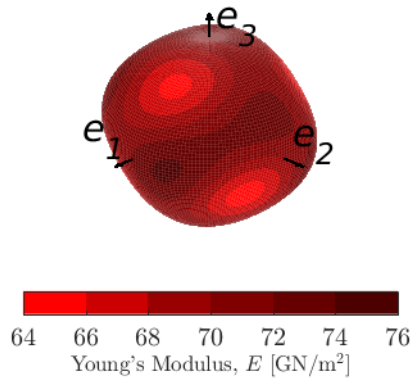

(a) 3-grain polycrystal of Aluminium.

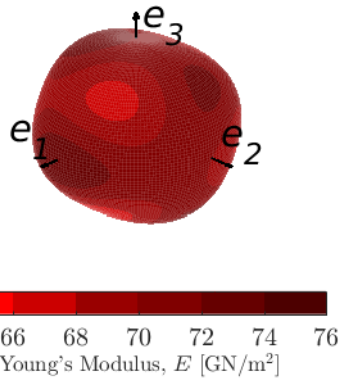

(b) 6-grain polycrystal of Aluminium.

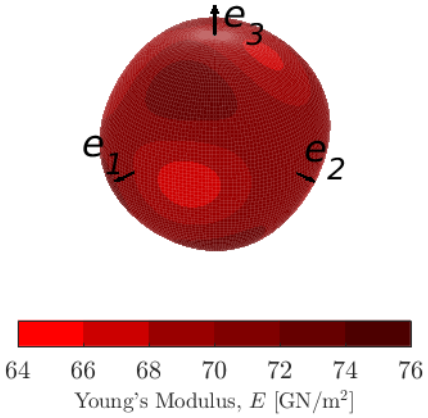

(c) 10-grain polycrystal of Aluminium.

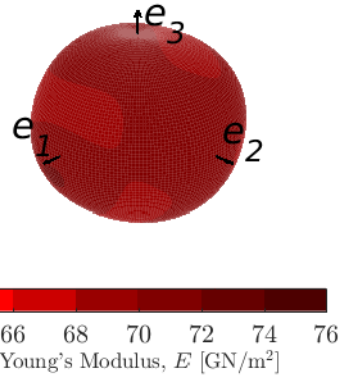

(d) 35-grain polycrystal of Aluminium.

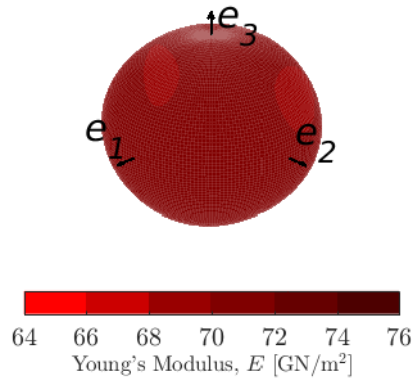

(e) 100-grain polycrystal of Aluminium.

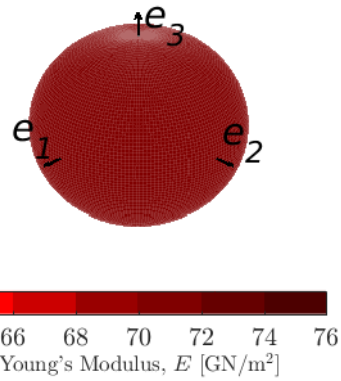

(f) 500-grain polycrystal of Aluminium.

Figure 5.20: Spatial distribution of the Young's modulus of polycrystals of Aluminium.

to describe the impact of considering different single-crystals (characterized by specific elastic anisotropies) on the evolution of the Young's modulus range with the number of grains. To put it another way, we want to express the dimensionless Young's modulus average and standard deviation as functions of the number of grains and of the elastic anisotropy of the constituent crystal. To that end, polycrystal meshes of Silver, Gold, Iron, Nickel and Lead were analysed: the underlying results were compiled in Figures 5.22 and 5.23 (together with the ones which we have already showed for Copper and Aluminium). In addition, rational and power functions were also included in those Figures, as they, respectively, provide the best fits for the evolution of the dimensionless Young's modulus average and standard deviation for each of the materials considered. The rational and power functions considered are of the form:

$$\mathrm{AVG}(E_{\mathrm{NG}})_{dim} = \frac{p_3}{\mathrm{NG}} + p_4, \tag{5.17}$$

$$\mathrm{STD}(E_{\mathrm{NG}})_{dim} = p_5 \cdot (\mathrm{NG})^{p_6}. \tag{5.18}$$

The parameters p_3, p_4, p_5 and p_6 were identified by least square fitting for all materials. After that, we have tried to find a relation between these parameters and the elastic anisotropy of the cubic crystals – those relations can be seen in Figures 5.24 to 5.27[8].

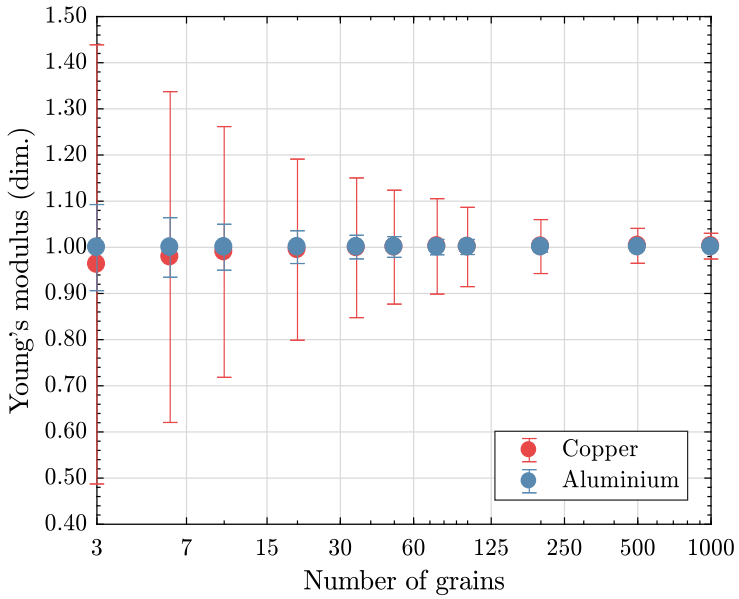

Figure 5.21: Evolution of the dimensionless Young's modulus range with the number of grains for polycrystals of Copper and Aluminium.

[8]In some Figures, "dev." is used as an abbreviation of "deviation".

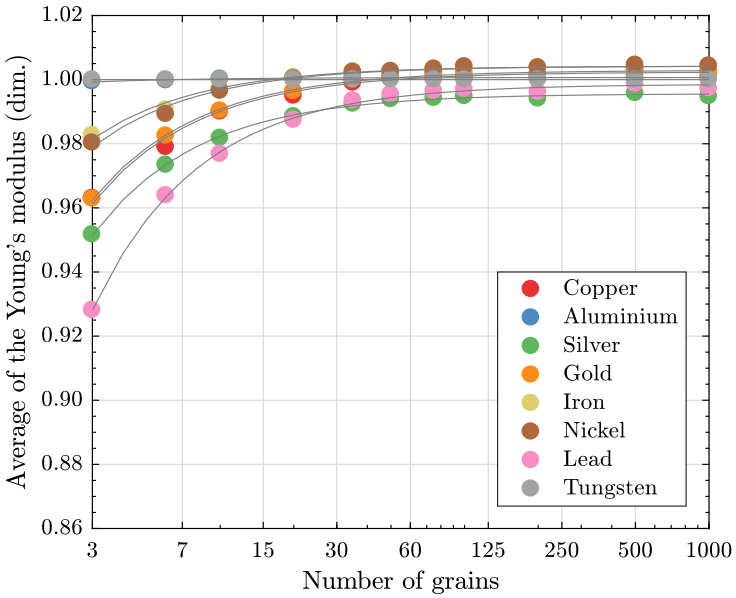

Figure 5.22: Evolution of the dimensionless Young's modulus average with the number of grains for several cubic crystal aggregates.

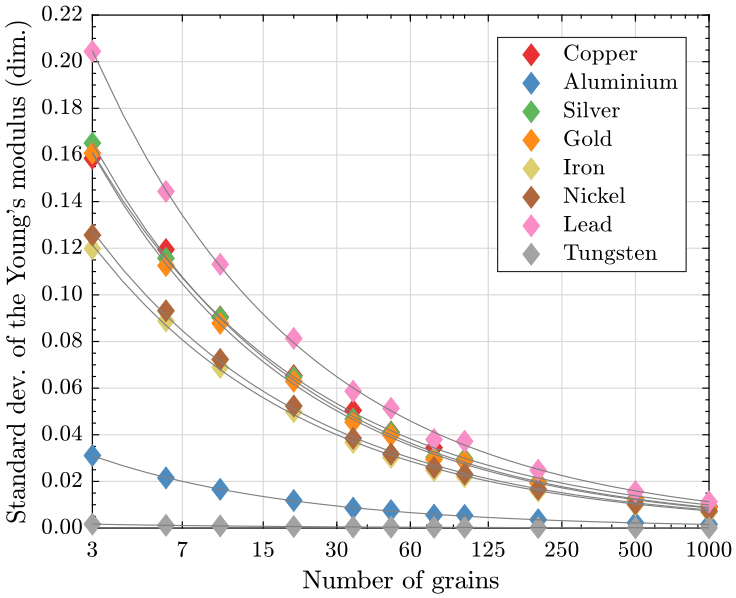

Figure 5.23: Evolution of the dimensionless Young's modulus standard deviation with the number of grains for several cubic crystal aggregates.

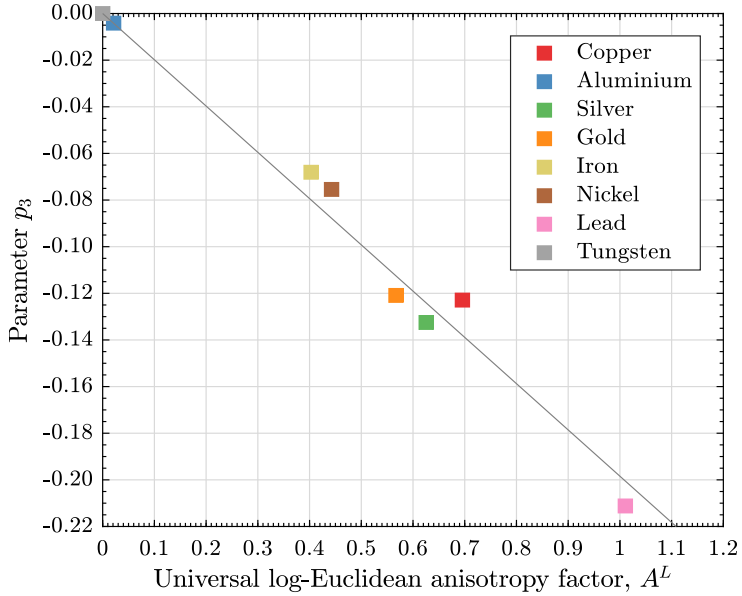

Figure 5.24: Dependency of the parameter p_3 on the elastic anisotropy of the single-crystals.

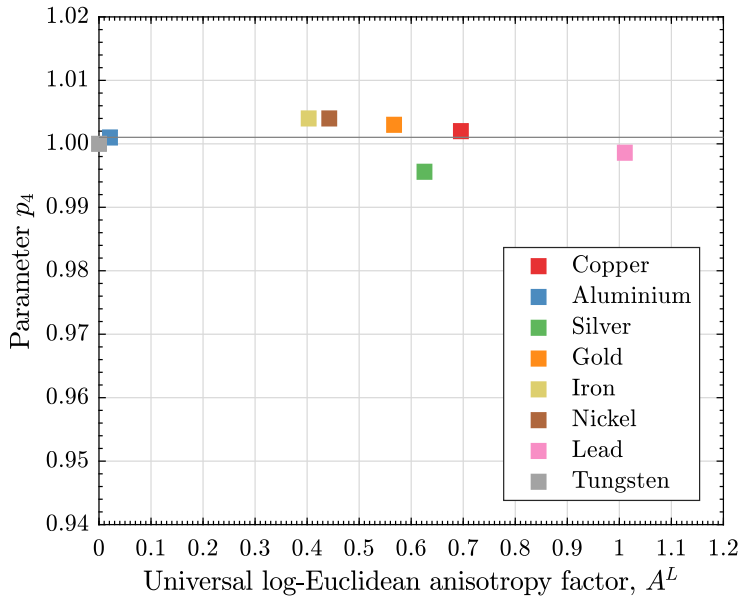

Figure 5.25: Dependency of the parameter p_4 on the elastic anisotropy of the single-crystals.

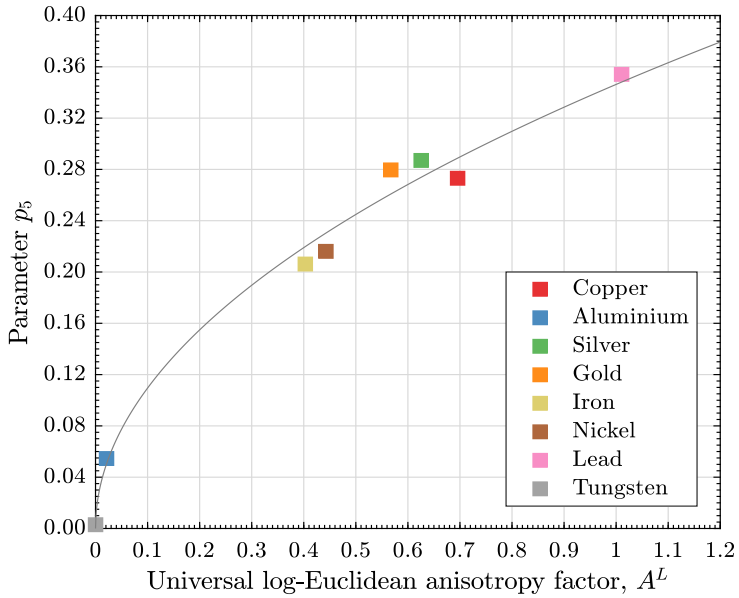

Figure 5.26: Dependency of the parameter p_5 on the elastic anisotropy of the single-crystals.

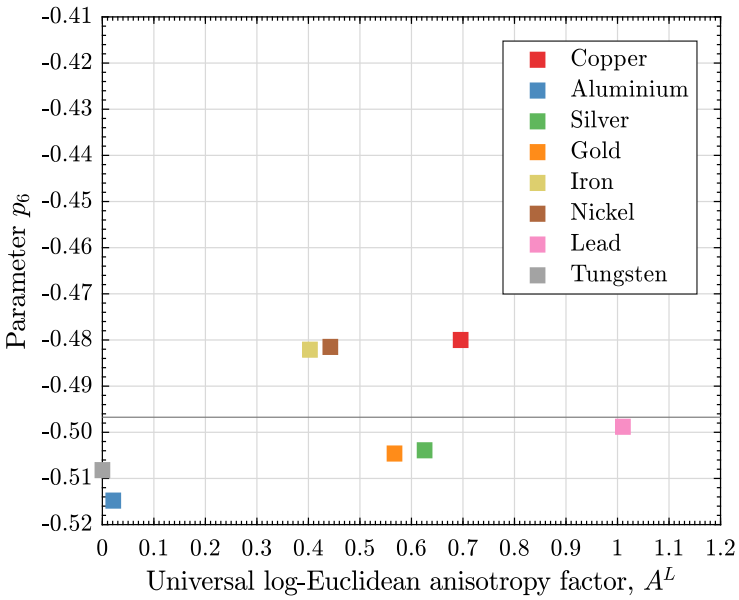

Figure 5.27: Dependency of the parameter p_6 on the elastic anisotropy of the single-crystals.

Analytical expressions for the parameters p_3, p_4, p_5 and p_6 were generated using least squares fitting, so that we have:

$$p_3 = -0.20 \cdot A^{\mathrm{L}}, \tag{5.19}$$

$$p_4 = 1.00, \tag{5.20}$$

$$p_5 = 0.35 \cdot \sqrt{A^{\mathrm{L}}}, \tag{5.21}$$

$$p_6 = -0.50. \tag{5.22}$$

In such case, the expressions for the dimensionless average and standard deviation of the Young's modulus may be rewritten in terms of the number of grains of the aggregate and of the elastic anisotropy:

$$\mathrm{AVG}(E_{\mathrm{NG}})_{dim} = -\frac{0.20 \cdot A^{\mathrm{L}}}{\mathrm{NG}} + 1.00, \tag{5.23}$$

$$\mathrm{STD}(E_{\mathrm{NG}})_{dim} = 0.35 \cdot \sqrt{\frac{A^{\mathrm{L}}}{\mathrm{NG}}}. \tag{5.24}$$

These expressions are in line with what was anticipated: on the one hand, the average Young's modulus is fundamentally constant and even in case polycrystal meshes with few grains are considered, its value is a good estimate for the isotropic Young's modulus; on the other hand, the standard deviation of the Young's modulus is directly proportional to the square root of the log-Euclidean anisotropy factor of the single-crystal and inversely proportional to the square root of the number of grains (so that the anisotropy of the single-crystal increases the standard deviation of the Young's modulus for a particular number of grains). In addition, it must be noted that the manipulation of these two expressions allows the characterisation of the elastic isotropic response of polycrystals using the procedure described in Section 5.1.1. Knowing that, in Section 5.2.1, an expression for the minimum number of grains required to obtain the isotropic behaviour is suggested, while in Section 5.2.2 we discuss the value of the numerical isotropic elastic parameters obtained (with particular emphasis being placed on considering the effect of mesh refinement on the numerical prediction of the isotropic Young's modulus).

5.2 Characterisation of the Elastic Response of Isotropic Polycrystals

The characterisation of isotropic elastic polycrystals through computational homogenisation procedures comprises two main steps:

1. Establishing the minimum number of grains which leads to the isotropic elastic behaviour (that is, the minimum size of the RVE for isotropic elastic polycrystals);
2. Defining the isotropic elastic parameters (i.e., the effective elastic response).

In this Section, these topics are addressed, with particular emphasis being placed on the former, since the latter has already been covered. In fact, for cubic crystal aggregates, analytical methods have simple mathematical expressions and, therefore, are widely used; in particular, the self-consistent scheme, which ensures the continuity of the strain and stress fields, has been supported by both numerical (Ranganathan and Ostoja-Starzewski, 2008a) and experimental (Kube and de Jong, 2016) studies. Thus, rather than trying to define new expressions for the elastic properties of isotropic polycrystals, we have attempted to ascertain whether our numerical method could provide results similar to the ones given by analytical methods (especially, the self-consistent approach). By doing that, we were essentially evaluating the accuracy of our numerical procedure (involving structured meshes) and also validating the whole framework. Note that the relevance of being aware of possible sources of numerical error must not be overlooked: as mentioned in Section 4.3, analytical methods do not always yield convenient and/or accurate estimates for the elastic properties and, in those cases, numerically-derived expressions may play a pivotal role in the characterisation of certain materials, so that it remains important to ensure the quality of the numerical results.

On balance, this Section essentially involves the interpretation and aggregation of the information presented previously. To be precise, in Section 5.2.1, we mostly manipulate expression (5.24), proposing a model for predicting the minimum RVE size of isotropic polycrystals, whereas, in Section 5.2.2, we consider the discussion made in Section 5.1.3 (regarding the impact of the mesh), as well as equation (5.23), and we briefly comment on the accuracy of using structured meshes in the determination of isotropic elastic parameters.

5.2.1 Determination of the Mininum Size of the RVE

Establishing the minimum size of the RVE for isotropic elastic polycrystalline materials is a central issue within the numerical characterisation of the constitutive behaviour of many components. In the context of numerical micromechanical studies, it is of paramount concern to establish the minimum number of grains which provides an isotropic behaviour, within a certain tolerance, due to the fact that less computational resources are needed when polycrystalline meshes with fewer grains are examined (supposing that the number of elements per grain is kept constant); simultaneously, the same computational effort can be applied to perform simulations on more refined meshes (which might be important, for instance, to study local phenomena). Another reason for the determination of the minimum number of grains that yields an isotropic response is related to the characterisation of the elastic behaviour of MEMS[9]. These micro-devices, which combine electrical and mechanical components, range from few micrometers to millimetres (Prime Faraday, 2002), so

[9] A detailed revision about MEMS is made in Prime Faraday (2002).

that they contain only a small number of grains (Jöchen, 2013). Therefore, in order to characterize their mechanical response, an important step involves evaluating if the number of grains of a certain micro-system leads to an isotropic or anisotropic response: in case we can answer this question, the experimental or numerical tests that have to be performed to determine their elastic properties may be reduced and their design and manufacturing optimized.

Amongst the most relevant contributions made to the prediction of the minimum number of grains required to estimate the effective isotropic properties of textureless polycrystals comprising cubic crystals, we highlight:

- The pioneering work of Nygårds (2003) who used the finite element method to establish a relation between the number of grains necessary to get representative grain structures and the anisotropy of the constituent crystal (for a given level of precision). In order to reach his final expression, the standard deviation of the von Mises equivalent stress was compared, for several loading cases, to a reference value (which was the average equivalent von Mises stress obtained with polycrystals with 500 grains).

- The work of El Houdaigui et al. (2007) where several numerical tests involving different boundary conditions were performed to estimate the effective isotropic properties of Copper polycrystals. A parallel can be drawn between the strategy followed by El Houdaigui et al. (2007) and the one implemented in this work because the minimum size of the RVE was deduced from the standard deviation of the apparent shear modulus (so that several realisations of polycrystals of Copper were considered). Moreover, in that work, an analytical expression is presented to estimate the minimum number of grains in terms of the number of realisations considered, the level of precision and the average and the standard deviation of the apparent shear modulus;

- The work of Ranganathan and Ostoja-Starzewski (2008a), where the main concept relies on assigning a certain value for a scaling function, so that the isotropic and anisotropic regions are separated. This scaling function is obtained from the numerical computation of the displacement and the traction controlled shear modulus in a procedure which is in line with the Hill-Mandel principle of macro-homogeneity and that links the scale of observation (number of grains of the aggregate) with the anisotropy of the single-crystals;

One common feature between the approaches described previously and the one adopted in this work is that, at some point of the procedure, a certain tolerance/error margin has to be specified in order to estimate the minimum size of the isotropic Representative Volume Element. In fact, note that expression (5.24) by itself does not shed light into the minimum number of grains required to obtain isotropic responses, unless we define a certain value for the maximum admissible dimensionless standard

deviation (which is a counterpart to the tolerance E_{tol} introduced in Figure 5.1) – this is because a null dimensionless standard deviation is never verified except when the number of grains is infinite or when the crystal is isotropic. Thus, the establishment of an appropriate value for the maximum dimensionless standard deviation is fundamental to the determination of the minimum RVE size. If we represent this value as $\mathrm{STD}(E_{\mathrm{NG}})_{dim-iso}$, Equation (5.24) may be modified, so that a more convenient expression to estimate the minimum number of grains required to obtain an isotropic response is derived:

$$\mathrm{NG}_{iso} = 0.12 \cdot \frac{A^{\mathrm{L}}}{\left(\mathrm{STD}(E_{\mathrm{NG}})_{dim-iso}\right)^2}. \tag{5.25}$$

As may be seen, the number of grains is inversely proportional to the square of our precision measure, $\mathrm{STD}(E_{\mathrm{NG}})_{dim-iso}$. If, for instance, a value of 1% for this parameter is adopted, the curve depicted in Figure 5.28 is obtained. This curve separates the region where the effective properties can be used (isotropic region) from the domain in which the apparent elastic parameters must be calculated (anisotropic domain). Consequently, it might be taken as a reference curve for the design of MEMS, since it clearly identifies the cases in which is valid to use the isotropic properties (that is, the cases in which the anisotropy of the aggregate can be neglected). Given that most MEMS consist of polycrystals of Silicon ($\mathsf{C}_{11} = 166.2$ GN/m^2; $\mathsf{C}_{12} = 64.4$ GN/m^2; $\mathsf{C}_{44} = 79.8$ GN/m^2 (Freund and Suresh, 2004); $A^{\mathrm{L}} = 0.11$), it is interesting to note that, for those aggregates, the isotropic properties can be used when the number of grains is greater than 132 (considering $\mathrm{STD}(E_{\mathrm{NG}})_{dim-iso} = 1\%$).

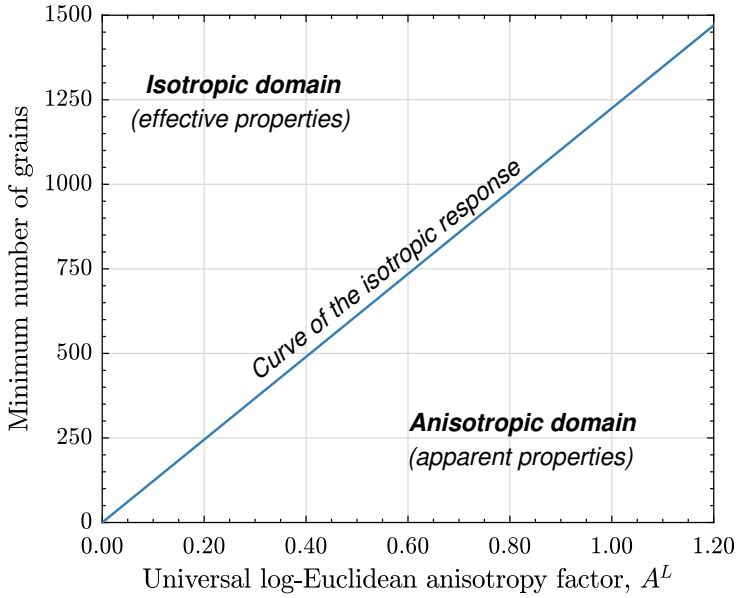

Figure 5.28: Estimate, using equation (5.25), of the number of grains required to obtain isotropic responses ($\mathrm{STD}(E_{\mathrm{NG}})_{dim-iso} = 1\%$).

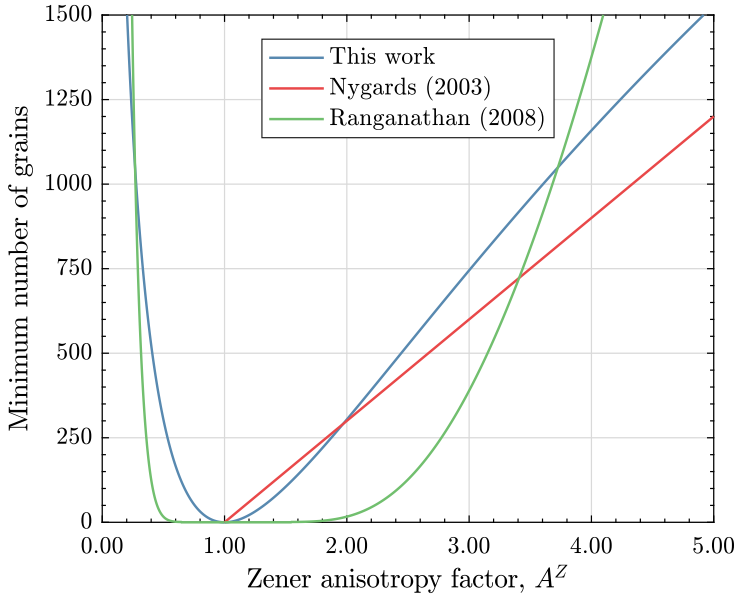

Figure 5.29: Comparison between models developed to predict the minimum number of grains which yield isotropic responses.

It is relevant to compare the model presented here with others existing in the literature, with the caveat that the conclusions drawn will be strongly affected by the value adopted for the dimensionless standard deviation (the value of 1% is maintained in what follows). In Figure 5.29, the minimum number of grains required to obtain isotropic responses is represented in terms of the Zener anisotropy index for our model[10] and for the models of Ranganathan and Ostoja-Starzewski (2008a) and Nygårds (2003). As can be seen, a good agreement is found between our approach and the one of Ranganathan and Ostoja-Starzewski (2008a) when the Zener anisotropy factor is smaller than one; on the other hand, when $A^{\mathrm{Z}} > 1$, the curve proposed by Nygårds (2003) is fairly similar to the one which results from the model here outlined. Despite that, we must highlight that our model involves the simplest mathematical expression and, since it is defined in terms of the log-Euclidean anisotropy index, it may be used with all types of polycrystals, regardless of the symmetry of the single-crystal[11]. Note that our work has, therefore, played a role in understanding the relation between the anisotropy and the number of grains required to obtain isotropic responses (for instance, the model of Nygårds (2003) does not define the relation between these parameters when $A^{\mathrm{L}} < 1$; on top of that, the proposal of Ranganathan and Ostoja-Starzewski (2008a) seems to underestimate the number of grains required for aggregates comprising crystals with $A^{\mathrm{L}} \in]1, 3[$ and to overestimate

[10]The number of grains necessary to obtain isotropic responses can be estimated from our model as a function of the Zener anisotropy index in case we combine expressions (4.58) and (5.25).

[11]Nonetheless, a question arises whether it can still provide accurate estimates in case other crystal symmetries are studied.

the influence of high crystalline anisotropies – $A^{\mathrm{L}} > 4$ – on the minimum size of the RVE). Furthermore, it is worth mentioning that our model also compares reasonably with the proposal of El Houdaigui et al. (2007) (which is only valid for polycrystals of Copper): indeed, our model suggest considering one realisation with 840 grains, while the former states that studying 10 realisations of polycrystals of Copper with 450 grains yields the isotropic properties.

5.2.2 Remarks on the Numerical Isotropic Elastic Parameters

The determination of the elastic properties of isotropic polycrystals has received widespread attention in the past, with several analytical methods having been developed (we reviewed the most relevant ones in Section 4.3). In this work, the accuracy of these analytical proposals has been verified, since numerical estimates for the Young's modulus which are essentially coincident with the upper Hashin-Shtrikman bound have been obtained. A similar convergence tendency was reported by Böhlke et al. (2010), who also performed numerical simulations on block-structured polycrystalline meshes, and found estimates for the isotropic Young's modulus close to the aforementioned bound. On the contrary, Fritzen et al. (2009) – who studied the elastic response of 3D unstructured periodic polycrystalline meshes – acquired estimates for the isotropic elastic properties which were located between the fifth-order bounds of Zeller and Dederichs (1973). This suggests that the meshing strategy directly affects the values obtained for the isotropic elastic properties. This effect can be reduced in case refined structured meshes are employed or polycrystals composed of single-crystals with low anisotropies are being analysed, as detailed in Section 5.1.3. In fact, using expression (5.12) we can estimate the error associated with the isotropic elastic properties of polycrystals comprising grains whose anisotropy is A^{L}: for Copper, the relative error associated with the prediction of the isotropic parameters (due to the mesh size) is of 1.74% (note that $n_{epg} \approx 10$). This error is below the ratio $(E^{\mathrm{HS}^+} - E^{\mathrm{SC}})/E^{\mathrm{SC}}$, so that a question arises whether using block-structured meshes can provide estimates coincident with the self-consist one. On the whole, we must be aware of the fact that structured meshes may not be able to adequately represent local phenomena, so that, in case the anisotropy of the grains is relevant, the estimates obtained for the isotropic properties may not be accurate. As a consequence, when the main idea of a numerical study is to derive accurate numerically-based expressions for the overall elastic properties of a polycrystalline specimen, we must use unstructured meshes, minimizing the error associated with the incorrect representation of the grain boundaries. Note that this aspect must not be overlooked, since in many cases there are no analytical expressions available and the development of laws based on the numerical data is the only way of predicting the elastic properties (this is the case, for example, of the work of Kamaya (2009) who derived expressions for the overall Young's modulus of textured polycrystals). That being said, it is apparent that a more accurate version of equation (5.23)

could have been found in case unstructured meshes (or more refined structured meshes) had been employed: notwithstanding, the accuracy thus obtained is not worth the additional computational cost, since the value of the isotropic properties of cubic-crystal aggregates is well-established and due to the fact that our prediction already involves an error smaller than 2%. In reality, it is important to keep in mind that elastic properties are computed from homogenized quantities and that most crystals with practical interest have relatively low anisotropies, making the errors in the elastic properties resulting from unrefined structured meshes markedly low. The adoption of a certain meshing strategy and level of refinement for characterising the elastic isotopic response of polycrystalline specimens must consider the main objectives of the study, the time available and the precision required.

5.3 Characterisation of the Elastic Response of Anisotropic Polycrystals

In Section 5.1, we have developed a procedure which can be employed to determine the minimum number of grains necessary to obtain the isotropic response of polycrystals, as well as the elastic (isotropic) properties. This method involves the analysis of the average and the standard deviation of the Young's modulus for 100 realisations of polycrystals containing NG grains, so that it allows the derivation of upper and lower bounds for the Young's modulus of anisotropic polycrystals comprising a generic number of grains. In fact, if we combine equations (5.2), (5.23) and (5.24), the minimum and maximum possible values for the Young's modulus $E(\boldsymbol{d})$ (denoted, respectively, E^{-}_{NG} and E^{+}_{NG}) of polycrystals with NG grains can be defined:

$$E^{-}_{\mathrm{NG}} = \left(1.00 - \frac{0.20 \cdot A^{\mathrm{L}}}{\mathrm{NG}} - 3 \cdot 0.35 \cdot \sqrt{\frac{A^{\mathrm{L}}}{\mathrm{NG}}}\right) \cdot E^{\mathrm{HS}^{+}}, \tag{5.26}$$

$$E^{+}_{\mathrm{NG}} = \left(1.00 - \frac{0.20 \cdot A^{\mathrm{L}}}{\mathrm{NG}} + 3 \cdot 0.35 \cdot \sqrt{\frac{A^{\mathrm{L}}}{\mathrm{NG}}}\right) \cdot E^{\mathrm{HS}^{+}}. \tag{5.27}$$

Expressions (5.26) and (5.27) shed light into the characterisation of the elastic behaviour of anisotropic polycrystals, as they postulate that for a particular number of grains NG, these upper and lower bounds of the Young's modulus are only dependent on the crystallographic anisotropy (i.e., they do not consider the morphological anisotropy). This is a consequence of considering a significant number of realisations and analysing them in a way similar to the one described in Section 5.1.2: for each value of NG, recall that we grouped the values of the Young's modulus (in all directions) of all the 100 distinct realisations and calculated this set's average and standard deviation. An important point to make is that this procedure can be employed to derive bounds for other elastic properties, making room for adapting the methodology to determine bounds on the 21 independent elastic constants of

anisotropic polycrystals.

In this Section, we approach the elastic response of anisotropic polycrystals by defining bounds on their 21 independent elastic parameters. In short, the previously introduced procedure is adapted: as can be seen in the next Section, since the range of some elastic constants is similar, only 4 different expressions have been used to define the bounds of the 21 elastic stiffnesses (Section 5.3.2).

5.3.1 Identification of Similar Elastic Constants

In the most general case, when a random realisation of an anisotropic polycrystal is studied, it is expected that each elastic stiffness constant will be different. Nonetheless, when several realisations are inspected, the average of the elastic constants of the same type (for instance, the average of all constants C_{11}) leads to an estimate of the isotropic elastic constants and, therefore, some of the averages of the elastic constants are similar (e.g. the averages of constants C_{11} and C_{22}). Moreover, it is reasonable to assume that the standard deviations of the elastic constants with identical average values are also similar[12]. In light of that, four groups of similar elastic constants arise:

1. *Group* C^{11}, which includes the elastic constants C_{11}, C_{22} and C_{33}. For isotropic materials, we have[13]:

$$\mathsf{C}_{11} = \mathsf{C}_{22} = \mathsf{C}_{33} = \frac{E \cdot (1-\nu)}{(1+\nu) \cdot (1-2\nu)}. \tag{5.28}$$

2. *Group* C^{12}, which contains the elastic constants C_{12}, C_{13} and C_{23}. For isotropic materials, these elastic constants verify the following equation:

$$\mathsf{C}_{12} = \mathsf{C}_{13} = \mathsf{C}_{23} = \frac{E \cdot \nu}{(1+\nu) \cdot (1-2\nu)}. \tag{5.29}$$

3. *Group* C^{44}, encompassing the elastic constants C_{44}, C_{55} and C_{66}. For isotropic materials, it is known that:

$$\mathsf{C}_{44} = \mathsf{C}_{55} = \mathsf{C}_{66} = \frac{E}{2 \cdot (1+\nu)}. \tag{5.30}$$

4. *Group* C^{14}, where the remaining 12 elastic constants are incorporated. They are all null for isotropic materials.

The average and the standard deviation of the 21 constants (or more precisely, of the sets comprising each one of the 21 elastic constants of the 100 realisations) are

[12] These averages and standard deviations are calculated in a similar way to the one described in Section 5.1.2, albeit concerning the 21 elastic constants instead of the Young's modulus. That is, 21 sets comprising 100 values – each one associated with one elastic constant C_{ij} – are considered; then, for each one of the 21 sets, a value for the average and standard deviation is computed.

[13] In equations (5.28) to (5.30), note that E and ν represent the isotropic Young's modulus and Poisson's ratio.

depicted in Figure 5.30 for polycrystals of Copper with different numbers of grains (the results generated with the polycrystal meshes of 10 elements per grain). As we may see, similar elastic constants were grouped (according to the discussion made above) and for each number of grains, the average of the values was calculated, so

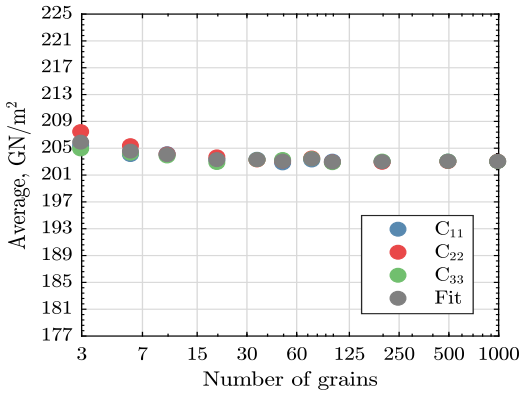

(a) Average of the C^{11}-type constants.

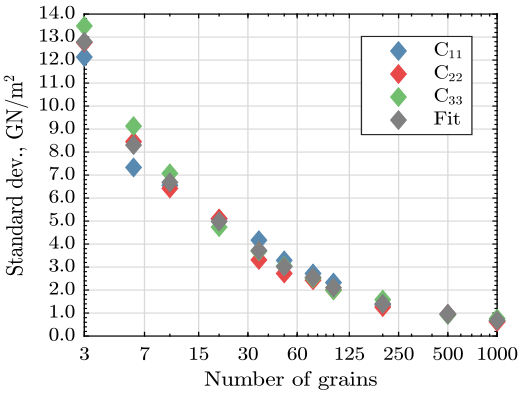

(b) Standard dev. of the C^{11}-type constants.

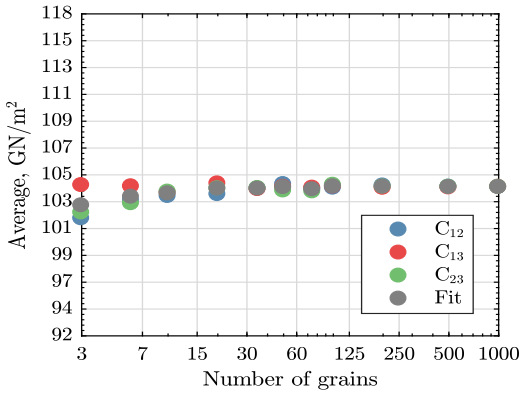

(c) Average of the C^{12}-type constants.

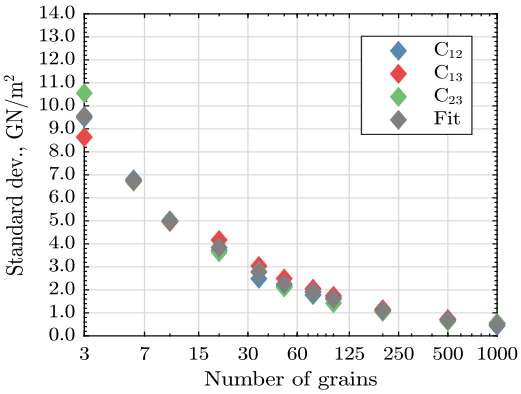

(d) Standard dev. of the C^{12}-type constants.

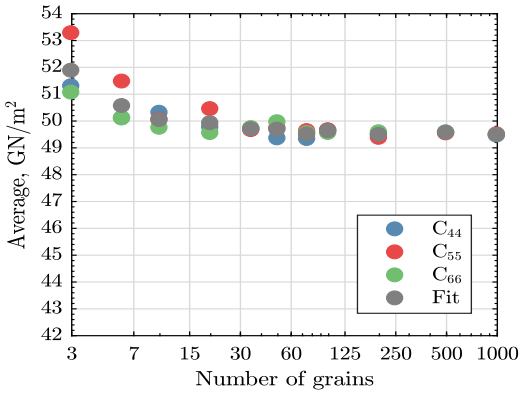

(e) Average of the C^{44}-type constants.

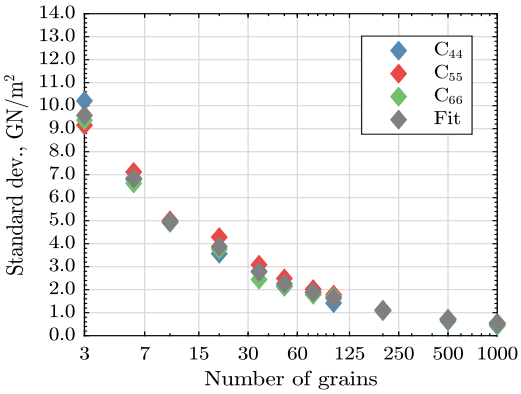

(f) Standard dev. of the C^{44}-type constants.

Figure 5.30: Relation between the average/standard deviation of the elastic constants of anisotropic polycrystals of Copper with the number of grains.

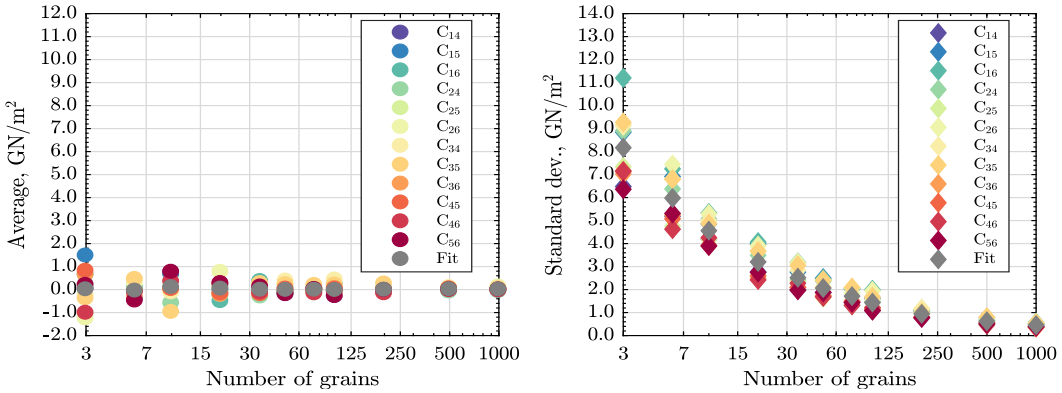

(g) Average of the C^{14}-type constants. (h) Standard dev. of the C^{14}-type constants.

Figure 5.30: Relation between the average/standard deviation of the elastic constants of anisotropic polycrystals of Copper with the number of grains (cont.).

that "fitting" points are obtained (identified by grey markers). These fitting points compare reasonably to the evolution of the elastic constants, so that the analysis of the 21 elastic constants was reduced to the study of the evolution of the fitting points with the number of grains (that is the subject of discussion in the following Section).

5.3.2 Determination of Bounds for the Elastic Constants

It is unsurprising that the average of the elastic constants is near the self-consistent estimate. In such instance, and in order to allow straightforward comparisons among the evolution of the elastic constants of different materials, we must consider dimensionless measures for the average and the standard deviation:

$$\mathrm{AVG}(\mathsf{C}^{ij}_{\mathrm{NG}})_{dim} = \frac{\mathrm{AVG}(\mathsf{C}^{ij}_{\mathrm{NG}})}{\mathsf{C}^{\mathrm{SC}}_{ij}}, \quad ij \in \{11, 12, 44\}, \tag{5.31}$$

$$\mathrm{STD}(\mathsf{C}^{ij}_{\mathrm{NG}})_{dim} = \frac{\mathrm{STD}(\mathsf{C}^{ij}_{\mathrm{NG}})}{\mathsf{C}^{\mathrm{SC}}_{ij}}, \quad ij \in \{11, 12, 44\}. \tag{5.32}$$

Since $\mathsf{C}^{\mathrm{SC}}_{14} = 0$, for the C^{14}-type elastic constants, we used:

$$\mathrm{AVG}(\mathsf{C}^{14}_{\mathrm{NG}})_{dim} = \frac{\mathrm{AVG}(\mathsf{C}^{14}_{\mathrm{NG}})}{\mathsf{C}^{\mathrm{SC}}_{11}}, \tag{5.33}$$

$$\mathrm{STD}(\mathsf{C}^{14}_{\mathrm{NG}})_{dim} = \frac{\mathrm{STD}(\mathsf{C}^{14}_{\mathrm{NG}})}{\mathsf{C}^{\mathrm{SC}}_{11}}. \tag{5.34}$$

In these equations, $\mathrm{AVG}(\mathsf{C}^{ij}_{\mathrm{NG}})$ and $\mathrm{STD}(\mathsf{C}^{ij}_{\mathrm{NG}})$ denote the average of the averages and the average of the standard deviations of the C^{ij}-type elastic constants (i.e, they identify the values ascribed to the C^{ik} fitting points in the representations of the average and of the standard deviation of the elastic constants), whilst $\mathrm{AVG}(\mathsf{C}^{ij}_{\mathrm{NG}})_{dim}$

and $\mathrm{STD}(\mathsf{C}^{ij}_{\mathrm{NG}})_{dim}$ are their dimensionless counterparts. Using these measures, we may analyse the information shown in Figure 5.30 where it becomes easier to study the influence of the single-crystal considered. In order to extract general conclusions about the relation between the dimensionless measures and the elastic anisotropy of

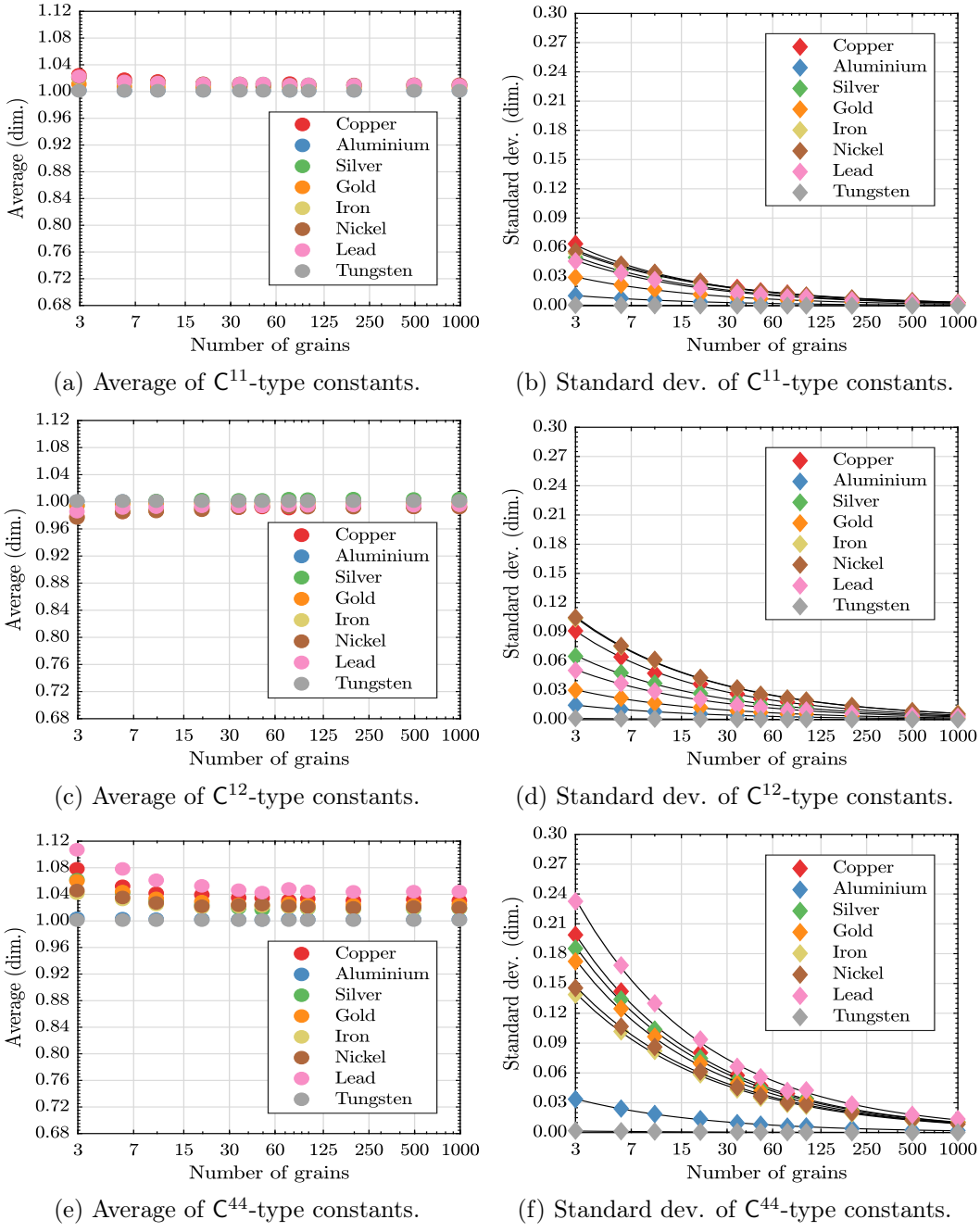

(a) Average of C^{11}-type constants.

(b) Standard dev. of C^{11}-type constants.

(c) Average of C^{12}-type constants.

(d) Standard dev. of C^{12}-type constants.

(e) Average of C^{44}-type constants.

(f) Standard dev. of C^{44}-type constants.

Figure 5.31: Relation between the dimensionless average/standard deviation of the elastic constants of several anisotropic polycrystals with the number of grains.

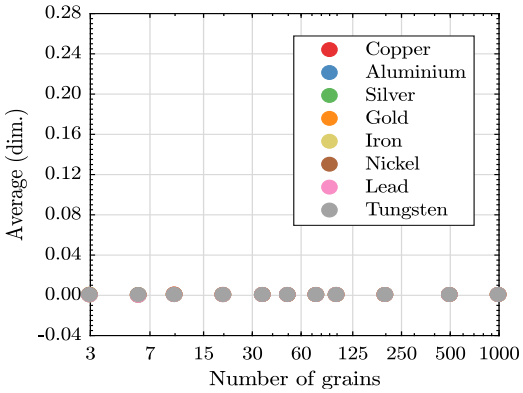

(g) Average of C^{14}-type constants.

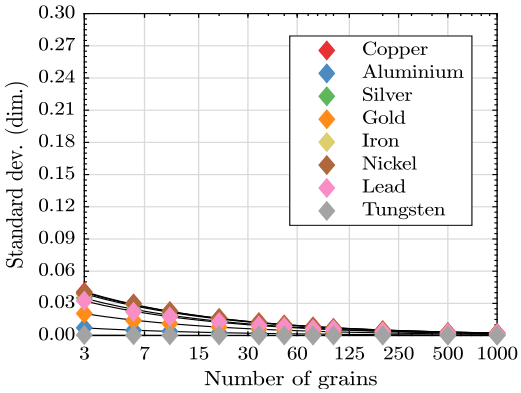

(h) Standard dev. of C^{14}-type constants.

Figure 5.31: Relation between the dimensionless average/standard deviation of the elastic constants of several anisotropic polycrystals with the number of grains (cont.).

the single-crystals, we calculated these for different polycrystal aggregates and compiled the results in Figure 5.31.

At this point, our focus is set on explaining the evolution of the dimensionless parameters from the anisotropy of the single-crystals. To simplify this process, only the dimensionless standard deviation was considered, because it is well-established that the average of the elastic constants tends to the self-consistent estimate[14]. Having said that, the dimensionless standard deviation can be expressed in terms of the number of grains in the following fashion:

$$\mathrm{STD}(\mathsf{C}^{ij}_{\mathrm{NG}})_{dim} = \mathrm{NG}^{p_7} \cdot p_8. \tag{5.35}$$

We have tried to define the parameters p_7 and p_8 in terms of the anisotropy of the constituent crystal – the graphical representation of the relations found is presented in Figure 5.32.

Table 5.4: Parameter p_9 associated with each group of elastic constants.

C^{ij}-type constants	p_9
C^{11}	0.11
C^{12}	0.16
C^{44}	0.40
C^{14}	0.07

[14]This is not exactly what happens in Figure 5.31, but, as we mentioned in 5.2.2, the discrepancies come from the fact that we are using low refinement structured meshes.

Generally speaking, it was verified that:

$$p_7 \approx -0.50, \tag{5.36}$$

$$p_8 = p_9 \cdot \sqrt{A^{\mathrm{L}}}, \tag{5.37}$$

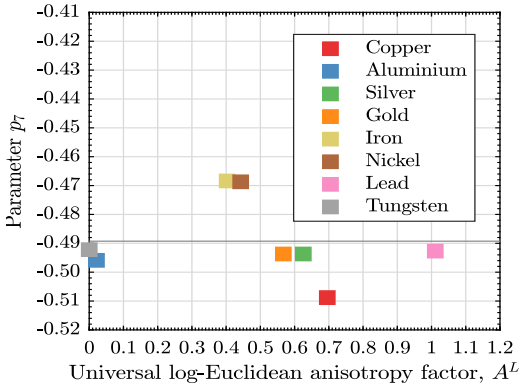

(a) Parameter p_7 for C^{11}-type constants.

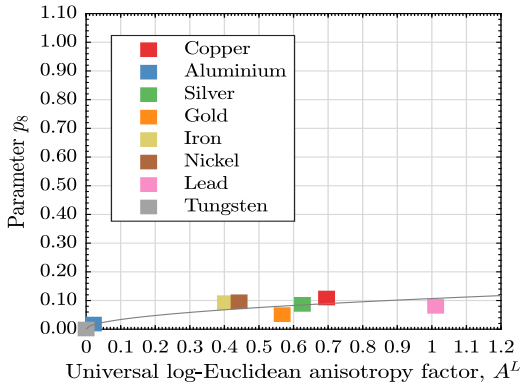

(b) Parameter p_8 for C^{11}-type constants.

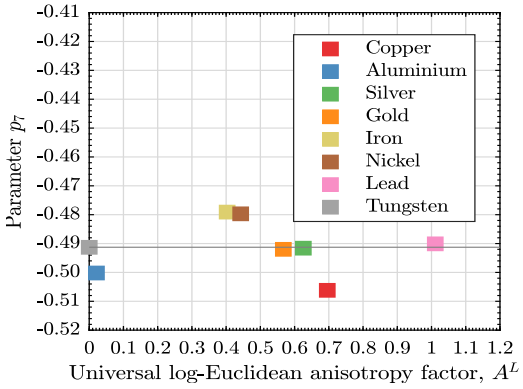

(c) Parameter p_7 for C^{12}-type constants.

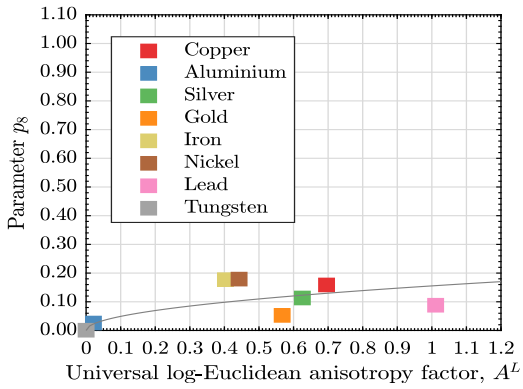

(d) Parameter p_8 for C^{12}-type constants.

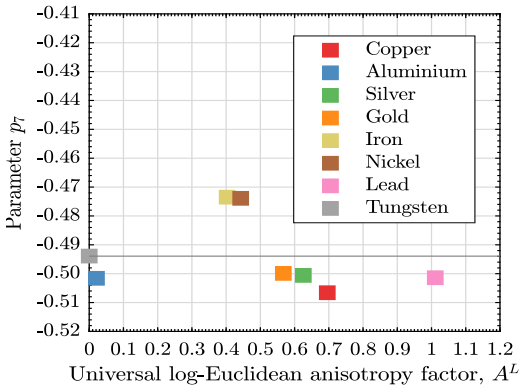

(e) Parameter p_7 for C^{44}-type constants.

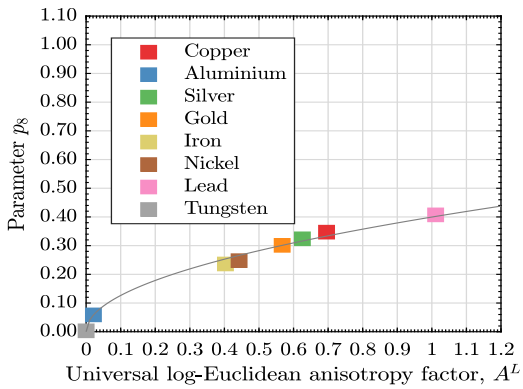

(f) Parameter p_8 for C^{44}-type constants.

Figure 5.32: Dependency of the parameters p_7 and p_8, associated with each of the elastic constant groups, on the elastic anisotropy of the single-crystals.

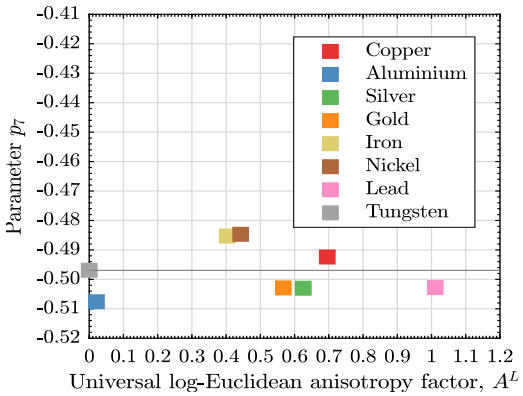

(g) Parameter p_7 for C^{14}-type constants.

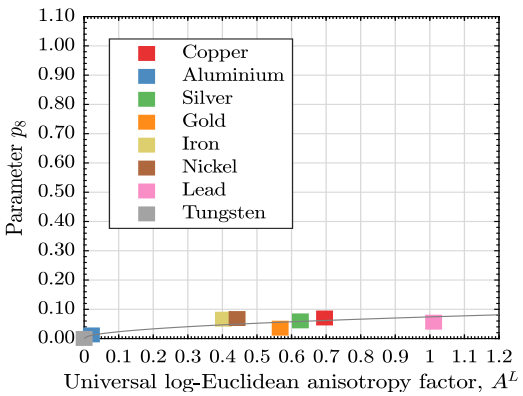

(h) Parameter p_7 for C^{14}-type constants.

Figure 5.32: Dependency of the parameters p_7 and p_8, associated with each of the elastic constant groups, on the elastic anisotropy of the single-crystals (cont.).

so that in all cases it was registered that the dimensionless standard deviation is (approximately) inversely proportional to the square root of the number of grains. The parameter p_9 which is necessary in equation (5.37) is presented in Table 5.4 for each of the elastic constant groups.

Given all these points, we might finally define lower and upper bounds for each type of elastic constants (respectively identified by the superscripts $-$ and $+$):

$$\mathsf{C}^{11,-} = \left(1.00 - 3 \cdot 0.11 \cdot \sqrt{\frac{A^{\mathrm{L}}}{\mathrm{NG}}}\right) \cdot \mathsf{C}^{\mathrm{SC}}_{11}, \tag{5.38}$$

$$\mathsf{C}^{11,+} = \left(1.00 + 3 \cdot 0.11 \cdot \sqrt{\frac{A^{\mathrm{L}}}{\mathrm{NG}}}\right) \cdot \mathsf{C}^{\mathrm{SC}}_{11}, \tag{5.39}$$

$$\mathsf{C}^{12,-} = \left(1.00 - 3 \cdot 0.16 \cdot \sqrt{\frac{A^{\mathrm{L}}}{\mathrm{NG}}}\right) \cdot \mathsf{C}^{\mathrm{SC}}_{12}, \tag{5.40}$$

$$\mathsf{C}^{12,+} = \left(1.00 + 3 \cdot 0.16 \cdot \sqrt{\frac{A^{\mathrm{L}}}{\mathrm{NG}}}\right) \cdot \mathsf{C}^{\mathrm{SC}}_{12}, \tag{5.41}$$

$$\mathsf{C}^{44,-} = \left(1.00 - 3 \cdot 0.40 \cdot \sqrt{\frac{A^{\mathrm{L}}}{\mathrm{NG}}}\right) \cdot \mathsf{C}^{\mathrm{SC}}_{44}, \tag{5.42}$$

$$\mathsf{C}^{44,+} = \left(1.00 + 3 \cdot 0.40 \cdot \sqrt{\frac{A^{\mathrm{L}}}{\mathrm{NG}}}\right) \cdot \mathsf{C}^{\mathrm{SC}}_{44}, \tag{5.43}$$

$$\mathsf{C}^{14,-} = -3 \cdot 0.07 \cdot \sqrt{\frac{A^{\mathrm{L}}}{\mathrm{NG}}} \cdot \mathsf{C}^{\mathrm{SC}}_{11}, \tag{5.44}$$

$$\mathsf{C}^{14,+} = 3 \cdot 0.07 \cdot \sqrt{\frac{A^{\mathrm{L}}}{\mathrm{NG}}} \cdot \mathsf{C}^{\mathrm{SC}}_{11}. \tag{5.45}$$

Chapter 6

On the Determination of the Yielding Response of Polycrystalline Aggregates

In Chapter 4, we discussed how multi-scale schemes based on computational homogenisation can be used for the determination of the elastic behaviour of polycrystalline materials, while in Chapter 5 we used that framework to derive critical relations between the micro- and the macro-parameters, so that the macroscopic elastic response of polycrystals could be explained from the underlying microscopic features. A question that often follows the characterisation of the linear elastic response concerns the definition of the critical loading scenarios in which that framework ceases to be valid. To put it another way, the computation and the analysis of the elastic parameters must be accompanied with the definition of the domain (i.e., stress and strain conditions) where they are applicable. In practice, the set of admissible stress states is contained in a hypersurface defined in the Cauchy stress space, the so-called *yield surface*. This surface separates the elastic and plastic domains and since materials are commonly designed to withstand loads that do not stress them outside the elastic region, the focus is often set on predicting the initial yield surface. To that end, we may use numerical strategies based on computational homogenisation (in other words, the same principles introduced in Chapters 4 and 5 can be applied). By that logic, we should begin by considering a yield function that might describe the yield surface of polycrystalline materials; then, we must perform several micro-scale analyses and identify the critical microscopic parameters, so that, in the final step, we are in condition to determine the coefficients of the macroscopic yield function (and, therefore, calibrate it from the micro-scale studies).

In this Chapter, we focus on determining of the yield response of textureless single-phase polycrystals comprising crystals with cubic symmetry – in particular, we concentrate on fcc polycrystals –, so that, in the following Chapter, we can establish the link between the macroscopic yield surfaces and the microscopic properties of these materials (namely the monocrystalline parameters). To formulate those

relations, it is paramount to be aware of the physical concepts associated with the plastic deformation of crystals. That is approached in Section 6.1 in the context of the presentation of the single-crystal constitutive model adopted. It must be emphasised that the referred constitutive model establishes the onset of yielding in fcc single-crystals, but it does not do so for polycrystalline materials. In fact, the initial yield surface of polycrystals can be defined in multiple ways and, because we are interested in describing the yielding behaviour of these materials, it is pertinent to expound on this topic. For this reason, in Section 6.2, we review some possible ways of defining the initial yield surface of fcc polycrystals. This is followed by the compilation of both phenomenological and micromechanical models that can be used to mathematically describe those surfaces (by adjusting the underlying parameters) – in Section 6.3, we then enumerate models that can be used to define the yielding surface of isotropic and anisotropic polycrystals (special attention is given to the isotropic models of Tresca (1864) and von Mises (1928), as well as to the micromechanical anisotropic approach of Darrieulat and Piot (1996)). Finally, in Section 6.4, we address the numerical multi-scale framework used in the following Chapter to characterize the yielding behaviour of polycrystals.

This Chapter provides the tools necessary to define the yielding response of fcc polycrystals by means of numerical multi-scale procedures based on computational homogenisation. Nonetheless, we must highlight that the material presented here is reduced to the minimum extent required and, as a result, the interested reader should consult other publications for more details on particular issues. For a more comprehensive account of the mechanisms of plastic deformation for fcc crystals we suggest Dieter (1988) and Kocks et al. (2000). In addition, it is worth emphasising that we based our presentation of the single-crystal constitutive model adopted on de Bortoli (2017); de Souza Neto et al. (2008) and McGinty (2001). In that context, we were brief on reviewing its possible extension to handle non-Schmid effects (which must be incorporated in the modelling of bcc single-crystals), but that is made by Gröger et al. (2008); Yalcinkaya et al. (2008) and Mapar et al. (2017). Regarding the discussion of the yield onset, we suggest the work of Brenner et al. (2009). Finally, for an overview on anisotropic yield functions we recommend consulting Habraken (2004).

6.1 Cubic Single-Crystal Constitutive Model

As we have reported in Section 4.1, crystalline materials enclose atoms packed in regular, three-dimensional patterns (unit cells) whose repetition in all spatial directions gives rise to the so-called crystal lattices. From the analysis of Figure 4.3, it becomes apparent that matter at the unit cell scale is discontinuous, so that the continuum hypothesis does not apply. This means that the simulation of the interactions that occur between atoms at that scale (which explain the behaviour

at the macro-scale) requires the use of atomistic models. As we have mentioned in the beginning of Chapter 2, atomistic approaches do not provide a practical way of addressing most engineering problems (the computational resources required are commonly prohibitive) and, for that reason, single-crystal continuum models (which are applicable at the micro-scale) are generally adopted. This is made because the deformation of a continuum can be linked to that of a lattice embedded in it: for instance, the *Cauchy-Born hypothesis* states that the lattice vectors deform like infinitesimal line elements in a continuum (Ericksen, 1984).

In this Section, a continuum single-crystal constitutive model is presented. The whole model is formulated in large strains, so that it can be employed to predict the response of single-crystals under infinitesimal or finite straining. The structure of the presentation is as follows. Firstly, physical aspects associated with the plastic deformation of cubic crystals are reviewed in Section 6.1.1. We then move on, in Section 6.1.2, to the description of one of the classical assumptions in general finite strain elastoplasticity, that is, we focus on the *multiplicative split of the deformation gradient*. In Section 6.1.3, we cast the anisotropic hyperelastic law adopted, before we discuss the stresses required to initiate permanent deformation in fcc single-crystals in Section 6.1.4. The yield function is then formulated in terms of those stresses in Section 6.1.5 and in order to describe its evolution both the plastic flow rule and the hardening law have to be defined: that is made, respectively, in Sections 6.1.6 and 6.1.7. In Section 6.1.8, final comments about the whole rate-independent single-crystal slip plasticity model are made and, since this formulation induces several algorithmic problems difficult to circumvent, an alternative rate-dependent approach (adopted on `Links`) is introduced.

6.1.1 Plastic Deformation by Slip

Although there are several plastic deformation mechanisms important for cubic crystals, the most relevant of all is the result of sliding between crystal blocks along certain crystallographic planes (Dieter, 1988). This plastic mechanism is known as *crystallographic slip* and it occurs preferentially between the planes of greatest atomic density, the *slip planes*. The reason for this results from the fact that stronger atomic bonds (i.e., more difficult to break) are associated smaller interatomic distances, such that when the blocks of crystal slide over one another, it is easier to break the bonds between atoms of neighbouring slip planes (since they are weaker, as the interatomic distance increases). In addition, the direction of sliding follows one of the directions with highest linear atomic density within the slip plane. These directions are referred to as *slip directions*. Note that the slip directions are always associated with a particular slip plane, so that the pair comprising a slip system and the underlying slip plane defines a *slip system*. In Figure 6.1, crystallographic slip is schematically represented. As can be seen, it presupposes the temporary cyclic

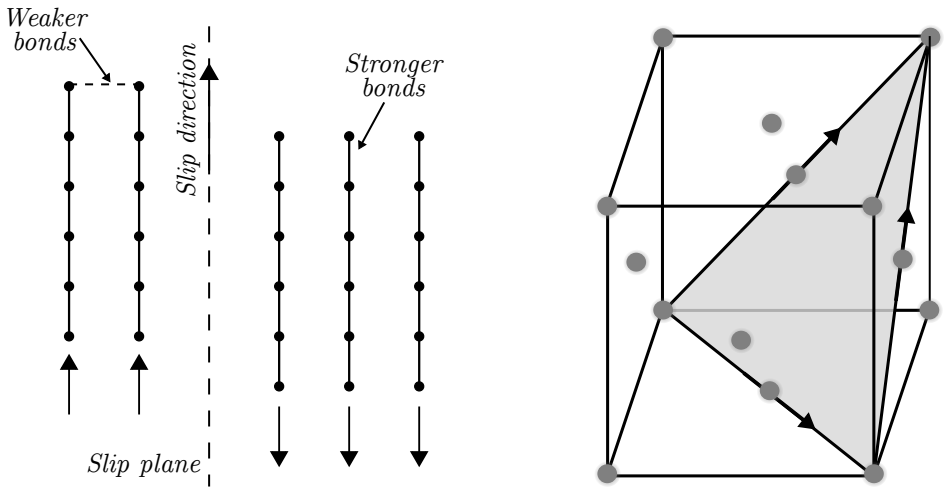

Figure 6.1: Slip planes and directions: (a) general concept; (b) slip systems in fcc crystals: one of the four slip planes with its three in-plane slip directions.

breakage and restoration of atomic bonds between the atoms of neighbouring slip planes.

In fcc crystals, the total number of slip systems is 12. All those slip systems are discriminated in Table 6.1, where $\boldsymbol{m}$ denotes the slip plane unit normal and $\boldsymbol{s}$ is the unit vector in the slip direction. From the analysis of the mentioned Table, it becomes apparent that there are just 4 different slip planes and that each one of them is associated with 3 slip directions. We have represented 3 of those slip systems in Figure 6.1, so that it is easier to identify the spatial locations where crystallographic slip takes place in these crystallites.

Table 6.1: Slip systems in fcc crystals.

	$\boldsymbol{m}$	$\boldsymbol{s}$		$\boldsymbol{m}$	$\boldsymbol{s}$
1	$\frac{1}{\sqrt{3}}[1,1,1]$	$\frac{1}{\sqrt{2}}[\bar{1},0,1]$	7	$\frac{1}{\sqrt{3}}[\bar{1},1,1]$	$\frac{1}{\sqrt{2}}[\bar{1},0,\bar{1}]$
2	$\frac{1}{\sqrt{3}}[1,1,1]$	$\frac{1}{\sqrt{2}}[0,1,\bar{1}]$	8	$\frac{1}{\sqrt{3}}[\bar{1},1,1]$	$\frac{1}{\sqrt{2}}[0,\bar{1},1]$
3	$\frac{1}{\sqrt{3}}[1,1,1]$	$\frac{1}{\sqrt{2}}[1,\bar{1},0]$	9	$\frac{1}{\sqrt{3}}[\bar{1},1,1]$	$\frac{1}{\sqrt{2}}[1,1,0]$
4	$\frac{1}{\sqrt{3}}[1,\bar{1},1]$	$\frac{1}{\sqrt{2}}[1,0,\bar{1}]$	10	$\frac{1}{\sqrt{3}}[1,1,\bar{1}]$	$\frac{1}{\sqrt{2}}[1,0,1]$
5	$\frac{1}{\sqrt{3}}[1,\bar{1},1]$	$\frac{1}{\sqrt{2}}[\bar{1},\bar{1},0]$	11	$\frac{1}{\sqrt{3}}[1,1,\bar{1}]]$	$\frac{1}{\sqrt{2}}[\bar{1},1,0]$
6	$\frac{1}{\sqrt{3}}[1,\bar{1},1]$	$\frac{1}{\sqrt{2}}[0,1,1]$	12	$\frac{1}{\sqrt{3}}[1,1,\bar{1}]$	$\frac{1}{\sqrt{2}}[0,\bar{1},\bar{1}]$

6.1.2 Multiplicative Split of the Deformation Gradient

One fundamental assumption in finite strain elastoplasticity involves the *multiplicative split of the deformation gradient* $\boldsymbol{F}$ into *elastic and plastic deformation gradients* (represented as $\boldsymbol{F}^e$ and $\boldsymbol{F}^p$):

$$\boldsymbol{F} = \boldsymbol{F}^e \boldsymbol{F}^p. \tag{6.1}$$

The multiplicative decomposition of the deformation gradient is attributed to Bilby et al. (1957) and it postulates the existence of a *local unstressed intermediate configuration* defined by the plastic deformation gradient $\boldsymbol{F}^p$. This is illustrated in Figure 6.2, where it becomes evident that the local intermediate configuration[1] can be obtained at each material point by elastic unloading from the deformed configuration defined by the deformation gradient $\boldsymbol{F}$ (de Bortoli, 2017). It must be noted that the initial slip system α (defined by the pair $\{\boldsymbol{s}_0^\alpha, \boldsymbol{m}_0^\alpha\}$[2]) remains unchanged in the intermediate configuration, given that the plastic deformation gradient $\boldsymbol{F}^p$ only takes into account the deformation related with plastic slip. On the contrary, the lattice (recoverable) distortion and the rigid rotations are measured by the elastic deformation gradient $\boldsymbol{F}^e$. In this context, it is relevant to mention that the rotations contained in $\boldsymbol{F}^e$ may be large, whilst the elastic lattice distortion is commonly infinitesimal in most metals (de Souza Neto et al., 2008). Given all these points, the deformed counterparts of initial unit vectors $\boldsymbol{s}_0^\alpha$ and $\boldsymbol{m}_0^\alpha$ read:

$$\boldsymbol{s}^\alpha = \boldsymbol{F}^e \boldsymbol{s}_0^\alpha, \tag{6.2}$$

$$\boldsymbol{m}^\alpha = (\boldsymbol{F}^e)^{-T} \boldsymbol{m}_0^\alpha, \tag{6.3}$$

so that these vectors are still orthogonal after the elastic deformation has been applied.

It must be emphasised that the multiplicative split of the deformation gradient yields the possibility of quantifying separately the elastic and plastic deformations, so that it embodies an extension of the standard *additive split of the infinitesimal strain tensor* $\boldsymbol{\varepsilon}$ (which is the basis of the small strain theory of plasticity):

$$\boldsymbol{\varepsilon} = \boldsymbol{\varepsilon}^e + \boldsymbol{\varepsilon}^p, \tag{6.4}$$

where $\boldsymbol{\varepsilon}^e$ and $\boldsymbol{\varepsilon}^p$ denote the elastic and the plastic strain tensors (where $\boldsymbol{\varepsilon}$ is the strain tensor).

As a final note, we draw attention for the fact that not only the multiplicative split of the deformation results in a convenient mathematical expression, as it also has sound justification in the slip theory of crystals (for more on this topic, see Reina and Conti (2014) and Peirce et al. (1982)).

[1] It must be remarked that, in most cases, the intermediate unstressed configuration cannot be physically achieved, that is, it is only defined locally. This is because, in general, there is no global displacement field associated to $\boldsymbol{F}^p$ that satisfies the compatibility conditions.

[2] As previously mentioned, the subscript in $(\cdot)_0$ indicates that $(\cdot)$ is defined in the initial configuration.

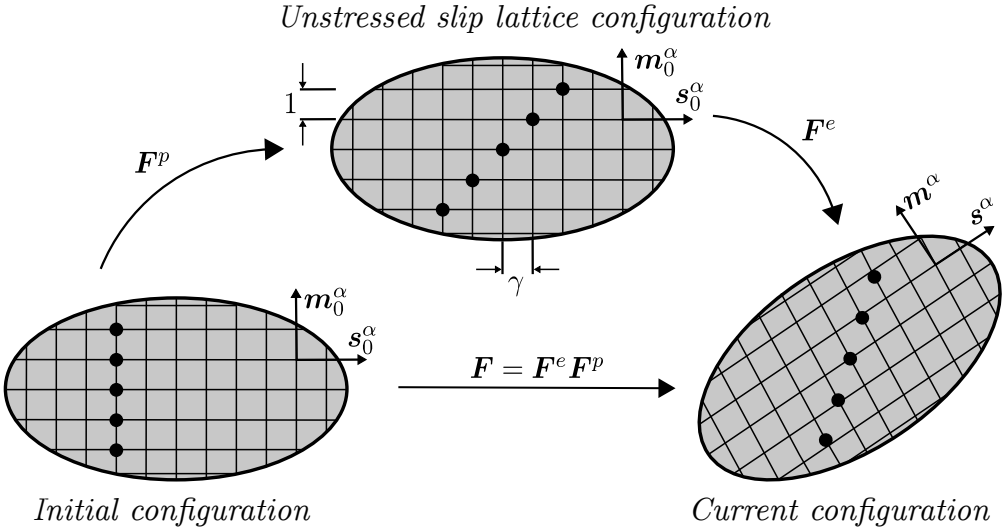

Figure 6.2: Schematic representation of the multiplicative decomposition of the deformation gradient.

6.1.3 Hyperelastic Law

Before crystallographic slip takes place (and neglecting other plastic deformation mechanisms), single-crystals only experience elastic deformation, so that we just have to examine the elastic deformation gradient. Since the stress levels necessary to induce plastic slip are in general low relative to the material's elastic moduli, the linear elasticity framework discussed in Chapter 4 can be applied. In such case, and due to the fact that our model is formulated in large strains, we have adopted the anisotropic hyperelastic law of *Saint-Venant Kirchhoff*, which has already been introduced in Section 4.5.2. As we have seen there (equation (4.61)), this law establishes a linear relation between the second Piola-Kirchhoff stress tensor $\boldsymbol{S}$ and the Green-Lagrange elastic strain tensor $\boldsymbol{E}^e$:

$$\boldsymbol{S} = \mathbf{C} : \boldsymbol{E}^e. \tag{6.5}$$

It must be remembered that, since we are developing a single-crystal constitutive model valid for cubic crystals, the elastic stiffness tensor just incorporates three independent elastic parameters (which remain constant independently of the deformation). Moreover, it is worth emphasising that the Green-Lagrange elastic strain tensor $\boldsymbol{E}^e$ can be expressed in terms of the elastic deformation gradient:

$$\boldsymbol{E}^e = \frac{1}{2}\left[(\boldsymbol{F}^e)^T \boldsymbol{F}^e - \boldsymbol{I})\right]. \tag{6.6}$$

Lastly, we must notice that the second Piola-Kirchhoff stress tensor can also be represented as:

$$\boldsymbol{S} = p_0 \frac{\partial \psi^e}{\partial \boldsymbol{E}^e}, \tag{6.7}$$

that is, it establishes the first derivative of the elastic strain energy function ψ^e in order to the Green-Lagrange elastic strain tensor $\boldsymbol{E}^e$. Note that the strain energy function is given by (Kim, 2014):

$$\psi^e = \frac{1}{2}\,\boldsymbol{E}^e : \mathbf{C} : \boldsymbol{E}^e. \tag{6.8}$$

6.1.4 Resolved Schmid Shear Stress and Schmid Law

In Section 6.1.1, we have introduced the most relevant mechanism of plastic deformation in cubic single-crystals, but no comments were made regarding the stresses required to initiate and sustain deformation (i.e., the stresses required to induce crystallographic slip). For fcc crystals, it is generally assumed that slip begins on a particular system when the component of stress parallel to the underlying slip direction reaches a critical value, the *critical resolved shear stress*. This principle is frequently referred to as *Schmid law* and, considering a generic slip system α, it postulates that crystallographic sliding on that slip system takes place when:

$$\tau_y^\alpha = \tau^\alpha, \tag{6.9}$$

where τ_y^α and τ^α denote, respectively, the critical resolved shear stress and the *Schmid resolved shear stress* of a generic slip system α. The Schmid resolved shear stress consists of the shear force transferred across the slip plane (defined by $\boldsymbol{m}$) in the direction of $\boldsymbol{s}$:

$$\tau^\alpha = \boldsymbol{\sigma} : (\boldsymbol{s}^\alpha \otimes \boldsymbol{m}^\alpha). \tag{6.10}$$

In the previous equation, both the Cauchy stress tensor $\boldsymbol{\sigma}$ and the dyadic product associated with the slip system α, $\boldsymbol{s}^\alpha \otimes \boldsymbol{m}^\alpha$, are defined in the deformed configuration. This dyadic product is sometimes replaced in equation (6.10) by the (spatial[3]) Schmid tensor $\boldsymbol{M}^\alpha$ which reads:

$$\boldsymbol{M}^\alpha = \boldsymbol{s}^\alpha \otimes \boldsymbol{m}^\alpha. \tag{6.12}$$

Considering relation (2.67) and the hyperelastic law (6.5), we may rewrite the Schmid equation (6.10) in the following fashion:

$$\tau^\alpha = \frac{1}{J^e}\,(\boldsymbol{F}^e)^T\,\boldsymbol{F}^e\,\boldsymbol{S} : \boldsymbol{M}_0^\alpha, \tag{6.13}$$

so that the influence of the hyperelastic law adopted on the resolved shear stress becomes apparent. In the previous equation, note that J^e is the determinant of the elastic deformation gradient.

[3]The Schmid tensor can be also expressed in terms of material quantities. In that case, we have:

$$\boldsymbol{M}_0^\alpha = \boldsymbol{s}_0^\alpha \otimes \boldsymbol{m}_0^\alpha. \tag{6.11}$$

To sum up, the extent of slip on a certain slip system depends on the magnitude of the resolved shear stress which, in turn, is commonly reliant on the temperature and on the slip history (de Souza Neto et al., 2008). By the same token, it is important to realize that, in general, small amounts of impurities and alloying elements increase the critical resolved shear stress of fcc metals (Dieter, 1988).

Another important point to make relies on the fact that the consideration of the Schmid law makes this plasticity model anisotropic[4]. Note that the hyperelastic law adopted is also anisotropic, so that the hypothesis of anisotropy has been assumed in both the elastic and plastic regions.

Schmid's law (6.9) describes the onset of plastic slip for fcc crystal structures, but its applicability for bcc crystallites is questionable and several alternative laws have been developed (Gröger et al., 2008; Mapar et al., 2017; Yalcinkaya et al., 2008). These alternative approaches consider the so-called *non-Schmid effects*. In fact, not only these laws involve a larger number of microscopic parameters, but also none of them is completely accepted as standard by the whole scientific community. For these reasons, and since our idea in the following Chapter is to establish the link between the microscopic parameters and the yielding surface of the aggregates, we have decided to focus on fcc polycrystals, as it simplified both achieving our objective and validating the results found. Nonetheless, we must bear in mind that the framework reported in the following Sections is also valid for bcc crystals, since we express the equations in terms of a generic resolved shear stress τ^α and a generic set of slip systems.

6.1.5 Yield Function

Knowing that the elastic and plastic domains are separated by the yield surface and that the onset of crystallographic slip (for fcc crystal structures) is defined by the Schmid law (6.9), we are in condition to mathematically formulate the yielding function. In reality, because fcc crystals have $n_{slip} = 12$ slip systems and slip can happen in any of them, we must consider n_{slip} yield functions of the form:

$$\Phi^\alpha(\tau^\alpha, \tau_y^\alpha) \equiv |\tau^\alpha| - \tau_y^\alpha, \quad \alpha = 1, ..., n_{slip}. \tag{6.14}$$

In the previous equation, the critical resolved shear stresses τ_y^α ($\alpha = 1, ..., n_{slip}$) are not necessarily equal in all slip systems and that their value may depend on the history of the deformation process (this topic is further developed in Section 6.1.7). Having said that, for a given value of τ_y^α, we can define n_{slip} hypersurfaces in the space of Cauchy stresses (one for each value of α):

$$\Phi^\alpha(\tau^\alpha(\boldsymbol{\sigma}), \tau_y^\alpha) = 0. \tag{6.15}$$

[4]As a matter of fact, even though the isotropic finite elastoplasticity formulation can be used successfully for the simulation of finite deformations of polycrystalline materials under a wide range of conditions, for single-crystal alloys, the assumption of isotropy cannot be introduced without significant loss of accuracy (de Souza Neto et al., 2008).

Accordingly, plastic slip in a system α may occur in case the stress state is contained on the hypersurface defined in (6.14); by the same token, the stress states on the referred surface determine the envelope of the elastic domain where the mechanical response of the crystals is reversible (de Souza Neto et al., 2008). In such case, the *elastic domain* is defined as follows:

$$\mathscr{E} \equiv \left\{ \boldsymbol{\sigma} \mid \Phi^{\alpha}(\tau^{\alpha}(\boldsymbol{\sigma}), \tau_y^{\alpha}) < 0, \quad \alpha = 1, ..., n_{slip} \right\}. \tag{6.16}$$

With the same logic, the set of *plastically admissible stresses* is the closure of $\mathscr{E}$, given by:

$$\bar{\mathscr{E}} \equiv \left\{ \boldsymbol{\sigma} \mid \Phi^{\alpha}(\tau^{\alpha}(\boldsymbol{\sigma}), \tau_y^{\alpha}) \leqslant 0, \quad \alpha = 1, ..., n_{slip} \right\}, \tag{6.17}$$

whereas the boundary of the elastic region is the *yield surface* $\mathscr{Y}$:

$$\mathscr{Y} \equiv \left\{ \boldsymbol{\sigma} \mid \Phi^{\alpha}(\tau^{\alpha}(\boldsymbol{\sigma}), \tau_y^{\alpha}) = 0, \quad \exists \alpha \quad \wedge \quad \Phi^{\beta}(\tau^{\beta}(\boldsymbol{\sigma}), \tau_y^{\beta}) \leqslant 0 \quad \forall \beta \neq \alpha \right\}. \tag{6.18}$$

The spatial visualisation of the above anisotropic yield surface is generally attempted in subspaces of the six-dimensional Cauchy stress space and, as can be seen in Kocks (1970), the sections of this yield surface are highly complex.

6.1.6 Plastic Flow Rule

In (6.18), the yielding function was defined, so that the conditions under which plastic straining may happen have been set (de Souza Neto et al., 2008). When the crystal experiences plastic deformation (i.e., when the stress state is on the yield surface), the plastic deformation gradient is non-null and in case a *plastic slip* of magnitude γ^{α} is associated with the slip system $\{\boldsymbol{s}_0^{\alpha}, \boldsymbol{m}_0^{\alpha}\}$, we may write that:

$$\boldsymbol{F}^p = \boldsymbol{I} + \gamma^{\alpha}\, \boldsymbol{s}_0^{\alpha} \otimes \boldsymbol{m}_0^{\alpha}. \tag{6.19}$$

The glide strain γ^{α} is one of the most important measures of plastic strain in single-crystals and, as can be seen in Figure 6.2, it denotes the relative displacement of two aligned slip planes separated at unit distance[5] (Dieter, 1988). The relation between the plastic deformation gradient and the glide strain is thereupon of significant importance and sometimes it is expressed in terms of their time derivatives. To obtain that relation, we must recall the concept of spatial velocity gradient (defined in equation (2.46)); by incorporating the multiplicative split of the deformation gradient (identity (6.1)), a new expression for the spatial velocity gradient $\boldsymbol{L}$ is obtained:

$$\boldsymbol{L} = \boldsymbol{L}^e + \boldsymbol{F}^e \boldsymbol{L}^p (\boldsymbol{F}^e)^{-1}, \tag{6.20}$$

[5]This is valid only for slip on a single system, starting from a state of no plastic deformation ($\boldsymbol{F}^p = \boldsymbol{I}$).

where $\boldsymbol{L}^e$ and $\boldsymbol{L}^p$ are the elastic and plastic[6] velocity gradients, which can be defined in the following fashion:

$$\boldsymbol{L}^e \equiv \dot{\boldsymbol{F}}^e (\boldsymbol{F}^e)^{-1}, \tag{6.21}$$

$$\boldsymbol{L}^p \equiv \dot{\boldsymbol{F}}^p (\boldsymbol{F}^p)^{-1}. \tag{6.22}$$

The inverse of the plastic deformation gradient is given by:

$$(\boldsymbol{F}^p)^{-1} = \boldsymbol{I} - \gamma^\alpha \boldsymbol{s}_0^\alpha \otimes \boldsymbol{m}_0^\alpha, \tag{6.23}$$

so that by combining equations (6.19), (6.22) and (6.23) we can obtain an alternative expression for the evolution of the plastic deformation gradient:

$$\boldsymbol{L}^p = \dot{\gamma}^\alpha \boldsymbol{s}_0^\alpha \otimes \boldsymbol{m}_0^\alpha. \tag{6.24}$$

Generalising to a crystal with n_{slip} *slip systems*, we can postulate that:

$$\boldsymbol{L}^p = \sum_{\alpha=1}^{n_{slip}} \dot{\gamma}^\alpha \boldsymbol{s}_0^\alpha \otimes \boldsymbol{m}_0^\alpha. \tag{6.25}$$

Similarly, taking (6.19) into account, it follows that:

$$\dot{\boldsymbol{F}}^p = \left[\sum_{\alpha=1}^{n_{slip}} \dot{\gamma}^\alpha \boldsymbol{s}_0^\alpha \otimes \boldsymbol{m}_0^\alpha \right] \boldsymbol{F}^p. \tag{6.26}$$

In equations (6.24) to (6.26), $\dot{\gamma}^\alpha$ denotes the *rate of plastic slip* in the slip system α. All plastic multipliers $\dot{\gamma}^\alpha$ ($\alpha = 1, ..., n_{slip}$) must comply with the *loading/unloading criteria*:

$$\Phi^a \leqslant 0, \tag{6.27}$$

$$\dot{\gamma}^\alpha \geqslant 0, \tag{6.28}$$

$$\Phi^a \dot{\gamma}^\alpha = 0. \tag{6.29}$$

Observe that summation on the repeated index is not implied in (6.29).

6.1.7 Hardening Law

In line with what we have exposed in Section 6.1.5, the initial yield surfaces Φ_0^α are defined in terms of the initial critical resolved shear stresses $\tau_{y,0}^\alpha$ of the underlying slip systems (here, "initial" means before plastic deformation has taken place). To model the evolution of the yield surfaces it is therefore necessary to establish hardening rules, so that the dependence of the critical resolved shear stresses upon the history of plastic deformation can be defined.

Generally speaking, two main groups of hardening laws can be distinguished: *isotropic hardening laws* and *anisotropic hardening laws*. In simplistic terms, the

[6]Note that the plastic velocity gradient $\boldsymbol{L}^p$ is defined in the intermediate configuration, despite the fact that the velocity gradient $\boldsymbol{L}$ is a spatial entity.

former establishes that the evolution of the yield surface with plastic deformation occurs without distortion, while the later encompasses the general case. Even though many complex hardening models have been proposed to describe the evolution of the resolved yield stress, a popular option consists of following the isotropic Taylor hardening assumption (Taylor, 1938). This assumption suggest that at a specific point of the continuum, the critical resolved shear stress for all the systems is the same. If τ_y denotes the common critical resolved shear stress, the yield functions are given by:

$$\Phi^{\alpha}(\tau^{\alpha}, \tau_y) = |\tau^{\alpha}| - \tau_y, \quad \alpha = 1, ..., n_{slip}. \tag{6.30}$$

Besides, the common resolved yield stress is assumed to be a function of the *accumulated slip* γ only, that is,

$$\tau_y = \tau_y(\gamma). \tag{6.31}$$

The accumulated slip γ is a hardening (internal) variable which reads:

$$\gamma \equiv \int_o^t \sum_{\alpha=1}^{n_{slip}} |\dot{\gamma}^{\alpha}| \, dt, \tag{6.32}$$

so that its evolution equation is given by:

$$\dot{\gamma} = \sum_{\alpha=1}^{n_{slip}} |\dot{\gamma}^{\alpha}|. \tag{6.33}$$

In reality, and despite the fact that the isotropic Taylor hardening assumption can provide adequate results in certain cases (Povall et al., 2014), it has been experimentally verified (Kocks, 1970) that the slip systems evolve at different rates. Within this context, the concepts of *self hardening* and *latent hardening* arise, depending on the coplanarity properties of the slip systems. In detail, the influence of an incremental plastic strain on the resolved yield stress of coplanar systems (systems that share the same vector $\boldsymbol{m}$) is defined as self hardening, while its effect on the critical resolved shear stress of non-coplanar slip systems is called latent hardening. Many authors suggest that latent hardening is of larger magnitude than self hardening and Kocks (1970) advocated that the ratio of latent hardening to self hardening – the *latent hardening ratio* q – is approximately 1.4. In order to take into consideration the concepts of self and latent hardening, we decided to use the model proposed by Asaro and Needleman (1985). It essentially expresses the rate of evolution of the critical resolved shear stress for a generic system α, $\dot{\tau}_y^{\alpha}$, in terms of the plastic multipliers associated with all slip systems $\dot{\gamma}^{\beta}$ ($\beta = 1, ..., n_{slip}$):

$$\dot{\tau}_y^{\alpha} = \sum_{\beta=1}^{n_{slip}} h^{\alpha\beta} |\dot{\gamma}^{\beta}|, \quad \alpha = 1, ..., n_{slip}. \tag{6.34}$$

Note that only the active slip systems (i.e., systems undergoing slip) influence $\dot{\tau}_y^{\alpha}$,

since, for all the others, $\dot{\gamma}^{\beta} = 0$. The relation between the $\dot{\tau}_y^{\alpha}$ and each one of the plastic multipliers $\dot{\gamma}^{\beta}$ is established by the hardening coefficients $h^{\alpha\beta}$. The hardening coefficients take into account the coplanarity between slip systems and the slope of the hardening law, $h(\gamma)$, so that they are given by:

$$h^{\alpha\beta} = h(\gamma) \cdot (q + (1 - q) \cdot \delta_{\alpha\beta}), \tag{6.35}$$

where γ is the accumulated plastic slip defined in (6.32) and $\delta_{\alpha\beta}$ denotes the Kronecker delta variable (from equation (2.139)). Frequently, the latent hardening ratio is specified in the interval $q \in [1, 1.4]$, so that when $q = 1$ the isotropic Taylor hardening assumption is recovered. Given these points, the matrix of hardening coefficients can be expressed as:

$$h^{\alpha\beta} = h(\gamma) \cdot A^{\alpha\beta}, \tag{6.36}$$

being $A^{\alpha\beta}$ the coplanarity matrix, defined as follows:

$$A^{\alpha\beta} = \begin{cases} 1, & \text{if } ||\boldsymbol{m}^{\alpha} \times \boldsymbol{m}^{\beta}|| = 0 \\ q, & \text{if } ||\boldsymbol{m}^{\alpha} \times \boldsymbol{m}^{\beta}|| \neq 0 \end{cases}. \tag{6.37}$$

Finally, the computation of $h(\gamma)$ requires a hardening law to be assumed. In our case, we decide to use an expression based on the Nadai-Ludwik power-law (Perdahcıoğlu and Geijselaers, 2012):

$$\tau_y = \tau_{y,0} + K \cdot (\gamma_0 + \gamma)^m, \tag{6.38}$$

where $\tau_{y,0}$, K, γ_0 and m denote, respectively, the initial yield stress, the hardening parameter, the accumulated slip offset and the hardening exponent. As a consequence, the slope of the hardening law is:

$$h(\gamma) = m \cdot K \cdot (\gamma_0 + \gamma)^{m-1}. \tag{6.39}$$

6.1.8 Final Remarks and Rate-Dependent Formulation

In this Section, a single-crystal constitutive model formulated under large strains was described. The whole presentation was based on the assumption that crystallographic slip is the only mechanism of plastic deformation in cubic metals. In addition, the Schmid law – which is valid for fcc crystal structures – was assumed. In this regard, it must be emphasised that alternative laws prepared to consider non-Schmid effects (for instance, the ones proposed by Gröger et al. (2008); Yalcinkaya et al. (2008) and Mapar et al. (2017)) typically define the onset of crystallographic slip in terms of a modified resolved Schmid shear stress, such that the expressions listed in Sections 6.1.5 to 6.1.7 remain valid for bcc crystal structures (note, however, that a different set of slip systems has to be considered for dealing with bcc unit cells). The constitutive model reviewed here mostly embodies the fundamental concepts and equations that are at the basis of the version implemented in `Links` to simulate the behaviour of fcc

crystals under finite strain. An important point to make is that `Links` can also be employed to simulate the mechanical response of polycrystalline aggregates, in which case the aforementioned constitutive model is assigned to all grains of the specimen. Note that this aspect assumes significant relevance, as we are interested in using the referred program to infer critical relations between the monocrystalline parameters and the coefficients associated with the yield functions of the polycrystals. That is made in Chapter 7, but before we reach that stage both the macroscopic yield functions that can be used to approximate the yielding surfaces of polycrystals and the computational framework used have to be described. For now, it is necessary to briefly address a slight modification of the model implemented in `Links` to the one that was discussed until this point. In fact, instead of the *rate-independent* formulation presented, a more versatile *rate-dependent* formulation is used (even when rate-dependent phenomena, like creep, are not important). This results from the fact that rate-independent formulations pose several algorithmic problems difficult to circumvent, especially concerning the search of active slip systems (the discussion of this computational issues is out of the scope of this work, but the interested reader is referred to de Bortoli (2017) or de Souza Neto et al. (2008)). In summary, a *viscoplastic rate law*, known as *Peric's law* (Perić, 1993), is used:

$$\dot{\gamma}^\alpha = \begin{cases} \frac{1}{\mu}\left[\left(\frac{\tau^\alpha}{\tau_y^\alpha}\right)^{1/\epsilon} - 1\right], & \text{if } \Phi^\alpha(\tau^\alpha, \tau_y^\alpha) \geqslant 0 \\ 0, & \text{if } \Phi^\alpha(\tau^\alpha, \tau_y^\alpha) < 0 \end{cases}, \tag{6.40}$$

where ϵ and $\frac{1}{\mu}$ denote the rate-sensitivity and viscosity-related parameters. It must be noted that this law yields an explicit functional expression for the rates of plastic deformation, so the yield condition and the loading/unloading criterion are no longer required. Moreover, it is important to bear in mind that when $\epsilon \to 0$ and $\mu \to 0$, the above law tends to the rate-independent formulation[7]. Under these circumstances, it becomes obvious that the rate-dependent formulation is highly versatile, since it enables the possibility of obtaining both formulations (rate-dependent and rate-independent) with a single constitutive model.

6.2 Discussion on the Onset of Yield in fcc Polycrystals

Despite the fact that the Schmid law is generally accepted to define the onset of yield in single-crystals with face-centered cubic Bravais lattices, the beginning of the plastic domain in fcc polycrystals can be delineated in multiple ways. On the one hand, from a macroscopic point of view (*macro-yield* approach), the initial yield

[7]Note, however, that, when the rate-independent limit is approached, the resulting system of return mapping equations tends to become severely stiff (de Bortoli, 2017; Ling et al., 2005; Steinmann and Stein, 1996).

surface of fcc polycrystals can be related to the lowest stress states which lead to non-linear stress-strain relations. In detail, when experimental (macroscopic) stress-strain curves are used, the initial *macro-yield stresses* of most fcc aggregates is commonly associated with an offset plastic strain[8] of 0.2% (this is schematically represented in Figure 6.3 using the equivalent von Mises stress σ^{VM} and the equivalent strain ε. On the other hand, from a microscopic point of view (*micro-yield* approach), the initial yield surface of fcc aggregates is associated with the onset of plastic slip. Several approaches have been developed to numerically capture the *micro-yield* condition and it is well-established that both the polycrystal mesh (if a numerical framework is employed) and the elastic properties of the single-crystals (especially their elastic anisotropy) influence the beginning of yield at the micro-scale (Brenner et al., 2009). Give these points, defining the initial yield surface of polycrystalline specimens is dependent on whether we follow a micro- or a macro-yield approach. In general, it is verified that the micro-yield stresses are significantly lower than the macro-yield stresses, so that they lead to macroscopic stress states where the linear elastic relation between stresses and strains is still valid, despite the fact that some grains might have already (partially) plastified. The study of the relation between the micro-yield stresses and the macroscopic stress-strain curve of polycrystals is made in the next Chapter, along with the analysis of the relation between the macro- and micro-yield surfaces and the monocrystalline parameters.

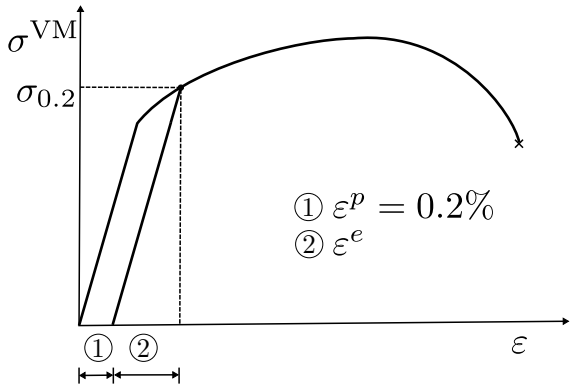

Figure 6.3: Macroscopic stress-strain curve and representation of the *conventional macro-yield stress* $\sigma_{0.2}$ (which is determined at a level of total strain of $\varepsilon^p = 0.2\%$).

In this Section, we discuss several ways of defining the initial yield surface of fcc polycrystals[9] which are suited for computational analyses. Since the definition of the macro-yield condition is reasonably well-established, we focus principally on

[8]The elastic and plastic equivalent strains (hereafter, denoted ε^e and ε^p) can be defined analogously to the equivalent total strain ε. This means that they can be computed using a similar expression to equation (5.3) – however, instead of being calculated in terms of the (total) deformation gradient $\boldsymbol{F}$, they are respectively reliant on the elastic, $\boldsymbol{F}^e$, and plastic, $\boldsymbol{F}^p$, deformation gradients.

[9]Most of them can be used for defining the initial yield surface of other types of polycrystalline aggregates.

approaches that intend to predict the initial micro-yield surface. Under these circumstances, we begin by introducing the "true micro-yield approach" in Section 6.2.1. Then, due to the fact that the true micro-yield approach is highly dependent on the level of discretization used (and therefore, not very well suited for numerical analysis based on the FEM), we consider the approach of Hutchinson (1970) (Section 6.2.2), clearly pointing out its major drawback, so that we can understand the advantages of the approach of Brenner et al. (2009), who refined Hutchinson's model. The model proposed by Brenner et al. (2009) is reviewed in Section 6.2.3. Finally, in Section 6.2.4, we address a more general approach based on the global plastic strain. This approach can be used to determine both the initial macro- and micro-yield surfaces, so that we may regard the conventional macro-yield criterion as a particular case of the global strain approach.

6.2.1 True Micro-Yield Approach

The *true micro-yield approach* embodies the most simple way of defining the initial yield surface of polycrystals. It outlines the micro-yield stress as the lowest macroscopic stress that is required to activate plastic slip within the polycrystal (considering all slip systems and all points). In such case, if we consider that the initial critical resolved shear stress is the same for all systems of all points of the micro-continuum, we may define the *micro-yield criterion* in the following fashion

$$\max_{\boldsymbol{x}_\mu \in \Omega_\mu} \max_{\alpha \in \mathscr{A}} |\tau^\alpha(\boldsymbol{x}_\mu)| = \tau_{y,0} \tag{6.41}$$

where $\mathscr{A}$ is the set comprising the slip systems and $\tau_{y,0}$ the shared initial critical resolved shear stress. Note that we have used the variable $\boldsymbol{x}_\mu$ to identify the points of the aggregate, in consistency with the notation introduced in Chapter 3.

Since the FEM is generally employed to numerically compute the *micro-yield surface*, it becomes apparent that condition (6.41) is just evaluated at the Gauss points. For this reason, Brenner et al. (2009) claimed that the level of discretization of the polycrystal mesh significantly influences the shape of the micro-yield surface obtained, leading them to suggest that other criteria (not so dependent on the level of discretization used) should be adopted to characterize the onset of micro-yield.

6.2.2 Hutchinson Approach

An early attempt to formulate the micro-yield criterion within the homogenisation framework goes back to Hutchinson (1970), who has used fields statistics information to obtain an estimate for the micro-yield stress. To be precise, Hutchinson's proposal for the micro-yield criterion is given by:

$$\max_{r \in \mathscr{N}} \max_{\alpha \in \mathscr{A}} |\langle \tau^\alpha \rangle^r| = \tau_{y,0}, \tag{6.42}$$

where $\mathscr{N}$ is the set comprising all the grains of the polycrystal and $\langle\tau^{\alpha}\rangle^{r}$ is the average resolved shear stress on slip system α of the grain r. This quantity is calculated in the following fashion:

$$\langle\tau^{\alpha}\rangle^{r} = \langle\boldsymbol{\sigma}\rangle^{r} : \boldsymbol{M}^{\alpha,r}, \tag{6.43}$$

where $\langle\boldsymbol{\sigma}\rangle^{r}$ is the average stress tensor of crystallite r and $\boldsymbol{M}^{\alpha,r}$ is the Schmid tensor associated with slip system α of grain r.

In his original presentation, Hutchinson (1970) used a self-consistent linear elastic scheme to estimate the average stress fields at the grains[10], so that he could derive an expression for the micro-yield function of fcc polycrystals comprising a very large number of grains (that is, applicable for isotropic fcc polycrystals):

$$\Phi^{\mathrm{Hut}}(\boldsymbol{\sigma}) = \frac{\sigma_{max} - \sigma_{min}}{2} - \tau_{y,0}^{\mathrm{Hut}}. \tag{6.44}$$

Hutchinson's proposal to the micro-yield surface is obtained when $\Phi^{\mathrm{Hut}} = 0$; fundamentally it consists of a modified Tresca yielding surface (see Section 6.3.1.1). In the previous equation, σ_{max} and σ_{min} denote the maximum and minimum overall principal stresses, i.e.

$$\sigma_{max} = \max(\sigma_1, \sigma_2, \sigma_3), \tag{6.45}$$

$$\sigma_{min} = \min(\sigma_1, \sigma_2, \sigma_3). \tag{6.46}$$

On the other hand, Hutchinson micro-yield stress $\tau_{y,0}^{\mathrm{Hut}}$ is defined in terms of the initial critical resolved shear stress and takes into account the anisotropy of the single-crystal:

$$\tau_{y,0}^{\mathrm{Hut}} = \tau_{y,0} \cdot \sqrt{\frac{3}{2 \cdot a^2 + b^2}}, \tag{6.47}$$

where the coefficients a and b depend on the elastic properties of the cubic crystallites which are encompassed within the aggregate:

$$a = \frac{\mathsf{C}_{11} - \mathsf{C}_{12}}{2 \cdot G^{\mathrm{SC}} \cdot (1 - \beta) + \beta \cdot (\mathsf{C}_{11} - \mathsf{C}_{12})}, \tag{6.48}$$

$$b = \frac{\mathsf{C}_{44}}{G^{\mathrm{SC}} \cdot (1 - \beta) + \beta \cdot \mathsf{C}_{44}}, \tag{6.49}$$

as well as on the parameter β:

$$\beta = \frac{6}{5}\left(\frac{K^{\mathrm{SC}} + 2 \cdot G^{\mathrm{SC}}}{3 \cdot K^{\mathrm{SC}} + 4 \cdot G^{\mathrm{SC}}}\right). \tag{6.50}$$

As evidenced by the dependency of $\tau_{y,0}^{\mathrm{Hut}}$ on the elastic parameters, Hutchinson (1970) developed an analytical model which establishes the link between the elastic

[10] Hutchinson (1970) approximated all grains by spheres and he assumed that all grain orientations were equally represented. Then, he computed the stress and strain fields within the grains using Eshelby's inclusion result (Eshelby, 1957).

anisotropy of the single-crystal and the onset of micro-yielding in polycrystals. Nonetheless, his modified Tresca yielding funtion (6.44) predicts higher micro-yield stresses for polycrystals consisting of crystals with higher elastic anisotropies, when, in reality, it is expected that the presence of elastic heterogeneities should decrease the micro-yield stress (Brenner et al., 2009). To emphasise this point, observe that among polycrysals comprising crystallites with Zener anisotropy indexes greater than or equal to 1, isotropic crystal aggregates are the ones with lowest micro-yield stresses ($\tau_{y,0}^{\text{Hut}} = 2 \cdot \tau_{y,0}$).

6.2.3 Brenner, Lebensohn and Castelnau Approach

Brenner et al. (2009) refined the micro-yield criterion proposed by Hutchinson (1970), as they also formulated the onset of micro-plasticity in fcc polycrystals in terms of local (grain) homogenised quantities, but, instead of considering only the grain-homogenised stress, they have also taken into consideration intragranular stress heterogeneities. The micro-yield criterion of Brenner et al. (2009) is given by:

$$\max_{r \in \mathscr{N}} \max_{\alpha \in \mathscr{A}} (\hat{\tau}^{\alpha})^r = \tau_{y,0}, \tag{6.51}$$

where $(\hat{\tau}^{\alpha})^r$ is the *reference resolved shear stress* which is computed in the following fashion:

$$(\hat{\tau}^{\alpha})^r = |\langle \tau^{\alpha} \rangle^r| + p \cdot (\tilde{\tau}^{\alpha})^r. \tag{6.52}$$

In the previous equation, $\langle \tau^{\alpha} \rangle^r$ is determined by equation (6.42) and $(\tilde{\tau}^{\alpha})^r$ is the standard deviation of the resolved shear stress on slip system α of grain r. This quantity keeps track of the intragranular stress fluctuations and it is calculated from equation (6.53).

$$(\tilde{\tau}^{\alpha})^r = \sqrt{\left\langle (\tau^{\alpha})^2 \right\rangle^r - \left(\langle \tau^{\alpha} \rangle^r \right)^2}, \tag{6.53}$$

with

$$\left\langle (\tau^{\alpha})^2 \right\rangle^r = \boldsymbol{M}^{\alpha,r} : \langle \boldsymbol{\sigma} \otimes \boldsymbol{\sigma} \rangle^r : \boldsymbol{M}^{\alpha,r}. \tag{6.54}$$

Parameter p must be non-negative and it influences the shape of the initial yield surface, as it is connected with the threshold volume fraction of the first plastifying grain that needs to be in yielding condition so as to consider that the micro-yield stress has been reached (Brenner et al., 2009). The greater this threshold volume fraction, the smaller the value of p: in case the field distributions in grains are strictly Gaussian, for $p = 1$, 15.85% of the first plastifying grain has to yield to consider that the polycrystal is at the ontset of micro-plasticity, while for $p = 3$ the threshold volume fraction of the grain where micro-plasticity initiates is reduced to 0.15%; by the same token, the model of Hutchinson (1970) presupposes that the onset of yield in the polycrystal occurs when 50% of the first plastifying grain has deformed plastically (Brenner et al., 2009). It must be noted that when the first plastifying grain reaches

the condition of micro-yield, other grains could have already plastified. In this case, it becomes apparent that Brenner's approach (associated with positive values of p) predicts lower values for the micro-yield stresses than Hutchinson's approach.

Brenner et al. (2009) also used a self-consistent scheme to predict the yielding surface of fcc polycrystals. In such case, if the value for p is chosen equal to 1, 2 or 3, it is possible to verify that polycrystals comprising crystals with higher anisotropies have smaller micro-yield stresses (Brenner et al., 2009). This not only is in line with what is expected from a physical point of view, as it also suggests that the self-consistent method does not present any intrinsic downside regarding the prediction of the micro-yield stress (Brenner et al., 2009). In fact, the major drawback of Hutchinson's yielding function may be explained from the fact that he has disregarded intragranular stress heterogeneities – that is, it stems from the specific choice of the resolved shear stress (Brenner et al., 2009). On the whole, amongst the models developed to predict the micro-yield surface of fcc polycrystals, the proposal of Brenner et al. (2009) involving non-null values for the parameter p is the most accurate, as it can capture the effect of the elastic anisotropy on the onset of plasticity on fcc polycrystals; besides this, in case we use numerical procedures, it is not overly dependent on the mesh discretisation, since it involves the computational of locally homogenized quantities (this is especially the case for lower values of p, e.g, $p = 0$ or $p = 1$).

6.2.4 Global Plastic Strain Approach

All the previous approaches were developed with the purpose of defining the micro-yield condition, not to mention that they all require the computation of the resolved shear stress on all slip systems of all points (or, in case finite element numerical framework is used, of all Gauss points). A more general approach, which can be also used with other kinds of materials, consists of defining the initial yield condition in terms of a globally homogenised strain measure. More specifically, the yield criterion may be established in terms of the global equivalent plastic strain ε^p.

The greatest advantage of this approach is that it is easy to compare the yielding response of fcc polycrystals with the ones exhibited by other materials. Moreover, note that the mentioned approach is highly flexible, since it can be used to study the initial micro-yield stress or the initial macro-yield stress. To clarify, if a low value is ascribed to the global plastic strain, we are near the onset of micro-plasticity (for instance, Scheunemann (2017) used a value of $\varepsilon^p = 3.3 \cdot 10^{-8}$ to evaluate the initial micro-yield surface of several polycrystalline structures); on the contrary, if we assign a high value, we may be close or even exceed the macro-yield condition (in fact, note that when $\varepsilon^p = 0.2\%$, we obtain the conventional macro-yield criterion, so that when higher values are assumed, we may be beyond the macroscopic elastic domain).

6.3 Description of the Yield Surface of fcc Polycrystals

In Section 6.2, we have described the distinct approaches that might be employed to define both the initial micro- and macro-yield surfaces of polycrystals. In particular, we have introduced several ways of specifying the initial micro-yield criterion and we have reviewed the conventional macro-yield condition. While doing that, we have not paid significant attention to the shape of the initial micro- and macro-yield surfaces, although we have presented an expression deduced by Hutchinson (1970) for the micro-yield function of polycrystals encompassing a large number of crystals with fcc lattices. The function proposed by Hutchinson actually corresponds to a modified version of the original Tresca (1864) yield function, since it was formulated to consider the elastic anisotropy of the single-crystals. However, Hutchinson's function might not lead to accurate results when the stress fluctuations within the grains of the polycrystals are relevant (that is, when considering single-crystal with high anisotropies). In fact, Brenner et al. (2009) showed that by neglecting the stress heterogeneities within the grains, Hutchinson (1970) obtained estimates for the micro-yield stresses of polycrystals comprising anisotropic crystallites which were larger than the ones verified for aggregates enclosing isotropic grains. This conclusion strongly disagrees with the fact that elastic heterogeneities should decrease the initial micro-yielding point (Brenner et al., 2009). In contrast, by incorporating field fluctuations ($p > 0$), Brenner et al. (2009) obtained physically meaningful results. Indeed, they verified that the maximum micro-yield stress occurs for aggregates with isotropic crystals and that an increase in the elastic anisotropy of the single-crystals conduces to lower values of the micro-yield stress. Furthermore, despite not having presented a closed expression for the micro-yield function, they have studied the shape of the micro-yield surface for different values of p: in short, they claimed that as the parameter p and the anisotropy of the constituent crystal increase, the micro-yield surface departs from a Tresca-type surface. Nonetheless, as might be seen in their representations of the micro-yield surfaces for fcc aggregates encompassing non-isotropically elastic crystals, Tresca-type functions are still adequate to approximate the shape of those micro-yielding surfaces. This is consistent with what is reported by Scheunemann (2017) who demonstrated that the yield surface of polycrystalline structures evolves from a Tresca- to a von Mises-type shape (as the levels of plastic deformation increase). Indeed, it is well-established that the isotropic models of Tresca (1864) and von Mises (1928) provide good representations of the initial yield surfaces of fcc aggregates comprising a large number of grains (isotropic), so that they are widely used to describe the yielding response of most metals. Even though most applications of interest involve isotropic polycrystals, there are some cases in which oligocrystals may be employed. In such cases, the isotropic functions of Tresca and von Mises may not be adequate and other formulations have to be considered. Hill (1948) was the first to developed a model that can be used to approximate the yield function of anisotropic polycrystals and since then other formulations have been

proposed. Most of them are phenomenological, even though some micromechanical anisotropic models have also been suggested. In general, regardless of whether we follow a micromechanical or a phenomenological approach, calibrating expressions for the yield surfaces of anisotropic polycrystals is far from trivial. On the contrary, calibrating yield models to define the yielding response of isotropic specimens is substantially easier, as the number of parameters incorporated is severely diminished (for example, the yield functions of Tresca and von Mises incorporate only one adjustable parameter).

In this Section, we focus on studying yield functions that can be used to approximate both the micro- and macro-yield surfaces of isotropic (Section 6.3.1) and anisotropic (Section 6.3.2) polycrystals. To clarify, in Section 6.3.1, the isotropic yield functions of Tresca (1864) (Section 6.3.1.1) and von Mises (1928) (Section 6.3.1.2) are presented, while in Section 6.3.2 we mainly concentrate on the micromechanical anisotropic yield function of Darrieulat and Piot (1996) (Section 6.3.2.1). Above all, it is important to remark that our intention is to clearly identify the parameters associated with the yield functions reviewed, as well as to understand how they might be calibrated. By doing that, note that we may use them to characterize yielding surfaces computed numerically.

6.3.1 Isotropic Yield Functions

Both Tresca (1864) and von Mises (1928) yield functions are commonly used to describe plastic yielding in metals. First and foremost, it is important to realize that one of the most important aspects of both Tresca and von Mises yield functions is that they are *isotropic functions* of the stress tensor. In other words, the value of the yield functions of Tresca and von Mises is unaffected by rotations of the stress state. If the variable Φ^{iso} designates a generic isotropic function, we have:

$$\Phi^{\text{iso}}(\boldsymbol{\sigma}) = \Phi^{\text{iso}}(\boldsymbol{R} \cdot \boldsymbol{\sigma} \cdot \boldsymbol{R}^T), \tag{6.55}$$

where $\boldsymbol{R}$ is the generic rotation tensor.

Other important property of both Tresca an von Mises yield functions is their *pressure-insensitivity*. This means that the hydrostatic pressure component p of the stress tensor (defined in (2.54)) does not affect yielding. To emphasize, observe that the Tresca yield function Φ^{Tr} (defined in (6.57)) remains unchanged in case we superimpose an arbitrary pressure p^* on the stress tensor:

$$\Phi^{\text{Tr}}(\boldsymbol{\sigma} + p^* \boldsymbol{I}) = \Phi^{\text{Tr}}(\boldsymbol{\sigma}). \tag{6.56}$$

This aspect is of paramount concern in the modelling of isotropic polycrystals, as for these materials it is accepted that the hydrostatic pressure can be neglected[11] on the characterisation of their yielding response.

[11] Note that this is due to the incompressibility of plastic deformation by slip.

To summarize, both yielding functions of Tresca and von Mises are isotropic and pressure-insensitive. More details about each one of the yielding functions, including their mathematical definition, are given in the next Sections: in Section 6.3.1.1 the yielding function of Tresca is casted, whereas in Section 6.3.1.2 the yield function of von Mises is discussed.

6.3.1.1 Tresca Yield Function

The Tresca yield function (Tresca, 1864) reads:

$$\Phi^{\mathrm{Tr}}(\boldsymbol{\sigma}, \sigma_y^{\mathrm{Tr}}) = (\sigma_{\max} - \sigma_{min}) - \sigma_y^{\mathrm{Tr}}, \tag{6.57}$$

with the onset of yielding being defined as $\Phi^{\mathrm{Tr}} = 0$, so that the elastic domain of Tresca $\mathscr{E}^{\mathrm{Tr}}$ is given by:

$$\mathscr{E}^{\mathrm{Tr}} = \left\{ \boldsymbol{\sigma} \mid \Phi^{\mathrm{Tr}}\big(\boldsymbol{\sigma}, \sigma_y^{\mathrm{Tr}}\big) < 0 \right\}. \tag{6.58}$$

It is very common to replace the maximum difference between the principal stresses by the equivalent Tresca stress σ^{Tr}:

$$\sigma^{\mathrm{Tr}} = \sigma_{max} - \sigma_{min}, \tag{6.59}$$

so that the Tresca yield function can be rewritten in the following fashion:

$$\Phi^{\mathrm{Tr}}(\boldsymbol{\sigma}, \sigma_y^{\mathrm{Tr}}) = \sigma^{\mathrm{Tr}} - \sigma_y^{\mathrm{Tr}}. \tag{6.60}$$

In the previous equations, σ_y^{Tr} denotes the Tresca yield stress. This stress represents the only adjustable parameter of this yield function and, in general, its value is the stress level at which yielding begins under uniaxial stress conditions. If we consider the Tresca yield stress equal to a generic yield stress σ_y, we can use Tresca's approach to verify if a given stress state (described by the underlying principal stresses) leads to plastic deformation. That happens if the difference between the maximum and the minimum principal stresses is larger than the prescribed value. The preceding principle constitutes the *Tresca yielding criterion.* It must be noted that once the maximum difference between the principal stresses reaches the initial yield stress σ_y, the value of the Tresca yielding stress must be updated according to the hardening law adopted (so that $\Phi^{\mathrm{Tr}} = 0$ continues to define the yielding condition).

In Figure 6.4, we have attempted a graphical representation of the Tresca yield surface in the plane $\sigma_3 = 0$ of the space of principal stresses. We must realize that to obtain the graphical representation shown, it is convenient to split the generic function (6.57) into six different yielding functions, depending on the relations between the principal stresses:

$$\Phi_1^{\mathrm{Tr}}(\boldsymbol{\sigma}, \sigma_y^{\mathrm{Tr}}) = \sigma_1 - \sigma_3 - \sigma_y^{\mathrm{Tr}}, \tag{6.61}$$

$$\Phi_2^{\mathrm{Tr}}(\boldsymbol{\sigma}, \sigma_y^{\mathrm{Tr}}) = \sigma_2 - \sigma_3 - \sigma_y^{\mathrm{Tr}}, \tag{6.62}$$

$$\Phi_3^{\mathrm{Tr}}(\boldsymbol{\sigma}, \sigma_y^{\mathrm{Tr}}) = \sigma_2 - \sigma_1 - \sigma_y^{\mathrm{Tr}}, \tag{6.63}$$

$$\Phi_4^{\mathrm{Tr}}(\boldsymbol{\sigma}, \sigma_y^{\mathrm{Tr}}) = \sigma_3 - \sigma_1 - \sigma_y^{\mathrm{Tr}}, \tag{6.64}$$

$$\Phi_5^{\mathrm{Tr}}(\boldsymbol{\sigma}, \sigma_y^{\mathrm{Tr}}) = \sigma_3 - \sigma_2 - \sigma_y^{\mathrm{Tr}}, \tag{6.65}$$

$$\Phi_6^{\mathrm{Tr}}(\boldsymbol{\sigma}, \sigma_y^{\mathrm{Tr}}) = \sigma_1 - \sigma_2 - \sigma_y^{\mathrm{Tr}}. \tag{6.66}$$

Note that, if we adopt this multisurface representation, the elastic domain for a given σ_y^{Tr} is written as:

$$\mathscr{E}^{\mathrm{Tr}} = \Big\{ \boldsymbol{\sigma} \mid \Phi_i^{\mathrm{Tr}}\big(\boldsymbol{\sigma}, \sigma_y^{\mathrm{Tr}}\big) < 0, \quad i = 1, 2, 3, 4, 5, 6 \Big\}. \tag{6.67}$$

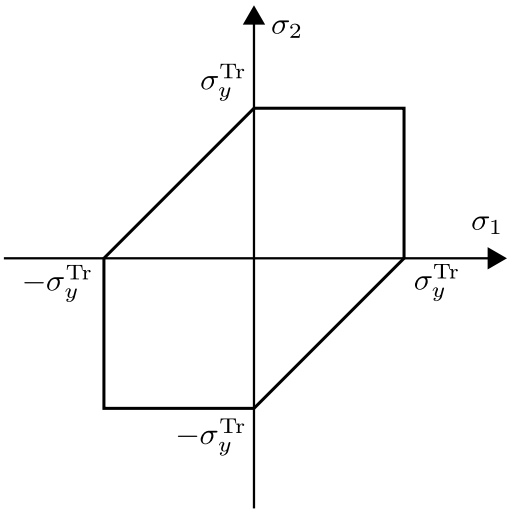

Figure 6.4: Graphical representation of the Tresca yielding surface in the plane $\sigma_3 = 0$ of the space of principal stresses.

6.3.1.2 Von Mises Yield Function

The yielding function of von Mises (von Mises, 1928) can be represented as:

$$\Phi^{\mathrm{VM}}(\boldsymbol{\sigma}, \sigma_y^{\mathrm{VM}}) = \sqrt{3 \cdot J_2(\boldsymbol{s}(\boldsymbol{\sigma}))} - \sigma_y^{\mathrm{VM}}. \tag{6.68}$$

where $J_2(\boldsymbol{s}(\boldsymbol{\sigma}))$ is the second invariant of the stress deviator and σ_y^{VM} denotes the von Mises yielding stress (which is the only adjustable parameter of the model). Similarly to the Tresca yield function, Φ^{VM} is sometimes formulated in the following way:

$$\Phi^{\mathrm{VM}}(\boldsymbol{\sigma}, \sigma_y^{\mathrm{VM}}) = \sigma^{\mathrm{VM}} - \sigma_y^{\mathrm{VM}}, \tag{6.69}$$

where σ^{VM} denotes the equivalent von Mises stress (see equation (5.4)). Using any of the expressions presented to describe the von Mises yield function, we may define the yielding surface associated with this model, which represents the boundary between

the elastic and plastic domains:

$$\mathscr{Y}^{\mathrm{VM}} = \Big\{ \boldsymbol{\sigma} \mid \Phi^{\mathrm{VM}}(\boldsymbol{\sigma}, \sigma_y^{\mathrm{VM}}) = 0 \Big\}. \tag{6.70}$$

Analogously to the Tresca yield stress, the von Mises yield stress is often considered equal to the stress level at which plastic yielding begins under uniaxial stress conditions. When a value is prescribed for the von Mises yielding stress ($\sigma_y^{\mathrm{VM}} = \sigma_y$), we can use von Mises model to verify whether a certain stress state leads to plastic or elastic deformation. Indeed, if the von Mises equivalent stress is equal to the value prescribed for the initial yield stress, plastic deformation is experienced, whereas in the opposite case, just elastic deformation occurs.

We have represented the von Mises yield surface in Figure 6.5 (again, the graphical representation is made in the plane $\sigma_3 = 0$ of the space of principal stresses). In the same Figure, we have shown the Tresca yield surface considering that $\sigma_y^{\mathrm{VM}} = \sigma_y^{\mathrm{Tr}}$ (i.e., they are set to match under uniaxial stress), so that, it becomes apparent that the von Mises yield surface is exterior to the Tresca yield surface. In reality, it is noteworthy to mention that the yield surface of most metals falls between the von Mises and Tresca surfaces (de Souza Neto et al., 2008).

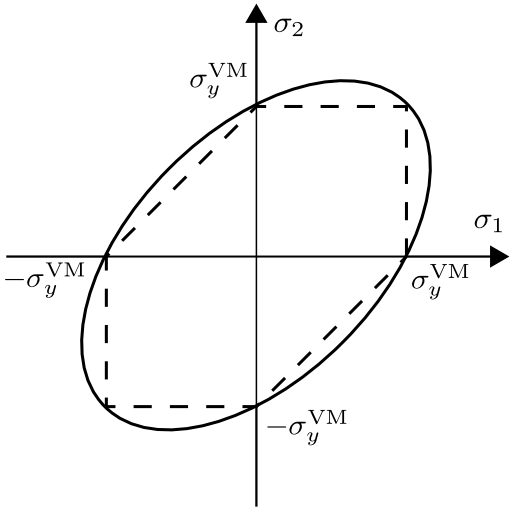

Figure 6.5: Graphical representation of the von Mises yielding surface in the plane $\sigma_3 = 0$ of the space of principal stresses (along with the Tresca yielding surface, supposing that they coincide under uniaxial stress).

6.3.2 Anisotropic Yield Functions

When we are analysing anisotropic polycrystals, neither the isotropic yielding functions of Tresca and von Mises might be adequate. This stems from the fact that they just incorporate one adjustable parameter and therefore they lack the flexibility necessary to describe more complex yield surfaces. As a matter of fact, when the material

is anisotropic, describing its yielding surface by means of an analytical expression is substantially more complex and isotropic yield functions often provide excessively simple (hence, inappropriate) approaches. For this reason several phenomenological anisotropic yield functions have been proposed and, in general, the larger the number of parameters involved in their formulation, the more flexible they are. Despite the fact that anisotropic phenomenological approaches can be employed to obtain accurate representations of the yielding surface of anisotropic specimens, a significant amount of them place restrictions on the elastic symmetries of the materials. As an illustration, the models of Hill (1948) and Barlat and Lian (1989), which are widely used and also available in many commercial codes, are applicable just for anisotropic materials exhibiting orthotropic symmetry (Habraken, 2004). Because textureless anisotropic polycrystals do not exhibit (in principle) any kind of elastic symmetry, this actually poses an important issue concerning the description of their yielding surface by means of anisotropic phenomenological models.

A possible alternative to phenomenological approaches involves the use of micromechanical models, like the one proposed by Darrieulat and Piot (1996). Amongst the possible advantages that result from the use of the model of Darrieulat and Piot (1996), we may mention the fact that: i) it only requires the calibration of three parameters; ii) it does not place any restrictions concerning the elastic symmetries of the polycrystals and iii) it was developed to predict the yielding surface of polycrystals encompassing crystals that follow Schmid's law. Despite these points, the aforementioned model has barely been employed to describe the yield surfaces of anisotropic polycrystals, so that it remains an open issue whether Darrieulat and Piot (1996) yielding function may represent a viable alternative to the classical phenomenological approaches. This probably results from the fact that it demands the consideration of microscopic information that is not always easy to obtain (namely the orientations and the volume fractions associated with all grains). This is not the case in this work, since the software used to create the polycrystal meshes (`Neper`) provides all the information required for the application of the model of Darrieulat and Piot (1996). For all the reasons discussed above, we study the model of Darrieulat and Piot (1996), so that we may be able to use it to describe the yielding functions of anisotropic polycrystals in the next Chapter.

6.3.2.1 Darrieulat and Piot Yield Function

The main idea underlying the yield function developed by Darrieulat and Piot (1996) to describe the yielding surfaces of fcc polycrystals is that they behave like single-crystals possessing $12 \cdot NG$ slip systems (note that fcc crystals comprise 12 slip systems). Additionally, it is also considered that:

- The stress is uniform within the polycrystal (as a consequence, the resolved shear stress on a slip system is constant within each grain and its value depends

only on the Schmid tensor associated with the referred slip system);

- The volume fraction of each grain influences the onset of yielding.

Using the above stated assumptions, Darrieulat and Piot (1996) proposed the following yielding function:

$$\Phi^{\mathrm{DP}}(\boldsymbol{\sigma}, m, n, \sigma_y^{\mathrm{DP}}) = \left(\sum_{r=1}^{\mathrm{NG}} v_r \left(\sum_{\alpha=1}^{12} |\boldsymbol{\sigma} : \boldsymbol{M}^{\alpha,r}|^n \right)^{\frac{m}{n}} \right)^{\frac{1}{m}} - \sigma_y^{\mathrm{DP}}. \tag{6.71}$$

where v_r denotes the volume fraction associated with grain r and m, n and σ_y^{DP} are the three parameters of the model. Note that $\boldsymbol{\sigma}$ represents the global stress tensor (constant within the whole polycrystal) and that $\boldsymbol{M}^{\alpha,r}$ identifies the Schmid tensor associated with slip system α of grain r. The computation of $\boldsymbol{M}^{\alpha,r}$ on a global reference system requires the knowledge of the orientation of all grains, so that both the volume fractions and the texture of the polycrystal have to be known. As we mentioned, this is a significant drawback of the model of Darrieulat and Piot (1996), as this information is generally unavailable. From another standing point, because the volume fraction and the distribution of grain orientations are incorporated in the yielding function, just 3 parameters are required to calibrate the yielding function (anisotropic models often incorporate more parameters). Regarding the parameters of the model, Darrieulat and Piot (1996) suggested that:

- The exponent n is related to the distribution of grain orientations and its value should be between 4 and 30;
- Large values of the exponent m make the yielding surface tend to an inner envelope, whereas small values move the yielding surface away from this inner envelope;
- The yield stress σ_y^{DP} can be used to ensure that certain points (vertices) are contained in the yielding surface and its value is commonly of the same order of magnitude of the critical resolved shear stress assumed.

Analogously to the previously reviewed models, it is important to bear in mind that the yielding surface related to this model is defined as:

$$\mathscr{Y}^{\mathrm{DP}} = \left\{ \boldsymbol{\sigma} \mid \Phi^{\mathrm{DP}}(\boldsymbol{\sigma}, m, n, \sigma_y^{\mathrm{DP}}) = 0 \right\}. \tag{6.72}$$

6.4 Numerical Multi-Scale Framework to Characterize the Yield Response of Polycrystalline Aggregates

In this Chapter, our main goal is to introduce the tools required to numerically characterize the yielding response of fcc polycrystals, so that, in Chapter 7, we are in condition of deducing critical relations between the monocrystalline parameters and the macroscopic yielding surfaces of these materials. At this point, we are well on

our way to accomplished that and what is missing is mostly discussing the numerical multi-scale framework which allows the computation of the yielding stresses. In short, the numerical procedure comprises the following steps:

1. Generate polycrystal meshes;
2. Assign the single-crystal constitutive model reviewed in Section 6.1 to all the grains of the aggregate and submit the polycrystal meshes to several loading conditions, so that stress states belonging to both micro- and macro-yielding surfaces can be obtained (note that the criteria introduced in Section 6.2 should be used to obtain these stresses);
3. Adjust the parameters of the yielding functions covered in Section 6.3, so that they can be used to describe the yielding stresses computed numerically. Once this has been made for several polycrystalline meshes (e.g., comprising different single-crystals), we must relate the parameters of the yielding functions with the microscopic features.

In this Section, the numerical procedure summarised above – apart from the generation of polycrystal meshes which has already been addressed in Section 4.5.1 – is scrutinised. This includes giving an account of the numerical strategy used to obtain points of both the micro- and macro-yield surfaces (Section 6.4.1) and explaining the main idea of the post-processing analysis (Section 6.4.2).

6.4.1 Numerical Strategy to Obtain Yield Surfaces

As we have made it clear in Section 4.5, once the polycrystal meshes are generated with `Neper`, additional data must be specified, so that `Links` can be used to perform the numerical simulations. To be precise, it is necessary to define i) the constitutive model assigned to each grain, ii) the boundary condition of the micro-scale equilibrium problem, iii) the macroscopic deformation gradient imposed on the micro-cell and iv) the number of load increments prescribed and the convergence tolerance adopted. Regarding the first point, a valid option is to assign the single-crystal constitutive model described in Section 6.1 to all the grains of the aggregate, since it is formulated under the assumption of large strains. In addition, it is common ground that the periodic boundary condition allows the use of fewer grains to simulate isotropic elastic behaviour (which means the need of fewer computational resources), so that it is justifiable to focus on this boundary condition. On the contrary, defining the remaining aspects is not as direct as the former two.

The main issue concerning the specification of the deformation gradient and of the incrementation scheme outcomes from the fact that the computational code used in this work (`Links`) is *strain-driven* (which means that the main input variable is the deformation gradient and the main output consists of the homogenised stress tensor – see Figure 3.7). As a consequence, it is not possible to directly impose

a given stress state (belonging to a particular stress subspace) on the polycrystal mesh. If we couple this with the fact that representations of the yield surfaces are generally attempted in subspaces of the six-dimensional stress space (for instance, in the two-dimensional subspace spanned by σ_1 and σ_2, as we have done in Figures 6.4 and 6.5), it becomes clear that we cannot obtain, at least in a straightforward fashion, those representations.

On balance, in order to analyse the shape of the yielding surface, it is of paramount importance to guarantee that we can obtain macroscopic stress states belonging to certain subspaces of the stress space. For the purpose of circumventing the fact that `Links` is strain-driven – and, by extension, to make it possible to achieve overall stress states aligned with specific loading directions –, a strategy similar to the one depicted in Figure 6.6 might be adopted. We must remark that the implementation of the aforementioned strategy was not carried out by the author of this dissertation, so that the computational framework involved in it is out of the scope of this work (this includes detailing the incrementation algorithm). In fact, what is relevant to understand is that an external iterative problem has to be resolved for each loading factor λ_n (for which purpose the Newton-Rapshon method is employed). To clarify, observe that, for a given increment n, the main objective is to find the deformation gradient $\boldsymbol{F}_n^i$ – i.e., the solution of the non-linear problem associated with iteration i – that leads to a homogenised stress state $\boldsymbol{\sigma}_n^i(\boldsymbol{F}_n^i)$, whose relative error to the reference stress $\boldsymbol{\sigma}_n^*$ is below a certain tolerance $\boldsymbol{\sigma}_{tol}$ (in such a way that the converged stress state $\boldsymbol{\sigma}_n^i \approx \boldsymbol{\sigma}_n^*$ is aligned with the prescribed stress tensor $\boldsymbol{\sigma}^*$). When this stress state is found, one (or more) yielding condition(s) are evaluated. The scheme associated with the evaluation of the yielding criteria is illustrated in Figure 6.7. As we may see, it fundamentally comprises two main steps: firstly, the value of parameter p_n which satisfies criterion (6.51) and the global equivalent plastic strain ε_n^p associated with increment n are computed; then, they are compared to reference values, which basically define the yielding conditions that we want to characterize. When the comparisons are made, three possibilites arise:

- One of the calculated parameters matches one of the reference values, in which case the information about the converged stress state must be stored and the value of n updated (increased), according to the incrementation algorithm;
- Both parameters p_n and ε_n^p do not match any of the reference values and there is not any reference value located between the values of the parameters of the current increment (p_n and ε_n^p) and the ones associated with the previous increment (p_{n-1} and ε_{n-1}^p). Even though the converged stress state is not associated with any yield criteria, it is stored in an output file which compiles all converged stress states (and the associated values of the global elastic strain ε^e, of the global plastic strain ε^p and of the global total strain ε, so that both stresses and strains associated with a specific loading path are

saved). Moreover, the value of n should be increased in consistency with the incrementation strategy;

- Both parameters p_n and ε_n^p do not match any of the reference values and at least one of the reference values is located between the values of the parameters of the current increment (p_n and ε_n^p) and the ones associated with the previous increment (p_{n-1} and ε_{n-1}^p). This means that the increase of the loading factor from the last increment was excessive, so that λ_n must be decreased to some value lying between λ_{n-1} and λ_n. In this case, the converged stress state is not saved.

By employing the procedure represented in Figure 6.7, it is possible to ensure that all yielding stresses of interest are calculated (provided that the magnitude of the prescribed stress state $\boldsymbol{\sigma}^*$ is large enough to reach those stresses). From another standing point, this means that, for a specific loading direction, we can obtain with a single simulation the underlying yield stresses (associated with the yield criteria considered), as well as the stress tensors and the global strain measures related to each one of the increments.

In Tables 6.2 and 6.3, we have listed the parameters which determine the yielding conditions considered. We must note that we decided not to compute the true micro-yielding stress, since its numerical calculation is not compatible with the computational approach described above[12]; instead, we have used the values suggested by Brenner et al. (2009) for the purpose of studying the micro-yield condition. Adding to this, we have also followed the approach based on the equivalent plastic strain, which allows us to study both the micro- and the macro-yielding stresses.

Table 6.2: Values of p which define considered yielding conditions.

Parameter	**Values**			
p	3	2	1	0

Table 6.3: Values of ε^p which define considered yielding conditions.

Parameter	**Values**				
ε^p	10^{-13}	10^{-6}	10^{-4}	$2 \cdot 10^{-3}$	10^{-2}

[12]The numerical computation of the true micro-yield stress requires that an additional simulation – which does not allow plastic deformation – has to be performed, so that the highest stress state in the elastic domain can be determined. As a consequence, it would be needed to double the number of simulations, in case we want to compute the true micro-yield stress (which was not viable considering the computational resources available). Nevertheless, observe that the condition established by $\varepsilon^p = 10^{-13}$ identifies a reasonable approximation of the true micro-yield condition.

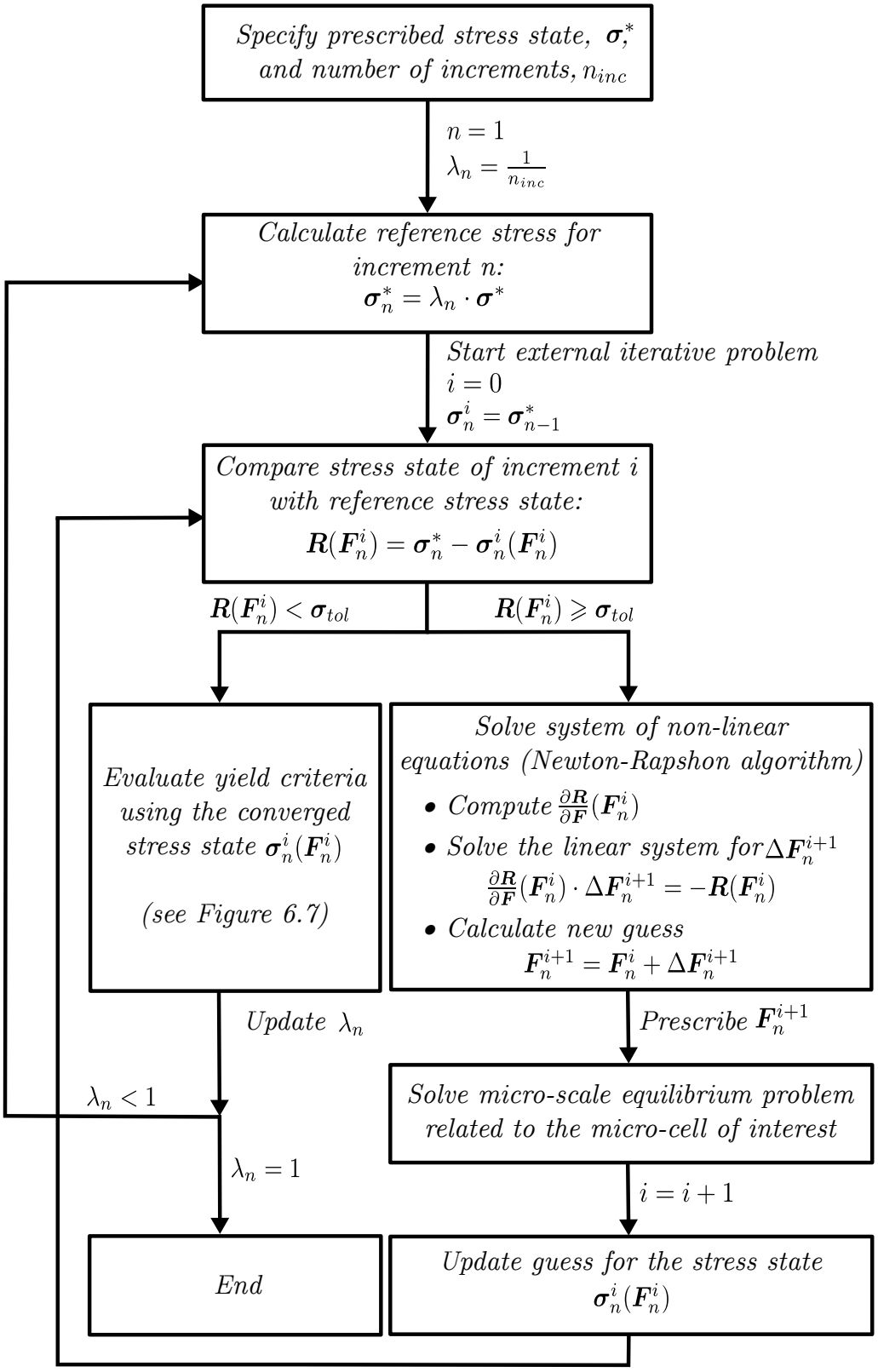

Figure 6.6: Strategy to impose stress states on the micro-cells.

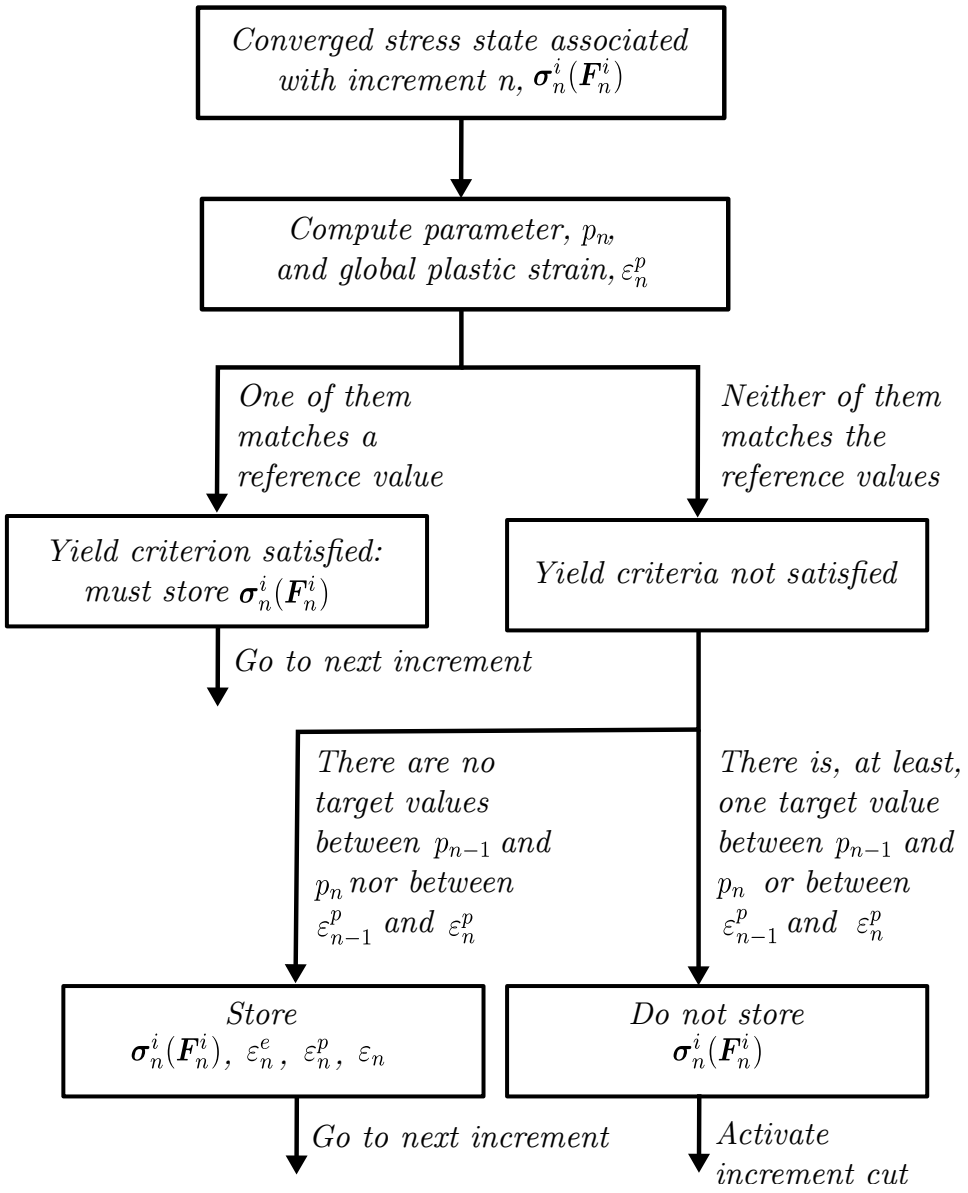

Figure 6.7: Evaluation of yielding criteria.

It is important to realize that the computational effort required to solve the iterative scheme depicted in Figure 6.6 is fairly high. For that reason, we decided to focus only on the subspace spanned by σ_1 and σ_2, so that we analysed a limited number of directions in the stress space. In such instance, each loading direction may be characterized by an angle θ and a radius r, i.e., the prescribed stress states are defined as:

$$\boldsymbol{\sigma}^*(\theta, r) = r \cdot \begin{bmatrix} \cos(\theta) & 0 & 0 \\ 0 & \sin(\theta) & 0 \\ 0 & 0 & 0 \end{bmatrix}. \tag{6.73}$$

We considered 48 spatial directions, that is, the computations were performed with 7.5° degree steps. Accordingly, each of the angles is expressed (in radians) as:

$$\theta_i = 7.5 \cdot \frac{\pi}{180} \cdot (i-1), \quad i = 1, ..., 48. \tag{6.74}$$

On the other hand, the value of r must be defined in order to guarantee that all yielding criteria are satisfied, that is, it must lead to prescribed stress states $\boldsymbol{\sigma}^*$ which exceed the yield stresses associated with all yielding criteria considered. Lastly, note that, theoretically speaking, any number of increments can be used, but the more the increment cuts, the greater the computational time required. For this reason, we have considered 50 increments in all analyses.

6.4.2 Post-Processing

In the previous Section, we have presented a computational strategy that allows the determination of stress states associated with yielding conditions defined by particular values of the parameter p or of the global plastic strain ε^p. In this context, it is pertinent to realize that each numerical simulation (associated with a specific loading direction) generates two main output files:

- One of them comprising all the converged macroscopic stress states and the underlying values of the equivalent total strain ε, the equivalent elastic strain ε^e and the equivalent plastic strain ε^p;
- The other compiling the yield stresses (specifying, for each one of them, the associated yielding criterion).

In such case, we must bear in mind that the output file containing all the converged stress states can be used to inspect the relation between stresses and strains, while the other allows the comparison between different yield criteria and the analysis of the shape of the yielding surfaces (provided that several loading directions are considered). An important point to make is that in order to characterize the yielding response of fcc polycrystals, several loading directions and different single-crystals have to be studied, so that, in practice, hundreds of output files are generated. The automated use, fast interpretation and manipulation of the information contained

in these output files is the main objective of the post-processing analysis and it embodies a crucial step of our work. To post-process the data computed numerically, we have used `Matlab`®. In summary, a significant amount of scripts were developed from scratch, so that the generation of graphical representations, the calibration of yielding functions (which approximate numerical yield stresses), and the comparison of the results linked to distinct yielding criteria could be easily performed. In this context, we must draw the attention to the fact that the implementation of the yielding function of Darrieulat and Piot and, in particular, the adjustment of the underlying parameters (using least squares fitting) to a set of numerical stress states, is not trivial.

The results and conclusions extracted from the post-processing analysis are reported in the next Chapter. Before we move on though it is relevant to recall that the fundamentals addressed in this Chapter are indispensable for the full comprehension of what comes next. In particular, reviewing Section 6.1 allows the identification of the critical micromechanical parameters: knowing that we are focusing on polycrystals comprising fcc crystals randomly oriented, it is expected that early stages of plasticity are essentially influenced by the monocrystalline elastic parameters and the initial critical resolved shear stress. Likewise, the reading of 6.2 enables the understanding of the differences between the concepts of micro- and the macro-yielding, not to mention that it allows the comprehension of the two approaches that we have followed to numerically estimate both micro- and macro-yield stresses (one of them based on the parameter p and the other on the global plastic strain ε^p). Finally, Section 6.4 provides the description of the numerical procedure adopted, along with the identification of the main numerical outputs and the challenges involved in the post-processing analysis (amongst them, we must highlight the description of the numerical yield stresses by means of the yielding functions treated in Section 6.3).

Chapter 7

Influence of the Monocrystalline Parameters on the Yielding Response of Polycrystalline Aggregates

Within the characterisation of the elastic response of both isotropic and anisotropic polycrystals (Chapter 5), we have ascertained that the microscopic distribution of stresses and strains (in the elastic domain) is intrinsically connected to the anisotropy of the single-crystal – specifically, it was noticed that the greater the anisotropy exhibited by the single-crystal, the greater the heterogeneities of both stress and strain fields. A direct consequence of the previous fact is that the macroscopic stress required to activate plastic slip within polycrystals encompassing anisotropic crystals is smaller than the one needed for aggregates enclosing isotropic grains. For the purpose of quantifying the influence of the monocrystalline parameters on the yielding response of fcc polycrystals we may use the numerical multi-scale framework presented in Section 6.4. In such instance, we should begin by performing several numerical tests (which may involve different single-crystals and distinct loading conditions). Then, the yielding functions introduced in Section 6.3 must be considered, so that the yielding stresses associated with a particular material can be described by means of an analytical expression. Once these functions are calibrated, their parameters must be related to the monocrystalline properties, namely the elastic anisotropy, so that critical relations, which explain the macroscopic behaviour based on microscopic features, can be deduced. It must be remarked that the strategy briefly resumed here can be used to delineate the dependency of both micro- and macro-yielding stresses on the monocrystalline parameters. In fact, although it is well-established that the elastic anisotropy has a significant impact on the earliest stage of elasto-plastic transition (Clausen, 1997), it is also relevant to study its effect on the macro-yield stress, as this mechanical property takes on utmost relevance in the design of most structural components (commonly, they are designed based on the principle that the macro-yield stress cannot be exceeded). To summarise, the use of the mentioned

numerical multi-scale procedure (together with the consideration of the remaining concepts covered in Chapter 6) allows establishing the bridge between micro- and macro-parameters, in such a way that the characterisation of the yielding response of fcc polycrystals can be accomplished. Adding to all this, note that by using the procedure detailed in Section 6.4, other important questions may be addressed: for instance, we may discuss the best approach to define the micro-yield condition.

In this Chapter, the characterisation of the yielding response of polycrystalline materials comprising single-phase face-centered cubic crystals randomly oriented is attempted (utilizing the numerical procedure of Section 6.4). Because we are dealing with textureless polycrystals, it is expected that their yielding response is mainly controlled by the monocrystalline parameters, insomuch that the whole framework presented in what follows is directed towards the deduction of relations between the mentioned parameters and the macro- and micro-yield stresses. It is important to emphasise that both isotropic (Section 7.1) and anisotropic (Section 7.2) polycrystals are approached, but since most polycrystalline systems belong to the first group, we devoted special attention towards the characterisation of the yielding response of isotropic polycrystals. Moreover, it is apposite to refer that both Sections 7.1 and 7.2 concern the same topics: i) the analysis of the micro-yield surface, ii) the evolution of the yield surface (considering low levels of plastic deformation), iii) the inspection of macroscopic stress-strain curves and iv) the determination of the relation between the yield stresses and the crystalline parameters.

The characterisation of the yielding response of single-phase textureless fcc polycrystalline materials through micro-scale studies based on computational homogenisation has been addressed extensively in the literature. In particular, we highlight the works of Brenner et al. (2009) and Scheunemann (2017) who, respectively, focused on the analysis of the micro-yielding response and on the evolution of the shape of the yielding surface of isotropic polycrystals. In this Chapter, we have used the results reported in these contributions as a reference for the numerical results. Within this context, it is noteworthy that the analytical results reported by Brenner et al. (2009) (besides the numerical results) and the conclusions announced by Clausen (1997) – regarding the effect of the elastic anisotropy on the deformation pattern – were also considered.

7.1 Characterisation of the Yielding Response of Isotropic fcc Polycrystals

Not only most polycrystalline systems of interest are isotropic, as they are also commonly designed to withstand loads that do not stress outside the elastic domain. If we couple this with the fact that there is a growing need for weight-optimized structures (so that oversizing must be avoided), it becomes apparent that the

accurate determination of the yielding stresses is a fundamental consideration for the mechanical design of components.

Since we are focusing on isotropic polycrystals, it is relevant to understand that the yielding response of these materials is mostly dictated by the monocrystalline parameters (especially the elastic anisotropy), insomuch that the influence of the morphological anisotropy can be neglected. For that reason, we decided to analyse just one isotropic polycrystal mesh (characterised by a specific distribution of grain orientations and geometric morphology), whose main features are specified in Table 7.1. In this Table, we have also included the additional data required to perform the numerical simulations, so that we have compiled the content discussed in Section 6.4.1 in a way that allows the rapid identification of the variables between analyses (namely, the monocrystalline elastic constants and the loading direction). Even though most of the aspects listed in Table 7.1 have already been dealt with, it is pertinent to make a few comments:

- Because we were interested in analysing a single isotropic polycrystal mesh, we had to ensure two things: first, the number of grains encompassed must be sufficiently large to provide elastic isotropic behaviours and, second, it must be as small as possible, so that the computational resources required might be minimised to what is strictly necessary. With this in mind, and because we just studied aggregates encompassing crystals for which $A^{\mathrm{L}} \leqslant 1$, we decided (based on equation (5.25)) to consider a polycrystal mesh with 1000 grains;
- Despite the fact that the use of low refinement structured polycrystalline meshes slightly influences the results obtained (see Section 5.1.3), the increase in accuracy from using more refined meshes or non-structured meshes does not compensate for the increase in computational time (taking into account the objectives of the work and the time available). For that reason, we considered a polycrystal mesh with 10648 elements, that is, with approximately 10 elements per grain on average (it must be remembered that the relative error associated with the prediction of the isotropic elastic properties is always under 5% in case this level of discretisation is employed for polycrystals meshes comprising crystals with $A^{\mathrm{L}} \leqslant 1$);
- If the initial critical resolved shear stress is assumed constant, the most important parameter for the characterisation of the initial yielding response of fcc polycrystalline materials is the elastic anisotropy. In such instance, as a simplification, we assumed the same hardening properties in all numerical simulations, regardless of the single-crystal considered.

In this Section, we endeavoured to characterize the yielding response of isotropic aggregates comprising crystals with face-centered cubic lattices. In specific, we focused on the study of the micro-yield surface (Sections 7.1.1 and 7.1.2) and of the macro-yield surface (Sections 7.1.3 to 7.1.5), as well on the analysis of stress-strain

curves (Section 7.1.4). An important point to make is that in the following Sections (7.1.1 to 7.1.5), we have used the isotropic yield functions of Tresca and von Mises to describe the sets of numerical yield stresses computed, so that, in practice, the yield stresses of Tresca and von Mises (i.e., the parameters of the yielding functions) were the macroscopic quantities used to establish the critical micro-macro relations.

Table 7.1: Parameters specified in the numerical simulations performed (for the determination of the yielding response of isotropic polycrystals).

Parameter	**Assigned value(s)**
Definition of the polycrystal mesh	
Type of Problem	3D
Mesh properties	Structured meshes with 10648 F-bar eight-noded hexahedra (22 elements per side of the cube)
Number of grains	1000
Number of phases	1 (single-phase)
Polycrystal geometry	Cubic shape
Polycrystal morphology	Regularized Poisson-Voronoi tessellations
Additional data required	
Macroscopic deformation gradient	Defined according to the procedure of Section 6.4.1, so that 48 spatial directions of the plane spanned by σ_1 and σ_2 were studied
Constitutive model of each grain	Described in Section 6.1. The elastic constants varied between analyses, but the hardening properties were maintained constant: $q = 1$, $\tau_{y,0} = 0.06$ GN/m^2, $K = 0.18$ GN/m^2, $\gamma_0 = 0.03$, $m = 0.56$
Boundary condition	Periodic
Load incrementation	50 evenly distributed increments

7.1.1 Study of the Micro-Yield Surface

It is well-established that the micro-yield stresses of fcc isotropic polycrystals are mostly dependent on the elastic anisotropy of the single-crystal, as this parameter

is deeply related to the distribution of stresses and strains within the aggregates in the elastic domain. In order to determine the relation between the micro-yield stress states and the elastic anisotropy, we should start by studying micro-yield surfaces, so that we may describe the yielding responses of polycrystalline aggregates using analytical expressions (yield functions). In such case, once the parameters of the considered yield functions are conveniently defined, their relation with the elastic anisotropy of the single-crystals can be studied and a micro-macro law may be inferred.

In line with what was stated in the previous paragraph, in this Section we concentrate on the analysis of the shape of the micro-yield surfaces, whereas in Section 7.1.2 we attempt to quantify the influence of the elastic anisotropy on the micro-yielding responses. An important point to make before proceeding is that the micro-yield stress states are not exclusively dependent on the elastic anisotropy of the single-crystals: in reality, the initial value of the critical resolved shear stress also affects the micro-yield stresses. Nonetheless, it is crucial to understand that this quantity only exerts influence on the order of magnitude of the micro-yielding stresses, that is, the shape of the micro-yielding surface is dissociated from the highlighted parameter. Within this discussion, it is also worth mentioning that once plastic slip begins, all the hardening parameters (including the initial critical resolved shear stress) have an impact on the macroscopic yielding behaviour – nevertheless, because the levels of plastic deformation involved are generally low for all criteria studied in this work, we have neglected their effect while studying the micro-yielding response of isotropic fcc aggregates. To summarise, the analysis of micro-yielding surfaces must be made in terms of dimensionless (macroscopic) principal stresses, defined as follows:

$$\sigma_{i,dim} = \frac{\sigma_i}{\tau_{y,0}}, \quad i = 1, 2, 3. \tag{7.1}$$

where $\tau_{y,0}$ identifies the initial critical resolved shear stress (in this case, as can be extracted from Table 7.1, $\tau_{y,0} = 0.06$ GN/m^2).

Now that we have established the dimensionless quantities which allow us to study the impact of the elastic anisotropy on the micro-yielding response of fcc isotropic aggregates (without the influence of any other micromechanical parameters), the first step consists of comparing the stress states associated with different micro-yielding criteria, so that we can get accurate estimates for the micro-yielding stresses. In other words, we must begin estimating the values of the micro-yield stresses and since there is not a unique definition of how they should be calculated, the results obtained with different criteria are compared in order to identify the one which leads to more accurate micro-yield stress states. Taking into account the numerical procedure described in Section 6.4, in principle, the approaches that conduct to the lowest values for the micro-yielding stresses are the ones involving the highest value of the parameter p (i.e., $p = 3$) and the lowest value of the total plastic strain (given

by $\varepsilon^p = 10^{-13}$). Numerically computed stress states associated with these criteria are shown in Figures 7.1 and 7.2 for polycrystalline aggregates of Copper and Aluminium. It is apparent that the numerical estimates for the micro-yielding stress states are practically coincident (this trend applies particularly for the isotropic polycrystal mesh of Aluminium which comprises less elastically anisotropic single-crystals). Furthermore, and despite the evident similarities of the stress states associated with the two different yielding conditions, it is noticeable that the criterion established by $p = 3$ leads to lower stress states, so that it is seemingly more appropriate to determine the onset of crystallographic slip. In Figures 7.3 and 7.4, we have compared the micro-yield stress states which arise from considering other criteria than the ones that result from the criterion given by $p = 3$. From the referred Figures, it becomes clear that the micro-yielding conditions $p = 0, 1, 2, 3$ are associated with overall levels of plastic deformations generally below 10^{-6}; besides this, we may note that the smaller the elastic anisotropy of the single-crystal, the closer the estimates for the micro-yield stress states – as a consequence, it is undeniable that Hutchinson (1970) approach ($p = 0$) produces coarse estimates for the micro-yield stresses if highly anisotropic single-crystals are considered (that is, neglecting the stress heterogeneities within the grains is not a reasonable assumption to compute the micro-yield stresses of aggregates comprising elastically anisotropic single-crystals, since their values are significantly larger than the ones obtained when the stress heterogeneities within the grains are taken into account).

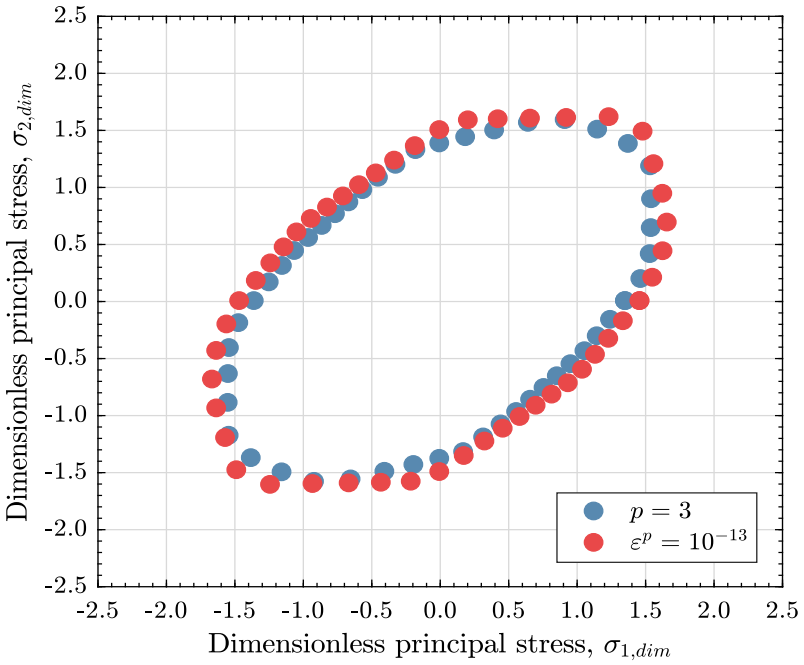

Figure 7.1: Numerical estimates for the stress states associated with the micro-yielding criteria defined by $p = 3$ and $\varepsilon^p = 10^{-13}$, considering 48 loading directions and an isotropic polycrystal mesh of Copper.

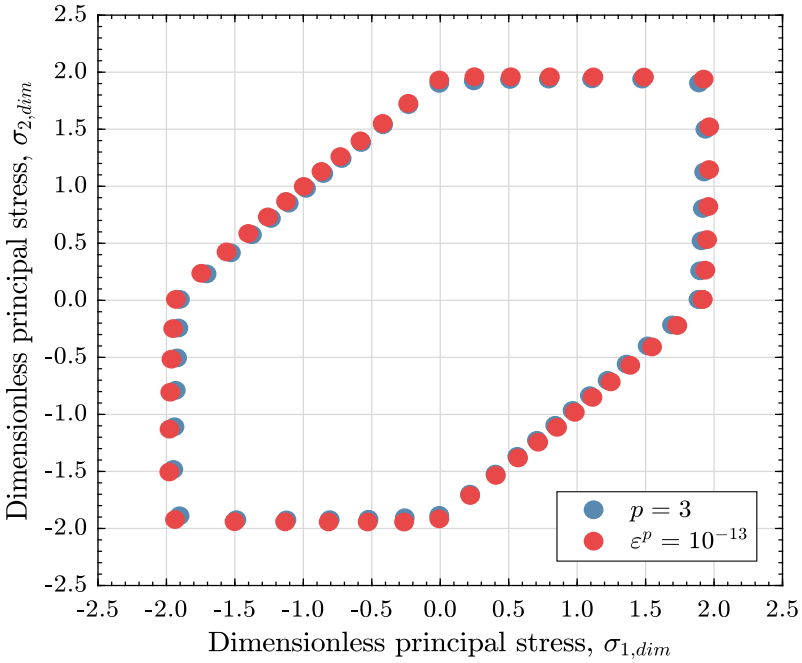

Figure 7.2: Numerical estimates for the stress states associated with the micro-yielding criteria defined by $p = 3$ and $\varepsilon^p = 10^{-13}$, considering 48 loading directions and an isotropic polycrystal mesh of Aluminium.

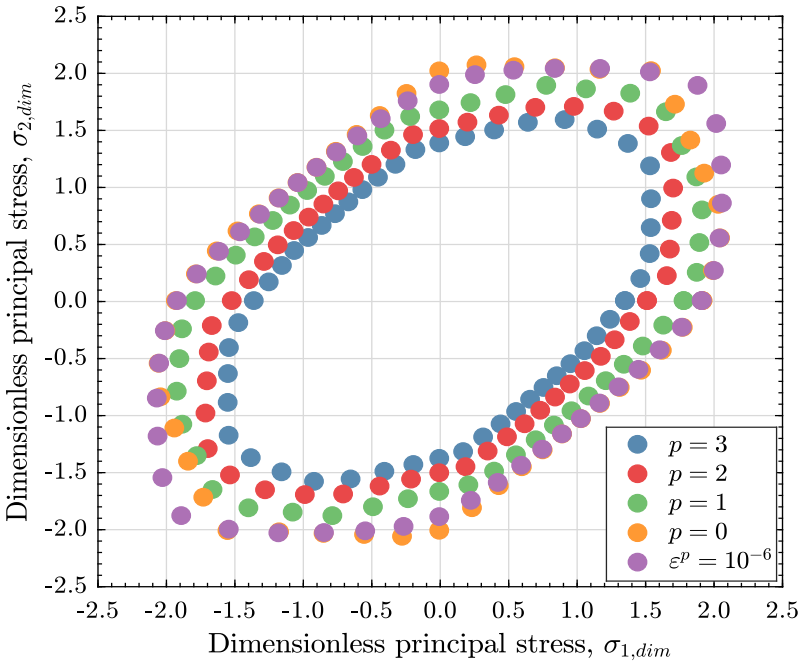

Figure 7.3: Numerical estimates for the stress states associated with several micro-yielding conditions, considering 48 loading directions and an isotropic polycrystal mesh of Copper.

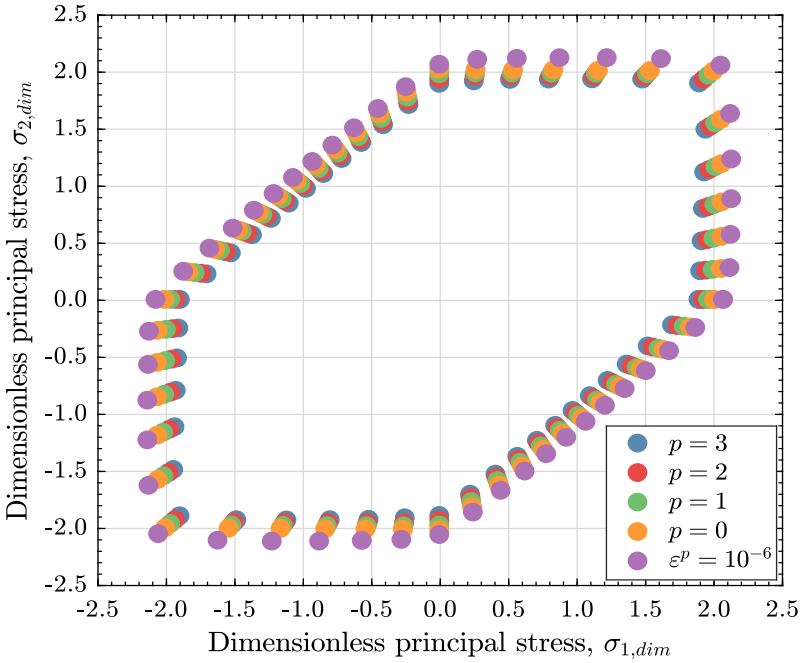

Figure 7.4: Numerical estimates for the stress states associated with several micro-yielding conditions, considering 48 loading directions and an isotropic polycrystal mesh of Aluminium.

The micro-yield criterion assumed strongly affects the results obtained for the micro-yield stresses. Because the condition $p = 3$ is linked to the lowest stress states, we may be tempted to consider that it embodies the most accurate proposal to define the onset of plastic slip. An important point to be made, however, is that the referred criterion does not necessarily imply that plastic slip has been activated within the polycrystal. Indeed, note that when $p > 0$, the average of the resolved shear stresses on slip system α of grain r ($\forall \alpha \in \mathscr{A}, r \in \mathscr{N}$) is below the critical resolved shear stress, so it may occur that the resolved shear stress has not reached the critical value $\tau_{y,0}$ in any slip system (considering all Gauss points of the polycrystalline mesh). This is likely to happen if high values of p are used. Therefore, we must understand that the stress states associated with values of p larger than 0 are related to the probability of the onset of plastic yielding to be located between them and the stress state defined by Hutchinson approach ($p = 0$) – for instance, $p = 3$ establishes that this probability is, at least, equal to 90% (for a Gaussian distribution, this value rises to 99.7%). It is important to recall that an alternative interpretation of the physical significance of p has been given in Section 6.2.3: according to that definition, for $p = 3$, 0.15% of the first plastifying grain has to deform plastically to consider that the plasticity onset has been reached; if, as in this case, coarse meshes are being analysed, this criterion is satisfied before any Gauss point deforms in the plastic domain (note that there are 80 Gauss points per grain; hence, $0.0015 \cdot 80 < 1$). On the whole, the numerical results linked to the micro-yielding conditions of Brenner et al.

(2009) might lead to misleading conclusions regarding the definition of the micro-yield surface. In our case, the results linked to the criterion $p = 3$ are fairly close to the ones which result from considering $\varepsilon^p = 10^{-13}$, so that it is reasonable to state that the former condition seems to provide accurate estimates for the micro-yield stresses.

In what follows, we have used the criterion $p = 3$ to define the micro-yielding condition. In such case, it is then of primary importance to describe the underlying numerical micro-yield stress states using an analytical expression. To that end, the yield functions of Tresca and von Mises were considered and the corresponding parameters (respectively, the yield stresses of Tresca and von Mises) were adjusted through the least squares methodology – the results can be seen in Figures 7.5 and 7.6. From these Figures, it is evident that both isotropic yield functions provide good descriptions of the numerical micro-yielding stress states, although it is also notorious that the Tresca yield function is more appropriate to describe the stress states associated with the Aluminium polycrystal, while its von Mises counterpart provides a better fit to the numerical micro-yield stress states obtained for the Copper polycrystal. In this context, it is relevant to state that similar conclusions have been drawn by Brenner et al. (2009) who used the self-consistent scheme to verify that higher values of p and A^{L} lead to more pronounced deviations from Tresca-type yield surfaces. In fact, based on the available numerical data, it seems that the von Mises yield function might give better approximations of the micro-yielding surfaces in case isotropic fcc aggregates consisting of elastically anisotropic crystals are studied.

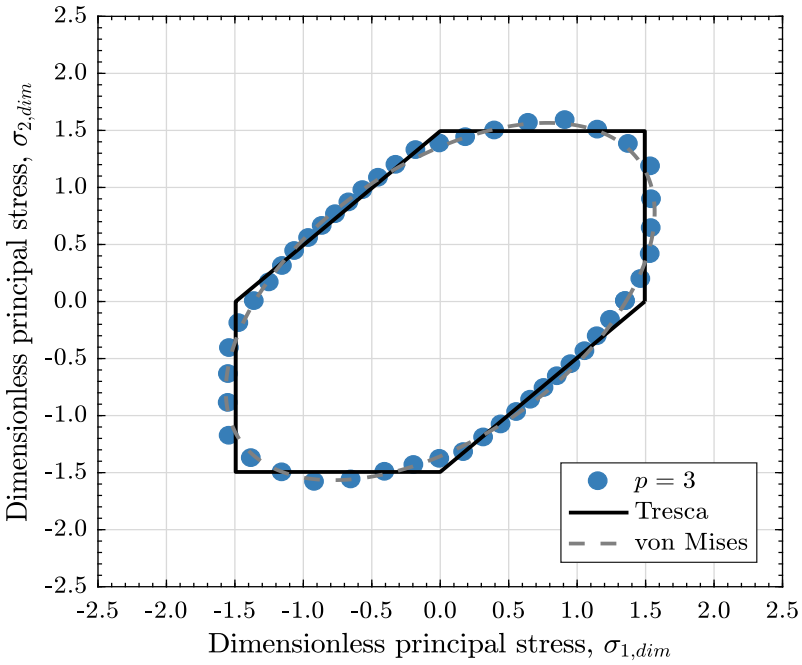

Figure 7.5: Description of the micro-yield surface of an isotropic polycrystal of Copper using the yield functions of Tresca and von Mises (the underlying parameters were computed using least squares fitting).

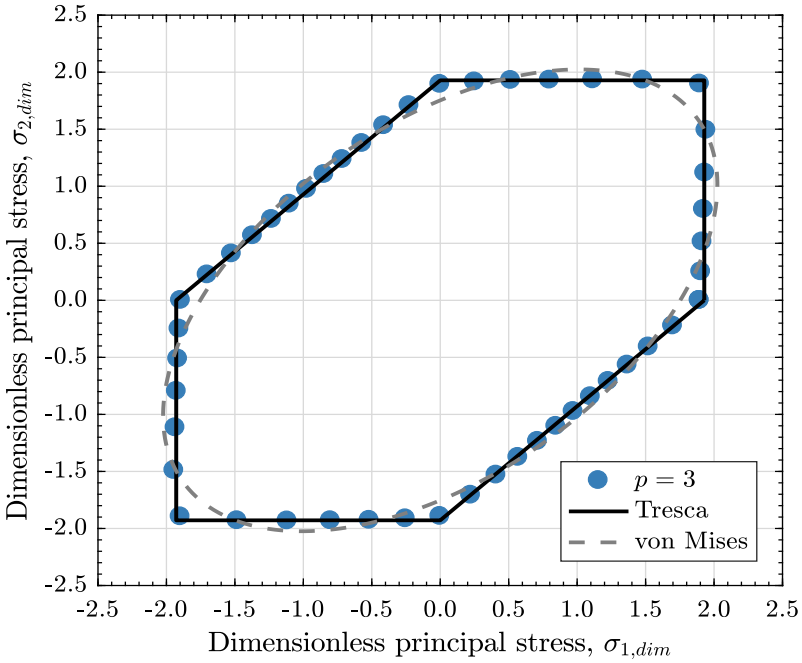

Figure 7.6: Description of the micro-yield surface of an isotropic polycrystal of Aluminium using the yield functions of Tresca and von Mises (the underlying parameters were computed using least squares fitting).

7.1.2 Determination of the Micro-Yield Stress

In the previous Section, we have ascertained that the Brenner et al. (2009) yielding condition $p = 3$ might be used to estimate the micro-yielding stress states, as it agrees well with an alternative approach based on the evaluation of a low level of global plastic strain. Besides, we have also noticed that both isotropic criteria of Tresca and von Mises can be employed to describe the micro-yield surface of isotropic polycrystals, with the former being more adequate for polycrystals comprising less elastically anisotropic crystals and the latter for more elastically anisotropic grains. All in all, either of the yield functions can be used to provide acceptable descriptions of the micro-yielding surfaces of isotropic fcc aggregates. As a consequence, a single parameter is enough to characterize the micro-yielding response of these materials (namely, the yield stress of Tresca or of von Mises, depending upon the considered yield function). As it is customarily done in cases in which the micro-yield functions of Tresca and von Mises produce proper descriptions of the yielding behaviour, we assumed that the aforementioned parameter corresponds to the micro-yielding stress under uniaxial stress conditions (hereafter, we will identify this quantity as σ_y^{uni}, in such a manner that its dimensionless counterpart $\sigma_{y,dim}^{uni}$ is defined analogously to the dimensionless principal stresses).

Since the micro-yield stress under uniaxial stress conditions is the only parameter that we need to calibrate to define the micro-yielding response of isotropic polycrystals,

several uniaxial tensile tests must be performed. Those tests may be executed on the same polycrystal morphology considered until this point (whose features are detailed in Table 7.1), however we now consider crystals other than Aluminium and Copper. In particular, we have considered fcc isotropic aggregates enclosing fcc crystals of Silver, Gold, Nickel and Lead, as well as a polycrystal mesh comprising nearly isotropic crystallites (the elastic constants utilized were the ones of Tungsten). The results of the tensile tests are depicted in Figure 7.7, in such a manner that it becomes evident that an exponential law of the form:

$$\sigma_{y,dim}^{uni} = e^{p_{10} \cdot A^{\mathrm{L}}} + 1, \tag{7.2}$$

outlines the dependency of the micro-yield stress on the elastic anisotropy of the single-crystal. We may observe that this law is applicable even if higher values of p are considered (the values of the parameter p_{10}, generated using least squares approximations, are resumed in Table 7.2). In fact, from the results obtained, it becomes apparent that the elastic anisotropy plays a decisive role on the onset of crystallographic slip. In detail, we have found that the micro-yield stress decreases exponentially with the log-Euclidean anisotropy factor A^{L}. The highest value of the micro-yield stress is thus related to the polycrystal comprising isotropic grains and its value coincides with the theoretical estimate for the maximum uniaxial stress required to activate plastic slip in a fcc single-crystal ($\sigma_y^{uni} = 2 \cdot \tau_{y,0}$). Indeed, as the stress and strain fields are constant within locally isotropic polycrystals, all the micro-yield conditions of Brenner et al. (2009) give rise to the same estimate for the micro-yield stress in this case. Finally, it is worth reinforcing that even for $p = 0$, we have verified that the micro-yield stresses decrease as polycrystals with more anisotropic grains are analysed. This contradicts the findings of Hutchinson (1970), who used the self-consistent scheme to establish the relation between the two previously highlighted parameters (see Section 6.2.2). Consequently, a question arises whether the self-consistent method can provide accurate estimates for the micro-yielding stresses in case the criterion defined by $p = 0$ is used; likewise, we should not exclude the possibility that the results reported here might have been influenced by the type of element and level of discretisation used or by the hardening properties assumed.

Table 7.2: Parameter p_{10} associated with each micro-yielding criteria of Brenner et al. (2009).

Yielding criterion	p_{10}
$p = 3$	-1.52
$p = 2$	-0.94
$p = 1$	-0.37
$p = 0$	-0.12

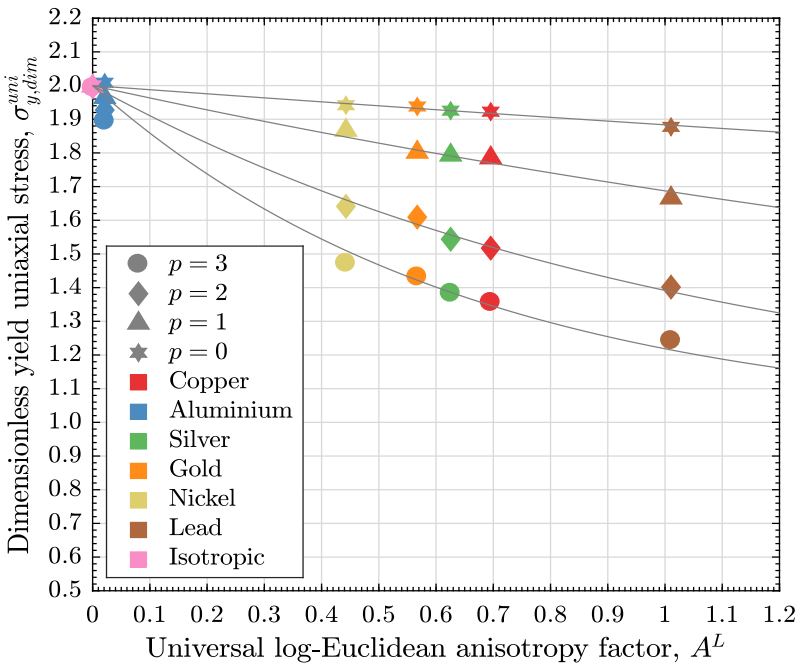

Figure 7.7: Relation between the numerical micro-yield stresses of Brenner et al. (2009) (under uniaxial stress conditions) and the elastic anistropy of the single-crystal.

7.1.3 Study of the Macro-Yield Surface

For the purpose of studying the macro-yielding response of isotropic fcc aggregates, it is necessary to examine the shape of the macro-yield surface. This can be accomplished if several stress states belonging to the mentioned surface are computed numerically. Specifically, because the macro-yield condition is conventionally associated with an offset plastic strain of 0.2%, we focused on the numerical calculation of the stress states associated with that level of global plastic strain. Furthermore, due to the fact that we are inspecting the yielding response of isotropic aggregates, the yield functions of Tresca and von Mises were again considered.

In Figures 7.8 and 7.9, the numerical stress states associated with the conventional macro-yield condition, along with the Tresca and von Mises yield functions obtained by least squares approximation, are shown (they are respectively linked to isotropic polycrystals of Copper and Aluminium). In brief, it happens that both sets of macro-yield stress states (of Copper and Aluminium) are remarkably similar: not only they can be accurately described by a von Mises-type yield function, as the dimensionless von Mises yield stress is essentially the same. As we have seen in Figures 7.5 and 7.6, the micro-yield surfaces of these materials are fairly different, so it is relevant to observe the evolution of the yielding surface – see Figures 7.10 and 7.11.

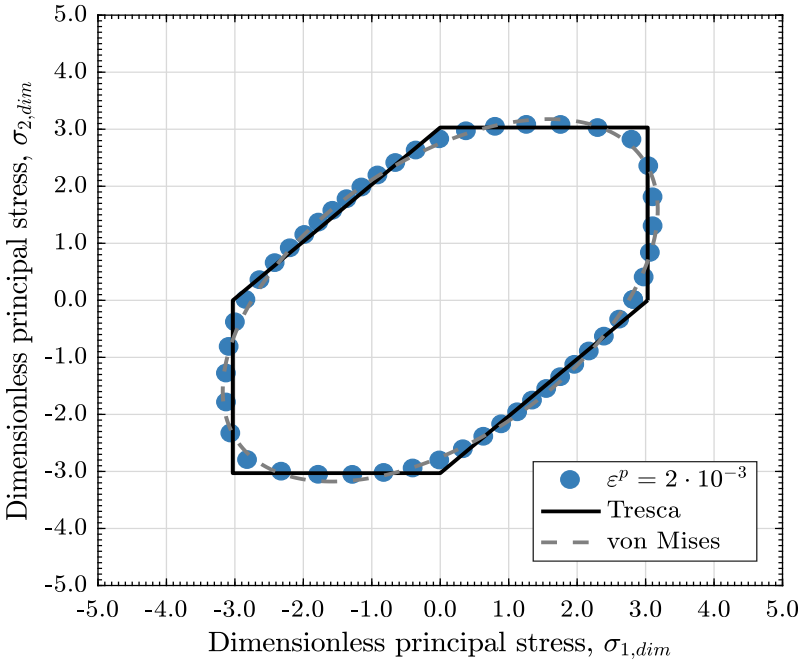

Figure 7.8: Description of the macro-yield surface of an isotropic polycrystal of Copper using the yield functions of Tresca and von Mises (the underlying parameters were computed using least squares fitting).

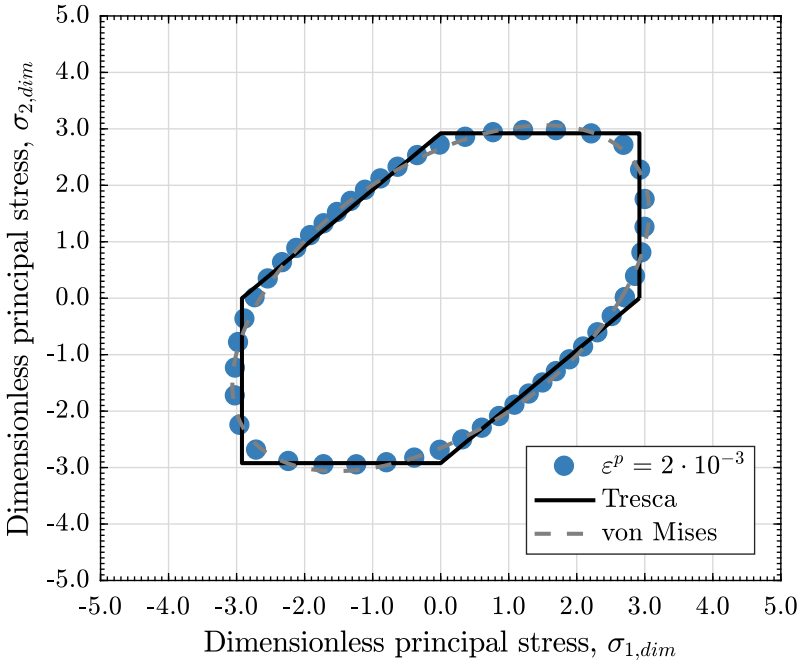

Figure 7.9: Description of the macro-yield surface of an isotropic polycrystal of Aluminium using the yield functions of Tresca and von Mises (the underlying parameters were computed using least squares fitting).

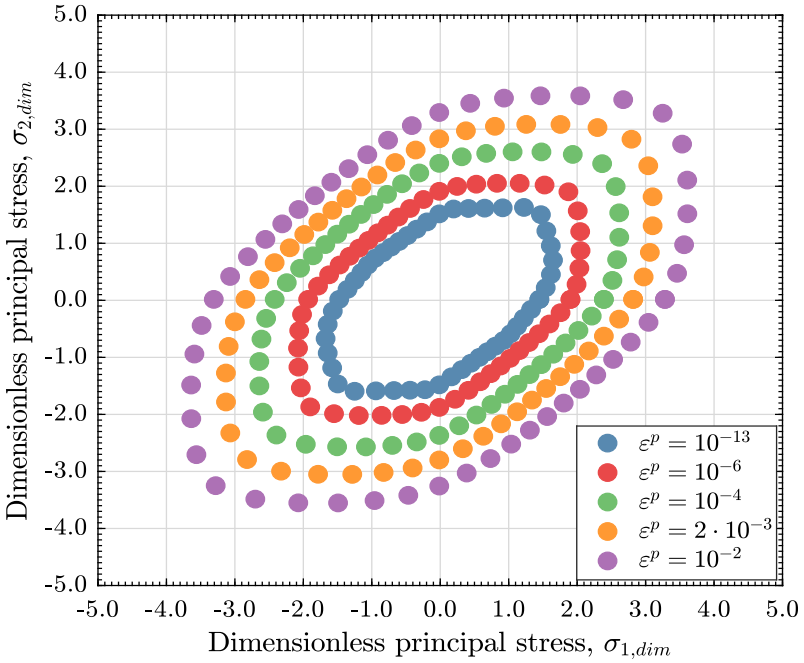

Figure 7.10: Evolution of the yield surface of an isotropic polycrystal of Copper.

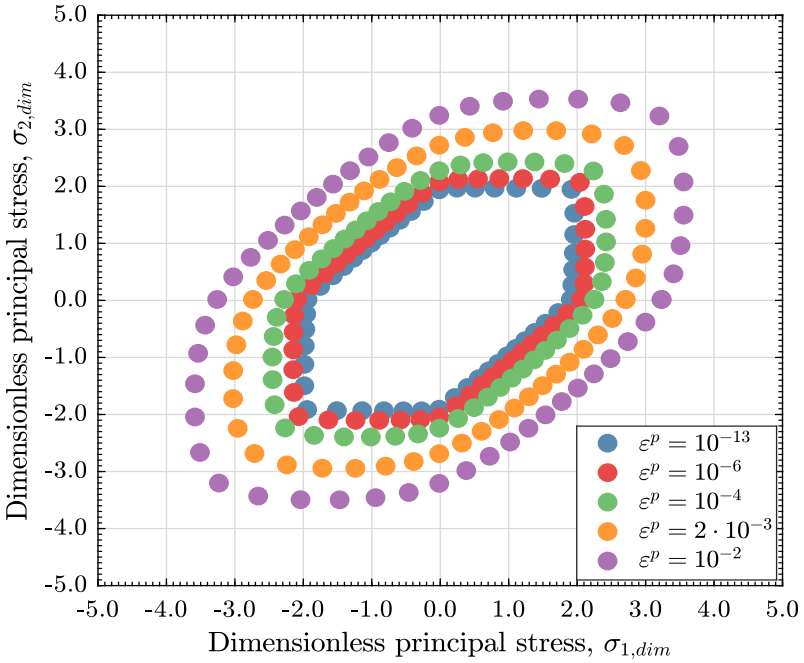

Figure 7.11: Evolution of the yield surface of an isotropic polycrystal of Aluminium.

From the previous Figures, we can affirm that, even though the yield stress states defined by low levels of plastic deformation ($\varepsilon^p \leqslant 10^{-4}$) are different, the yield stress states associated with global plastic strains of 0.2% and 1% are practically coincident. Within this context, it is crucial to recall that we have assumed the same

hardening parameters to describe the evolution of the critical resolved shear stresses in all materials, in such a manner that the presented results might indicate that the behaviour of isotropic fcc polycrystalline materials is controlled by the hardening properties after a certain level of plastic deformation is reached (in other words, once all grains plastify, the response of the polycrystal remains virtually unaffected by the elastic properties of the single-crystal). This question is investigated in greater detail in the next Section, but, first, it is pertinent to comment on the shape of the macro-yield surface. In simplistic terms, given that $q = 1$, an isotropic hardening behaviour is verified. This means that the von Mises yield surface is obtained after a certain level of plastic deformation is reached and that the expansion of the yield surface (once that level has been achieved) occurs without distortion. This is applicable to aggregates comprising isotropic and anisotropic single-crystals, in such a way that the yield surface of the former group evolves from a Tresca-type condition to a von Mises-type shape. Similar findings to the ones reported here are announced by Scheunemann (2017) who considered the same isotropic hardening law and studied the evolution of the yield surface of polycrystals comprising isotropic grains.

7.1.4 Study of Stress-Strain Curves

In the previous Section, we have realized that once a certain level of plastic deformation is reached, the shape of the yielding surface of fcc isotropic polycrystals seems to be independent of the single-crystal elastic parameters. Specifically, it was noticed that, in case the same hardening properties are ascribed to polycrystals of Copper and Aluminium, the macro-yield surfaces of these materials are remarkably similar. To acquire a greater in-depth view of the relation between the macro-yielding response of fcc isotropic polycrystals and the monocrystalline parameters, the analysis of stress-strain curves takes on particular relevance. This is because the isolated study of macro-yield surfaces does not give a full understanding of the macroscopic constitutive response, especially regarding the identification of the global plastic strain for which the macroscopic linear elastic relation between stresses and strains ceases to be valid. This strain level determines the stress states from which plastic slip (i.e., the microscopic hardening properties) starts to control the macroscopic behaviour. Theoretically speaking, the conventional macro-yield criterion intends to estimate this level of stress, but as will be shown later, what often occurs is that, for most metals, it actually leads to stress states far beyond the end of the macroscopic linear elastic region.

In this Section, we are mostly concerned about shedding light into the influence of the monocrystalline parameters on the macro-yielding response of isotropic fcc polycrystals. For that purpose, we have considered the stress-strain curves illustrated in Figures 7.12 and 7.13, which are, respectively, associated with isotropic polycrystals of Copper and Aluminium. In this context, a key point to understand is that the analysis of these curves is sufficient to characterize the macroscopic response of both

materials, since we have previously ascertained that they behave isotropically in the elastic and plastic domains (this presupposes that the model being used can be fully calibrated from this curve). In this particular case, it is worth mentioning that the curves were obtained under uniaxial stress conditions. Moreover, we must emphasise that the order of magnitude of the strain measures is deeply connected to the order of magnitude of the initial critical resolved shear stress, which means the absolute values of the dimensionless uniaxial stress and of the strain measures must be interpreted cautiously.

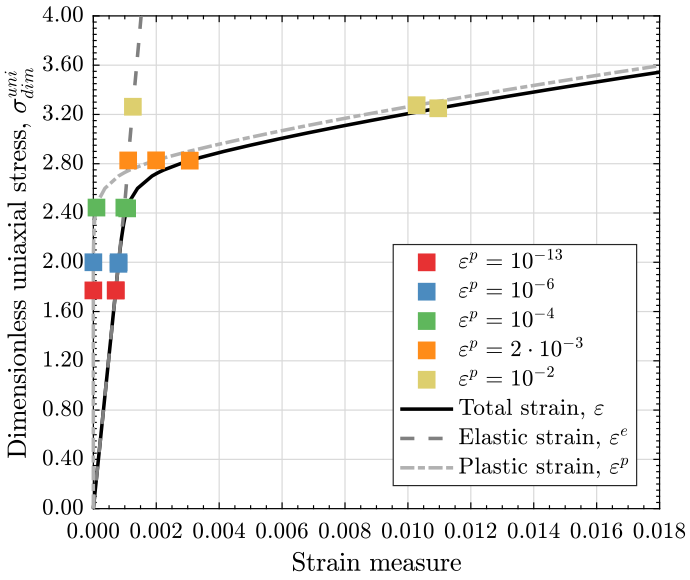

Figure 7.12: Stress-strain curve of an isotropic polycrystal of Copper.

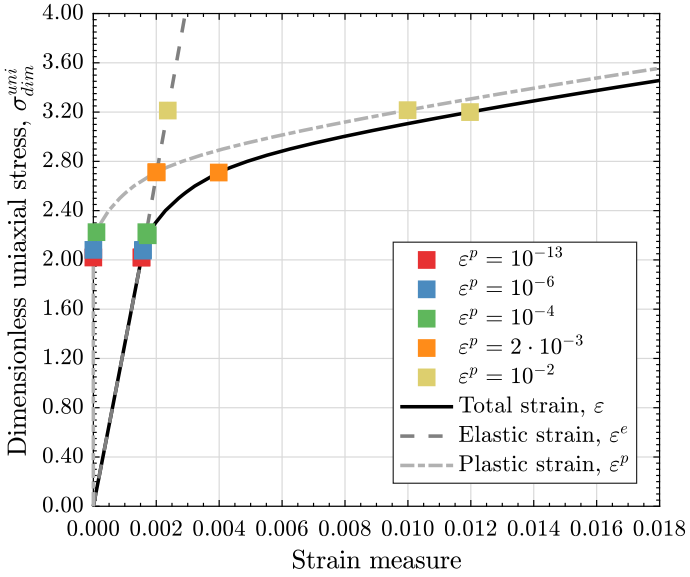

Figure 7.13: Stress-strain curve of an isotropic polycrystal of Aluminium.

From Figures 7.12 and 7.13, we must highlight that:

- The micro-yielding stresses (here defined for a global plastic strain of 10^{-13}) are significantly lower than the conventional macro-yield stresses. In other words, when crystallographic slip begins, the macroscopic stress-strain linear elastic relation remains valid. Additionally, it is clear that the greater the anisotropy of the single-crystal, the greater the relative difference between the micro- and macro-yield stresses;
- As plastic deformation increases, the levels of global stress verified in both polycrystal meshes tend to coincide. In fact, when the macro-yield condition is reached, the stress levels are fundamentally the same for both polycrystal meshes. Hence, the monocrystalline elastic properties have a reduced impact on the yielding response of these materials above a certain level of plastic deformation (which is fairly low);
- The major difference between the macro-yielding states of Copper and Aluminium relies on the level of elastic deformation obtained. Unsurprisingly, the global elastic deformation of the polycrystal comprising crystals of Aluminium is larger, since this material has a smaller Young's modulus;
- For both polycrystals, the dimensionless uniaxial stress is virtually the same for a plastic strain of 1%. To put it differently, when high levels of plastic deformation are achieved, the only difference between the response of Copper and Aluminium is the level of elastic deformation experienced. Nonetheless, because it is small compared to its plastic counterpart and somewhat similar for both materials, we may understand why the elastic isotropic assumption is often considered when we intend to simulate large deformations of polycrystals;
- The conventional macro-yield stress seems to be reasonably higher than the stress level from which a non-linear relation between stresses and strains is verified. To clarify, note that a dimensionless uniaxial stress located between 2.2 and 2.3 seems to define the end of the linear elastic region, while the macro-yield stress appears near a value of 2.8. Thus, the ratio between the macro-yield stress and the stress level which determines the end of the linear elastic stress-strain relation is larger than 1.2. If we couple this with the fact that safety factors larger than 1.2 are generally employed in the design of metallic structural components, we may comprehend that one of the factors contributing to the oversizing of these components stems from the fact that the yielding stresses are generally overestimated. In fact, since many industries are concerned with the development of weight-optimized components, a viable alternative would be to define the macro-yield stress for a lower level of plastic deformation.

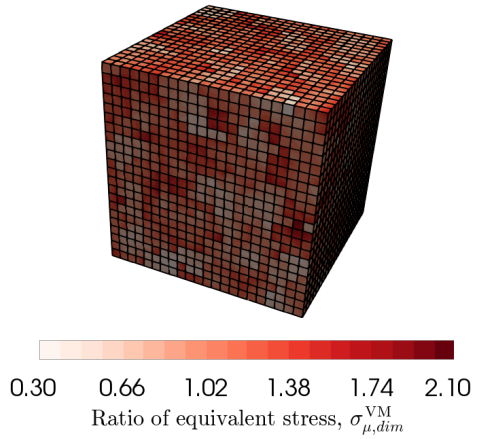

(a) Stress field of an isotropic polycrystal mesh of Copper ($\varepsilon^p = 10^{-13}$).

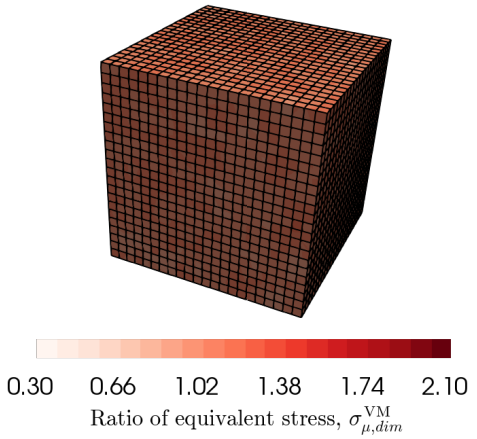

(b) Stress field of an isotropic polycrystal mesh of Aluminium ($\varepsilon^p = 10^{-13}$).

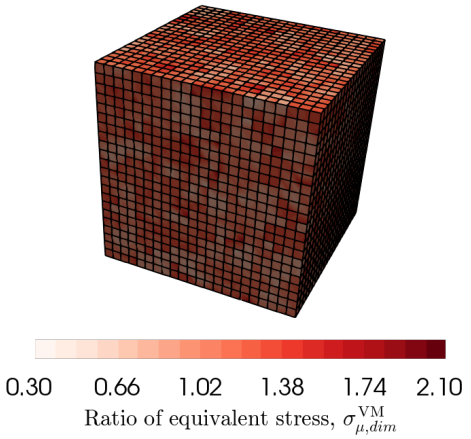

(c) Stress field of an isotropic polycrystal mesh of Copper ($\varepsilon^p = 2 \cdot 10^{-3}$).

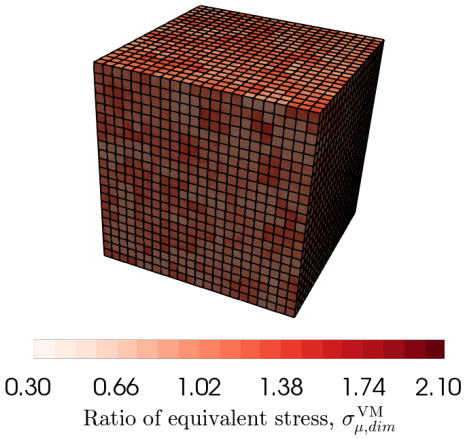

(d) Stress field of an isotropic polycrystal mesh of Aluminium ($\varepsilon^p = 2 \cdot 10^{-3}$).

Figure 7.14: Representations of the dimensionless stress fields of the same polycrystal mesh comprising 10648 elements and 1000 grains of Aluminium and Copper for different global levels of plastic strain.

For the most part, the conventional macro-yield stress depends on the hardening properties of the single-crystal, particularly the initial critical resolved shear stress. On the contrary, once a certain level of plastic deformation is reached, the monocrystalline elastic parameters apparently have a reduced impact on the macroscopic response (they just influence the elastic deformation experienced which, in most situations, is substantially smaller than its plastic counterpart). Indeed, Clausen (1997) suggested that the elastic anisotropy has practically no effect on the response of fcc polycrystals at 0.1% plastic strain, a statement which is consistent with our findings. To emphasise

this point, we decided to study (Figure 7.14) the dimensionless stress fields[1] of the polycrystals of Copper and Aluminium associated with the micro- and macro-yield conditions (respectively, given by $\varepsilon^p = 10^{-13}$ and $\varepsilon^p = 2 \cdot 10^{-3}$). As can be seen, while they have undeniably distinct stress distributions when the level of plastic deformation is low, once the macro-yield condition is reached, the dimensionless stress fields are fairly similar.

7.1.5 Final Remarks on the Macro-Yield Stress

The accurate determination of the macro-yield stress requires distinct hardening properties to be considered in case different cubic crystal aggregates are being studied. In this work, tough, the same hardening properties were employed in all analyses and, as a consequence, it is not possible to draw solid conclusions about the dependency of the macro-yield stresses on these parameters. Although this is true, we must keep in mind that our estimate for the ratio between the macro-yield stress and the initial critical resolved shear stress (equal to 2.8) is likely to provide a plausible relation between the highlighted parameters. In fact, Clausen (1997), who conducted several studies on textureless polycrystals of Aluminium and Copper, has verified that, even though these materials comprise crystals with different hardening properties, they exhibit comparable deformation patterns. In such case, and taking into account that the initial critical resolved shear stress used here is of the same order of magnitude of the values generally assigned to this property (Dieter, 1988), it is reasonable to state that our results might not be far from the ones that would be obtained in case distinct hardening properties were to be considered for the single-crystals.

7.2 Characterisation of the Yielding Response of Anisotropic fcc Polycrystals

The characterisation of the constitutive response of randomly oriented anisotropic aggregates comprising face-centered cubic crystals has not received significant attention in the past due to the fact that the vast majority of textureless polycrystals with practical interest are isotropic. Nonetheless, provided that some industries (e.g., the industry of MEMS) actually work with anisotropic polycrystalline specimens, it is relevant to analyse these materials.

In this Section, we focus on characterizing the yielding response of anisotropic polycrystals. As seen in Chapter 5, the number of grains, the morphology and the distribution of grain orientations are important factors that must not be overlooked when studying the global constitutive behaviour of these materials. Consequently, the characterisation of anisotropic polycrystals demands the consideration of several polycrystalline meshes (in contrast to what occurs with isotropic polycrystals for

[1] The dimensionless stress measure employed is defined in section 5.1.3.

which the analysis of one realisation is enough to extract overall conclusions). Due to the fact that the computational power required to analyse the yielding response of a single polycrystal realisation is appreciably high, it is not viable to provide an exhaustive review of the yielding response of anisotropic polycrystals in the context of this dissertation. This explains why we directed our attention towards the study of polycrystalline meshes enclosing 10 grains and 125 elements: on the one hand, the consideration of such number of grains (and elements) allows reducing the computational resources needed and, on the other hand, it allows general features related to the description of the yielding response of anisotropic materials to be deduced (this is because an increase/decrease in the number of grains fundamentally makes the behaviour of these materials less/more anisotropic).

The topics covered in this Section are mostly the same that have been addressed in Section 7.1. In fact, we have concentrated on the study of micro-yield surfaces (Section 7.2.1), on the determination of micro-yield stresses (Section 7.2.2), on the analysis of macro-yield surfaces (Section 7.2.3) and on the inspection of stress-strain curves (Section 7.2.4). We must highlight that, in Section 7.2.1, we have also shed light into the practicality of using the yield function of Darrieulat and Piot (1996) to describe the micro-yielding surface of the anisotropic polycrystals.

7.2.1 Study of the Micro-Yield Surface

For the purpose of describing the micro-yielding response of anisotropic fcc polycrystals, we employed a similar strategy to the one used within the context of the characterisation of the micro-yield behaviour of isotropic polycrystals: first (in this Section), we discuss the yield stress states which result from considering different micro-yield criteria, so that (in the next Section) we are able to establish the relation between the micro-yield stress of anisotropic fcc aggregates and the monocrystalline parameters that influence the overall micro-yielding response (namely the elastic anisotropy).

The yield stress states associated with the micro-yield criteria defined by $p = 3$ (Brenner approach) and $\varepsilon^p = 10^{-13}$ (global plastic strain approach) are shown in Figures 7.15 and 7.16 for a polycrystal mesh comprising, respectively, 10 grains of Copper and of Aluminium. Similarly to what was verified for isotropic polycrystals, the stresses associated with the criterion $p = 3$ are located in the vicinity of the stress states determined by the condition $\varepsilon^p = 10^{-13}$. Adding to this, it must be noted that the former stress states are generally lower than the latter and that the discrepancies between them are attenuated for polycrystals encompassing less anisotropic grains. Hence, most of the conclusions drawn in Section 7.2.1 are also valid here, meaning that both criteria can be used to determine the micro-yield stresses.

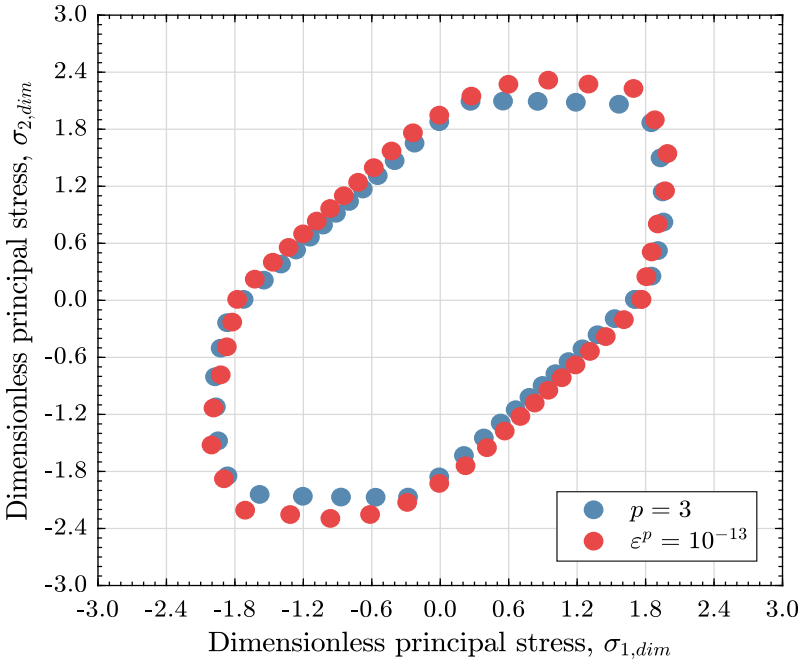

Figure 7.15: Numerical estimates for the stress states associated with the micro-yielding criteria defined by $p = 3$ and $\varepsilon^p = 10^{-13}$, considering 48 loading directions and an anisotropic polycrystal mesh of Copper.

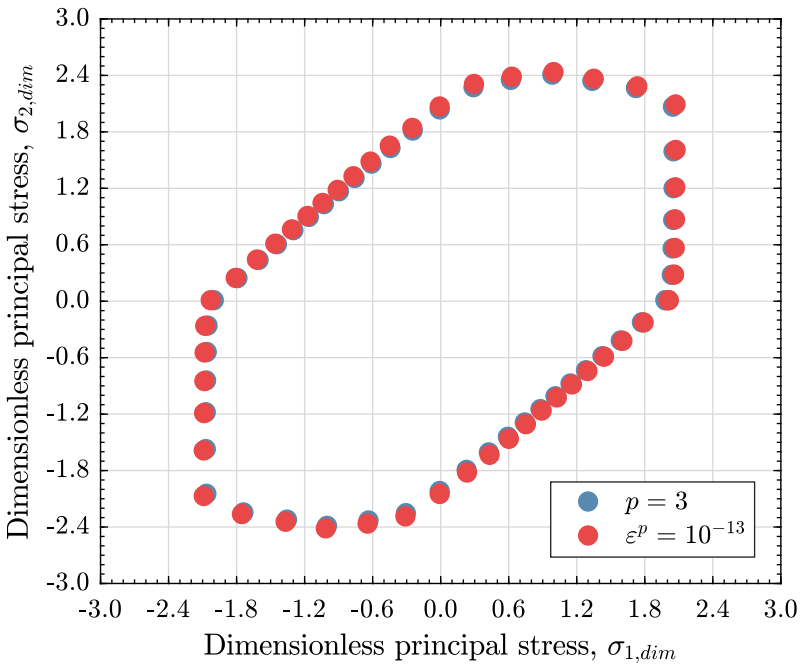

Figure 7.16: Numerical estimates for the stress states associated with the micro-yielding criteria defined by $p = 3$ and $\varepsilon^p = 10^{-13}$, considering 48 loading directions and an anisotropic polycrystal mesh of Aluminium.

The most obvious difference between the sets of micro-yield stress states represented in Figures 7.15 and 7.16 and the ones depicted in Figures 7.1 and 7.2 relies on the fact that the former cannot be accurately described by the isotropic functions of Tresca and von Mises. In fact, even though the micro-yield surfaces of the oligocrystals of Copper and Aluminium can, respectively, be characterized in an acceptable fashion by a von Mises- and a Tresca-type yield function, the truth is that neither of the mentioned yield functions can provide an accurate approximation of the sets of numerical stress states.

One example of an anisotropic micromechanical yielding function is the one proposed by Darrieulat and Piot (1996). Recalling what was presented in Section 6.3.2.1, this function incorporates three parameters and it also demands the knowledge of the distribution of grain orientations and of the volume fraction of each grain. Because the open-source software package `Neper`, employed to generate the polycrystalline meshes analysed with `Links`, provides the information needed to the use of the yield function of Darrieulat and Piot (1996), we are in condition to verify if this yielding function can provide improved descriptions of the yield stress states in relation to those produced by the isotropic functions of Tresca and von Mises. In view of comparing the quality of the descriptions of the sets of numerical stress states provided by the mentioned yield functions, the following error measure was employed:

$$e_{adj} = \frac{1}{\mathrm{NLD}} \sum_{i=1}^{\mathrm{NLD}} |r_f(\theta_i) - r_n(\theta_i)|, \tag{7.3}$$

where NLD denotes the number of spatial directions covered (i.e., the number of stress states computed – in this case, note that NLD = 48) and $r_f(\theta_i)$ and $r_n(\theta_i)$ identify, respectively, the radius (measured from the origin of the plane spanned by σ_1 and σ_2) of the theoretical (computed using one of the yield functions) and of the numerical stress state associated with the spatial direction defined by θ_i (which is determined in equation (6.74)).

In what follows, we focus exclusively on the description of the micro-yield stress states associated with the oligocrystal of Copper because (as it will soon become clear) the computation of the parameters of the yield function of Darrieulat is not trivial. In fact, even though the least squares method can successfully be applied to determine the optimal parameters of the Tresca and of the von Mises yield functions (respectively, the yield stresses of Tresca and of von Mises), we could not use it[2] to generate the parameters m, n and σ_y^{DP} which minimize equation (7.3) (it always converges to local minima). An alternative strategy, which we employed to find better parameters than the ones obtained with the least squares method, involves the manual adjustment of the variables of the yield function of Darrieulat. The

[2]The `Matlab`® function *fit* was used to compute the parameters which minimize expression (7.3) and, despite the fact that different starting points for the mentioned parameters were tested, we could not obtain global minima.

description of the reasoning that lead to the final parameters used is briefly addressed next (note that we first tried to use simpler formulations than the one involving the three adjustable parameters):

- In a first approach, we fixed the values of m and σ_y^{DP} and we tried to obtain the parameter n which minimized equation (7.3). Due to the fact that Darrieulat and Piot (1996) suggested that smaller values of m (i.e., $m \leqslant 1$) provide, in general, better approximations of the experimental data, we considered $m = 1$. In addition, because in their analyses, they commonly used $\sigma_y^{\mathrm{DP}} = \tau_{y,0}$, we decided to adopt this value. Under these circumstances, we found that the parameter n fundamentally influences the order of magnitude of the yielding stresses, as it does not affect the shape of the yielding function obtained. As can be seen in Figure 7.17, higher values of n lead to higher stress states, but, even for the parameter n which minimizes (7.3) ($n = 4.37$), the description of the numerical data is not satisfactory – in fact, the error of the adjustment based on the best value of n is larger than the error associated with the use of the yield functions of von Mises and of Tresca;

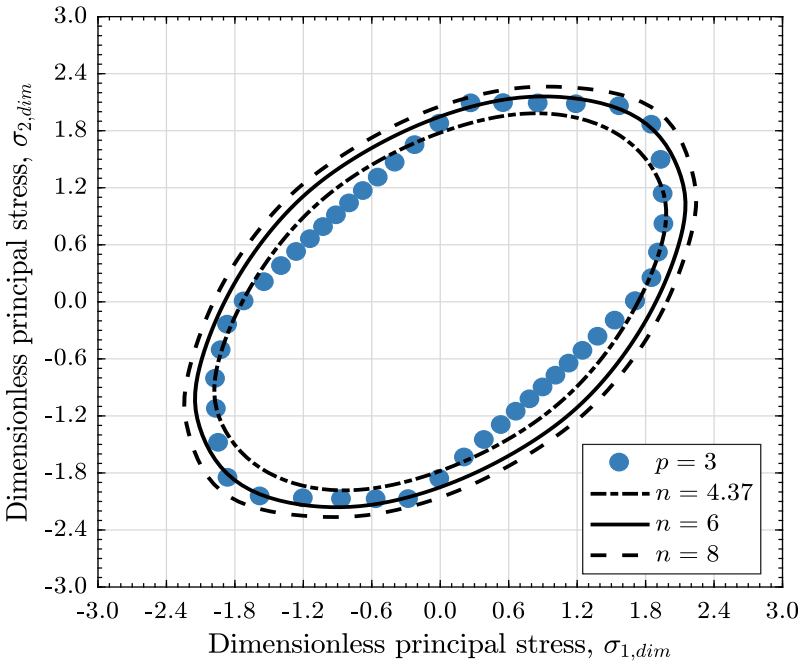

Figure 7.17: Description of the micro-yield surface of an anisotropic polycrystal of Copper with 10 grains using the yield function of Darrieulat ($m = 1$; $\sigma_y^{\mathrm{DP}} = \tau_{y,0}$).

- We then used a single-exponent formulation ($m = n$) with the same fixed value for σ_y^{DP} (see Figure 7.18). As predicted by Darrieulat and Piot (1996), the best combination ($m = n = 4.92$) occurred for a value of n (or m) smaller than 10. Moreover, the error e_{adj} associated with the best pair of values for m

and n was smaller than the one associated with the Tresca yield function, but still larger than the one provided by the von Mises yield function;

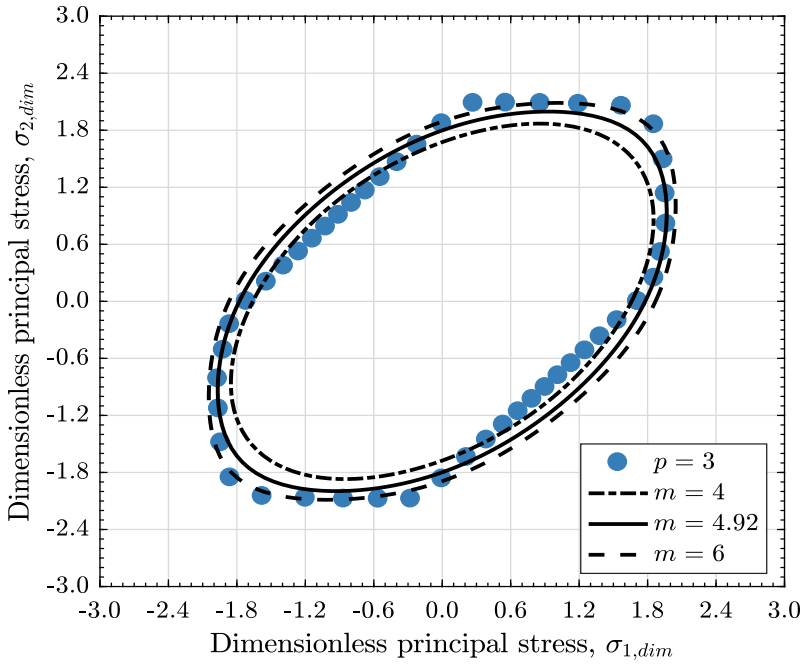

Figure 7.18: Description of the micro-yield surface of an anisotropic polycrystal of Copper with 10 grains using the yield function of Darrieulat ($m = n$; $\sigma_y^{\mathrm{DP}} = \tau_{y,0}$).

- Finally, we tried the most general approach ($m \neq n$; $\sigma_y^{\mathrm{DP}} \neq \tau_{y,0}$). In particular, we tested values of n ranging between 4 and 30, values of m varying between 1 and 128 and yield stresses of Darrieulat situated in the interval $[0.6, 1.4] \cdot \tau_{0,y}$. Amongst all combinations studied, the one which provided the lowest error e_{adj} is obtained for $n = 6.3$; $m = 128$; $\sigma_y^{\mathrm{DP}} = \tau_{y,0}$ and it provides a better description of the numerical yield stress states than both the yield functions of Tresca and von Mises. In Figure 7.19, we represent the numerical stress states, along with the functions of Darrieulat (using the aforementioned parameters) and of von Mises (the yield stress of von Mises was obtained using the least squares methodology).

The analysis of Figure 7.19 shows that, in this particular case, the use of the yield function of Darrieulat does not provide significant improvements concerning the description of the numerical stress states (compared to the yield function of von Mises). If we couple this with the difficulties involved in the calibration of the underlying parameters[3], it becomes clear that this function does not provide a viable way of describing the micro-yielding response of oligocrystals. On the whole, not

[3]We must remark that, since a manual adjustment of the parameters was performed, we cannot ensure that the parameters found provide the best adjustment possible to the numerical stress states (i.e., that they are global minima of expression (7.3)).

only the yielding function of Darrieulat and Piot (1996) requires the knowledge of information which is not generally available, but it also is not trivial to find the parameters which provide the best description of the computed stress states.

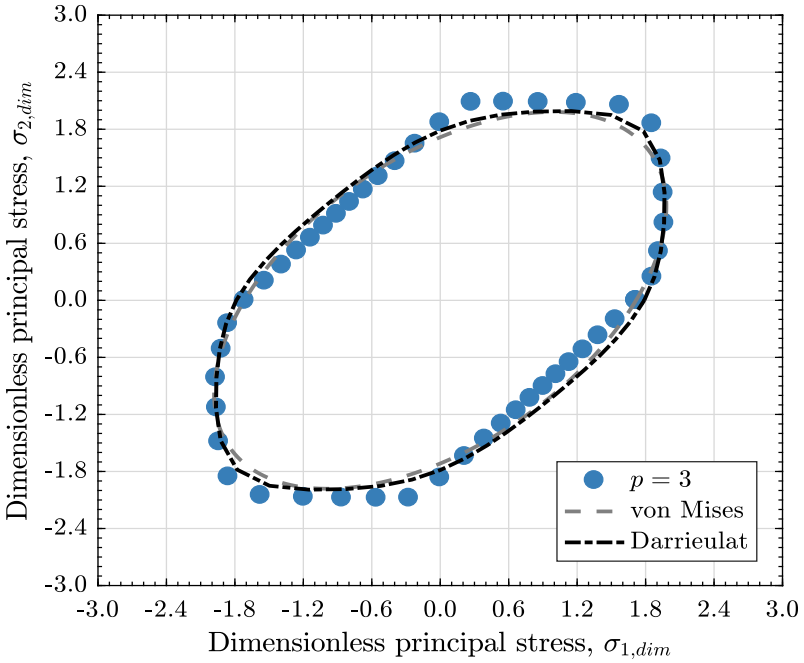

Figure 7.19: Description of the micro-yield surface of an anisotropic polycrystal of Copper with 10 grains using the yield functions of von Mises (the underlying parameter was computed using least squares fitting) and of Darrieulat ($m = 128$; $n = 6.3$; $\sigma_y^{\mathrm{DP}} = \tau_{y,0}$).

7.2.2 Determination of the Micro-Yield Stresses

In this Section, our main goal is to study the relation between the micro-yield stresses of oligocrystals with 10 grains and the monocrystalline parameters. Since these materials are elastically anisotropic, it is expected that the shape of the micro-yield surfaces may vary among different realisations. Consequently, it should be remarked that general conclusions cannot be drawn unless several realisations are considered.

In the previous Section, we have seen that both yield functions of Tresca and of von Mises provide acceptable descriptions of the micro-yielding surfaces (with the former being more appropriate for characterizing sets of micro-yield stress states of polycrystals encompassing less anisotropic grains). In such case, the definition of minimum and maximum values for the yield stresses of Tresca and of von Mises provide an interesting option to characterize the micro-yielding behaviour of oligocrystals. These bounds on the micro-yield stresses are analogous to the bounds computed for the elastic properties in Chapter 5 and, for that reason, we assumed that the examination of 100 realisations is enough to calculate them in an accurate way. In

order to obtain the referred bounds, the first step consists of computing the equivalent Tresca/von Mises stresses associated with all numerical stress states (all loading directions and all realisations are considered, that is, $48 \cdot 100 = 4800$ equivalent Tresca/von Mises stresses are computed); then, each one of the equivalent stresses is used to obtain a yield stress of Tresca/von Mises which satisfies equation (6.57) and (6.68). Once the set enclosing all 4800 yielding stresses of Tresca/von Mises is generated, we estimate its average and standard deviation, in such a way that we acquire the measures needed to establish the bounds. Indeed, from *Chebishev's inequality*, it is known that there is at least a 90% chance that a generic Tresca[4] equivalent stress, σ_n^{T}, is located between the bounds given by $\mathrm{AVG}(\sigma_y^{\mathrm{T}}) \pm 3 \cdot \mathrm{STD}(\sigma_y^{\mathrm{T}})$ (where $\mathrm{AVG}(\sigma_y^{\mathrm{T}})$ and $\mathrm{STD}(\sigma_y^{\mathrm{T}})$ are, respectively, the average and standard deviation of the 4800 Tresca yield stresses). In the light of the previous statement, it is reasonable to assume that a random Tresca equivalent stress (associated with one of the 4800 numerical stress states), σ_n^{T}, is located in the following interval:

$$\sigma_n^{\mathrm{T}} \in \left[\mathrm{AVG}(\sigma_y^{\mathrm{T}}) - 3 \cdot \mathrm{STD}(\sigma_y^{\mathrm{T}}), \mathrm{AVG}(\sigma_y^{\mathrm{T}}) + 3 \cdot \mathrm{STD}(\sigma_y^{\mathrm{T}})\right]. \tag{7.4}$$

Analogously, for a generic von Mises equivalent stress σ_n^{VM}, we claim that:

$$\sigma_n^{\mathrm{VM}} \in \left[\mathrm{AVG}(\sigma_y^{\mathrm{VM}}) - 3 \cdot \mathrm{STD}(\sigma_y^{\mathrm{VM}}), \mathrm{AVG}(\sigma_y^{\mathrm{VM}}) + 3 \cdot \mathrm{STD}(\sigma_y^{\mathrm{VM}})\right]. \tag{7.5}$$

In Figures 7.20 and 7.21, we have, respectively, represented the yield surfaces of Tresca and of von Mises which arise from the consideration of the average and of the lower and upper bounds for the micro-yield stresses of Copper (we have also displayed the 4800 numerical micro-yield stress states computed numerically). A similar portrayal is given in Figures 7.22 and 7.23, taking into account the bounds and the numerical yield stresses computed for Aluminium oligocrystals. As it is apparent, the upper and lower yield surfaces of Tresca and von Mises define reasonable inner and outer envelopes for the numerical micro-yield stress states. Moreover, the standard deviation of the yield stresses is larger for the polycrystals of Copper – since Copper is more anisotropic than Aluminium, it is not surprising to verify that the variability of the micro-yielding stress states is larger in that case. In order to quantify the influence of the elastic anisotropy of the crystals on the average and on the standard deviation of the yield stresses, we have analysed other polycrystals comprising grains of Silver, Gold, Nickel and Lead (a polycrystal comprising nearly isotropic grains was also studied – the elastic constants used are those of Tungsten). The results obtained are compiled in Figures 7.24 to 7.27.

[4] A similar statement can be made with respect to a generic von Mises equivalent stress, σ_n^{VM} which should be located between the bounds defined by: $\mathrm{AVG}(\sigma_y^{\mathrm{VM}}) \pm 3 \cdot \mathrm{STD}(\sigma_y^{\mathrm{VM}})$ (where $\mathrm{AVG}(\sigma_y^{\mathrm{VM}})$ and $\mathrm{STD}(\sigma_y^{\mathrm{VM}})$ are, respectively, the average and standard deviation of the 4800 von Mises yield stresses).

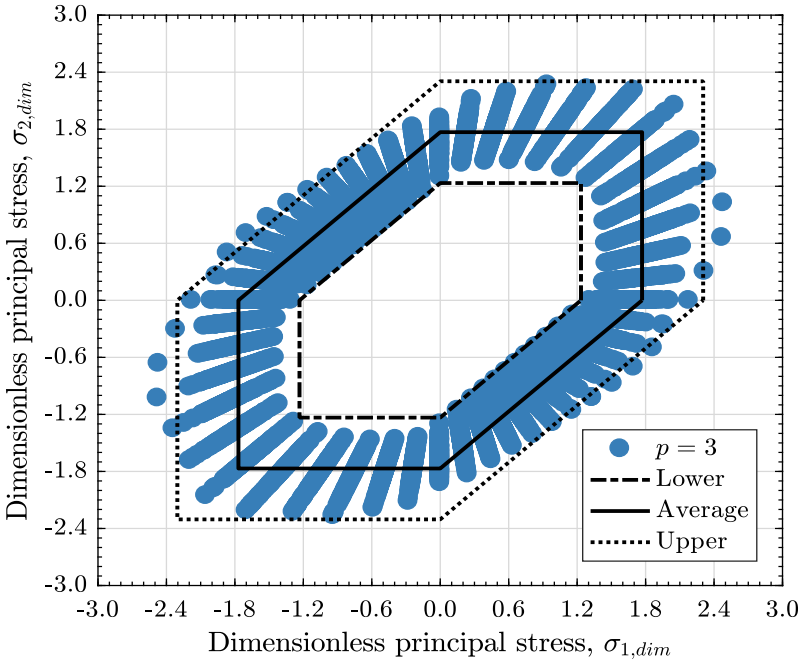

Figure 7.20: Representation of 4800 micro-yield stress states (condition $p = 3$) associated with 100 realisations of polycrystals of Copper with 10 grains and of the average and of the lower and upper bounds of Tresca yield stresses.

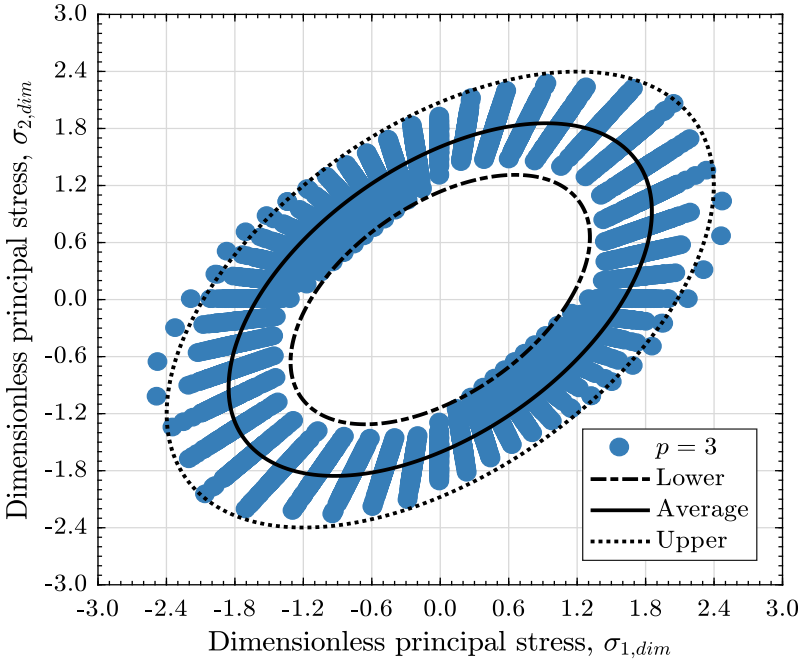

Figure 7.21: Representation of 4800 micro-yield stress states (condition $p = 3$) associated with 100 realisations of polycrystals of Copper with 10 grains and of the average and of the lower and upper bounds of von Mises yield stresses.

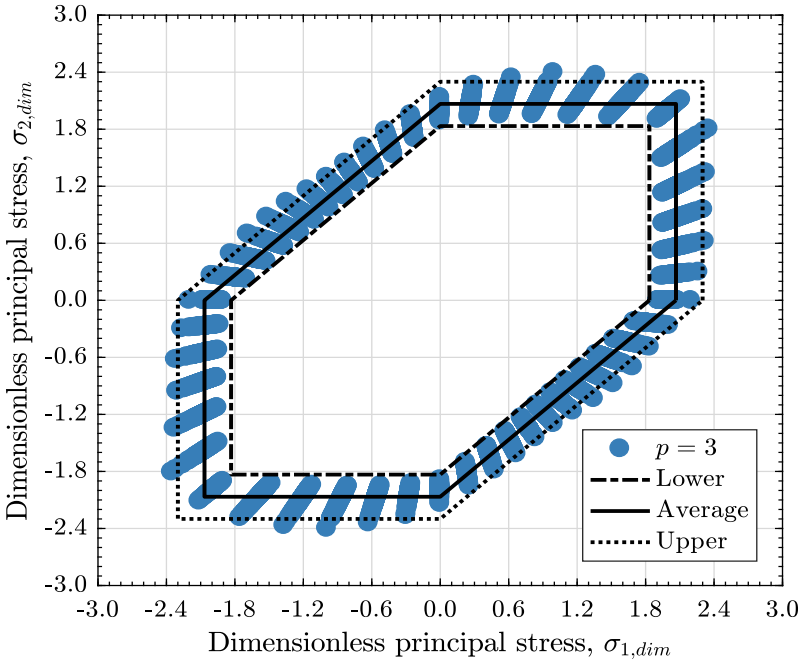

Figure 7.22: Representation of 4800 micro-yield stress states (condition $p = 3$) associated with 100 realisations of polycrystals of Aluminium with 10 grains and of the average and of the lower and upper bounds of Tresca yield stresses.

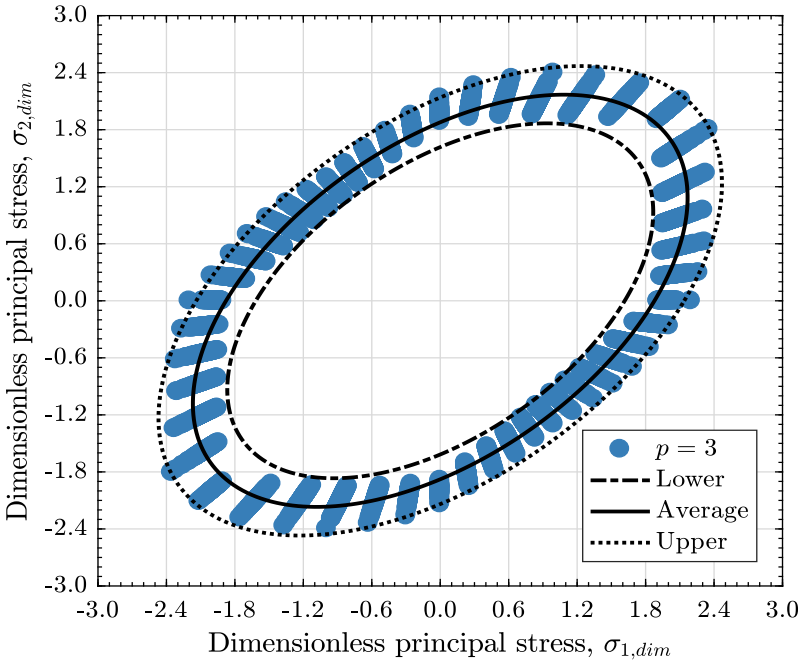

Figure 7.23: Representation of 4800 micro-yield stress states (condition $p = 3$) associated with 100 realisations of polycrystals of Aluminium with 10 grains and of the average and of the lower and upper bounds of von Mises yield stresses.

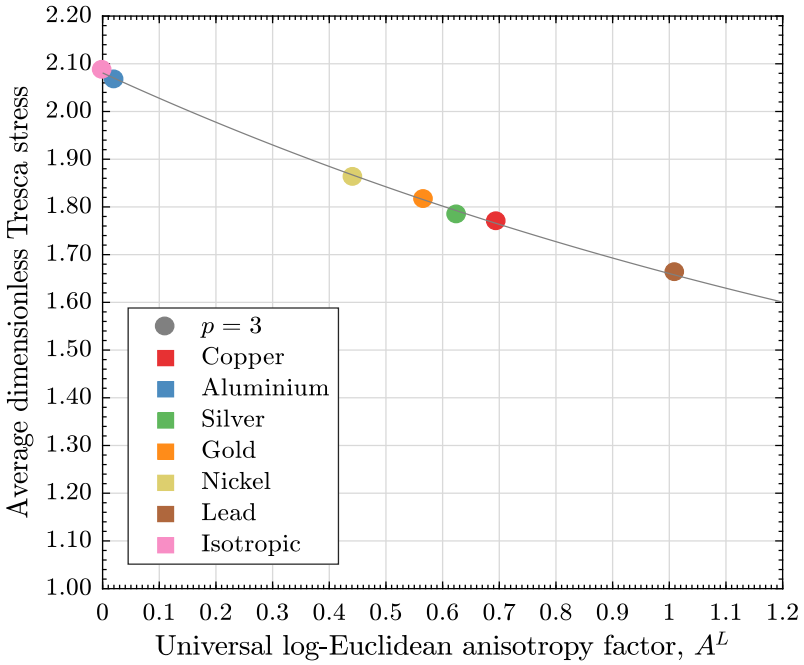

Figure 7.24: Relation between the average of the Tresca yield stresses and the elastic anisotropy of the single-crystal.

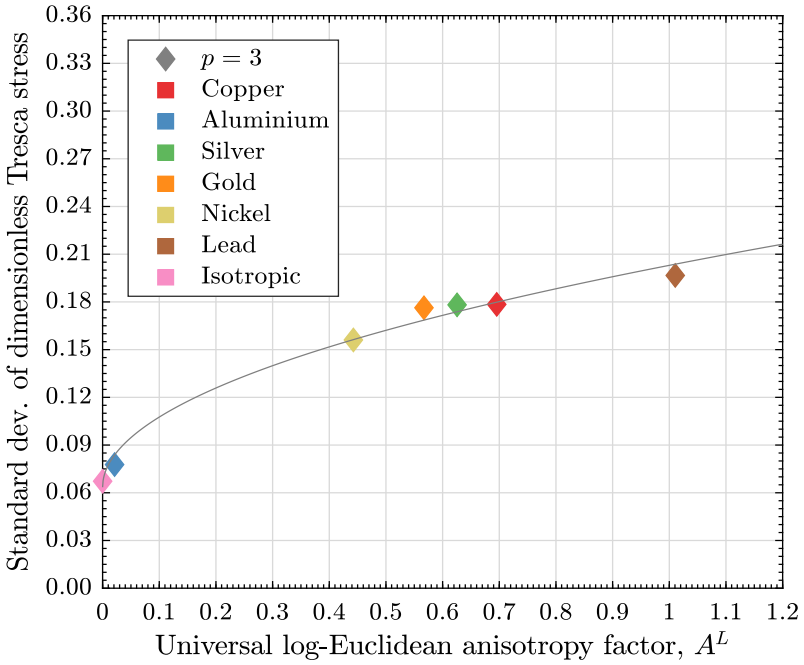

Figure 7.25: Relation between the standard deviation of the Tresca yield stresses and the elastic anisotropy of the single-crystal.

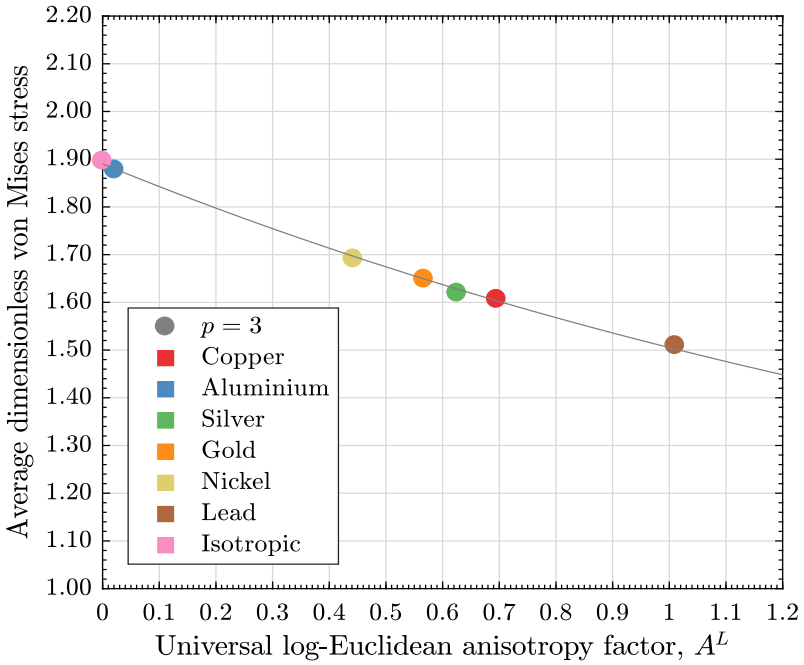

Figure 7.26: Relation between the average of the von Mises yield stresses and the elastic anisotropy of the single-crystal.

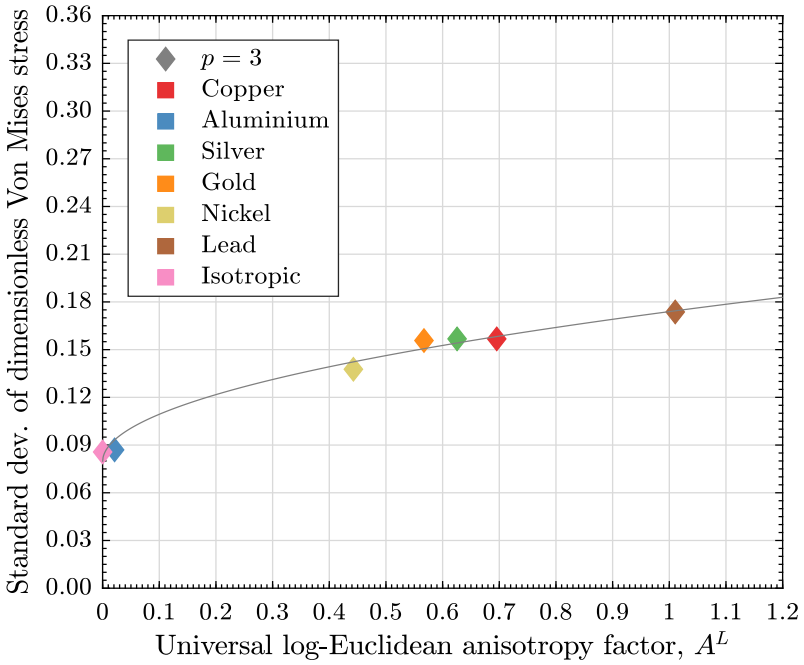

Figure 7.27: Relation between the standard deviation of the von Mises yield stresses and the elastic anisotropy of the single-crystal.

As can be extracted from the previous Figures, the average of the yield stresses of Tresca and von Mises decreases exponentially with the elastic anisotropy. In particular, using the least squares methodology, the following relations were derived:

$$\mathrm{AVG}(\sigma_y^{\mathrm{T}}) = (e^{-0.55 \cdot A^{\mathrm{L}}} + 1.08) \cdot \tau_{y,0}, \tag{7.6}$$

$$\mathrm{AVG}(\sigma_y^{\mathrm{VM}}) = (e^{-0.49 \cdot A^{\mathrm{L}}} + 0.89) \cdot \tau_{y,0}. \tag{7.7}$$

Likewise, it was noticed that the greater the elastic anisotropy of the single-crystal, the greater the standard deviation of the yield stresses of Tresca and von Mises. To be precise, the standard deviation of the yield stresses of Tresca and von Mises is directly proportional to square root of the log-Euclidean anisotropy index, as we might see below (again, these equations were obtained using the least squares method):

$$\mathrm{STD}(\sigma_y^{\mathrm{T}}) = (0.14 \cdot \sqrt{A^{\mathrm{L}}} + 0.06) \cdot \tau_{y,0}, \tag{7.8}$$

$$\mathrm{STD}(\sigma_y^{\mathrm{VM}}) = (0.09 \cdot \sqrt{A^{\mathrm{L}}} + 0.08) \cdot \tau_{y,0}. \tag{7.9}$$

Utilizing the former expressions and taking into account the bounds defined in equations (7.4) and (7.5), we may derive lower and upper limits for the equivalent Tresca and von Mises yield stresses of oligocrystals with 10 grains. In this context, it is of utmost importance to understand that the study of a larger number of grains would certainly conduce to similar dependencies between the average and the standard deviation of the micro-yield stresses and the elastic anisotropy of the single-crystals. In fact, it is expected that the number of grains mostly affects the dispersion of the numerical stress states associated with different realisations (that is, the value of the standard deviation of the Tresca and von Mises yield stresses); in the limit, when a sufficiently large number of grains is considered, the standard deviation must be approximately null and the relation between the average of the yield stresses and the elastic anisotropy must be given by equation (7.2) (using $p_{10} = -1.52$).

7.2.3 Study of the Macro-Yield Surface

For the purpose of analysing the macro-yielding response of oligocrystals, it must be remembered that the same hardening properties have been assumed for all single-crystals. This aspect is of paramount relevance for understanding the results presented in Figures 7.28 and 7.29, where the evolution of the yielding stresses of oligocrystals of Copper and Aluminium are shown (the morphology of the polycrystal studied is the same). If, on the one hand, it is clear that the shapes of the yielding surfaces are remarkably different for low levels of plastic deformation ($\varepsilon^p \leqslant 10^{-6}$), on the other hand, it is also true that, once the macro-yield condition is reached (that is, when $\varepsilon^p \geqslant 2 \cdot 10^{-3}$), the yield stress states are basically the same for both polycrystals. Because the same hardening properties were used, this is not surprising and, indeed, confirms that the elastic properties have a small impact on the evolution

of the yielding stress states once the macro-yielding condition is achieved. Besides this, it is also interesting to note that, since $q = 1$ (isotropic hardening behaviour), a von Mises-type yield surface is obtained. On the whole, the findings reported in Section 7.1.3 are also applicable here, so that we can conclude that the elastic properties of the single-crystals do not influence the yielding response of anisotropic and isotropic polycrystals, once the macro-yielding condition has been reached.

7.2.4 Study of Stress-Strain Curves

In contrast to isotropic polycrystals, anisotropic aggregates do not exhibit the same Young's modulus in all spatial directions (see Chapter 5) and, for this reason, the analysis of stress-strain curves must be made in a cautious way, since the levels of elastic deformation when the micro- and macro-yielding conditions are reached may not be representative of what occurs in all spatial directions. That being said, we can concentrate on the examination of the stress-strain curves depicted in Figures 7.30 and 7.31, which are, respectively, associated with oligocrystals of Copper and Aluminium with 10 grains. In consistency with was stated in the previous Section, it is important to note that the stress levels associated with low levels of plastic deformation vary between the materials, but, once the macro-yielding condition is reached, they are essentially the same. In fact, it becomes clear that the elastic properties of the single-crystals do not influence the behaviour of the materials on the non-linear region, except for the fact that the levels of elastic deformation depend on the Young's modulus; however, because the elastic deformations experienced are generally low, it is fair to consider that materials comprising crystals with different elastic properties, but with the same hardening parameters, have identical responses from the point the macro-yield condition is achieved. Additionally, observe that, for both materials, the micro-yield stress is significantly lower than the macro-yielding stress, in such a manner that the macroscopic linear elastic behaviour still continues when crystallographic slip begins. Altogether, the general conclusions drawn in Section 7.1.4 remain valid here.

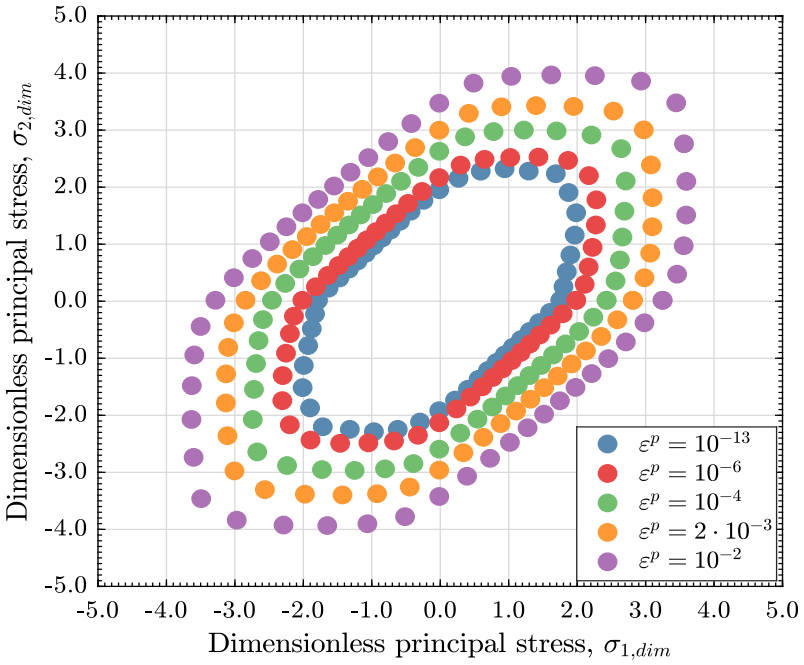

Figure 7.28: Evolution of the yield surface of an oligocrystal of Copper with 10 grains.

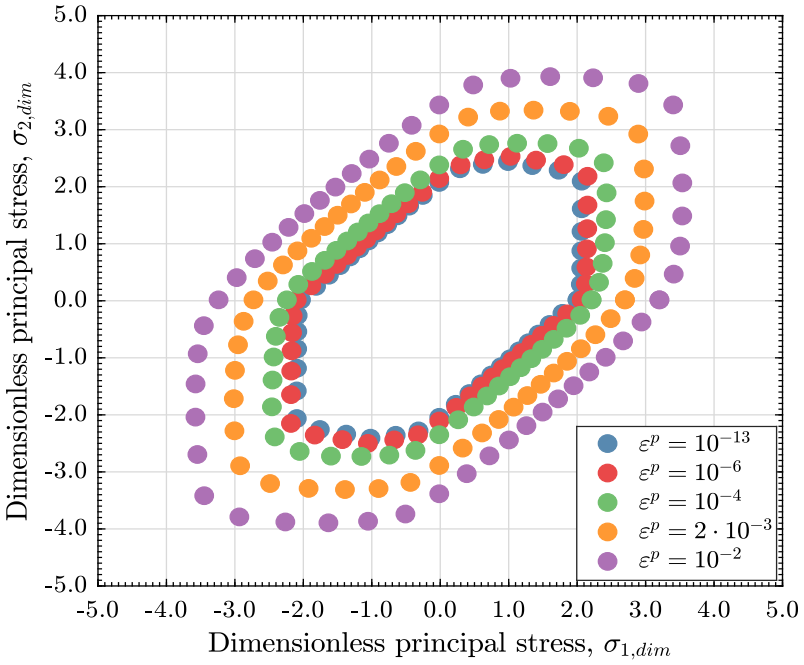

Figure 7.29: Evolution of the yield surface of an oligocrystal of Aluminium with 10 grains.

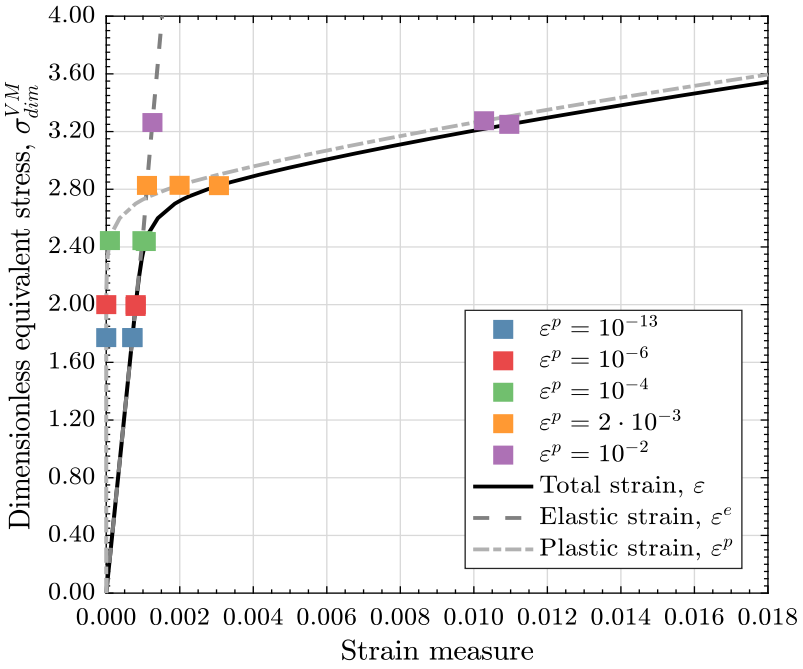

Figure 7.30: Stress-strain curve of an oligocrystal of Copper with 10 grains (the loading direction aligned with σ_1 was considered).

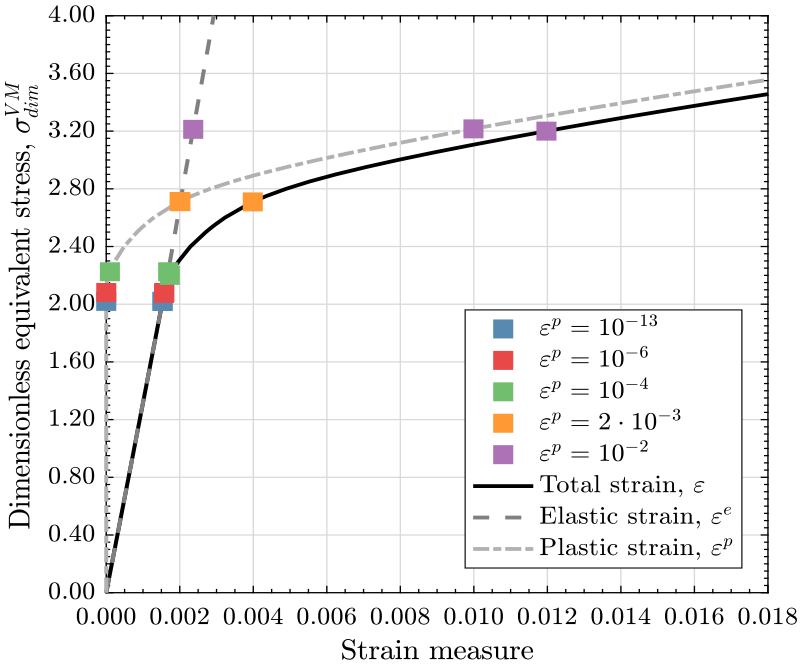

Figure 7.31: Stress-strain curve of an oligocrystal of Aluminium with 10 grains (the loading direction aligned with σ_1 was considered).

Chapter 8

Conclusions and Future Works

The main goal of the present work consisted of characterising the elastic and yielding response of polycrystalline aggregates by means of numerical microscopic studies based on computational homogenisation techniques. To that end, several laws establishing the bridge between the critical microscopic parameters and the macroscopic constitutive responses have been developed, with special attention given to the impact of the elastic anisotropy of the single crystals on the homogenized parameters; in addition, relevant scientific issues were discussed and not only results consistent with the literature have been found, as relevant topics, which are still under discussion in the scientific community, have been addressed. Moreover, with the experience gained while applying multi-scale schmes to the study of macroscopic consitutive behaviours, it will be possible to extend the procedures here reviewed to the analysis of more complex materials.

That being said, in this Chapter, the main conclusions taken are compiled in Section 8.1 and suggestions for future works are presented in Section 8.2.

8.1 Main Conclusions

For the purpose of establishing the linear elastic response of a certain material using computational homogenisation procedures, six analyses have to be performed on the underlying RVE, each one of them using a single non-null component of the infinitesimal strain tensor and, therefore, allowing the determination of one column of the stiffness matrix. For this reason, the numerical prediction of the macroscopic elastic behaviour of polycrystalline materials comprising a very large number of grains can be computationally very costly, especially in case highly refined polycrystal meshes are studied. If we couple this with the fact that in order to infer critical relations between the microscopic parameters and the macroscopic behaviour, several studies have to be performed, it becomes apparent that polycrystal meshes

should be designed in order to minimize the computational resources required, while still being capable of providing results within the desired accuracy.

Given that most polycrystalline systems of interest are isotropic, the former issue mostly corresponds to the definition of the minimum number of grains and mesh size that leads to isotropic responses. Both questions have been addressed in this work for polycrystalline aggregates comprising cubic crystals. Since these materials always have isotropic bulk moduli, a procedure has been developed to characterise their elastic response based exclusively on the analysis of the spatial distribution of the Young's modulus of several realisations of the same polycrystals. In short, it was verified that the elastic anisotropy of the single crystal plays a pivotal role regarding the definition of the isotropic conditions. This can be explained from the fact that the larger the anisotropy of the single crystal, the larger the non-uniformity of the stress and strain fields.

Being able to correctly represent the stress and strain fields at the grain boundaries is intrinsically linked to the meshing strategy adopted. In case block structured polycrystalline meshes are studied, the element boundaries and the grain boundaries do not coincide and, as a result, coarse representations of the field variables near the grain boundaries are often obtained. This was corroborated in the current work and a relation linking the number of elements per grain required to minimize the error associated with the elastic homogenized properties and the anisotropy of the single crystal was derived (it postulates that these variables are linearly proportional). However, it should be remarked that, since the macroscopic elastic parameters are computed from homogenized quantities, the error associated with the use of low refined structured meshes is generally low; this means that unstructured meshing (which often requires more computational resources) is worthwhile only when we intend to study local phenomena or when the local anisotropy is extremely relevant.

The minimum number of grains that gives rise to elastic isotropic properties assumes utmost importance while studying the constitutive behaviour of isotropic polycrystalline specimens. In this work, we have deduced an expression that can be used to estimate the minimum number of grains that yields isotropic responses. This expression describes a direct proportionality between the number of grains and the elastic anisotropy of the single crystal (for a given level of precision). Furthermore, it was defined in terms of the log-Euclidean anisotropy index (which can be used to quantify the elastic anisotropy of non-cubic crystals), so that it may eventually be applied to predict the minimum size of the RVE of elastic isotropic polycrystals comprising non-cubic crystals. Additionally, it compares well to previous works in this field and it can be adjusted according to the level of precision desired.

The elastic properties of single-phase isotropic aggregates enclosing crystals with cubic symmetry can be determined using the computational framework mentioned before or, alternatively, from analytical methods. We have noticed that analytical models produce estimates remarkably close to the results generated numerically

and due to the fact that, for cubic crystal aggregates, they do not include complex mathematical expressions, they provide a practical way of determining the elastic parameters of those materials. Nonetheless, we must be aware of the fact that neither can they be used to analyse non-isotropic aggregates nor can they give more information beyond the elastic properties. As a result, they must not be seen as a alternative to numerical methods (which are undeniably more versatile and powerful), but rather as a tool for validating the numerical results (they are still useful for those interested in the elastic properties only).

Regarding the determination of the yielding response of polycrystals, an important point relies on the numerical procedure that must be used to ensure that the global stress states computed in all increments belong to the section of the stress space that we want to study. Since `Links` (like many other computational codes) is strain-driven, this can only be accomplished if a non-linear iterative problem (external to the micro-scale equilibrium problem) is solved. A major drawback of this procedure, however, is that it incurs in considerable additional computational cost, making it impractical to analyse large amounts of polycrystalline meshes, especially if the number of elements is significantly high.

There are several ways of defining the micro-yield condition and, based on the numerical results obtained in this work for both isotropic and anisotropic polycrystals, we have verified that the criterion $p = 3$ proposed by Brenner et al. (2009) and the criterion $\varepsilon^p = 10^{-13}$ (which is based on a low value of the global plastic strain) provide similar results, so that either of them can be used to obtain the micro-yield stresses – nevertheless, because the latter criterion is more versatile and simple, we recommend its use over the former. On the contrary, the criterion of Hutchinson (1970) ($p = 0$) – which neglects the heterogeneities of stress within all grains – generates coarse results for the micro-yield stresses when polycrystals comprising highly anisotropic grains are considered.

While the micro-yield surfaces of polycrystals encompassing elastically isotropic crystallites are well described by the Tresca yield function, the micro-yield surfaces of isotropic aggregates consisting of elastically anisotropic grains depart from Tresca-type surfaces. In fact, the von Mises yield function may provide improved descriptions of the set of numerical micro-yield stress states when the anisotropy of the single-crystal is relevant. Moreover, regardless of the isotropic yield function used to characterize the micro-yield response of isotropic polycrystals, the value of the underlying parameter (Tresca or von Mises yield stress) decreases exponentially as the anisotropy increases. To put it differently, the maximum micro-yield stress under uniaxial stress conditions, occurs for the polycrystal containing isotropic grains (and is given by $2 \cdot \tau_{y,0}$).

We have investigated the practicability of using the yield function of Darrieulat to describe the micro-yielding stress states of oligocrystals and, in summary, we concluded that the calibration of its parameters is not straightforward.

Once a certain level of plastic deformation is reached, the elastic parameters of the single-crystals have virtually no influence on the yielding response of polycrystals. This justifies why two polycrystals enclosing single-crystals with different elastic properties, but with the hardening parameters, exhibit similar stress fields once the macro-yield condition has been achieved. Thus, it is evident that, in the plastic domain, the constitutive response of polycrystalline materials is mostly controlled by the hardening properties of the single-crystal. In particular, if isotropic hardening behaviour is assumed ($q = 1$), the yield surface assumes a von Mises-type shape.

8.2 Future Works

In this work we have covered the description of the elastic and yielding response of single-phase polycrystalline aggregates comprising cubic crystals. Concerning the studies performed in the elastic domain, it would be interesting to analyse other kinds of polycrystalline materials. In particular, we suggest to:

- Verify if the conclusions drawn are also applicable to describe the elastic response of isotropic polycrystals comprising non-cubic crystals. It should be noted that the expression deduced for the number of grains required to obtain isotropic responses should be tested, as it may eventually be valid (it is defined in terms of an universal anisotropy measure);
- Study textured polycrystals. In this case, the morphological anisotropy has to be taken into consideration and most analytical methods cannot be used, so numerical schemes assume capital relevance on the characterisation of the elastic response of textureless polycrystals. Nonetheless, an obstacle to the deduction of critical relations concerns properly accounting the influence of the morphological anisotropy;
- Examine multi-phase polycrystals and analyse the influence of the volume fractions of each phase on the elastic response of these materials. We must remark that since many real components made of crystalline materials are multi-phasic, their elastic characterisation is a matter of unquestionable practical utility.

Studying the yielding response of the polycrystals mentioned above is also interesting and, in most cases, would be possible with the available resources. An exception, though, involves the study of crystals with symmetries other than cubic, since `Links` does not incorporate, at this moment, the underlying constitutive models. Notwithstanding, `Links` allows studying bcc polycrystals and, therefore, analysing these materials would definitely entail an interesting future project, since numerical studies beyond the elastic domain often focus on fcc polycrystals. Another equally attractive possibility consists of inspecting the relation between the micro- and the macro-hardening laws (that is, the determination of the so-called *M-factors*), as a

stepping stone towards a more complete characterisation of the plastic response of polycrystalline specimens.

Finally, it would be of interest to concentrate on other multi-scale techniques that can be employed to the characterisation of the constitutive behaviour of isotropic polycrystalline materials. This would be especially valuable when we are dealing with crystals with higher anisotropies, because, as previously stated, a large number of grains and highly refined meshes are required to accurately describe their constitutive response. Such alternative procedures might rely on analysing several *statistical volume elements* (i.e., microscopic domains smaller than the RVE, but still larger than the microscopic heterogeneities) using advanced statistical concepts or machine learning techniques (e.g. Liu et al. (2018)).

This page was intentionally left with this sentence.

Appendix A

Euler Angles

In order to define the orientation of a generic grain (e.g., of a polycrystalline aggregate), three parameters, known as the Euler angles, are generally employed. Note that, in this context, two different coordinate systems must be clearly distinguished: the aggregate/specimen coordinate system and the crystal coordinate system (the unit vectors associated with the global and local coordinate systems are denoted $\boldsymbol{e}_i^g$ and $\boldsymbol{e}_i^l$, where $i = 1, 2, 3$). These coordinate systems might be regarded, respectively, as the global and the local coordinate systems. In brief, the Euler angles refer to three rotations that transform the aggregate/specimen (global) coordinate system onto the crystal (local) coordinate system. The mentioned rotations must be performed in a fixed sequence:

1. Rotation φ_1 about the axis defined by $\boldsymbol{e}_3^g$, so that $\boldsymbol{e}_1^{g'}$ is normal to the plane containing the unit vectors $\boldsymbol{e}_3^{g'}$ $(= \boldsymbol{e}_3^g)$ and $\boldsymbol{e}_3^l$;
2. Rotation ϕ about the new axis defined by $\boldsymbol{e}_1^{g'}$, in such a way that $\boldsymbol{e}_3^{g''}$ and $\boldsymbol{e}_3^l$ coincide;
3. Rotation φ_2 about the axis $\boldsymbol{e}_3^{g''}$, in a such a fashion that the local and the rotated coordinate system (defined by unit vectors $\boldsymbol{e}_i^{g'''}$, $i = 1, 2, 3$) coincide.

The rotation sequence can be depicted in Figure A.1, where $\boldsymbol{e}_i^{g'}$ denotes the position of unit vector $\boldsymbol{e}_i^g$ after the first rotation (vectors $\boldsymbol{e}_i^{g''}$ and $\boldsymbol{e}_i^{g'''}$ are defined analogously). The Euler angles φ_1, ϕ and φ_2 are defined according to Bunge convention, so that they are valid in the following ranges: $\varphi_1 \in [0°, 360°[$, $\phi \in [0°, 180°[$ and $\varphi_2 \in [0°, 360°[$. Having all this in mind, the rotation tensor, which rotates the global coordinate system onto the crystal coordinate system, is given by:

$$\boldsymbol{R} = \boldsymbol{R}_{\varphi_1} \boldsymbol{R}_{\phi} \boldsymbol{R}_{\varphi_2} \tag{A.1}$$

where the three rotations are:

$$\boldsymbol{R}_{\varphi_1} = \begin{bmatrix} \cos(\varphi_1) & \sin(\varphi_1) & 0 \\ -\sin(\varphi_1) & \cos(\varphi_1) & 0 \\ 0 & 0 & 1 \end{bmatrix}, \tag{A.2}$$

$$\boldsymbol{R}_{\phi} = \begin{bmatrix} 1 & 0 & 0 \\ 0 & \cos(\phi) & \sin(\phi) \\ 0 & -\sin(\phi) & \cos(\phi) \end{bmatrix}, \tag{A.3}$$

$$\boldsymbol{R}_{\varphi_2} = \begin{bmatrix} \cos(\varphi_2) & \sin(\varphi_2) & 0 \\ -\sin(\varphi_2) & \cos(\varphi_2) & 0 \\ 0 & 0 & 1 \end{bmatrix}. \tag{A.4}$$

From the straightforward manipulation of equations (A.1) to (A.4), we can write the components $R_{ij}(i,j=1,2,3)$ of the rotation matrix $\boldsymbol{R}$ as follows:

$$R_{11} = \cos(\varphi_1)\cos(\varphi_2) - \sin(\varphi_1)\sin(\varphi_2)\cos(\phi), \tag{A.5}$$

$$R_{12} = \sin(\varphi_1)\cos(\varphi_2) + \cos(\varphi_1)\sin(\varphi_2)\cos(\phi), \tag{A.6}$$

$$R_{13} = \sin(\varphi_2)\sin(\phi), \tag{A.7}$$

$$R_{21} = -\cos(\varphi_1)\sin(\varphi_2) - \sin(\varphi_1)\cos(\varphi_2)\cos(\phi), \tag{A.8}$$

$$R_{22} = -\sin(\varphi_1)\sin(\varphi_2) + \cos(\varphi_1)\cos(\varphi_2)\cos(\phi), \tag{A.9}$$

$$R_{23} = \cos(\varphi_2)\sin(\phi), \tag{A.10}$$

$$R_{31} = \sin(\varphi_1)\sin(\phi), \tag{A.11}$$

$$R_{32} = -\cos(\varphi_1)\sin(\phi), \tag{A.12}$$

$$R_{33} = \cos(\phi). \tag{A.13}$$

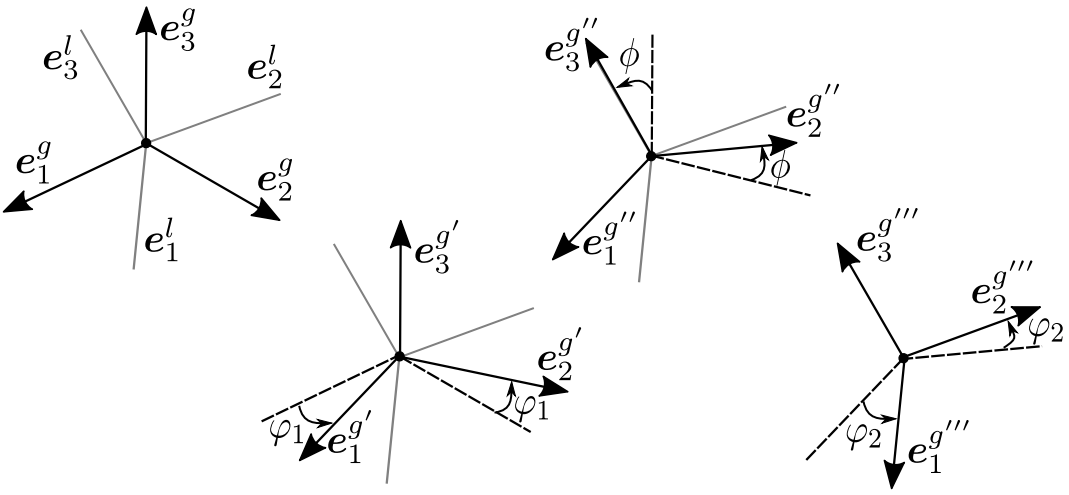

Figure A.1: Description of the rotation from the global (specimen) coordinate system onto the local (crystal) coordinate system through Euler angles.

Appendix B

Hooke's Law in Matrix Notation following Voigt Notation

In this Appendix some aspects related to the generalized Hooke's law defined in a matrix basis are approached. In particular, the Voigt mapping is scrutinised in Appendix B.1 (along with the discussion of Hooke's law in a matrix basis following Voigt notation). Then, in Appendix B.2, the stiffness matrices associated with different material symmetry groups are compiled. The case of isotropic symmetry is considered in Appendix B.3, where the relations between several elastic parameters are established.

B.1 Obtaining Hooke's Law in Matrix Basis following the Voigt Scheme

The generic fourth-order stiffness tensor $\mathbf{C}$ exhibits major and minor symmetries, as discussed in Section 4.2:

$$\mathsf{C}_{ijkl} = \mathsf{C}_{jikl} = \mathsf{C}_{ijlk} = \mathsf{C}_{klij} \tag{B.1}$$

and, as a consequence, we might consider transforming it into a two-dimensional array. If we adopt the Voigt mapping to perform the transformation $\mathsf{C}_{ijkl} \longrightarrow \mathsf{C}_{mn}$, the following relations between the indices ij or kl of the fourth-order rank tensor components and the indices m or n associated with the 2D array components have to be considered:

$$m = i\,\delta_{ij} + (1 - \delta_{ij})(9 - i - j), \tag{B.2}$$

$$n = k\,\delta_{ij} + (1 - \delta_{kl})(9 - k - l). \tag{B.3}$$

By taking these relations into consideration, we might define the matrix representation of the stiffness tensor as follows:

$$\mathbf{C} = \begin{bmatrix} \mathsf{C}_{1111} & \mathsf{C}_{1122} & \mathsf{C}_{1133} & \mathsf{C}_{1123} & \mathsf{C}_{1113} & \mathsf{C}_{1112} \\ & \mathsf{C}_{2222} & \mathsf{C}_{2233} & \mathsf{C}_{2223} & \mathsf{C}_{2213} & \mathsf{C}_{2212} \\ & & \mathsf{C}_{3333} & \mathsf{C}_{3323} & \mathsf{C}_{3313} & \mathsf{C}_{3312} \\ & & & \mathsf{C}_{2323} & \mathsf{C}_{2313} & \mathsf{C}_{2312} \\ & & & & \mathsf{C}_{1313} & \mathsf{C}_{1312} \\ \text{sym.} & & & & & \mathsf{C}_{1212} \end{bmatrix} \tag{B.4}$$

$$= \begin{bmatrix} \mathsf{C}_{11} & \mathsf{C}_{12} & \mathsf{C}_{13} & \mathsf{C}_{14} & \mathsf{C}_{15} & \mathsf{C}_{16} \\ & \mathsf{C}_{22} & \mathsf{C}_{23} & \mathsf{C}_{24} & \mathsf{C}_{25} & \mathsf{C}_{26} \\ & & \mathsf{C}_{33} & \mathsf{C}_{34} & \mathsf{C}_{35} & \mathsf{C}_{36} \\ & & & \mathsf{C}_{44} & \mathsf{C}_{45} & \mathsf{C}_{46} \\ & & & & \mathsf{C}_{55} & \mathsf{C}_{56} \\ \text{sym.} & & & & & \mathsf{C}_{66} \end{bmatrix}.$$

Analogously, the compliance matrix reads:

$$\mathbf{S} = \begin{bmatrix} \mathsf{S}_{1111} & \mathsf{S}_{1122} & \mathsf{S}_{1133} & 2\mathsf{S}_{1123} & 2\mathsf{S}_{1113} & 2\mathsf{S}_{1112} \\ & \mathsf{S}_{2222} & \mathsf{S}_{2233} & 2\mathsf{S}_{2223} & 2\mathsf{S}_{2213} & 2\mathsf{S}_{2212} \\ & & \mathsf{S}_{3333} & 2\mathsf{S}_{3323} & 2\mathsf{S}_{3313} & 2\mathsf{S}_{3312} \\ & & & 4\mathsf{S}_{2323} & 4\mathsf{S}_{2313} & 4\mathsf{S}_{2312} \\ & & & & 4\mathsf{S}_{1313} & 4\mathsf{S}_{1312} \\ \text{sym.} & & & & & 4\mathsf{S}_{1212} \end{bmatrix} \tag{B.5}$$

$$= \begin{bmatrix} \mathsf{S}_{11} & \mathsf{S}_{12} & \mathsf{S}_{13} & 2\mathsf{S}_{14} & 2\mathsf{S}_{15} & 2\mathsf{S}_{16} \\ & \mathsf{S}_{22} & \mathsf{S}_{23} & 2\mathsf{S}_{24} & 2\mathsf{S}_{25} & 2\mathsf{S}_{26} \\ & & \mathsf{S}_{33} & 2\mathsf{S}_{34} & 2\mathsf{S}_{35} & 2\mathsf{S}_{36} \\ & & & 4\mathsf{S}_{44} & 4\mathsf{S}_{45} & 4\mathsf{S}_{46} \\ & & & & 4\mathsf{S}_{55} & 4\mathsf{S}_{56} \\ \text{sym.} & & & & & 4\mathsf{S}_{66} \end{bmatrix}.$$

Note that the last three lines and columns of the compliance array $\mathbf{S}$ involve multiplicative factors which are used to ensure that the same results are obtained whether we perform our calculations with the tensor or the matrix form of the compliance or the stiffness arrays. These multiplicative factors appear as a consequence of the different treatment associated with strain and stress quantities which is inherent to Voigt's formulation. In fact, the same conclusion can be reached from the analysis of the strain and stress vectors, as we may see next. For the determination of the stress and strain arrays, the relations (B.2) and (B.3) remain valid and, in addition, it is

also verified that:

$$\sigma_m = \sigma_{ij}, \tag{B.6}$$

$$\varepsilon_n = (2 - \delta_{kl})\varepsilon_{kl}. \tag{B.7}$$

Taking these points into consideration, the Cauchy stress vector following the Voigt mapping is given by:

$$[\boldsymbol{\sigma}] = \begin{bmatrix} \sigma_{11} & \sigma_{12} & \sigma_{13} \\ \sigma_{21} & \sigma_{22} & \sigma_{23} \\ \sigma_{31} & \sigma_{32} & \sigma_{33} \end{bmatrix} \longrightarrow \boldsymbol{\sigma} = \begin{Bmatrix} \sigma_{11} \\ \sigma_{22} \\ \sigma_{33} \\ \sigma_{23} \\ \sigma_{13} \\ \sigma_{12} \end{Bmatrix} \equiv \begin{Bmatrix} \sigma_1 \\ \sigma_2 \\ \sigma_3 \\ \sigma_4 \\ \sigma_5 \\ \sigma_6 \end{Bmatrix} \tag{B.8}$$

whereas the infinitesimal strain vector reads:

$$[\boldsymbol{\varepsilon}] = \begin{bmatrix} \varepsilon_{11} & \varepsilon_{12} & \varepsilon_{13} \\ \varepsilon_{21} & \varepsilon_{22} & \varepsilon_{23} \\ \varepsilon_{31} & \varepsilon_{32} & \varepsilon_{33} \end{bmatrix} \longrightarrow \boldsymbol{\varepsilon} = \begin{Bmatrix} \varepsilon_{11} \\ \varepsilon_{22} \\ \varepsilon_{33} \\ 2\varepsilon_{23} \\ 2\varepsilon_{13} \\ 2\varepsilon_{12} \end{Bmatrix} \equiv \begin{Bmatrix} \varepsilon_1 \\ \varepsilon_2 \\ \varepsilon_3 \\ \varepsilon_4 \\ \varepsilon_5 \\ \varepsilon_6 \end{Bmatrix}. \tag{B.9}$$

This strain vector is also called the *engineering strains* vector, as shear strain components are multiplied by a factor of 2 in order to preserve the internal product between stress- and strain-like tensors:

$$[\boldsymbol{\varepsilon}] : [\boldsymbol{\sigma}] = \boldsymbol{\sigma}^T \boldsymbol{\varepsilon}. \tag{B.10}$$

Given all these points, the generalised Hooke's law outlined as:

$$\varepsilon_{ij} = \mathsf{S}_{ijkl}\, \sigma_{kl}, \tag{B.11}$$

$$\sigma_{ij} = \mathsf{C}_{ijkl}\, \varepsilon_{kl} \tag{B.12}$$

can be written in a matrix basis (following Voigt notation) as:

$$\varepsilon_m = \mathsf{S}_{mn}\, \sigma_n, \tag{B.13}$$

$$\sigma_m = \mathsf{C}_{mn}\, \varepsilon_n. \tag{B.14}$$

B.2 Effect of Material Symmetry on the Elasticity Matrix

In this Section, we present 8 elasticity matrices, each one related to a different group of material symmetry. The names of the material symmetries are indicated in each one of the listed entries, along with the *Number of Independent Elastic Components* (NIEC) and the *Number of Planes of Elastic Symmetry* (NPES):

1. *Triclinic symmetry* (NIEC = 21; NPES = 0):

$$\mathbf{C} = \begin{bmatrix} \mathsf{C}_{11} & \mathsf{C}_{12} & \mathsf{C}_{13} & \mathsf{C}_{14} & \mathsf{C}_{15} & \mathsf{C}_{16} \\ & \mathsf{C}_{22} & \mathsf{C}_{23} & \mathsf{C}_{24} & \mathsf{C}_{25} & \mathsf{C}_{26} \\ & & \mathsf{C}_{33} & \mathsf{C}_{34} & \mathsf{C}_{35} & \mathsf{C}_{36} \\ & & & \mathsf{C}_{44} & \mathsf{C}_{45} & \mathsf{C}_{46} \\ & & & & \mathsf{C}_{55} & \mathsf{C}_{56} \\ \text{sym.} & & & & & \mathsf{C}_{66} \end{bmatrix}; \tag{B.15}$$

2. *Monoclinic symmetry* (NIEC = 13; NPES = 1):

$$\mathbf{C} = \begin{bmatrix} \mathsf{C}_{11} & \mathsf{C}_{12} & \mathsf{C}_{13} & \mathsf{C}_{14} & 0 & 0 \\ & \mathsf{C}_{22} & \mathsf{C}_{23} & \mathsf{C}_{24} & 0 & 0 \\ & & \mathsf{C}_{33} & \mathsf{C}_{34} & 0 & 0 \\ & & & \mathsf{C}_{44} & 0 & 0 \\ & & & & \mathsf{C}_{55} & \mathsf{C}_{56} \\ \text{sym.} & & & & & \mathsf{C}_{66} \end{bmatrix}; \tag{B.16}$$

3. *Orthotropic/Rhombic symmetry* (NIEC = 9; NPES = 3):

$$\mathbf{C} = \begin{bmatrix} \mathsf{C}_{11} & \mathsf{C}_{12} & \mathsf{C}_{13} & 0 & 0 & 0 \\ & \mathsf{C}_{22} & \mathsf{C}_{23} & 0 & 0 & 0 \\ & & \mathsf{C}_{33} & 0 & 0 & 0 \\ & & & \mathsf{C}_{44} & 0 & 0 \\ & & & & \mathsf{C}_{55} & 0 \\ \text{sym.} & & & & & \mathsf{C}_{66} \end{bmatrix}; \tag{B.17}$$

4. *Trigonal symmetry* (NIEC = 6; NPES = 3):

$$\mathbf{C} = \begin{bmatrix} \mathsf{C}_{11} & \mathsf{C}_{12} & \mathsf{C}_{13} & \mathsf{C}_{14} & 0 & 0 \\ & \mathsf{C}_{11} & \mathsf{C}_{13} & \mathsf{C}_{24} & 0 & 0 \\ & & \mathsf{C}_{33} & 0 & 0 & 0 \\ & & & \mathsf{C}_{44} & 0 & 0 \\ & & & & \mathsf{C}_{44} & 0 \\ \text{sym.} & & & & & \mathsf{C}_{66} \end{bmatrix}; \tag{B.18}$$

where

$$\mathsf{C}_{24} = -\mathsf{C}_{14}, \tag{B.19}$$

$$\mathsf{C}_{66} = \frac{\mathsf{C}_{11} - \mathsf{C}_{22}}{2} \tag{B.20}$$

5. *Tetragonal symmetry* (NIEC = 6; NPES = 5):

$$\mathbf{C} = \begin{bmatrix} \mathsf{C}_{11} & \mathsf{C}_{12} & \mathsf{C}_{13} & 0 & 0 & 0 \\ & \mathsf{C}_{11} & \mathsf{C}_{13} & 0 & 0 & 0 \\ & & \mathsf{C}_{33} & 0 & 0 & 0 \\ & & & \mathsf{C}_{44} & 0 & 0 \\ & & & & \mathsf{C}_{44} & 0 \\ \text{sym.} & & & & & \mathsf{C}_{66} \end{bmatrix}; \tag{B.21}$$

6. *Hexagonal symmetry* (NIEC = 5; NPES = $1 + \infty$):

$$\mathbf{C} = \begin{bmatrix} \mathsf{C}_{11} & \mathsf{C}_{12} & \mathsf{C}_{13} & 0 & 0 & 0 \\ & \mathsf{C}_{11} & \mathsf{C}_{13} & 0 & 0 & 0 \\ & & \mathsf{C}_{33} & 0 & 0 & 0 \\ & & & \mathsf{C}_{44} & 0 & 0 \\ & & & & \mathsf{C}_{44} & 0 \\ \text{sym.} & & & & & \mathsf{C}_{66} \end{bmatrix}; \tag{B.22}$$

where

$$\mathsf{C}_{66} = \frac{\mathsf{C}_{11} - \mathsf{C}_{22}}{2} \tag{B.23}$$

7. *Cubic symmetry* (NIEC = 3; NPES = 9):

$$\mathbf{C} = \begin{bmatrix} \mathsf{C}_{11} & \mathsf{C}_{12} & \mathsf{C}_{12} & 0 & 0 & 0 \\ & \mathsf{C}_{11} & \mathsf{C}_{12} & 0 & 0 & 0 \\ & & \mathsf{C}_{11} & 0 & 0 & 0 \\ & & & \mathsf{C}_{44} & 0 & 0 \\ & & & & \mathsf{C}_{44} & 0 \\ \text{sym.} & & & & & \mathsf{C}_{44} \end{bmatrix}; \tag{B.24}$$

8. *Isotropic symmetry* (NIEC = 2; NPES = ∞):

$$\mathbf{C} = \begin{bmatrix} \mathsf{C}_{11} & \mathsf{C}_{12} & \mathsf{C}_{12} & 0 & 0 & 0 \\ & \mathsf{C}_{11} & \mathsf{C}_{12} & 0 & 0 & 0 \\ & & \mathsf{C}_{11} & 0 & 0 & 0 \\ & & & \mathsf{C}_{44} & 0 & 0 \\ & & & & \mathsf{C}_{44} & 0 \\ \text{sym.} & & & & & \mathsf{C}_{44} \end{bmatrix}. \tag{B.25}$$

where

$$\mathsf{C}_{44} = \frac{\mathsf{C}_{11} - \mathsf{C}_{12}}{2} \tag{B.26}$$

B.3 Relation between Elastic Constants for Isotropic Solids

In this Section, we present the mathematical relations between some of the most common elastic constants used to describe the elastic response of isotropic relations. In Table B.1, the relations between the Young's modulus E, the shear modulus G, the Poisson's ratio ν and the bulk modulus K are established.

Table B.1: Relations between elastic constants for isotropic solids.

	G	E	ν	K
G , E	G	E	$\frac{E-2G}{2G}$	$\frac{GE}{3(3G-E)}$
G , ν	G	$2G(1+\nu)$	ν	$\frac{2G(1+\nu)}{3(1-2\nu)}$
G , K	G	$\frac{9KG}{3K+G}$	$\frac{3K-2G}{6K+2G}$	K
E , ν	$\frac{E}{2(1+v)}$	E	ν	$\frac{E}{3(1-2\nu)}$
E , K	$\frac{3KE}{9K-E}$	E	$\frac{3K-E}{6K}$	K
ν , K	$\frac{3K(1-2\nu)}{2(1+\nu)}$	$3K(1-2\nu)$	ν	K

This page was intentionally left with this sentence.

References

Asaro, R. J. and Needleman, A. (1985). Overview no. 42: Texture development and strain hardening in rate dependent polycrystals. *Acta Metallurgica*, 33(6):923–953.

Barlat, F. and Lian, K. (1989). Plastic behavior and stretchability of sheet metals. Part I: A yield function for orthotropic sheets under plane stress conditions. *International Journal of Plasticity*, 5(1):51–66.

Berryman, J. G. (2005). Bounds and self-consistent estimates for elastic constants of random polycrystals with hexagonal, trigonal, and tetragonal symmetries. *Journal of the Mechanics and Physics of Solids*, 53(10):2141–2173.

Bilby, A., Lardner, L., and Stroh, A. (1957). Continuous distributions of dislocations and the theory of plasticity. In *Actes Du IXe Congres International de Mecanique Appliquee*, volume 8, page 35e44. Bruxelles.

Böhlke, T., Jöchen, K., Kraft, O., Löhe, D., and Schulze, V. (2010). Elastic properties of polycrystalline microcomponents. *Mechanics of Materials*, 42(1):11–23.

Bonet, J., Gil, A. J., and Wood, R. D. (2016). *Nonlinear Solid Mechanics for Finite Element Analysis: Statics*. Cambridge University Press.

Bower, A. F. (2009). *Applied Mechanics of Solids*. CRC Press.

Brenner, R., Lebensohn, R., and Castelnau, O. (2009). Elastic anisotropy and yield surface estimates of polycrystals. *International Journal of Solids and Structures*, 46(16):3018–3026.

Carvalho, R. P. (2015). *Análise do comportamento elasto-plástico de materiais dúcteis baseada em homogeneização computacional*. Master's dissertation, University of Porto.

Cho, S. W. and Chasiotis, I. (2007). Elastic Properties and Representative Volume Element of Polycrystalline Silicon for MEMS. *Experimental Mechanics*, 47(1):37–49.

Chung, D. H. and Buessem, W. R. (1967). The Elastic Anisotropy of Crystals. *Journal of Applied Physics*, 38(5):2010–2012.

Clausen, B. (1997). *Characterisation of Polycrystal Deformation by Numerical Modelling and Neutron Diffraction Measurements*. Number 985 in Risø-R. Risø National Laboratory, Roskilde. OCLC: 246383603.

Coenen, E., Kouznetsova, V., and Geers, M. (2012). Novel boundary conditions for strain localization analyses in microstructural volume elements. *International Journal for Numerical Methods in Engineering*, 90(1):1–21.

Coleman, B. D. and Gurtin, M. E. (1969). *Thermodynamics with Internal State Variables*. Defense Technical Information Center.

Cottrell, S. A. H. (1964). *The Mechanical Properties of Matter*. Wiley.

Darrieulat, M. and Piot, D. (1996). A method of generating analytical yield surfaces of crystalline materials. *International Journal of Plasticity*, 12(5):575–610.

de Bortoli, D. (2017). *Towards a Predictive Multi-Scale, Thermodynamically Consistent Constitutive Model for Mechanically-Induced Martensitic Phase Transformations*. PhD thesis, Swansea University.

de Souza Neto, E. and Feijóo, R. (2006). Variational Foundations of Multi-Scale Constitutive Models of Solid: Small and Large Strain Kinematical Formulation. *LNCC R&D Report*.

de Souza Neto, E. A. and Feijóo, R. A. (2008). On the equivalence between spatial and material volume averaging of stress in large strain multi-scale solid constitutive models. *Mechanics of Materials*, 40(10):803–811.

de Souza Neto, E. A., Perić, D., and Owen, D. R. J. (2008). *Computational Methods for Plasticity: Theory and Applications*. John Wiley & Sons.

Dieter, G. E. (1988). *Mechanical Metallurgy*. McGraw-Hill, 3 edition.

El Houdaigui, F., Forest, S., Gourgues, A.-F., and Jeulin, D. (2007). On the Size of the Representative Volume Element for Isotropic Elastic Polycrystalline Copper. In Bai, Y. L., Zheng, Q. S., and Wei, Y. G., editors, *IUTAM Symposium on Mechanical Behavior and Micro-Mechanics of Nanostructured Materials: Proceedings of the IUTAM Symposium Held in Beijing, China, June 27-30, 2005*, Solid Mechanics and Its Applications. Springer Netherlands.

Engler, O. and Randle, V. (2009). *Introduction to Texture Analysis: Macrotexture, Microtexture, and Orientation Mapping, Second Edition*. CRC Press.

Ericksen, J. (1984). The Cauchy and Born hypothesis for crystals. In *Phase Transformations and Material Instabilities in Solids*, pages 61–77. Elsevier.

Eshelby, J. D. (1957). The determination of the elastic field of an ellipsoidal inclusion, and related problems. *Proc. R. Soc. Lond. A*, 241(1226):376–396.

Evesque, P. (2005). Fluctuations, Correlation and Representative Elementary Volume (REV) in Granular Materials. *arXiv:cond-mat/0506385*.

Ferreira, B. P. (2017). *Avaliação da precisão de um modelo de dano contínuo através de um modelo multi-escala baseado em homogeneização computacional*. Master's dissertation, University of Porto.

Freund, L. B. and Suresh, S. (2004). *Thin Film Materials: Stress, Defect Formation and Surface Evolution*. Cambridge University Press, Cambridge.

Friák, M., Counts, W. A., Ma, D., Sander, B., Holec, D., Raabe, D., and Neugebauer, J. (2012). Theory-Guided Materials Design of Multi-Phase Ti-Nb Alloys with Bone-Matching Elastic Properties. *Materials*, 5(10):1853–1872.

Fritzen, F., Böhlke, T., and Schnack, E. (2009). Periodic three-dimensional mesh generation for crystalline aggregates based on Voronoi tessellations. *Computational Mechanics*, 43(5):701–713.

Gairola, B. K. D. and Kröner, E. (1981). A simple formula for calculating the bounds and the self-consistent value of the shear modulus of a polycrystalline aggregate of cubic crystals. *International Journal of Engineering Science*, 19(6):865–869.

Gitman, I. M., Askes, H., and Sluys, L. J. (2007). Representative volume: Existence and size determination. *Engineering Fracture Mechanics*, 74(16):2518–2534.

Gröger, R., Racherla, V., Bassani, J. L., and Vitek, V. (2008). Multiscale modeling of plastic deformation of molybdenum and tungsten: II. Yield criterion for single crystals based on atomistic studies of glide of $1/2\langle 111\rangle$ screw dislocations. *Acta Materialia*, 56(19):5412–5425.

Guedes, J. and Kikuchi, N. (1990). Preprocessing and postprocessing for materials based on the homogenization method with adaptive finite element methods. *Computer Methods in Applied Mechanics and Engineering*, 83:143–198.

Gurtin, M. E. (1981). *An Introduction to Continuum Mechanics*. Academic Press, New York.

Habraken, A. M. (2004). Modelling the plastic anisotropy of metals. *Archives of Computational Methods in Engineering*, 11(1):3–96.

Hashin, Z. (1983). Analysis of composite materials – A survey. *Journal of Applied Mechanics*, 50(3):481–505.

Hashin, Z. and Shtrikman, S. (1962). A variational approach to the theory of the elastic behaviour of polycrystals. *Journal of the Mechanics and Physics of Solids*, 10(4):343–352.

Hill, R. (1948). A theory of the yielding and plastic flow of anisotropic metals. *Proc. R. Soc. Lond. A*, 193(1033):281–297.

Hill, R. (1952). The Elastic Behaviour of a Crystalline Aggregate. *Proceedings of the Physical Society. Section A*, 65(5):349–354.

Hill, R. (1963). Elastic properties of reinforced solids: Some theoretical principles. *Journal of the Mechanics and Physics of Solids*, 11(5):357–372.

Hill, R. (1965). A self-consistent mechanics of composite materials. *Journal of the Mechanics and Physics of Solids*, 13(4):213–222.

Holzapfel, G. A. (2000). *Nonlinear Solid Mechanics: A Continuum Approach for Engineering*. Wiley.

Hutchinson, J. W. (1970). Elastic-plastic behaviour of polycrystalline metals and composites. *Proc. R. Soc. Lond. A*, 319(1537):247–272.

Jöchen, K. (2013). *Homogenization of the Linear and Non-Linear Mechanical Behavior of Polycrystals*. KIT Scientific Publishing.

Kamaya, M. (2009). A procedure for estimating Young's modulus of textured polycrystalline materials. *International Journal of Solids and Structures*, 46(13):2642–2649.

Kanit, T., Forest, S., Galliet, I., Mounoury, V., and Jeulin, D. (2003). Determination of the size of the representative volume element for random composites: Statistical and numerical approach. *International Journal of Solids and Structures*, 40(13):3647–3679.

Karafillis, A. P. and Boyce, M. C. (1993). A general anisotropic yield criterion using bounds and a transformation weighting tensor. *Journal of the Mechanics and Physics of Solids*, 41(12):1859–1886.

Kim, H.-G. (2014). The effect of different forms of strain energy functions in hyperelasticity-based crystal plasticity models on texture evolution and mechanical response of face-centered cubic crystals. *International Journal for Numerical Methods in Engineering*, 100(4):300–320.

Ko, W. H. (2007). Trends and frontiers of MEMS. *Sensors and Actuators A: Physical*, 136(1):62–67.

Kocks, U. F. (1970). The relation between polycrystal deformation and single-crystal deformation. *Metallurgical and Materials Transactions*, 1(5):1121–1143.

Kocks, U. F., Tomé, C. N., Wenk, H.-R., and Beaudoin, A. J. (2000). *Texture and Anisotropy: Preferred Orientations in Polycrystals and Their Effect on Materials Properties*. Cambridge University Press.

Kröner, E. (1977). Bounds for effective elastic moduli of disordered materials. *Journal of the Mechanics and Physics of Solids*, 25(2):137–155.

Kube, C. M. (2016). Elastic anisotropy of crystals. *AIP Advances*, 6(9):095209.

Kube, C. M. and de Jong, M. (2016). Elastic constants of polycrystals with generally anisotropic crystals. *Journal of Applied Physics*, 120(16):165105.

Ledbetter, H. and Migliori, A. (2006). A general elastic-anisotropy measure. *Journal of Applied Physics*, 100(6):063516.

Ledbetter, H. M. and Naimon, E. R. (1974). Elastic Properties of Metals and Alloys. II. Copper. *Journal of Physical and Chemical Reference Data*, 3(4):897–935.

Ling, X., Horstemeyer, M. F., and Potirniche, G. P. (2005). On the numerical implementation of 3D rate-dependent single crystal plasticity formulations. *International Journal for Numerical Methods in Engineering*, 63(4):548–568.

Liu, Z., Kafka, O. L., Yu, C., and Liu, W. K. (2018). Data-Driven Self-consistent Clustering Analysis of Heterogeneous Materials with Crystal Plasticity. In Oñate, E., Peric, D., de Souza Neto, E., and Chiumenti, M., editors, *Advances in Computational Plasticity: A Book in Honour of D. Roger J. Owen*, Computational Methods in Applied Sciences, pages 221–242. Springer International Publishing, Cham.

Lopes, I. A. R. (2016). Computational Strategies for the Solution of Coupled Multi-Scale Problems. Technical Report, Faculdade de Engenharia da Universidade do Porto.

Mandel, J. (1971). *Plasticité classique et viscoplasticité: course held at the Department of Mechanics of Solids, September-October, 1971*, volume 97 of *CISM Courses and Lectures*. Springer-Verlag.

Mapar, A., Ghassemi-Armaki, H., Pourboghrat, F., and Kumar, K. S. (2017). A differential-exponential hardening law for non-Schmid crystal plasticity finite element modeling of ferrite single crystals. *International Journal of Plasticity*, 91:268–299.

McGinty, R. D. (2001). *Multiscale Representation of Polycrystalline Inelasticity*. PhD thesis, Georgia Institute of Technology.

Nemat-Nasser, S. (1999). Averaging Theorems in Finite Deformation Plasticity. *Mechanics of Materials*, (31):493–523.

Nemat-Nasser, S. and Hori, M. (1993). *Micromechanics: Overall Properties of Heterogeneous Materials*. Elsevier.

Nordmann, J., Aßmus, M., and Altenbach, H. (2018). Visualising elastic anisotropy: Theoretical background and computational implementation. *Continuum Mechanics and Thermodynamics*, pages 1–20.

Nygårds, M. (2003). Number of grains necessary to homogenize elastic materials with cubic symmetry. *Mechanics of Materials*, 35(11):1049–1057.

Peirce, D., Asaro, R. J., and Needleman, A. (1982). An analysis of nonuniform and localized deformation in ductile single crystals. *Acta Metallurgica*, 30(6):1087–1119.

Perdahcıoğlu, E. S. and Geijselaers, H. J. M. (2012). A macroscopic model to simulate the mechanically induced martensitic transformation in metastable austenitic stainless steels. *Acta Materialia*, 60(11):4409–4419.

Perić, D. (1993). On a class of constitutive equations in viscoplasticity: Formulation and computational issues. *International Journal for Numerical Methods in Engineering*, 36(8):1365–1393.

Povall, T. M., McBride, A. T., and Reddy, B. D. (2014). Finite element simulation of large-strain single-crystal viscoplasticity: An investigation of various hardening relations. *Computational Materials Science*, 81:386–396.

Prime Faraday, P. (2002). *An Introduction to Mems*. Prime Faraday Partnership.

Quek, S. S. and Liu, G. R. (2003). *Finite Element Method: A Practical Course*. Elsevier.

Quey, R. (2018). Neper Reference Manual - The documentation for Neper 3.1.1. A software package for polycrystal generation and meshing.

Quey, R., Dawson, P. R., and Barbe, F. (2011). Large-scale 3D random polycrystals for the finite element method: Generation, meshing and remeshing. *Computer Methods in Applied Mechanics and Engineering*, 200(17–20):1729–1745.

Ranganathan, S. I. and Ostoja-Starzewski, M. (2008a). Scaling function, anisotropy and the size of RVE in elastic random polycrystals. *Journal of the Mechanics and Physics of Solids*, 56(9):2773–2791.

Ranganathan, S. I. and Ostoja-Starzewski, M. (2008b). Universal elastic anisotropy index. *Physical Review Letters*, 101(5):055504.

Reina, C. and Conti, S. (2014). Kinematic description of crystal plasticity in the finite kinematic framework: A micromechanical understanding of F=FeFp. *Journal of the Mechanics and Physics of Solids*, 67:40–61.

Reis, F. J. d. P. (2014). Multi-Scale Modelling and Analysis of Heterogeneous Solids at Finite Strains.

Reis, F. J. P. and Andrade Pires, F. M. (2014). A mortar based approach for the enforcement of periodic boundary conditions on arbitrarily generated meshes. *Computer Methods in Applied Mechanics and Engineering*, 274:168–191.

Reuss, A. (1929). Berechnung der Fließgrenze von Mischkristallen auf Grund der Plastizitätsbedingung für Einkristalle . *ZAMM - Journal of Applied Mathematics and Mechanics / Zeitschrift für Angewandte Mathematik und Mechanik*, 9(1):49–58.

Scheunemann, L. (2017). *Scale-Bridging of Elasto-Plastic Microstructures Using Statistically Similar Representative Volume Elements*. Wissenschaftliche Abschlussarbeiten » Dissertation, Universität Duisburg-Essen, Fakultät für Ingenieurwissenschaften » Bauwissenschaften.

Stanimirović, Z. S. a. I. (2009). Mechanical Properties of MEMS Materials. *Micro Electronic and Mechanical Systems*.

Steinmann, P. and Stein, E. (1996). On the numerical treatment and analysis of finite deformation ductile single crystal plasticity. *Computer Methods in Applied Mechanics and Engineering*, 129(3):235–254.

Suwas, S. and Ray, R. K. (2014). *Crystallographic Texture of Materials*. Springer London.

Tadmor, E. B., Miller, R. E., and Elliott, R. S. (2012). *Continuum Mechanics and Thermodynamics: From Fundamental Concepts to Governing Equations*. Cambridge University Press.

Taylor, G. (1938). Plastic strain in metals. *Plastic Strain in Metals*, pages 307–324.

Terada, K., Hori, M., Kyoya, T., and Kikuchi, N. (2000). Simulation of the multi-scale convergence in computational homogenization approaches. *International Journal of Solids and Structures*, 37(16):2285–2311.

Ting, T. C. T. (1996). *Anisotropic Elasticity: Theory and Applications*. Oxford University Press.

Tresca, H.-E. (1864). *Mémoire sur l'écoulement des corps solides soumis à de fortes pressions*. Gauthier-Villars.

Truesdell, C. (1969). *Rational Thermodynamics*. McGraw-Hill, New York.

Vieira de Carvalho, M. (2016). *Computational Framework for Multi-Scale Analysis of Heterogeneous Materials Using Digital Image Recognition.* Master's dissertation, University of Porto.

Voigt, W. (1910). *Lehrbuch der kristallphysik (mit ausschluss der kristalloptik).* Leipzig, Berlin, B.G. Teubner.

von Mises, R. (1928). Mechanik der plastischen Formänderung von Kristallen. *ZAMM - Journal of Applied Mathematics and Mechanics / Zeitschrift für Angewandte Mathematik und Mechanik*, 8(3):161–185.

Watanabe, I. and Terada, K. (2010). A method of predicting macroscopic yield strength of polycrystalline metals subjected to plastic forming by micro–macro de-coupling scheme. *International Journal of Mechanical Sciences*, 52(2):343–355.

Yalcinkaya, T., Brekelmans, W. A. M., and Geers, M. G. D. (2008). BCC single crystal plasticity modeling and its experimental identification. *Modelling and Simulation in Materials Science and Engineering*, 16(8):085007.

Zeller, R. and Dederichs, P. H. (1973). Elastic Constants of Polycrystals. *physica status solidi (b)*, 55(2):831–842.

Zener, C. M. and Siegel, S. (1949). Elasticity and Anelasticity of Metals. *The Journal of Physical and Colloid Chemistry*, 53(9):1468–1468.

Zienkiewicz, O. C., Taylor, R. L., and Fox, D. (2014). *The Finite Element Method for Solid and Structural Mechanics.* Butterworth-Heinemann, 7th edition.

Zienkiewicz, O. C., Taylor, R. L., and Zhu, J. Z. (2013). *The Finite Element Method: Its Basis and Fundamentals.* Butterworth-Heinemann, 7th edition.